Saint Petersburg State University

As a manuscript

Kurnosenko Sergei Alekseevich

# New photocatalysts of hydrogen generation processes based on layered perovskite-like titanates $HLnTiO_4$ and $H_2Ln_2Ti_3O_{10}$ (Ln = La, Nd)

Specialty 1.4.4. Physical chemistry

Dissertation for the degree of candidate of chemical sciences

Translation from Russian

Scientific supervisor:
doctor of chemical sciences,
professor
Zvereva Irina Alekseevna

Saint Petersburg
2024

## Table of contents

# Introduction

## Relevance of the topic

In the context of depleting reserves of fossil fuels and tightening environmental legislation, hydrogen is considered as one of the most promising energy sources, which compares favorably with traditional analogues by its environmental friendliness in use and high calorific value. However, currently widely used methods of industrial hydrogen production (in particular, steam reforming of hydrocarbons and coal gasification) are extremely energy-intensive due to the need to create high temperatures and rely on continuously declining mineral reserves. In view of this, the development of alternative methods for producing hydrogen fuel, such as photocatalytic decomposition of water and aqueous solutions of organic compounds representing components or products of processing plant biomass (bioalcohols, carbohydrates, etc.), is of particular importance. Such processes involve publicly available shareware resources in the form of water and solar radiation, as well as renewable plant biomass, the components of which themselves are characterized by a relatively low calorific value, but can be photocatalytically processed to produce significantly more energy-intensive hydrogen fuel, which in the long term seems to be an effective solution from both an environmental and economic point of view. Moreover, photocatalytic production of hydrogen can simultaneously serve as a method for purifying aqueous media if the organic compounds decomposed in this process act as pollutants.

In view of this, one of the actively developing areas of modern chemical science is the design of new photocatalytically active materials for the needs of hydrogen energy. The most studied photocatalysts at the moment are materials based on simple semiconductor oxides ($TiO_2$, $ZrO_2$, $Ta_2O_5$, ZnO and others), but their activity is often insufficient for widespread practical use due to the intense recombination of photogenerated charge carriers, small specific surface area and inability to use visible light. In this regard, in research of the last decade, special attention has been paid to photocatalysts based on layered perovskite-like oxides, the high activity of which is determined both by the unique structure of the perovskite layer, which promotes efficient separation of electron-hole pairs, and by the composition of the interlayer space, considered as an additional reaction zone in a photocatalytic process. Structural and chemical features of these objects, which distinguish them from non-layered compounds, make it possible to purposefully implement such approaches to the creation of new highly efficient

photocatalysts for hydrogen generation, such as modification of the composition of the interlayer space and liquid-phase exfoliation into nanosheets, the systematic study of which is the subject of this work.

**Degree of the topic development**

Over the past two decades, layered perovskite-like oxides have been one of the intensively studied classes of heterogeneous photocatalysts that are superior in activity to traditional non-layered materials. To further improve their photocatalytic properties, methods of cationic and anionic substitution in the perovskite layer, interlayer ion exchange, creation of composites with particles of cocatalysts and photosensitizers, as well as exfoliation into nanosheets are widely used.

At the same time, there are a number of significant gaps in the available literature on layered perovskite-like photocatalysts for hydrogen generation. Firstly, outside the applicant's publications, the literature does not cover the issue of studying hybrid organic-inorganic photocatalysts – materials obtained by modifying the interlayer space of layered perovskite-like oxides with organic components, which, as will be shown below, can lead to an increase in photocatalytic activity by more than two orders of magnitude. Accordingly, questions remain unexplored about the relationship between the composition of the interlayer reaction zone and the activity exhibited, as well as about the potential transformations of interlayer modifiers under photocatalysis conditions. Secondly, the creation of photocatalysts based on perovskite nanosheets, despite the known efficiency of this approach, has been sufficiently studied only for a narrow range of layered oxides that undergo liquid-phase exfoliation relatively easily (in particular, Dion-Jacobson niobates $HA_2Nb_3O_{10}$ (A = Ca, Sr)). At the same time, information on the activity of nanosheets of other promising photocatalysts, such as Ruddlesden-Popper titanates $HLnTiO_4$ and $H_2Ln_2Ti_3O_{10}$ (Ln = La or lanthanide), is practically absent in the literature. In addition, the available literature does not address the fundamentally important issue of the relationship between the form of perovskite nanosheets used (initial nanosheets without reassembly and nanosheets reassembled by different methods) and the photocatalytic activity exhibited by them. As will be shown below, the form of such photocatalysts used greatly influences the efficiency of hydrogen generation, and the nature of this influence depends, among other things, on the composition of the reaction solution. Thirdly, the photocatalytic activity of layered perovskite-like oxides has practically not been studied in the

processes of producing hydrogen from carbohydrate solutions, which are one of the key components of plant biomass.

Thus, despite the large number of known layered perovskite-like photocatalysts, some promising approaches to improving their photocatalytic activity (in particular, interlayer organic modification and exfoliation into nanosheets) require separate detailed study.

**Purpose and objectives of the work**

The purpose of this work is development and comprehensive investigation of photocatalysts for hydrogen generation based on organic-inorganic derivatives and nanosheets of layered perovskite-like titanates $HLnTiO_4$ and $H_2Ln_2Ti_3O_{10}$ (Ln = La, Nd). To achieve this goal, the following tasks are set:

1. Synthesis of amine and alcohol derivatives of the titanates with different lengths of the hydrocarbon chain of the interlayer organic modifier using methods developed and optimized by the applicant;
2. Synthesis of the titanate derivatives with aromatic photosensitizing modifiers;
3. Obtaining initial titanate nanosheets, as well as those reassembled by two approaches (filtration, acid precipitation) using methods developed and optimized by the applicant;
4. Physical-chemical study of the structure, quantitative composition, light absorption region, position of the energy band edges, luminescence lifetimes, morphology and specific surface area of the obtained samples;
5. Study of the kinetics of photoinduced hydrogen evolution from aqueous solutions of methanol, D-glucose, D-xylose, as well as pure water under ultraviolet and visible radiation using the obtained organic-inorganic derivatives, nanosheets and their composites with Pt nanoparticles as a cocatalyst;
6. Study of the stability and potential structural-chemical transformations of the obtained photocatalysts under operating conditions;
7. Comparative analysis of the photocatalysts based on organic-inorganic derivatives and nanosheets of titanates with each other and with photocatalysts based on niobates $HA_2Nb_3O_{10}$ (A = Ca, Sr), studied separately by the applicant. Identification of the main factors influencing the photocatalytic activity of the organic-inorganic derivatives and nanosheets.

**Methodology**

When performing the experimental part of the work, a wide range of synthetic approaches, physical-chemical characterizations and kinetic methods for studying photocatalytic reactions were involved, as well as analysis, systematization, generalization, comparison and other general scientific methods were used in interpreting the data obtained.

The initial layered compounds were synthesized using the high-temperature ceramic technology, and, to subsequently obtain the desired photocatalysts, they were subjected to various topochemical modifications using «soft chemistry» approaches: ion exchange, intercalation and grafting of organic compounds, liquid-phase exfoliation into nanosheets and their reassembly. General chemical characterization of the resulting photocatalysts was carried out using X-ray diffraction analysis, Raman spectroscopy, nuclear magnetic resonance spectroscopy, atomic emission spectroscopy, energy-dispersive X-ray microanalysis, thermogravimetry, elemental CHN-analysis and other methods. To establish the region of their own light absorption and the position of the energy band edges, the photocatalysts were studied using diffuse reflectance spectroscopy with the Kubelka-Munk transformation, as well as photoelectron spectroscopy. The average lifetimes of photogenerated charge carriers were estimated from time-resolved luminescence spectroscopy data. The morphology of the samples was studied by scanning, transmission and atomic force microscopy, and their specific surface area was determined using the Brunauer, Emmett and Teller multipoint method. To control particle sizes, as well as the stability and composition of photocatalyst suspensions, methods of dynamic light scattering, laser granulometry, spectrophotometry and pH-metry were used. The photon flux of the light sources used in photocatalytic experiments was measured by ferrioxalate actinometry. Kinetics of photocatalytic reactions of hydrogen evolution was studied on a specially designed laboratory setting with an online gas chromatograph. After photocatalytic measurements, standard mathematical processing of the kinetic curves was carried out, followed by calculation of the rate and apparent quantum efficiency of the reactions, as well as the factor of increase in the rate when adding a cocatalyst. The concentration dependence of photocatalytic activity was considered within the framework of the standard Langmuir-Hinshelwood model for heterogeneous catalysis. The stability of the most active photocatalysts was studied both from the point of view of the maintaining photocatalytic activity, and from the point of view of changes in their structure and

composition, detected using the above physical-chemical methods. The interpretation of the photocatalytic properties was carried out taking into account the literature concepts of layered perovskite-like photocatalysts and, in particular, the probable functioning of their interlayer space as an additional reaction zone under photocatalysis conditions.

**Main scientific results**

1. 60 organic-inorganic derivatives of layered perovskite-like titanates $HLnTiO_4$ and $H_2Ln_2Ti_3O_{10}$ (Ln = La, Nd), representing the products of intercalation of primary amines, grafting of alcohols and aromatic compounds in the interlayer space, have been successfully synthesized and characterized in detail. It has been established that organic modification leads to a significant expansion of the interlayer space, proportional to the size of the introduced components. In the amine derivatives, ionic bonding occurs between the inorganic matrix and the organic component; in the alcohol derivatives and those containing aromatic modifiers, covalent bonding occurs. The resulting derivatives contain on average 0.4 units of an organic component per proton of the initial titanate, as well as a certain amount of intercalated water [224–226,230];
2. It has been established that during the formation of amine and alcohol derivatives, the optical band gap of the titanates changes slightly and the long-wavelength light absorption edge remains in the near ultraviolet region [229,230], while grafting of aromatic compounds leads to its pronounced shift to the visible range;
3. Amine and alcohol derivatives of the titanates have been systematically studied as photocatalysts for hydrogen generation from aqueous-organic mixtures, as well as pure water under ultraviolet radiation. It has been shown that organic modification of the interlayer space is a highly effective approach to increasing photocatalytic activity, the increase factor of which reaches 117 times. The most active among the obtained samples is the platinum-modified ethanol derivative $H_2La_2Ti_3O_{10}\times EtOH/Pt$, in the presence of which the rate (apparent quantum efficiency) of hydrogen evolution from a 1% (mol.) aqueous solution of methanol reaches 120 $mmol\cdot h^{-1}\cdot g^{-1}$ (40.1%) [229,230];
4. It has been shown that in many cases the photocatalytic activity of the samples in the series of amine and alcohol derivatives changes symbatically with the degree of hydration of the interlayer space [229,230];

5. Using the example of selected organic-inorganic titanate derivatives, it is shown that the dependences of photocatalytic activity on the concentration of methanol, the concentration of the photocatalyst, and the fraction of the platinum cocatalyst pass through a maximum [231,232]. At the same time, optimization of these parameters makes it possible to achieve the activity of 175 $mmol \cdot h^{-1} \cdot g^{-1}$ (58%);
6. It has been established that the most active titanate derivatives can also serve as efficient photocatalysts for hydrogen generation from 1% (mol.) aqueous solutions of D-glucose and D-xylose, exhibiting the activity up to 14.3 $mmol \cdot h^{-1} \cdot g^{-1}$ (6.0%) and 16.8 $mmol \cdot h^{-1} \cdot g^{-1}$ (7.0%), respectively [233]. When generating hydrogen from pure water using the same derivatives, the activity up to 3.6 $mmol \cdot h^{-1} \cdot g^{-1}$ (1.5%) is achieved;
7. It has been shown that interlayer organic modifiers of the amine and alcohol derivatives undergo partial degradation during photocatalysis in aqueous-organic media, but this does not affect the activity of the corresponding samples, which is stably maintained for a long time, and hydrogen is actually released from the reaction solution [229,230,232];
8. It has been established that the titanate derivatives with aromatic modifiers are capable of functioning as photocatalysts not only under ultraviolet, but also under purely visible radiation. In this case, the most active and stable is the platinized 4-phenylphenol derivative $H_2La_2Ti_3O_{10}$×PhPhOH/Pt, whose activity in the reaction of hydrogen generation from a 1% (mol.) aqueous solution of methanol under purely visible light with a wavelength of 425 nm is 0.82 $mmol \cdot h^{-1} \cdot g^{-1}$ (0.041%);
9. Possible reasons for the high photocatalytic activity of the organic-inorganic derivatives are analyzed. The main one is that organic modifiers expand the interlayer reaction zone and thereby significantly increase its accessibility to reactant molecules. Moreover, despite the partial degradation of the organic modifiers, this zone can remain expanded at least as long as the photocatalyst is in the reaction medium, which explains the consistently high activity [229,230,232];
10. A highly efficient method for the liquid-phase exfoliation of titanates $HLnTiO_4$ and $H_2Ln_2Ti_3O_{10}$ (Ln = La, Nd) into nanosheets in an aqueous solution of tetrabutylammonium hydroxide has been developed and optimized, providing a concentration of the latter in suspensions of up to 2.1 g/L and a yield of up to 95% [245,246];

11. Photocatalysts have been successfully obtained based on the initial nanosheets and those reassembled by two different methods (filtration and acid precipitation). It has been established that the exfoliation followed by reassembly is accompanied by a decrease in the optical band gap of the titanates;
12. It was found that the reassembly method significantly affects the physical-chemical properties of the nanosheets. Filtered nanosheets, in contrast to those restacked by acid, contain tetrabutylammonium cations firmly bound to the surface, exhibit increased luminescence lifetimes and are more easily dispersed in aqueous media, which provides a larger specific surface area in suspensions;
13. Photocatalysts based on the titanate nanosheets have been systematically studied in the reactions of hydrogen generation from aqueous-organic mixtures, as well as pure water under ultraviolet radiation. It has been shown that exfoliation into nanosheets leads to an increase in the activity of the titanates up to 88 times. The most promising are platinized photocatalysts based on the nanosheets of $H_2La_2Ti_3O_{10}$, the activity of which in 1% (mol.) aqueous solutions of methanol, D-glucose and D-xylose reaches 54.8 $mmol \cdot h^{-1} \cdot g^{-1}$ (14.2 %), 14.0 $mmol \cdot h^{-1} \cdot g^{-1}$ (3.6%) and 17.1 $mmol \cdot h^{-1} \cdot g^{-1}$ (4.4%), respectively, and in pure water – 12.2 $mmol \cdot h^{-1} \cdot g^{-1}$ (3.2%). That being said, the nanosheets without reassembly demonstrate the greatest activity in an aqueous solution of methanol, and those reassembled by filtration – in aqueous solutions of carbohydrates. The nanosheets restacked by acid are in all cases inferior in the activity to the filtered ones;
14. It has been established that, other things being equal, the photocatalysts based on three-layer titanates $H_2Ln_2Ti_3O_{10}$ are significantly superior in the activity to the samples based on single-layer compounds $HLnTiO_4$ [229,230];
15. It has been shown that the photocatalysts based on the organic-inorganic titanate derivatives are the most promising for producing hydrogen from aqueous-organic mixtures [231,232], while the nanosheet-based photocatalysts – from pure water.

**Scientific novelty**

1. More than 40 new organic-inorganic derivatives of the titanates $HLnTiO_4$ and $H_2Ln_2Ti_3O_{10}$ (Ln = La, Nd) were obtained for the first time using methods optimized by the applicant and were comprehensively characterized;

2. It was shown for the first time that amine and alcohol derivatives of the titanates demonstrate consistently high photocatalytic activity in the reactions of hydrogen production from aqueous-organic mixtures, exceeding the activity of the initial unmodified titanates and the «gold standard» in photocatalysis $TiO_2$ P25 Degussa up to 117 and 87 times, respectively. A total of 120 organically modified photocatalysts were tested;
3. For the first time, the structural-chemical transformations of some amine and alcohol derivatives were studied during the photocatalytic generation of hydrogen from an aqueous solution of methanol and it was shown that they do not affect the activity, which is stably maintained for a long time;
4. The photocatalytic activity and stability of the titanates photosensitized by covalently bonded interlayer aromatic modifiers were studied for the first time;
5. A highly efficient method for the liquid-phase exfoliation of the titanates into nanosheets has been developed and optimized, providing a concentration of the latter in suspensions of up to 2.1 g/L and a yield of up to 95%;
6. For the first time, the influence of the method of reassembly of perovskite nanosheets on their physical-chemical properties and photocatalytic activity was studied. It has been shown that the method of nanosheet restacking with acid, widely used in the literature, is not optimal from the point of view of the achieved activity in hydrogen generation reactions;
7. For the first time, the activity of photocatalysts based on the above titanates in the reactions of hydrogen production from aqueous solutions of D-glucose and D-xylose as typical products of processing plant biomass was studied;
8. The generality of the trends regarding the photocatalytic properties of organic-inorganic derivatives and perovskite nanosheets has been shown for the titanates $HLnTiO_4$ and $H_2Ln_2Ti_3O_{10}$ (Ln = La, Nd) and niobates $HA_2Nb_3O_{10}$ (A = Ca, Sr).

**Theoretical and practical significance**

The theoretical significance of the work consists in identification and explanation of the relationships between the structure, composition, physical-chemical properties and photocatalytic activity of the materials based on layered perovskite-like oxides, which can

serve as the foundation for further scientifically based creation of new highly active and durable photocatalysts.

The practical significance of the work is due to the development of a new highly efficient approach to multiple increasing of the photocatalytic activity of layered perovskite-like materials – interlayer organic modification, as well as improving the technology for creating photocatalysts based on perovskite nanosheets. The results obtained are of significant importance for the development of environmentally friendly hydrogen energy, which is one of the key areas within the framework of existing sustainable development programs.

**Provisions for defense**

1. Methods of synthesis and results of physical-chemical characterization of the organic-inorganic derivatives of titanates $HLnTiO_4$ and $H_2Ln_2Ti_3O_{10}$ (Ln = La, Nd);
2. Methods for obtaining and results of physical-chemical characterization of the initial and reassembled titanate nanosheets;
3. Methods for studying the photocatalytic activity and stability of the obtained samples in the reactions of hydrogen generation from aqueous-organic mixtures under ultraviolet and visible radiation;
4. Photocatalytic activity and stability of the organic-inorganic titanate derivatives in the hydrogen generation reactions. Analysis of the main factors determining their photocatalytic activity;
5. Photocatalytic activity of the titanates exfoliated into nanosheets in the hydrogen generation reactions. The influence of the used form of nanosheets (initial, filtered, acid-restacked) on their photocatalytic activity;
6. Comparative analysis of the photocatalysts based on organic-inorganic derivatives and nanosheets of layered perovskite-like oxides.

**Degree of reliability and approbation of results**

A high degree of reliability of the results presented in the work is ensured by the use of a wide range of complementary research methods, as well as by the internal consistency, coherence and reproducibility of the data obtained.

The research was supported by grants from the Russian Science Foundation № 19-13-00184 «Composite photocatalysts based on layered oxides for hydrogen production from products of processing plant biomass» (2019–2023), № 20-73-00027 «Obtaining nanoparticles

of exfoliated organic-inorganic derivatives of layered perovskite-like titanates and niobates» (2020–2022) and № 22-73-10110 «Creation of nanostructured photocatalysts by the method of electrostatic self-assembly of nanosheets obtained by exfoliation of layered perovskite-like oxides and layered double hydroxides» (2022–2025).

The main results of the work were published in the following articles:

1. Silyukov O. I., Kurnosenko S. A., Zvereva I. A. Intercalation of methylamine into the protonated forms of layered perovskite-like oxides $HLnTiO_4$ (Ln = La and Nd) // Glas. Phys. Chem. 2018. Vol. 44, № 5. P. 428–432. DOI: 10.1134/S1087659618050176.
2. Rodionov I. A., Maksimova E. A., Pozhidaev A. Y., Kurnosenko S. A., Silyukov O. I., Zvereva I. A. Layered titanate $H_2Nd_2Ti_3O_{10}$ intercalated with *n*-butylamine: a new highly efficient hybrid photocatalyst for hydrogen production from aqueous solutions of alcohols // Front. Chem. 2019. Vol. 7, article № 863. DOI: 10.3389/fchem.2019.00863.
3. Kurnosenko S. A., Silyukov O. I., Mazur A. S., Zvereva I. A. Synthesis and thermal stability of new inorganic-organic perovskite-like hybrids based on layered titanates $HLnTiO_4$ (Ln = La, Nd) // Ceram. Int. 2020. Vol. 46, № 4. P. 5058–5068. DOI: 10.1016/j.ceramint.2019.10.249.
4. Kurnosenko S. A., Silyukov O. I., Minich I. A., Zvereva I. A. Exfoliation of methylamine and *n*-butylamine derivatives of layered perovskite-like oxides $HLnTiO_4$ and $H_2Ln_2Ti_3O_{10}$ (Ln = La, Nd) into nanolayers // Glas. Phys. Chem. 2021. Vol. 47, № 4. P. 372–381. DOI: 10.1134/S1087659621040131.
5. Kurnosenko S. A., Voytovich V. V., Silyukov O. I., Rodionov I. A., Kirichenko S. O., Minich I. A., Malygina E. N., Khramova A. D., Zvereva I. A. Photocatalytic activity of *n*-alkylamine and *n*-alkoxy derivatives of layered perovskite-like titanates $H_2Ln_2Ti_3O_{10}$ (Ln = La, Nd) in the reaction of hydrogen production from an aqueous solution of methanol // Catalysts. 2021. Vol. 11(11), article № 1279. DOI: 10.3390/catal11111279.
6. Kurnosenko S. A., Voytovich V. V., Silyukov O. I., Minich I. A., Malygina E. N., Zvereva I. A. Inorganic-organic derivatives of layered perovskite-like titanates $HLnTiO_4$ (Ln = La, Nd) with *n*-amines and *n*-alcohols: synthesis, thermal, vacuum and hydrolytic stability // Ceram. Int. 2022. Vol. 48, № 5. P. 7240–7252. DOI: 10.1016/j.ceramint.2021.11.284.

7. Kurnosenko S. A., Voytovich V. V., Silyukov O. I., Rodionov I. A., Zvereva I. A. Photocatalytic hydrogen production from aqueous solutions of glucose and xylose over layered perovskite-like oxides $HCa_2Nb_3O_{10}$, $H_2La_2Ti_3O_{10}$ and their inorganic-organic derivatives // Nanomaterials. 2022. Vol. 12(15), article № 2717. DOI: 10.3390/nano12152717.
8. Rodionov I. A., Gruzdeva E. O., Mazur A. S., Kurnosenko S. A., Silyukov O. I., Zvereva I. A. Photocatalytic hydrogen generation from aqueous methanol solution over *n*-butylamine-intercalated layered titanate $H_2La_2Ti_3O_{10}$: activity and stability of the hybrid photocatalyst // Catalysts. 2022. Vol. 12(12), article № 1556. DOI: 10.3390/catal12121556.
9. Kurnosenko S. A., Voytovich V. V., Silyukov O. I., Rodionov I. A., Zvereva I. A. Photocatalytic activity and stability of organically modified layered perovskite-like titanates $HLnTiO_4$ (Ln = La, Nd) in the reaction of hydrogen evolution from aqueous methanol // Catalysts. 2023. Vol. 13(4), article № 749. DOI: 10.3390/catal13040749.
10. Kurnosenko S. A., Minich I. A., Silyukov O. I., Zvereva I. A. Highly efficient liquid-phase exfoliation of layered perovskite-like titanates $HLnTiO_4$ and $H_2Ln_2Ti_3O_{10}$ (Ln = La, Nd) into nanosheets // Nanomaterials. 2023. Vol. 13(23), article № 3052. DOI: 10.3390/nano13233052.

The results of the work were also presented in the form of reports at all-Russian and international scientific conferences, the main ones of which are given below:

1. Kurnosenko S. A. A study of methylamine intercalation into the interlayer space of protonated layered perovskite-like titanates $HLnTiO_4$ (Ln = La, Nd) // International student conference «Science and Progress – 2017», Saint Petersburg, Russia, 2017.
2. Kurnosenko S. A. New experimental data on synthesis and protonation of layered perovskite-like titanates $K_2Ln_2Ti_3O_{10}$ (Ln = La, Nd) // International student conference «Science and Progress – 2017», Saint Petersburg, Russia, 2017.
3. Kurnosenko S. A., Silyukov O. I., Zvereva I. A. Synthesis of amine derivatives of protonated layered perovskite-like titanates $HLnTiO_4$ and $H_2Ln_2Ti_3O_{10}$ (Ln = La, Nd) // All-Russian conference with international participation «Solid state chemistry and functional materials – 2018», Saint Petersburg, Russia, 2018.

4. Kurnosenko S. A., Silyukov O. I., Zvereva I. A. New inorganic-organic hybrids based on layered perovskite-like titanates $HLnTiO_4$ and $H_2Ln_2Ti_3O_{10}$ (Ln = La, Nd) // International student conference «Science and Progress – 2018», Saint Petersburg, Russia, 2018.
5. Kurnosenko S. A., Silyukov O. I., Rodionov I. A., Zvereva I. A. Synthesis and exfoliation of layered perovskite-like titanates $HLnTiO_4$ and $H_2Ln_2Ti_3O_{10}$ intercalated by amines (Ln = La, Nd) // International student conference «Science and Progress – 2018», Saint Petersburg, Russia, 2018.
6. Kurnosenko S. A., Silyukov O. I., Zvereva I. A. Synthesis and exfoliation of intercalated perovskite-like titanates $HLnTiO_4$ and $H_2Ln_2Ti_3O_{10}$ (Ln = La, Nd) // International Conference «State-of-the-art trends of scientific research of artificial and natural nanoobjects – 2018» («STRANN – 2018»), Moscow, Russia, 2018.
7. Kurnosenko S. A., Silyukov O. I., Zvereva I. A. New alkoxy derivatives of layered perovskite-like titanates $HLnTiO_4$ and $H_2Ln_2Ti_3O_{10}$ (Ln = La, Nd) // XI International conference on chemistry for young scientists «Mendeleev – 2019», Saint Petersburg, Russia, 2019.
8. Kurnosenko S. A., Voytovich V. V., Silyukov O. I., Rodionov I. A., Zvereva I. A. Synthesis of organically modified layered perovskite-like titanates $H_2Ln_2Ti_3O_{10}$ (Ln = La, Nd) and their photocatalytic activity towards hydrogen production from aqueous methanol // International student conference «Science and Progress – 2020», Saint Petersburg, Russia, 2020.
9. Kurnosenko S. A., Silyukov O. I., Rodionov I. A., Zvereva I. A. Efficient liquid exfoliation of layered perovskite-like titanates $HLnTiO_4$ and $H_2Ln_2Ti_3O_{10}$ (Ln = La, Nd) into nanosheets // International student conference «Science and Progress – 2020», Saint Petersburg, Russia, 2020.
10. Kurnosenko S. A., Voytovich V. V., Silyukov O. I., Rodionov I. A., Zvereva I. A. Inorganic-organic derivatives of layered perovskite-like titanates $H_2Ln_2Ti_3O_{10}$ (Ln = La, Nd): thermal stability and photocatalytic activity // XVI International conference on thermal analysis and calorimetry in Russia (RTAC – 2020), Moscow, Russia, 2020.
11. Kurnosenko S. A., Voytovich V. V., Silyukov O. I., Rodionov I. A., Zvereva I. A. Synthesis and photocatalytic activity of inorganic-organic derivatives of layered

perovskite-like titanates $H_2Ln_2Ti_3O_{10}$ (Ln = La, Nd) in the reaction of hydrogen production from aqueous methanol // International conference «Catalysis for a sustainable world», Moscow, Russia, 2020.

12. Kurnosenko S. A., Voytovich V. V., Silyukov O. I., Rodionov I. A., Zvereva I. A. Organic-inorganic derivatives of layered perovskite-like titanates $H_2Ln_2Ti_3O_{10}$ (Ln = La, Nd) as photocatalysts for hydrogen generation from a water-methanol solution // XIX All-Russian youth scientific conference with elements of the scientific school «Functional materials: synthesis, properties, application», Saint Petersburg, Russia, 2020.
13. Kurnosenko S. A. Organically modified layered perovskite-like titanates $H_2Ln_2Ti_3O_{10}$ (Ln = La, Nd) as heterogeneous photocatalysts for hydrogen production // International scientific student conference – 2021 (ISSC–2021), Novosibirsk, Russia, 2021.
14. Kurnosenko S. A., Voytovich V. V., Silyukov O. I., Rodionov I. A., Zvereva I. A. Organically modified layered perovskite-like titanates $H_2Ln_2Ti_3O_{10}$ as heterogeneous photocatalysts for hydrogen production // XXVIII International scientific conference for undergraduate and graduate students and young scientists «Lomonosov – 2021», Moscow, Russia, 2021.
15. Kurnosenko S. A., Voytovich V. V., Silyukov O. I., Rodionov I. A., Zvereva I. A. Synthesis and photocatalytic activity of organically modified layered perovskite-like titanates $HLnTiO_4$ (Ln = La, Nd) // XII International conference on chemistry for young scientists «Mendeleev – 2021», Saint Petersburg, Russia, 2021.
16. Kurnosenko S. A., Voytovich V. V., Silyukov O. I., Rodionov I. A., Zvereva I. A. Organic modification of layered perovskite-like titanates $HLnTiO_4$ (Ln = La, Nd) as an efficient approach to the enhancement of their photocatalytic performance towards hydrogen production // International student conference «Science and Progress – 2021», Saint Petersburg, Russia, 2021.
17. Kurnosenko S. A., Voytovich V. V., Silyukov O. I., Rodionov I. A., Zvereva I. A. «Stability of hybrid inorganic-organic photocatalysts based on the layered perovskite-like titanate $H_2La_2Ti_3O_{10}$ in the reaction of hydrogen generation from aqueous methanol // International student conference «Science and Progress – 2021», Saint Petersburg, Russia, 2021.

18. Kurnosenko S. A., Voytovich V. V. Stability of inorganic-organic photocatalysts based on layered perovskite-like titanate $H_2La_2Ti_3O_{10}$ in the reactions of hydrogen production // International scientific student conference – 2022 (ISSC–2022), Novosibirsk, Russia, 2022.
19. Kurnosenko S. A., Minich I. A. New photocatalysts of hydrogen generation based on layered perovskite-like titanate $H_2La_2Ti_3O_{10}$ with grafted aromatic modifiers // International scientific student conference – 2023 (ISSC–2023), Novosibirsk, Russia, 2023.
20. Kurnosenko S. A., Voytovich V. V. Influence of the reassembly method on photocatalytic performance of perovskite nanosheets // International scientific student conference – 2023 (ISSC–2023), Novosibirsk, Russia, 2023.

In total, the applicant is the author of 24 articles in the journals indexed in Scopus and Web of Science systems, as well as has more than 50 abstracts of reports at conferences on the development and research of photocatalytically active layered materials.

**Personal contribution of the applicant**

The applicant's personal contribution consists in searching and critically analyzing literature; setting goals and objectives; planning research work; development of new photocatalysts based on the amine and alcohol derivatives, as well as titanate nanosheets; directly conducting experiments on the physical-chemical characterization of the obtained photocatalysts using a number of instrumental methods (X-ray diffraction analysis, diffuse reflectance spectroscopy, spectrophotometry and pH-metry of the reaction suspensions), as well as preparing samples for research by other methods on the basis of resource centers (RC) of the Research park of Saint Petersburg State University; setting up and maintaining a laboratory photocatalytic setting; testing the activity and stability of the photocatalysts in hydrogen generation reactions; processing, analysis and interpretation of the data obtained, as well as preparation of publications and reports based on them. In cases where some studies were carried out by the applicant's colleagues in the scientific group or with their direct participation, the corresponding fact is noted in the experimental section of this work.

**Structure and scope of the work**

This work consists of an introduction, a literature review, an experimental section, a discussion of the results, a resume, conclusions, bibliography and acknowledgments. The

English version of the work is presented on 225 pages, includes 84 figures and 21 tables. The bibliography contains 250 sources.

# 1. Literature review

## 1.1. Basics of heterogeneous photocatalysis

Over the past decades, heterogeneous photocatalysis has been one of the most rapidly developing areas of chemical science due to the great importance of this process for solving actual problems in alternative energetics, ecology, chemical industry and other areas. Particular attention of researchers and engineers is attracted by photocatalytic reactions of hydrogen [1] and oxygen production [2], decomposition of water [3] and air pollutants [4], reduction of nitrogen [5] and carbon dioxide [6] to practically valuable compounds, as well as fine organic synthesis [7].

Despite the constantly growing number of works in the field of heterogeneous photocatalysis, a number of difficulties still arise in the theoretical description and experimental study of photocatalytic processes, largely due to the interdisciplinary nature of research at the intersection of chemical kinetics, photochemistry, electrochemistry, colloid chemistry, as well as solid state physics and chemistry. In the simplest case, a heterogeneous photocatalytic system consists of one photonic subsystem (radiation) and two electronic subsystems (photocatalyst and reactants), between which a set of interactions occurs, including through phase boundaries [8]. Physicochemical processes in such systems are characterized by a large number of parameters (crystalline and electronic structure of the photocatalyst, its optical properties, morphology and specific surface area, composition of the reaction medium, radiation spectrum and power, temperature and pressure in the system, etc.) that should be controlled to manage the photocatalytic process [9]. As a consequence, one of the most important tasks at present is to establish relationships between these parameters and photocatalytic activity for subsequent prediction of the optimal values of these parameters that provide the best activity under certain conditions, and the targeted development of highly efficient photocatalysts.

### 1.1.1. Concept and classification of photocatalytic reactions

In accordance with the definition proposed by academician V. N. Parmon, photocatalysis is a phenomenon of changing the rate of a chemical reaction or its initiation under the influence of ultraviolet, visible or infrared radiation absorbed by a special substance (photocatalyst) participating in the chemical transformations of reactants and regenerating its

state after each cycle of such transformations [10]. Thus, the simplest photocatalytic reaction can be represented as a two-stage scheme

$$\begin{cases} K + h\nu \rightarrow K^* \\ A + K^* \rightarrow B + K \end{cases}$$

where A – generalized reactants, B – generalized products, K – catalyst, hν – radiation quantum (photon). In accordance with the definition, the mechanism of true photocatalysis involves the absorption of light by the catalyst K, which then goes into the activated state K* and interacts with the reactants. In other words, in a photocatalytic reaction, the photonic subsystem (radiation) interacts with the electronic subsystem (reactants) not directly, but through another electronic subsystem, which is the catalyst. It is important to understand that radiation itself is not a catalyst, since it is not regenerated. Reactions are also possible in which radiation is absorbed directly by reactants A, which then go into the activated state A* and then catalytically transform into products B:

$$\begin{cases} A + h\nu \rightarrow A^* \\ A^* + K \rightarrow B + K \end{cases}$$

Since such processes do not fall under the above definition of photocatalysis, they are more correctly called catalytic photoreactions. However, this distinction in the literature is not completely established, and when considering such reactions, the term «photocatalysis» is also used in some cases.

When considering photocatalysis thermodynamically, two types of photocatalytic reactions are distinguished – allowed and prohibited in the dark mode, also called in English literature as «downhill reactions» and «uphill reactions», respectively [11]. The first type includes chemical processes characterized by a negative change in free energy ($\Delta G^0 < 0$) and therefore capable of occurring spontaneously from a thermodynamic point of view. Examples of such processes are the oxidation reactions of organic substances to water and carbon dioxide:

$$CH_4 + 2O_2 \rightarrow CO_2 + 2H_2O$$

The presented process is thermodynamically favorable, but under normal conditions its rate is negligible due to the high activation energy. The photocatalytic approach allows it to be accelerated without resorting to additional heating or ignition of the reaction mixture. In this case, dissipation of light energy occurs, the role of which is to facilitate the reactants to overcome the activation barrier [8]. However, one of the key features of photocatalysis

compared to dark catalysis is the possibility of carrying out reactions of the second type, which are thermodynamically forbidden without irradiation. Such reactions, in particular, include the decomposition of water into simple substances, characterized by a positive change in free energy ($\Delta G^0$ = 237 kJ/mol):

$$2H_2O \rightarrow 2H_2 + O_2$$

This reaction cannot be realized using dark catalysis, since a standard catalyst, by definition, does not shift the chemical equilibrium (does not affect the change in thermodynamic potentials during the reaction), but only changes its mechanism with a decrease in activation energy, thereby accelerating the process if it is in allowed in principle. When a reaction is carried out in the photocatalytic mode, one of its implicit participants is radiation, which ensures that, with sufficient photon energy, the value $\Delta G$ is negative. Thus, the photocatalytic approach makes it possible to carry out processes that are not feasible in the dark mode with partial storage of radiation energy in the resulting products [8].

Photocatalysis is a special case of redox catalysis. Depending on the location of the reactants and photocatalyst in the same or different phases, homogeneous and heterogeneous photocatalysis are distinguished, respectively [12]. The first option is most often implemented in liquid phase using transition metal complexes as photocatalysts [13], while the second option usually involves the presence of reactants in the liquid or gaseous phase with a solid semiconductor material as a photocatalyst [14]. In this case, various design options for the implementation of heterogeneous photocatalytic systems are possible: suspensions of powder photocatalysts in reaction solutions [15], immobilized photocatalysts on carrier materials (in particular, self-cleaning photocatalytic coatings) [16] and photocatalysts presented in the form of photoelectrodes as part of photoelectrochemical cells [17]. Further, unless special reservations are made, we will talk mainly about powder photocatalysts dispersed in liquid media.

### 1.1.2. Mechanism and thermodynamic criteria for proceeding of photocatalytic reactions

In the general case, the mechanism of heterogeneous photocatalysis can be represented in the form of a diagram (Fig. 1) [12]. The irradiated semiconductor photocatalyst, being in contact with the reactants, absorbs photons with an energy exceeding the band gap $E_g$. In this case, an internal photoelectric effect occurs – the transition of photoexcited electrons $e^-$ from the valence band of the semiconductor to the conduction band with the formation of positively

charged vacancies in the first – holes $h^+$. Charge carriers of both types migrate to the surface of the photocatalyst, where they enter into redox reactions with the adsorbed reactants; that being said, the electron acts as a reducing agent, and the hole acts as an oxidizing agent. Accordingly, during the reduction half-reaction, the electron leaves the conduction band of the photocatalyst, and during the oxidative half-reaction, the electron from the reactant enters the valence band, neutralizing the vacancy, after which desorption of the resulting products occurs. With further irradiation, the described cycle is repeated. The main side process that reduces the efficiency of heterogeneous photocatalysis is the recombination of photogenerated charge carriers, which takes place both in the bulk of the photocatalyst material and on its surface [18].

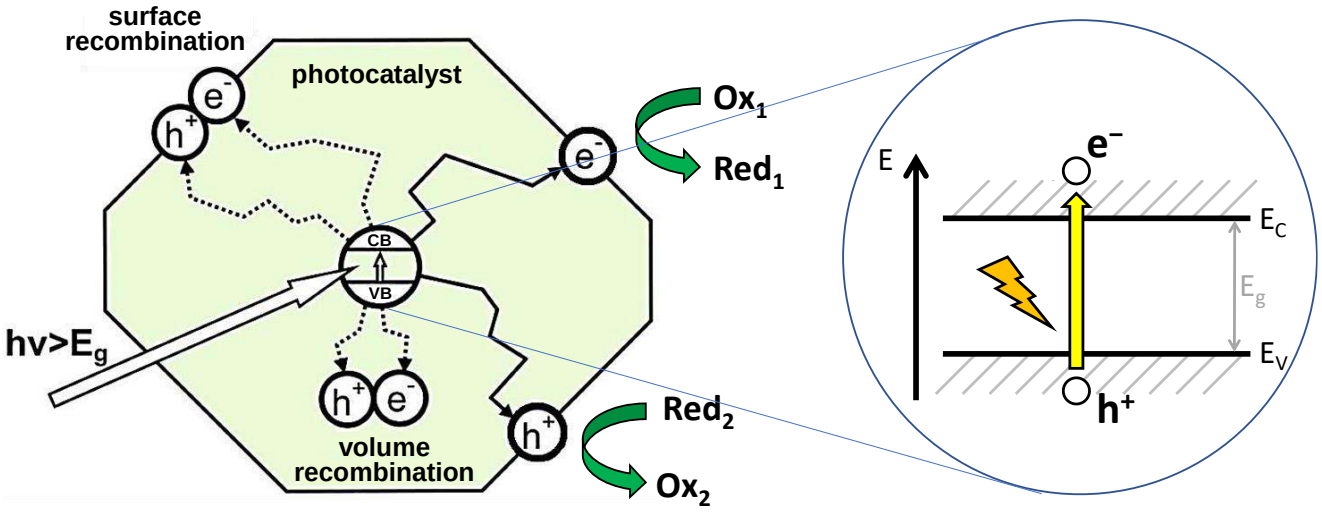


Fig. 1. Mechanism of heterogeneous photocatalysis

Let us dwell in more detail on the processes occurring in a semiconductor photocatalyst. Being fermions, electrons in a semiconductor obey the Fermi-Dirac distribution

$$f(E,T) = \frac{1}{1 + e^{\frac{E-F}{kT}}}$$

where f is the population of the energy state, E is its energy, F is the Fermi level, k is the Boltzmann constant, T is the absolute temperature. In accordance with this distribution, the Fermi level F is the energy of the state with half population (f = 0.5); it is one of the most important parameters of an equilibrium semiconductor, depending on its composition and structure and characterizing the electrochemical potential of charge carriers in the semiconductor [8]. When semiconductor photocatalysts are irradiated with light with a photon energy exceeding the band gap $E_g$, the generation of nonequilibrium charge carriers occurs – electrons in the conduction band and holes in the valence band. An increase in concentration of

the carriers gradually accelerates the process of their neutralization due to recombination with each other and participation in redox transformations of adsorbed reactants until the onset of a stationary mode, in which the rates of formation and disappearance of electron-hole pairs are equalized. Despite the nonequilibrium of the electronic system of the irradiated semiconductor as a whole, thermal equilibrium for the subsystems of conduction electrons and holes separately is usually established at constant radiation parameters, which makes it possible to introduce into consideration the values of $F_e$ and $F_h$, which characterize the reducing ability of conduction electrons and the oxidizing ability of holes, respectively, and called quasi-Fermi levels (Fig. 2) [8].

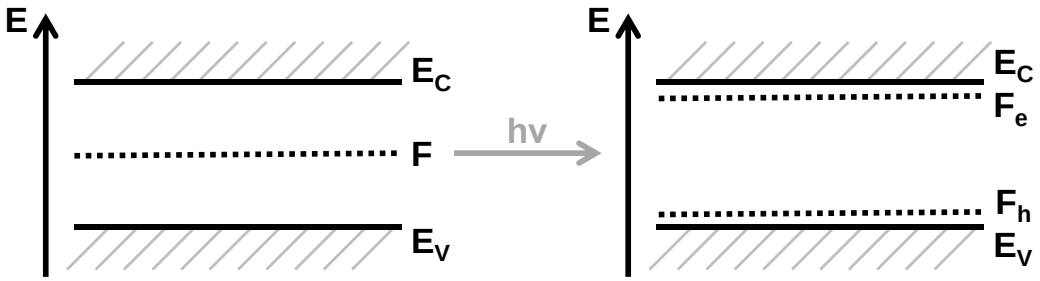


Fig. 2. Fermi level splitting in an irradiated semiconductor

The thermodynamic criterion for the allowance of a reaction on an irradiated semiconductor photocatalyst is the location of the reduction potentials of half-reactions between quasi-Fermi levels. When using an electrochemical potential scale relative to a standard hydrogen electrode (SHE), this means that the potential of the oxidative half-reaction $E_{Ox}$ should lie above $F_h$ (be less positive), and the potential of the reduction half-reaction $E_{Red}$ should lie below $F_e$ (be less negative):

$$\begin{cases} E_{Ox} < F_h \\ E_{Red} > F_e \end{cases}$$

However, at a sufficiently high radiation intensity, $F_h$ tends to the top of the valence band $E_V$, and $F_e$ tends to the bottom of the conduction band $E_C$, and therefore the criteria for the thermodynamic allowance of the reaction can be presented in the form

$$\begin{cases} E_{Ox} < E_V \\ E_{Red} > E_C \end{cases}$$

This form of notation is most widely used in the literature due to the greater simplicity of the experimental determination of the position of the boundaries of energy bands in a semiconductor compared to quasi-Fermi levels. If instead of the electrochemical scale of

potentials the physical scale of energy relative to vacuum is used, the signs of the above inequalities are reversed.

Thus, thermodynamically necessary, but insufficient conditions for the photocatalytic decomposition of water into simple substances at pH = 0 are the potential of the valence band top of the photocatalyst $E_V > 1.23$ V and the potential of the conduction band bottom $E_C < 0$ V relative to SHE (Fig. 3). Accordingly, photocatalysts with a band gap $E_g \leq 1.23$ eV are fundamentally unsuitable for this reaction. However, in practice, even with a slightly larger band gap, the probability of the reduction potentials of both half-reactions entering the gap between the band edges is small, and the processes of evolution of gaseous hydrogen and oxygen occur with a significant overpotential, which necessitates the use of significantly wider bandgap photocatalysts [12].

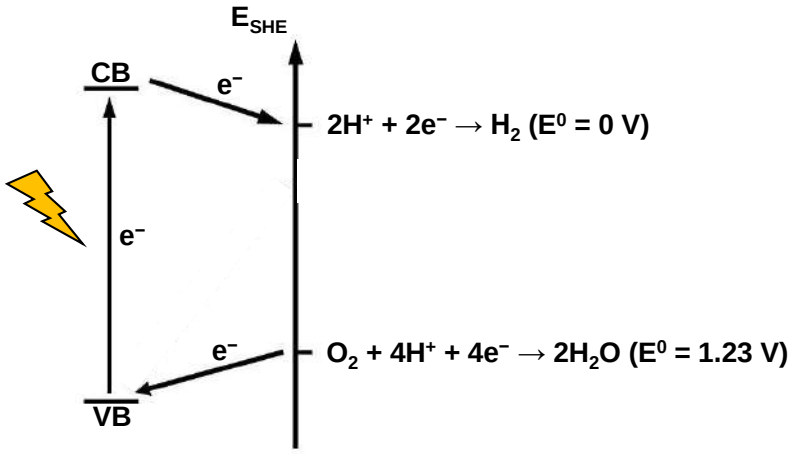


Fig. 3. Energy diagram of the photocatalytic decomposition of water into simple substances at pH = 0

Taking into account the above, when developing new photocatalysts, the experimental determination or calculation of the band positions relative to the potentials of those half-reactions that are planned to be carried out is of particular importance. That being said, the curvature of the band edges at the interface of the photocatalyst with the solution should also be taken into account due to the formation of a double electrical layer and the dependence of the half-reaction potentials on the pH of the medium [19].

### 1.1.3. Photocatalytic activity and methods for its evaluation

One of the key characteristics of any photocatalyst is its photocatalytic activity, which can be defined as the difference in the rates of a particular reaction when it is carried out in the photocatalytic mode and in the absence of a photocatalyst, other conditions being constant. When considering reactions that do not occur without a photocatalyst (for example, the

decomposition of water into simple substances), the photocatalytic activity will be equal to the reaction rate. The latter is usually measured by the reaction participant that is of main practical interest or is easier to detect experimentally (hydrogen, decomposing pollutant of the aqueous medium, etc.). Instead of the reaction rate directly, the degree of conversion of a reactant over a certain time, the time to reach a fixed degree of conversion, and other related quantities can be used as a measure of photocatalytic activity [20]. However, a strict comparison of different materials with each other according to the photocatalytic activity determined in this way is only possible if for all of them it is measured under completely identical conditions, and therefore a number of difficulties arise when comparing the results obtained by different scientific teams.

One of the widespread practices in modern literature is the normalization of the rate of a heterogeneous photocatalytic reaction per unit mass of the photocatalyst [21], apparently borrowed from standard heterogeneous catalysis. This approach is based on the assumption that the reaction rate is directly proportional to the area of the active surface of the catalyst, which, in turn, is proportional to its weight. This assumption is valid for conventional heterogeneous catalytic reactions [20], however, when working with suspensions of heterogeneous photocatalysts, a number of effects occur that make the dependence of the reaction rate on the mass of the catalyst nonlinear (side light scattering, internal filter effect, and others) [22–24]. As a consequence, a strict comparison of the achieved values of photocatalytic activity is possible only with comparable catalyst loadings and similar geometry of the reactors used. Another common practice is to compare the photocatalytic activity of the materials under study with the activity of some widely known and well-established standard (for example, titanium dioxide $TiO_2$ P25 Degussa), tested under identical conditions [25].

Photocatalytic activity, defined as the reaction rate, is an absolute value and, as a consequence, does not allow one to compare the achieved efficiency of the photocatalytic process with the highest theoretically achievable under experimental conditions. In this regard, the energy efficiency of photocatalysis is also characterized using the concepts of a quantum yield, quantum efficiency and apparent quantum efficiency [26].

A quantum yield represents a ratio of the observed rate of a photocatalytic reaction to the rate at which the photocatalyst absorbs photons of a fixed energy. Due to the non-monochromatic nature of radiation sources used in practice, the concept of a quantum yield

can be replaced by the concept of quantum efficiency, which takes into account the absorption of light at all wavelengths available to the photocatalyst. However, the experimental determination of both quantities is associated with significant technical difficulties due to side light scattering, the intensity of which must be measured in all directions in parallel with monitoring the rate of the reaction under study. In view of this, a more convenient definition for practical purposes is the apparent quantum efficiency – the ratio of the reaction rate to the rate of entry into the reaction cell of photons available for absorption. It should be understood that the apparent quantum efficiency does not take into account light scattering and, as a consequence, gives only a lower estimate of the true quantum efficiency of the process.

### 1.1.4. Key parameters of photocatalysts affecting their activity

#### 1.1.4.1. Bandgap energy and position of band edges

A bandgap energy $E_g$ represents the minimum photon energy required to generate an electron-hole pair, and is one of the most important characteristics of any semiconductor photocatalyst, since it determines the spectral region of its operation – the range of its intrinsic (fundamental) light absorption. The influence of the $E_g$ value on the possibilities of photocatalytic applications of semiconductors is ambiguous. On the one hand, its reduction allows the use of a photocatalyst under radiation with lower energy and, accordingly, to utilize in the implementation of target processes not only ultraviolet, but also visible and infrared light, which predominate in the solar spectrum. In particular, titanium dioxide $TiO_2$ and many other oxide photocatalysts are characterized by the value of $E_g > 3.1$ eV, which is why they are able to function only under ultraviolet radiation ($\lambda < 400$ nm), while a significant fraction of nitride and chalcogenide materials have $E_g = 1.0$–$2.5$ eV, which allows them to absorb visible ($\lambda = 400$–$700$ nm) and, in some cases, also near-infrared light ($\lambda > 700$ nm) (Fig. 4) [27]. However, a decrease in the bandgap energy reduces the range of reactions available to a photocatalyst, since the condition for their thermodynamic allowance is the location of the reduction potentials of the half-reactions within its boundaries. Thus, lead sulfide PbS and cadmium telluride CdTe, despite the wide range of their intrinsic light absorption ($E_g = 0.9$ eV, $\lambda < 1378$ nm and $E_g = 1.4$ eV, $\lambda < 886$ nm, respectively), cannot decompose pure water into simple substances due to the failure of the above condition. In addition, reactions on wider-gap semiconductors, as a rule, proceed with greater quantum efficiency due to the lower intensity of recombination of photogenerated charge carriers and the greater driving force of the process

on the part of the photocatalyst, which was demonstrated by the example of the series of isostructural tantalates $ATaO_3$ (A = Li, Na, K ) and $BTa_2O_6$ (B = Ca, Sr, Ba) [28,29].

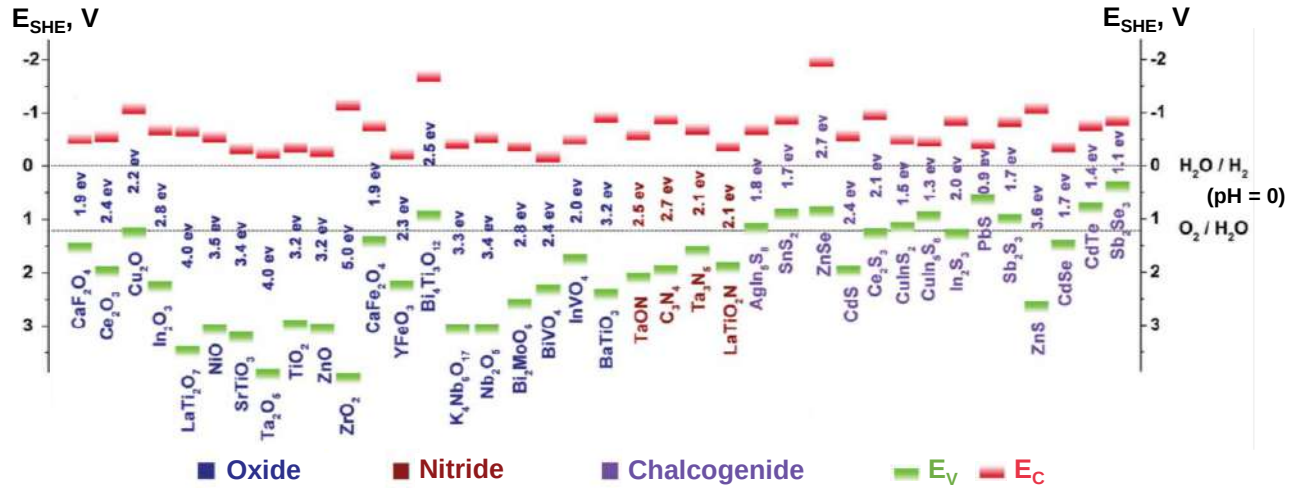


Fig. 4. Positions of energy band edges of some photocatalysts [27]

In titanium dioxide $TiO_2$ and most other oxide photocatalysts, the valence band is formed predominantly by 2p-orbitals of oxygen, and the conduction band is formed by vacant d-orbitals of the transition metal. The main experimental approach to managing the band structure of such materials is partial cationic and anionic substitution [30]. However, based on an extensive array of experimental data, it has been established [31] that for metal oxides that do not contain partially filled d-orbitals (that is, having a $d^0$ or $d^{10}$ configuration), the relationship between the flat band potential $E_{fb}$, being approximately equal to the potential of the conduction band bottom $E_C$ on the electrochemical scale, is expressed by the equation:

$$E_{fb} \approx E_C \approx 2.94 - E_g$$

Thus, there is a direct relationship between the band gap of oxide photocatalysts and its position on the potential scale (Fig. 5) and separate variation of these parameters is not possible, which imposes certain restrictions on the creation of photocatalysts with a given energy structure. In particular, for the release of hydrogen from water at pH = 0 the value $E_C < 0$ V ($E_g > 2.94$ eV) is formally required, due to which metal oxides not containing partially filled d-orbitals are able to function as photocatalysts for hydrogen generation almost only under ultraviolet radiation.

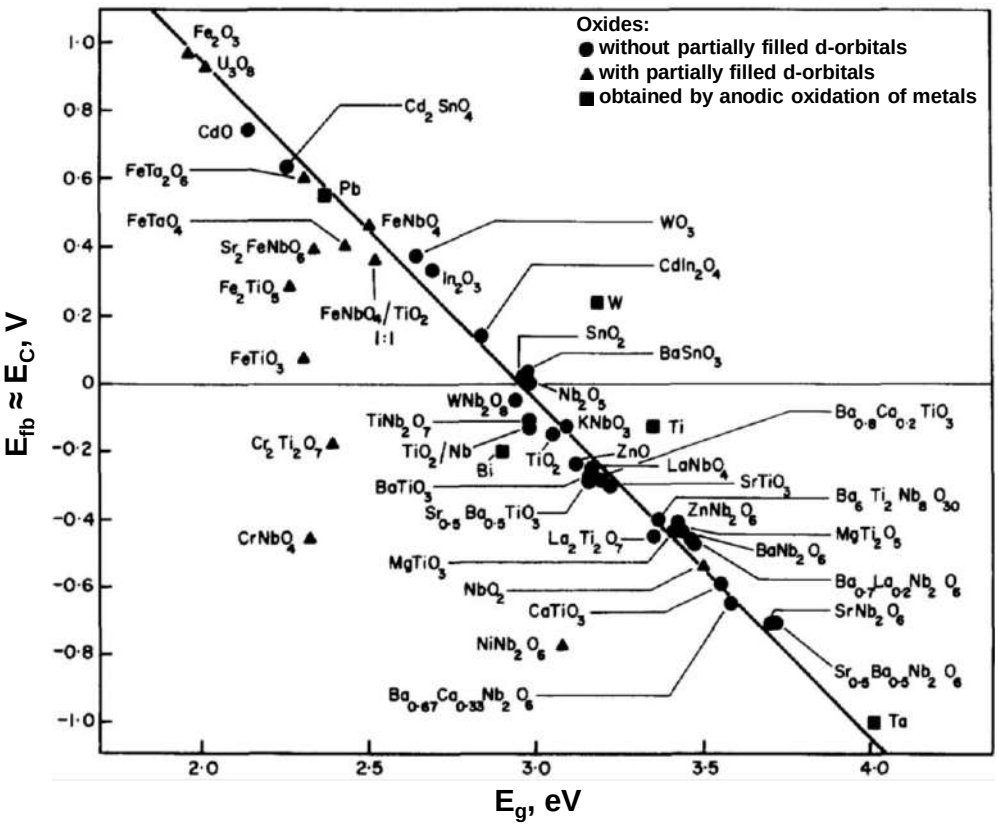


Fig. 5. Relationship between the flat band potential and bandgap energy of oxide photocatalysts [31]

However, in the light of the photocatalytic production of hydrogen, it is of interest to create materials that correspond in their band structure to the lower left part of Fig. 5. Achieving this goal can be facilitated by the introduction into the oxide structure of metal cations with partially filled d-orbitals, which, along with oxygen, can contribute to the formation of the valence band, increasing its top $E_V$ and thereby ensuring the negativity of the bottom of the conduction band $E_C$ sufficient for the reaction to be allowed at a moderate value of $E_g$, providing absorption of visible light. This approach has been studied in most detail using the example of titanium dioxide $TiO_2$, the partial replacement of titanium in which with cations of vanadium, chromium, manganese, iron and other metals was accompanied by an expansion of its operating range from the ultraviolet to the visible area [32]. In some cases, introduced cations can lead to the emergence of individual allowed states within the band gap that do not merge with the existing bands. Formally, in such cases, the band gap of the initial material is preserved, but the transition of electrons from these new states to the conduction band requires less photon energy than from the valence band, which expands the spectral range of the photocatalyst operation. The described approach was, in particular, successfully applied to layered bismuth titanate $Bi_4Ti_3O_{12}$, characterized by the value of $E_g = 3.08$ eV, the partial

replacement of titanium with chromium in the structure of which made it possible to realize, due to the 3d-orbitals of chromium, allowed energy levels within the band gap and ensure non-zero photocatalytic activity of the sample in the reaction of hydrogen evolution from an aqueous solution of methanol under purely visible light ($\lambda > 400$ nm) [33]. Another method of shifting the valence band top is partial replacement of oxygen anions with anions of nitrogen (nitridation), sulfur (sulfidation) and other non-metals to form oxynitrides, oxysulfides, etc., respectively [34]. However, materials obtained in this way are often less resistant to photodegradation under photocatalytic conditions.

1.1.4.2. Additional photosensitization

Photocatalytic materials based on relatively wide-gap semiconductors, whose region of intrinsic light absorption is limited by ultraviolet light, can use longer wavelength radiation when their surface is modified with a special organic or inorganic light absorber – a photosensitizer. The operation principle of the latter in the general case consists in the photoinduced formation of mobile electrons and their transfer to the conduction band of the semiconductor with subsequent regeneration of the photosensitizer by the reducing agent from the reaction medium (Fig. 6). Typical photosensitizers used are organic dyes [35] and transition metal complexes [36], which, as a rule, bind to the surface of the photocatalyst by chemisorption. In addition, a photosensitizing function can be performed by relatively narrow-gap semiconductors in composite photocatalysts (for example, CdS during the formation of a heterojunction with $TiO_2$) and nanoparticles of noble metals (in particular, Ag, Au), in which surface plasmon resonance is possible under visible radiation [37]. The main requirements for molecular and semiconductor photosensitizers are the location of their excited electronic state above the bottom of the conduction band of the semiconductor used, a wide range of light absorption, and stability towards photodegradation under operation conditions.

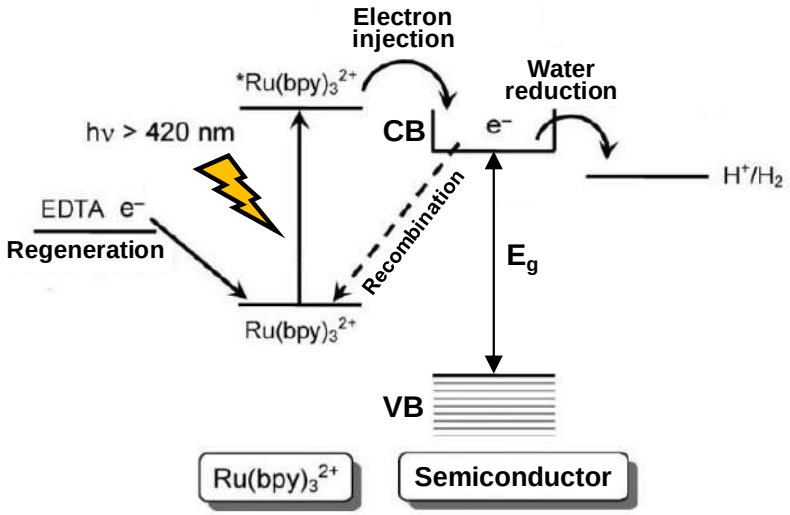


Fig. 6. The operation principle of a photosensitizer using the example of a ruthenium bipyridine complex [38]

1.1.4.3. Specific surface area

A specific surface area, along with the light absorption region, is one of the key characteristics of any heterogeneous photocatalyst, since it is the surface that serves as the localization site for catalytically active centers [12]. As a rule, in a certain range of conditions, a linear or close to linear relationship is observed between the rate of a heterogeneous photocatalytic reaction and the specific surface area, and therefore, as already noted, the activity of heterogeneous photocatalysts is often normalized to their mass or unit surface area, when the latter is known [21]. More developed surface is one of the main advantages of suspensions of powder photocatalysts over immobilized analogues and photoelectrochemical cells [39]. However, for suspensions of photocatalysts, the dependence of the photocatalytic reaction rate on the specific surface area often deviates from linearity [40,41], since the completeness of radiation absorption by them significantly depends on the side effects of light scattering and screening, the severity of which, in turn, depends on the morphology and specific surface area of the photocatalyst. In addition, increasing the specific surface area is ineffective in cases where the reaction rate is limited by other factors – in particular, low concentration of reactants or radiation power.

In addition to an increase in the number of catalytically active centers, an increase in the specific surface area is accompanied by a decrease in the specific volume and, as a consequence, the undesirable effect of volume electron-hole recombination on the efficiency of photocatalysis. In this case, recombination processes are mainly transferred to the surface of

the photocatalyst, where it is easier to control them than in its bulk, by creating conditions for the spatial separation of charge carriers [42].

In view of the above, one of the actively exploring areas is the creation and improvement of methods for producing photocatalysts with a developed surface, including those based on already well-proven materials. Thus, the use of «softer» synthesis methods (solvothermal, sol-gel, coprecipitation in solutions) instead of the standard high-temperature ceramic technology makes it possible to obtain oxide photocatalysts with smaller particle sizes and, accordingly, a more developed surface, which often has a beneficial effect on their photocatalytic activity. This trend was shown by the example of the activity of samples of bismuth molybdate $Bi_2MoO_6$ and tungstate $Bi_2WO_6$ synthesized by different methods in the reaction of rhodamine B decomposition [43], strontium $Sr_3Ti_2O_7$ [44] and lanthanum-potassium titanates $K_2La_2Ti_3O_{10}$ [45] in the processes of producing hydrogen, as well as many other photocatalysts. However, it should be noted that under real experimental conditions, varying the specific surface area by itself while fully maintaining the other properties of the photocatalyst is not possible. In this regard, behind the dependences of photocatalytic activity on the specific surface area presented in the literature there is a simultaneous influence of other related factors. Thus, in [46], it was found that the activity of bismuth tungstate $Bi_2WO_6$ in the reaction of acetaldehyde decomposition increases linearly with the specific surface area in the range of 10–25 $m^2/g$ and then deviates from linearity towards lower values due to the appearance of impurity amorphous phases in the samples, while in the study [45] samples of titanate $K_2La_2Ti_3O_{10}$ with different specific surface areas also differ in phase composition and position of the fundamental absorption edge. In addition, reproducible synthesis techniques under relatively mild conditions are known not for all photocatalysts of interest; therefore, to achieve a high active surface area, other approaches are widely used, such as template synthesis of porous materials [47] and exfoliation of layered compounds into nanosheets [48].

1.1.4.4. Degree of crystallinity

The theoretical basis for enhancing the efficiency of heterogeneous photocatalysis is to increase the proportion of photogenerated charge carriers that successfully reach the surface and participate in redox transformations of the reactants [49]. One of the conditions for this is to minimize the volume recombination of electron-hole pairs, the main centers of which are crystal defects. The crystallinity of semiconductor compounds is largely determined by the

synthesis method used and correlates with its temperature [50]. In particular, the synthesis of many complex oxides that are of interest as photocatalysts is carried out using the high-temperature ceramic technology. In this case, a higher degree of crystallinity is achieved with increasing temperature and duration of calcination (within the limits of the thermal stability of the compound of interest), which makes it possible to reduce the severity of volume electron-hole recombination. At the same time, the specific surface area of the sample decreases due to the enlargement of the crystals and their more intense sintering with each other. In the case of the widely used solvothermal synthesis method, the crystallinity of the samples usually also increases with the temperature and duration of heating, but the large size of the growing crystals causes a smaller specific surface area. As a consequence, the dependence of photocatalytic activity on temperature and duration of synthesis often passes through a maximum corresponding to the optimal ratio of crystallinity and specific surface. These patterns were, in particular, shown using the example of bismuth molybdate $Bi_2MoO_6$ samples synthesized by different methods [51,52]. However, defects in the crystal structure are not a purely negative phenomenon in the field of heterogeneous photocatalysis and, in some cases, are created deliberately in order to improve certain characteristics of photocatalysts [53]. Particularly, the introduction of impurity elements into the crystal lattice, already mentioned earlier, serves as a method of controlling the energy structure of the material, allowing one to expand the light absorption region by narrowing the band gap or creating allowed states within it. In this case, the intensity of recombination, as a rule, increases, but this effect is compensated by the ability of the photocatalyst to function under longer wavelength radiation.

1.1.4.5. Spatial separation of reaction centers

Photocatalytic activity significantly depends on the intensity of not only volume but also surface recombination of photogenerated charge carriers, as well as on the occurrence of undesirable chemical processes with the target products – in particular, reverse reactions. In this regard, the spatial separation of oxidation and reduction centers is of particular importance. It is most effectively implemented in photoelectrochemical cells – devices for converting light energy into chemical energy, in the simplest case, built on the basis of two electrodes connected to each other by ohmic and liquid contacts (through a semi-permeable membrane or salt bridge) (Fig. 7). At least one electrode of the cell must be photoactive, i.e. capable of generating electron-hole pairs upon irradiation, while a standard metal electrode can

be used as the second. A photoelectrode typically consists of a metal slab coated with a layer of semiconductor material. The operating principle of the model cell for water splitting shown in Fig. 7 consists in the photogeneration of charge carriers in the semiconductor material of the photoanode, followed by the capture of a hole by the surface of the semiconductor and its oxidation of water, as well as the transfer of an electron through the metal slab and external circuit to the metal cathode, which serves to reduce protons diffusing to its surface from the photoanode. In such a cell, the centers of hydrogen and oxygen evolution are spatially separated, which prevents proceeding of the undesirable reverse reaction between the gaseous products and provides the possibility of their convenient separation [54]. The surface of photoelectrodes can be additionally modified by particles of cocatalysts that serve as sinks for electrons (for the photocathode) or holes (for the photoanode), increasing the efficiency of their separation and, accordingly, suppressing recombination [17].

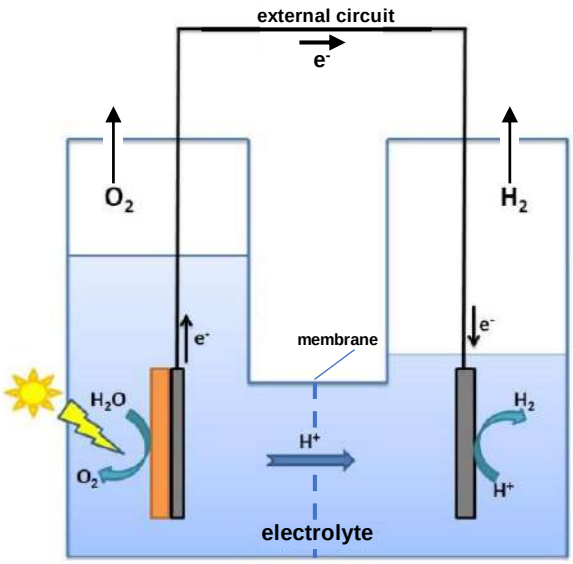


Fig. 7. Photoelectrochemical cell for water splitting [54]

In the case of powder photocatalysts, the idea of spatial separation of oxidation and reduction centers can be implemented by creating composite materials of the semiconductor–metal and semiconductor–semiconductor types. In this case, of course, the problem of practical separation of reaction products (for example, hydrogen and oxygen) remains, since they inevitably mix in the reaction medium, however, photocatalytic activity, as a rule, increases many times due to the suppression of surface electron-hole recombination and undesirable reverse reactions [55]. The theoretical basis for the creation and operation of composite photocatalysts is discussed in more detail in subsection 1.1.6.

### 1.1.5. Influence of reaction conditions on photocatalytic activity

The observed activity of a heterogeneous photocatalyst in a specific chemical reaction is determined not only by its properties, but also by the conditions of the process – the concentration of the reactants and the photocatalyst itself, pH of the medium, temperature, spectral composition and radiation intensity, as well as other factors.

#### 1.1.5.1. Reactant concentration

To describe the dependence of the photocatalytic reaction rate on the concentration of reactants, the Langmuir-Hinshelwood kinetic model [56], which comes from traditional heterogeneous catalysis [20], is usually used. The derivation of the equation for the rate ω of the simplest heterogeneous photocatalytic reaction occurring with the participation of one reactant in a conditionally inert solvent is based on the law of acting surfaces, the principle of quasi-stationary concentrations for photogenerated charge carriers, as well as the standard Langmuir model for single-layer adsorption. The final equation then has the form

$$\omega = k_r \frac{k_{ads} c}{k_{ads} c + 1}$$

where c is the concentration of the reactant in the solution, $k_r$ is the apparent reaction rate constant and $k_{ads}$ is the adsorption constant. The $k_r$ value includes the rate constants of oxidation, reduction and recombination processes, as well as the radiation intensity, which is assumed to be unchangeable. According to the presented equation, the dependence of the reaction rate ω on the volume concentration of the reactant c, with other conditions being constant, has the form of a classic Langmuir isotherm: in the region of low concentrations there is an almost linear increase in ω with increasing c, and in the region of high concentrations there is a gradual exit of the value of ω to a plateau, explained by the occupancy all active centers of the photocatalyst by particles of the adsorbed reactant (Fig. 8, a). For the convenience of presenting experimental data, the Langmuir-Hinshelwood equation can be linearized by moving to the coordinates $\omega^{-1} - c^{-1}$ (Fig. 8, b):

$$\omega^{-1} = \frac{1}{k_r k_{ads}} c^{-1} + \frac{1}{k_r}$$

Despite the fact that this model does not take into account the specifics of microscopic processes in real photocatalytic systems, it, as a rule, satisfactorily describes experimental data and is therefore widely used in the literature [56].

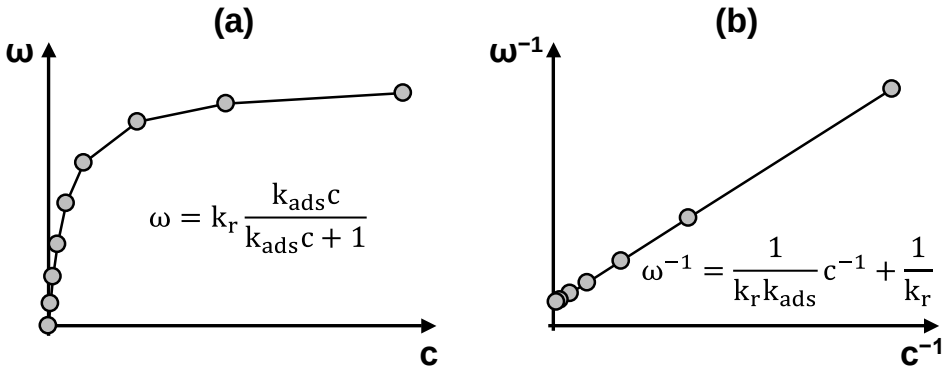


Fig. 8. Dependence of the photocatalytic reaction rate on reactant concentration according to the Langmuir-Hinshelwood kinetic model in standard (a) and linearizing coordinates (b)

1.1.5.2. Photocatalyst concentration

In traditional heterogeneous catalysis, the reaction rate usually increases with increasing catalyst loading, since the surface area on which active sites are localized increases. In the case of heterogeneous photocatalysis, the corresponding dependence is more complex and often passes through a maximum (Fig. 9), which is confirmed by both experimental data and model calculations [57–59]. The key reasons for the decrease in the reaction rate at high volume concentrations of the photocatalyst are lower completeness of light absorption in a highly scattering medium, a slowdown in the diffusion of reactants and products in solution, and an increase in the intensity of reverse reactions.

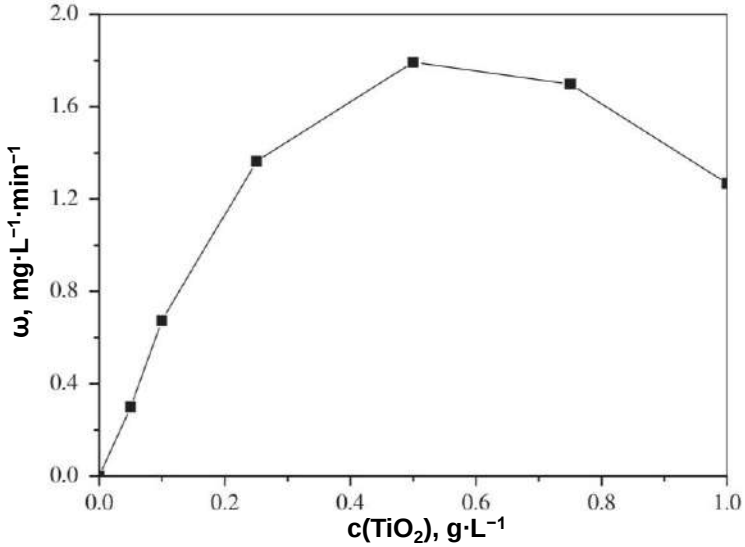


Fig. 9. Dependence of the rate of photocatalytic decomposition of nuclear red dye on the volume concentration of $TiO_2$ [57]

1.1.5.3. pH of the reaction solution

The dependence of the observed photocatalytic activity on the pH of the medium is largely individual and determined by the specifics of a particular photocatalytic system. The

pH value affects the state of the surface of photocatalysts, the displacement of the boundaries of energy zones in the surface layers, chemical and aggregation-sedimentation stability, the form of reactant existence in the solution, as well as the redox potentials of half-reactions. Thus, in the case of photocatalytic water splitting, the dependence of the latter on pH is described by the expression

$$E_{SHE} = E^0_{SHE} - 0.059 \cdot pH$$

At the same time, the shift of the band edges in the near-surface layers of the photocatalyst with a change in pH depends on the chemical nature of the material [60]. It has also been established [61] that in the case of titanium dioxide $TiO_2$ and related oxide photocatalysts, the efficiency of adsorption of reactants containing hydroxyl groups (water, alcohols, carbohydrates) significantly depends on the state of the surface hydroxyl groups of the photocatalyst (Ti)–OH, with the preferred one for adsorption being their neutral (non-ionized) form. When the environment is acidified, surface hydroxyl groups transform into the cationic form (Ti)–$OH_2^+$, and when alkalized, into the anionic form (Ti)–$O^-$, which complicates the adsorption of reactants. In the case of $TiO_2$, the largest number of undissociated groups is achieved at pH ≈ 8–9, which corresponds to the maximum rate of photocatalytic hydrogen generation from aqueous solutions of alcohols (Fig. 10).

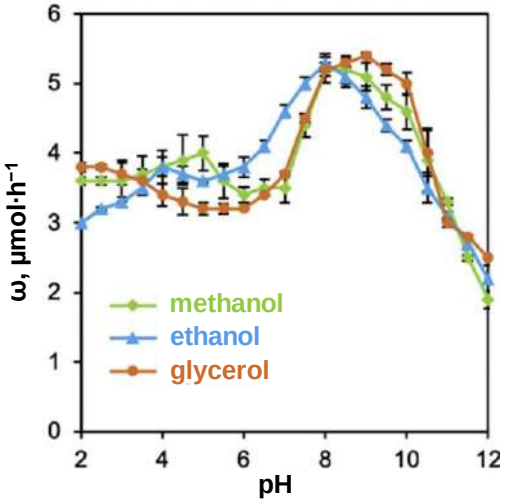


Fig. 10. Dependence of the photocatalytic hydrogen evolution rate in the presence of $TiO_2$ on the pH of aqueous solutions of alcohols [61]

1.1.5.4. Temperature

The temperature influence on photocatalytic activity is ambiguous, since the photocatalytic reaction is a complex multi-stage process and the rate constants of different stages depend on this parameter differently. In particular, as the temperature increases, the

chemical transformations themselves accelerate in accordance with the standard Arrhenius equation, while the desorption of reactants begins to prevail over adsorption, since the former is usually an endothermic process, and the latter is an exothermic one. As a result, the highest photocatalytic activity, as a rule, is achieved at a certain intermediate reaction temperature that corresponds to the optimal ratio of the rate constants of the chemical transformations themselves and the adsorption of reactants. Thus, in [62] it was shown that the rate of photocatalytic decomposition of the methylene blue dye in the presence of titanium dioxide $TiO_2$ increases with increasing temperature from 0 °C to 20 °C and then up to 50 °C, but with further heating to 70 °C it decreases (Fig. 11).

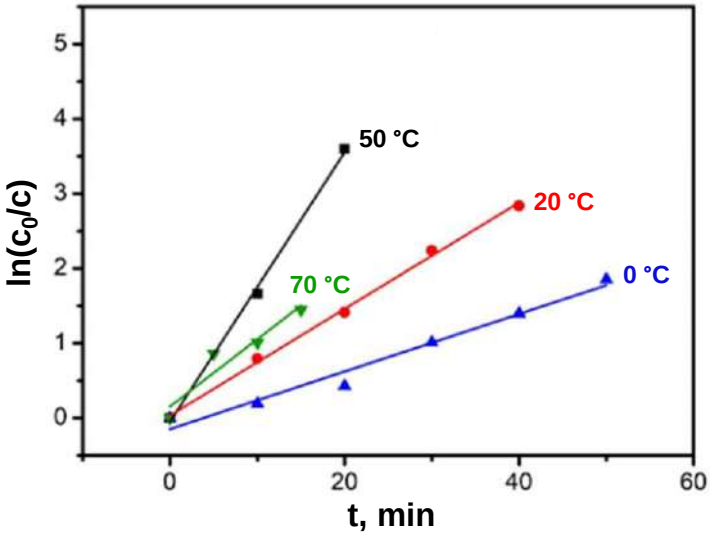


Fig. 11. Kinetic curves of photocatalytic decomposition of methylene blue dye in the presence of $TiO_2$ at different temperatures [62]

1.1.5.5. Spectral composition and radiation intensity

Despite the fact that a semiconductor photocatalyst is potentially capable of using any photons with energy $h\nu > E_g$ to carry out target reactions, the efficiency of the photocatalytic process significantly depends on the spectral composition of the absorbed radiation, and the quantum yield, as a rule, decreases with increasing wavelength. Thus, in [63] it was shown that the photonic efficiency of the photocatalytic oxidation of methanol to formaldehyde in the presence of titanium dioxide $TiO_2$ decreases monotonically with increasing wavelength of the light used (Fig. 12). In particular, when moving from 365 nm to 385 nm, its value decreases by 3 times, and when moving to 400 nm – by almost 25 times. That being said, the dependence of the photonic efficiency of the reaction on the wavelength practically coincides (up to a constant factor) with the dependence of the specific light absorption coefficient of the

photocatalyst on the same parameter (Fig. 12). Thus, photons with an energy slightly exceeding the bandgap width are weakly absorbed by the semiconductor and therefore do not make a significant contribution to the observed rate of the photocatalytic reaction occurring under polychromatic radiation.

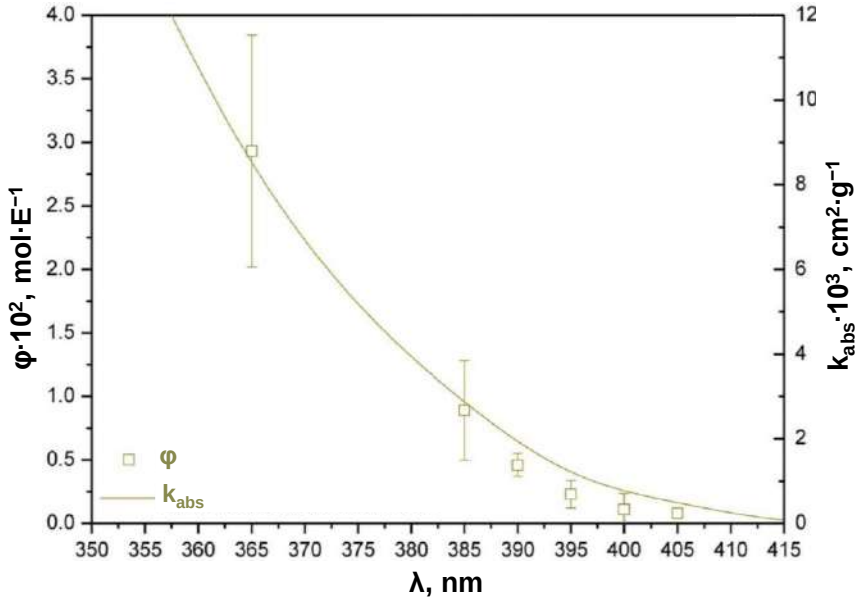


Fig. 12. Dependence of the photonic efficiency φ of methanol oxidation in the presence of $TiO_2$ and the specific light absorption coefficient of the photocatalyst $k_{abs}$ on radiation wavelength [63]

When the spectral composition of the absorbed radiation is constant, the rate of the photocatalytic reaction increases with increasing its intensity, and at relatively low light intensities this dependence is often close to linear, while at higher ones it is proportional to the square root of the light flux [64]. This type of the dependence was, in particular, shown by the example of the reaction of photocatalytic decomposition of the herbicide alachlor on titanium dioxide $TiO_2$ at a fixed duration of irradiation of the reaction solution (Fig. 13) [65].

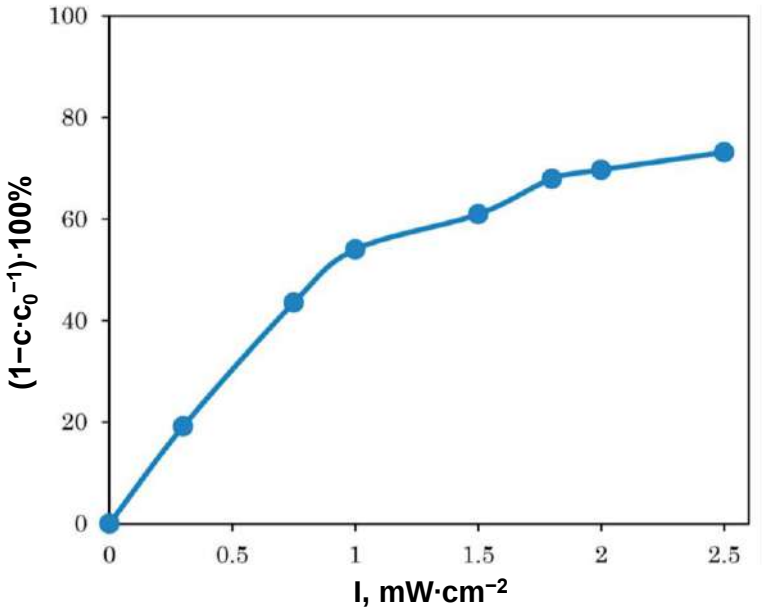


Fig. 13. Dependence of the degree of photocatalytic decomposition of the herbicide alachlor in the presence of $TiO_2$ on the radiation intensity I [65]

1.1.6. Creation of composite photocatalysts

Currently, the design of composite photocatalysts is the leading approach to obtaining new effective materials for using solar energy in practically significant chemical reactions [66]. That being said, the key goals of creating composites include suppression of electron-hole recombination, organization of spatial separation of oxidation and reduction centers, expansion of the spectral range of the photocatalyst, as well as the range of reactions available to it from the thermodynamic point of view. Most composite photocatalysts can be divided into two groups according to the nature of their components: semiconductor-metal and semiconductor-semiconductor materials.

1.1.6.1. Semiconductor–metal composites

Depending on the relative position of the Fermi levels of the semiconductor $F_S$ and the metal $F_M$, two options for implementing their electrical contact are possible [39]. In the case when $F_S$ lies higher in energy (more negative on the electrochemical potential scale) than $F_M$, a transition of electrons from the semiconductor to the metal occurs, as a result of which a contact potential difference arises at the phase boundary and the value of $F_S$ decreases, while $F_M$ increases until electrochemical equilibrium is established $F_S = F_M$. In this case, an electron-deficient region is formed in the near-surface layer of the semiconductor – a depleted (blocking) layer with reduced electrical conductivity, within which a bending of the energy band boundaries is observed. In the case of the reverse arrangement of Fermi levels, when $F_S$ is

located lower (more positive on the electrochemical scale) than $F_M$, electrons transfer from the metal to the semiconductor with the formation of an electron-rich region in the near-surface region of the latter – an enriched (anti-blocking) layer with increased conductivity. In the first case, the semiconductor-metal junction is called a Schottky barrier, in which the transport of electrons from the semiconductor to the metal is difficult (Fig. 14, a), and in the second – an ohmic contact, in which conduction electrons freely flow to the metal (Fig. 14, b).

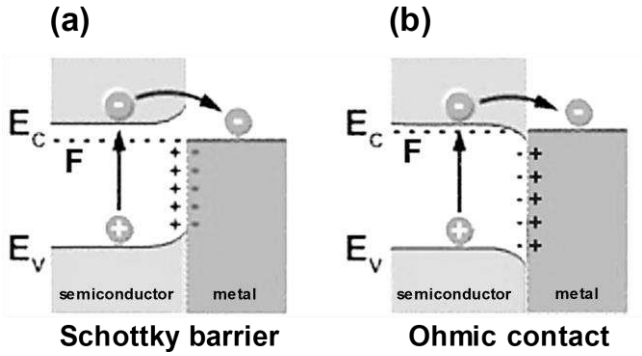


Fig. 14. Semiconductor–metal composite photocatalysts

The ohmic contact of a semiconductor photocatalyst with a metal is of interest as a method of spatial charge separation and is implemented in the creation of composites with metal cocatalysts. In particular, platinum group metals deposited on the surface in the form of nanoparticles are usually used to modify oxide photocatalysts for hydrogen generation [67]. The limited range of metals used is due to a number of factors. Firstly, the relative position of the energy levels of the metal and semiconductor must provide the possibility of the transfer of conduction electrons to the metal. Moreover, in widely studied oxide photocatalysts, such as titanium dioxide $TiO_2$ and titanates, the Fermi level is located relatively high, and only ruthenium is able to form an ohmic contact with them, while in the case of platinum and rhodium this is possible only after dissolving hydrogen in them, leading to a rise in the Fermi level (Fig. 15) [39]. Secondly, platinum metals (especially platinum itself) have their own catalytic properties that make it possible to reduce the overpotential of hydrogen evolution and thereby accelerate the target reaction. Thirdly, the chemical stability of the cocatalyst (in particular, to oxidation), which distinguishes noble metals from other representatives of this class of substances, is of great importance under photocatalysis conditions. Each semiconductor photocatalyst particle modified with a metal cocatalyst functions as a microscopic photoelectrochemical cell in which the metal is the cathode and the semiconductor is the anode. As a consequence, oxidation and reduction processes are spatially separated,

which suppresses surface recombination and undesirable reverse reactions, leading to a multiple increase in photocatalytic activity compared to the activity exhibited by the initial unmodified semiconductor [55].

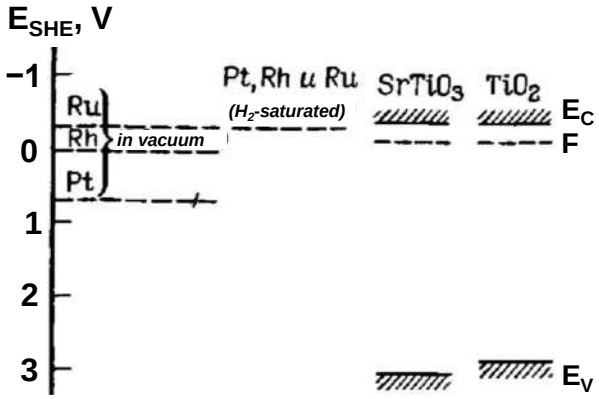


Fig. 15. Relative arrangement of energy levels of oxide photocatalysts and metal cocatalysts [39]

1.1.6.2. Composites based on two semiconductors

Composite photocatalysts based on two semiconductors traditionally include heterojunctions of types I, II and III, p-n junctions, as well as Z-schemes and S-schemes [68], the energy structure and fundamental mechanisms of operation of which are shown in Fig. 16.

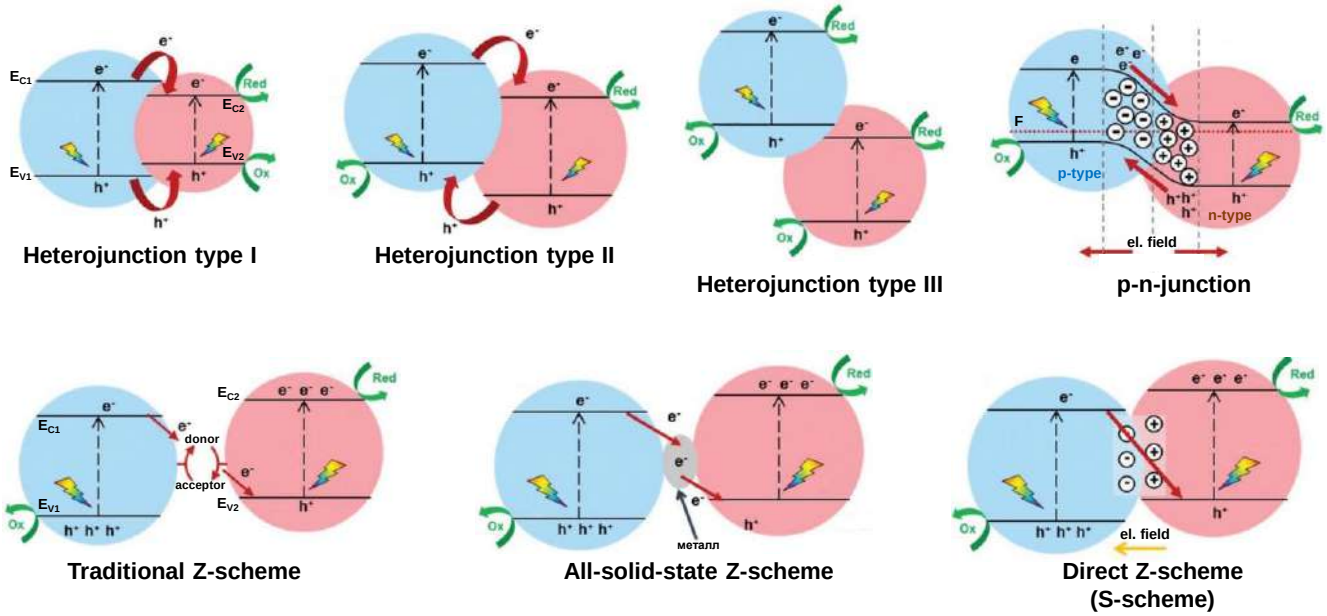


Fig. 16. Composite photocatalysts based on two semiconductors [68]

A type I heterojunction occurs when a wider-gap semiconductor comes into contact with a narrower-gap one, if the potentials of the valence band top and the conduction band bottom of the second lie within the boundaries of the band gap of the first. In this case, photogenerated electrons and holes from the first semiconductor move to the conduction band and valence band of the second, respectively, and both half-reactions occur predominantly on

the surface of the second semiconductor. A type I heterojunction is not of great practical importance due to the fact that spatial separation of charges is not realized in it and the photocatalytic potential of a wider-gap semiconductor is not revealed, electrons and holes from which migrate to a narrower-gap semiconductor with the inevitable weakening of their reducing and oxidizing abilities. However, in a number of cases, photocatalysts based on type I heterojunctions are still superior in activity to the initial components due to some particular effects that occur in specific composites. An example of such a heterojunction is the $TiO_2/Fe_2O_3$ system [69].

In a type II heterojunction, the band gaps of the two semiconductors partially overlap, with the valence band top and conduction band bottom of one semiconductor being higher than the other. In this configuration, conduction electrons from the first semiconductor flow into the conduction band of the second, and holes from the second flow into the valence band of the first, due to which the spatial separation of charges and reaction centers is realized. In this case, oxidative processes occur predominantly on the first semiconductor, and reduction processes – on the second. If there is a significant difference in the band gap of two semiconductors, the more narrow-gap one in such a heterojunction can be considered as a photosensitizer in relation to the other, wider-gap one. Type II heterojunctions are widely used in the creation of new photocatalysts based on most known semiconductor materials. Their prime examples are $TiO_2/g\text{-}C_3N_4$ [70], $TiO_2/CdS$ [71], $ZrO_2/g\text{-}C_3N_4$ [72], $WO_3/BiVO_4$ [73] and many other composites.

In a type III heterojunction band gaps of two semiconductors are spaced apart at the energy scale and do not overlap, due to which the charge transfer between the materials practically does not occur and photocatalytic properties of the composite generally represent the superposition of properties of the components functioning on one's own. However, with the hypothetical implementation of charge transfer between the semiconductors, unusually high values of the redox potentials of photogenerated carriers can be achieved, which motivates researchers to continue the development of such heterojunctions. Particularly, it was found that the problem of charge transfer between two semiconductors with non-overlapping band gaps can be solved by creating a three-component composite containing a metal (for example, silver) as a «contact» between the semiconductors, in which surface plasmon resonance is possible. The efficiency of such composites, called type B heterojunctions, was demonstrated,

in particular, using the example of the systems $Ag_3PO_4/Ag/GdCrO_3$, $CuWO_4/Ag/GdCrO_3$, $WO_3/Ag/GdCrO_3$ and $Bi_2WO_{6-x}F_{2x}/Ag/GdCrO_3$ [74,75].

In photocatalysts based on p-n junctions, the spatial separation of photogenerated charge carriers is achieved due to not only the relative shift of the energy band edges, as in the case of a type II heterojunction, but also the contact potential difference that arises at the interface between two semiconductors with different types of conductivity. In this case, oxidative processes occur on a hole semiconductor (p-type), and reduction processes occur on an electronic semiconductor (n-type). Examples of composite photocatalysts with a p-n junction are $TiO_2/NiO$ [76], $KNbO_3/Ag_2O$ [77] and $ZnIn_2S_4/CuInS_2$ [78].

A key disadvantage of widely used type II heterojunctions is the weakening of the reduction and oxidation ability of photogenerated electrons and holes, which narrows the range of the reactions allowed on these photocatalysts from a thermodynamic point of view. Attempts to overcome this problem led to the creation of so-called Z-schemes – photocatalysts, in which the sequential absorption of two photons is realized, which makes it possible to significantly spread the potentials of electrons and holes along the energy scale. In the traditional Z-scheme, the concept of which was proposed in 1979 [79], two semiconductors with partial overlapping of band gaps are used, charge transfer between which is carried out through a mediator – a redox couple in the solution (for example, $Fe^{3+}/Fe^{2+}$). In this case, there is no direct physical contact between the semiconductors, which is why such a photocatalyst is not composite in the usual sense. When a light quantum is absorbed by the first semiconductor, which has a lower position of the band edges, an electron-hole pair is generated, after which an electron from the conduction band of the first semiconductor is transferred by a mediator in solution to the valence band of the second semiconductor, from where, under the influence of another light quantum, it passes into its conduction band. In such a system, the target oxidation processes occur predominantly on the first semiconductor, and reduction processes on the second, and the potentials of reactive electrons and holes are greater, the closer the conduction band bottom of the first semiconductor $E_{C1}$ and the valence band top of the second $E_{V2}$ are located with comparable bandgap widths (Fig. 16). The need to use two photons per one act of the chemical reaction in Z-schemes certainly leads to a decrease in the quantum yield, but allows processes such as the decomposition of pure water to be carried out on two relatively

narrow-gap semiconductors that effectively absorb visible light but, due to their energy structure, are not capable of decomposing water when taken separately [80].

Traditional Z-schemes can only be used in liquid media (solutions), and their efficiency suffers from side processes involving a redox mediator. In view of this, in 2006, all-solid-state Z-schemes were proposed [81] – composite photocatalysts, in which charge transfer between semiconductors occurs through a metal (for example, gold) or another conducting material. For the first time, such a scheme was successfully implemented by the authors of the above-mentioned work in the $TiO_2$/Au/CdS composite. However, despite the efficiency of charge transfer through a metal contact and the possibility of functioning of all-solid-state Z-schemes in a gaseous environment, the creation of such composites is a complex procedure from a preparative point of view. As a result, there is growing interest in the development of so-called direct Z-schemes, in which there exist a direct contact between two semiconductors without any mediator. For the first time, a similar configuration of a composite photocatalyst was implemented in 2009 using the example of ZnO/CdS [82], which was followed by a rapid increase in the number of publications devoted to photocatalysts based on heterojunctions and, in particular, Z-schemes [83]. In 2020, in order to avoid confusion between all-solid-state (containing a metal mediator) and direct Z-schemes, it was proposed to use a separate term «S-scheme» for the latter [84], which is now widely used as a synonym for a direct Z-scheme.

The direct Z-scheme (S-scheme) represents a heterojunction based on two semiconductors, the first of which has energy band edges and the Fermi level lower than those of the second. When direct contact is established between the semiconductors, electrons migrate from the second semiconductor to the first until an equilibrium value of the Fermi level is established in the contact area. As a result, an electron-rich region is formed in the first semiconductor, and an electron-deficient region is formed in the second, which leads to the appearance of an electric potential gradient. The indicated potential gradient, the curvature of the band edges in the contact area and Coulomb forces ensure the transition of photogenerated electrons from the conduction band of the first semiconductor to the valence band of the second, where they recombine with the holes located there. Thus, «unnecessary» charge carriers from a practical point of view are mutually neutralized, and «useful» photogenerated electrons in the conduction band of the second semiconductor and holes in the valence band of the first retain their high reducing and oxidizing ability to carry out target half-reactions [85].

Due to the extremely efficient charge separation and suppression of recombination, the development of direct Z-schemes (S-schemes) is currently considered one of the most promising approaches to the creation of new highly active photocatalysts.

1.1.7. Photocatalytic hydrogen production: problems and prospects

The photocatalytic water splitting into simple substances under the influence of ultraviolet radiation was first demonstrated by Japanese researchers Fujishima and Honda in 1972, using a photoelectrochemical cell with a photoanode made of titanium dioxide $TiO_2$ [86]. It was this work that marked the beginning of the rapid development of «hydrogen» photocatalysis, which remains the leading direction of heterogeneous photocatalysis to this day in light of the great importance of alternative energy for the sustainable development of mankind. Historically, water was considered as the main raw material for photocatalytic hydrogen production – a widely available shareware resource that does not require preliminary processing. The process of water decomposition into simple substances, which can be represented in the form of a scheme

$$2H_2O = 2H_2 + O_2$$

$$\begin{cases} 2H^+ + 2e^- = H_2 \\ 2H_2O + 4h^+ = O_2 + 4H^+ \end{cases}$$

is thermodynamically forbidden in the absence of irradiation ($\Delta G^0$ = 237 kJ/mol). Although this reaction is feasible in the photocatalytic mode, its thermodynamic-kinetic features significantly limit the efficiency of hydrogen production [87]. Particularly, due to the significant difference in the standard potentials for the evolution of hydrogen and oxygen (1.23 V), as well as the overpotential during the formation of these gaseous products, the decomposition of water requires relatively wide-gap photocatalysts, the positions of the band edges of which satisfy the criteria for the thermodynamic allowance of the process, which limits the possibility of using visible and especially near-infrared light. In addition, the half-reaction of oxygen evolution from pure water is a kinetically complex four-electron process that strongly limits the rate of the overall reaction. To increase the efficiency of hydrogen generation from water, various approaches to modifying photocatalysts, discussed earlier, are used – deposition of metal cocatalysts on the surface to accelerate half-reactions, creating Z-schemes for carrying out the reaction on relatively narrow-gap semiconductors, etc. However, despite the significant progress achieved in this direction over the past decade [88–90], the

energy-efficient splitting of pure water into simple substances still remains a serious challenge for researchers and engineers. In particular, while efficient cocatalysts for hydrogen evolution are well known (platinum metals, nickel), the search for suitable cocatalysts for oxygen evolution still remains an urgent task [12].

Another actively developing area of modern heterogeneous photocatalysis is the production of hydrogen from aqueous solutions of organic compounds [91]. It should immediately be noted that in the literature such reactions are also often called water splitting, which, strictly speaking, is not entirely correct. The theoretical basis for the hydrogen generation from aqueous-organic mixtures is the replacement of the kinetically inhibited half-reaction of oxygen evolution, which takes place during the decomposition of pure water, with the half-reaction of oxidation of organic matter (the so-called «sacrificial agent»), usually characterized by a lower absolute value of the reduction potential and proceeding with a significantly higher rate, which, in turn, makes it possible to achieve greater hydrogen evolution performance. In particular, during the photocatalytic production of hydrogen from aqueous solutions of primary alcohols, in the simplest case, processes described by the scheme can occur:

$$C_nH_{2n+1}OH = C_nH_{2n}O + H_2$$

$$\begin{cases} 2H^+ + 2e^- = H_2 \\ C_nH_{2n+1}OH + 2h^+ = C_nH_{2n}O + 2H^+ \end{cases}$$

The most promising application of such processes seems to be the photocatalytic production of hydrogen from components and products of processing of renewable plant biomass – bioalcohols, carboxylic acids, carbohydrates and other organic compounds, which themselves are characterized by a relatively low calorific value, but can be photocatalytically transformed into much more energy-intensive hydrogen fuel. That being said, bioalcohols (in particular, methanol) remain the most studied substrates at the moment, while less attention has been paid to the photocatalytic reforming of carbohydrates in the literature [92]. In addition, the development of photocatalysts for producing hydrogen by purifying aqueous media from organic pollutants is currently underway [93–95]. In such works, special attention is paid not only to the rate of hydrogen generation, but also to the completeness of the oxidation of toxic substrates to harmless compounds.

In general, in the field of design of modern photocatalytic systems for generating hydrogen from water and water-organic mixtures, along with the focus on achieving high activity and durability, the following trends can also be noted:

- Development of hybrid systems that combine traditional photocatalysis (internal photoelectric effect in a semiconductor) with additional thermal or ultrasonic effects (thermophotocatalysis [96], piezophotocatalysis [97]);
- Focus on the effective use of not only ultraviolet, but also visible and near-infrared radiation, which predominates in the solar spectrum [98];
- Creation of photocatalysts that do not contain toxic and/or expensive elements [99];
- Creation of photocatalysts based on nanoparticles or using them to achieve a developed active surface [48] and implement specific «nanoscale» effects, such as surface plasmon resonance [37];
- Development of easy-to-implement and at the same time effective approaches to increasing the photocatalytic activity of already known materials.

The last trend in the presented list is of fundamental importance for the creation of photocatalytic systems that will have wide practical application in the future. For instance, in the literature one can find numerous references to highly active photocatalysts that provide hydrogen generation with a quantum yield close to 100%. However, such photocatalysts are often extremely difficult to create from a preparative point of view, and the declared activities can be achieved only under narrow specific conditions (fixed wavelength of radiation, a certain sacrificial agent in solution, etc.), which is why the corresponding materials may not be of significant practical interest.

### 1.2. Photocatalysts based on layered perovskite-like oxides

The experimental discovery of the photocatalytic decomposition of water on titanium dioxide $TiO_2$ in 1972 [86] initiated the rapid development of new photocatalysts based on this material, as well as other semiconductor oxides ($ZrO_2$, $Ta_2O_5$, ZnO, $SrTiO_3$), sulfides, selenides, tellurides, nitrides, phosphides and carbides. At the same time, oxide photocatalysts still remain one of the central objects of research in the field of photocatalysis due to their energy structure suitable for water decomposition, photochemical stability under operating conditions, and accessibility. At the end of the 1980s, in reactions of hydrogen generation from water and aqueous methanol, an oxide photocatalyst based on layered potassium hexaniobate

$K_4Nb_6O_{17}$ was first studied, the modification of which with nickel oxide NiO led to the achievement of an unsurpassed quantum efficiency of ≈ 3.5% at that time under ultraviolet radiation [100,101]. The high activity of this material was explained by the authors by the layered type of its structure, which led to intensive study of new photocatalysts based on layered compounds and, in particular, layered perovskite-like oxides, which continues to this day [102–104].

### 1.2.1. Structure and classification of layered perovskite-like oxides

Layered perovskite-like oxides are solid crystalline compounds built according to the block principle, in which two-dimensional blocks with the structural type of the perovskite mineral $CaTiO_3$ (in general, $ABO_3$) alternate with interlayer spaces containing simple cations A' or cationic structural units. Perovskite blocks consist of n layers connected by the vertices of metal-oxygen octahedra $BO_6$ with a cation B in the center, the cuboctahedral spaces between which are occupied by cations A [105]. Depending on the value of n, there are usually single- (n = 1), double- (n = 2), three- (n = 3) and four-layer (n = 4) oxides (Fig. 17), however, it is possible to form the structures with a greater thickness of perovskite blocks, as well as with alternating blocks of different thicknesses; the limiting case n = ∞ corresponds to a non-layered perovskite. In addition, some layered perovskite-like oxides have two different types of interlayer spaces, as shown in Fig. 17 at the example of a single-layer compound.

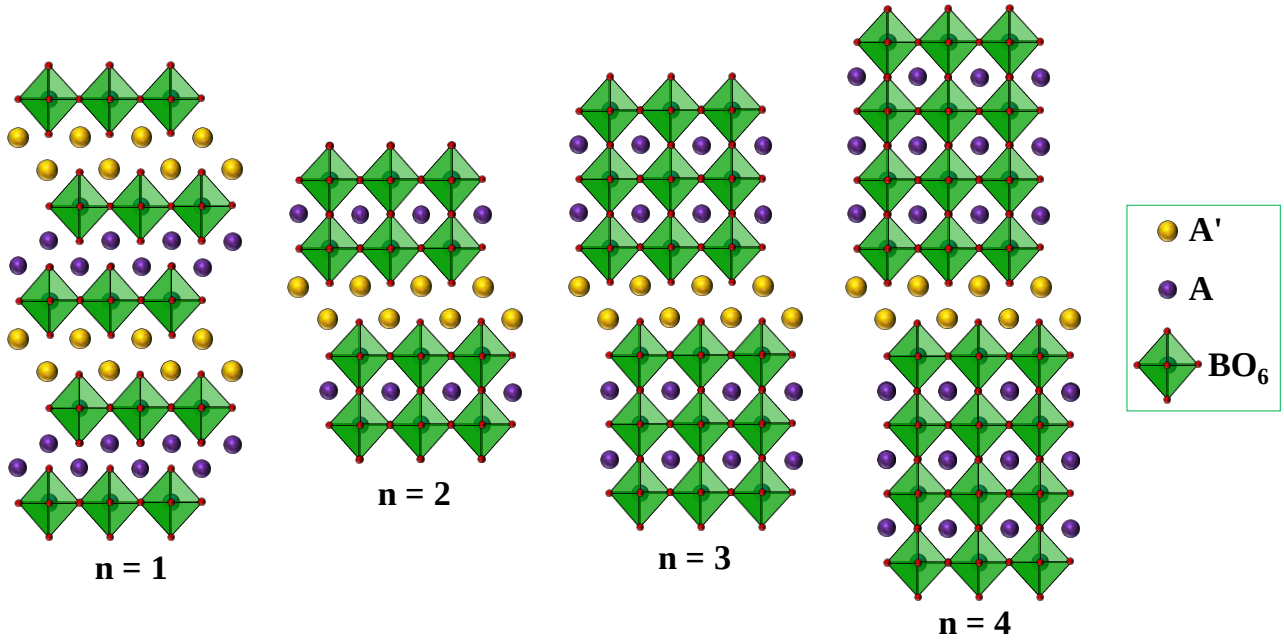


Fig. 17. Layered perovskite-like oxides with a different thickness n of the perovskite block

In accordance with the structural features of the interlayer space, there are three main classes of layered perovskite-like oxides, named after their first researchers: the Dion-Jacobson, Ruddlesden-Popper and Aurivillius phases (Fig. 18) [105].

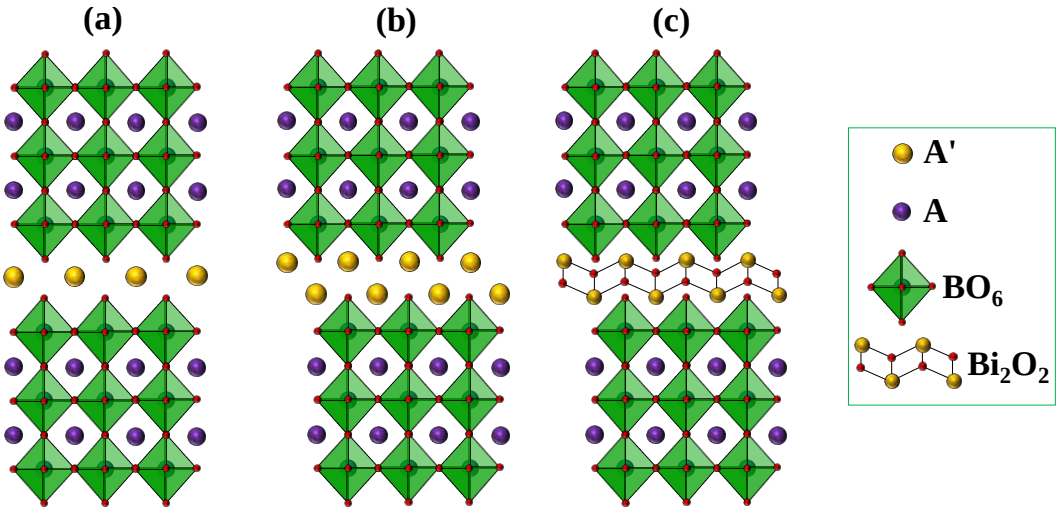


Fig. 18. Dion-Jacobson (a), Ruddlesden-Popper (b) and Aurivillius phases (c)

Dion-Jacobson phases (Fig. 18, a) are described by a general formula of the form $A'[A_{n-1}B_nO_{3n+1}]$ ($n \geq 2$) or $ABO_4$ ($n = 1$), where A' is a singly charged interlayer cation, A is a cation of an alkaline earth or transition element, B is a four- or, most often, five-charged transition cation (niobium, tantalum). These phases are characterized by a relatively low interlayer charge density. The horizontal relative position of adjacent perovskite blocks (the so-called conformation) depends on the size of A' [106]. In the case of relatively large cations A' = Rb, Cs, an eclipsed conformation is more typical, in which the oxygen vertices of the octahedra of one perovskite block directed into the interlayer space are located directly above the vertices of the other, as shown in Fig. 18, while in the case of smaller cations A' = Li, Na, K, a shifted (semi-staggered) or staggered conformation with a relative displacement of adjacent perovskite blocks along one or both horizontal axes by half the corresponding lattice parameter is more likely. Typical representatives of Dion-Jacobson phases are double-layer niobates $A'LaNb_2O_7$, as well as three-layer niobates $A'Ca_2Nb_3O_{10}$ and tantalates $A'Sr_2Ta_3O_{10}$.

Composition of Ruddlesden-Popper phases (Fig. 18, b) in a general case can be represented in the form $A'_2[A_{n-1}B_nO_{3n+1}]$, where A', A, B are the designations of cations used above, and cation B is most often titanium or tantalum. The structure of Ruddlesden-Popper phases can be described by alternating perovskite blocks with layers having the rock salt (NaCl) structure. They are characterized by a high interlayer charge density, as well as a staggered conformation, in which there is a relative shift of adjacent perovskite blocks along

both horizontal axes by half the corresponding lattice parameters, as a result of which the vertex of each terminal octahedron of one block is located between the four vertices of the octahedra of the neighboring one [107]. Examples of Ruddlesden-Popper phases include single-layer and three-layer titanates $A'LaTiO_4$ and $A'_2La_2Ti_3O_{10}$, studied in this work, as well as double-layer tantalates $A'_2CaTa_2O_7$.

Aurivillius phases (Fig. 18, c) represent compounds of the form $(Bi_2O_2)[A_{n-1}B_nO_{3n+1}]$, in which perovskite blocks alternate with the layers possessing the fluorite ($CaF_2$) structure, formed by bismuth and oxygen. In this case, cations B can formally be three-, four-, five- and six-charged [108]. Most of them, like the Ruddlesden-Popper phases, are characterized by a relative shift of adjacent perovskite blocks (staggered conformation). An important feature of Aurivillius phases is the participation of 6s-orbitals of $Bi^{3+}$ cations along with 2p-orbitals of oxygen in the formation of the valence band, which determines the higher position of its top and, accordingly, the possibility of intrinsic absorption of visible light [109]. Typical representatives of Aurivillius phases are single-layer molybdate $Bi_2MoO_6$ and tungstate $Bi_2WO_6$, double-layer niobate $PbBi_2Nb_2O_9$ and three-layer titanate $Bi_4Ti_3O_{12}$.

### 1.2.2. Chemical properties of layered perovskite-like oxides

Synthesis of most of the initial layered perovskite-like oxides is carried out using the high-temperature ceramic technology based on simple oxides, carbonates or nitrates of the required elements. In some cases, methods of synthesis in molten salts, coprecipitation, solvothermal and sol-gel synthesis can also be successfully used, but the corresponding approaches have been developed only for a limited range of compounds of interest [104]. To further control the practically significant properties of layered perovskite-like oxides and create new materials based on them, a wide range of topochemical transformations are used – reactions during which the composition of the layered compound partially changes while maintaining the structure of the relatively rigid perovskite matrix as a whole, due to which the products of the corresponding transformations have significant similarities with the initial objects [110–113]. Topochemical reactions make it possible to obtain many perovskite-like compounds and their derivatives that cannot be synthesized directly due to thermal instability or other reasons.

Most chemical reactions involving layered perovskite-like oxides can be divided into two groups: reactions in the perovskite block and reactions in the interlayer space. The first

group mainly includes isovalent and non-isovalent substitution (mainly anionic), which is widely used in the case of non-layered compounds. For instance, in the light of the creation of photocatalysts capable of functioning under visible radiation, nitridation reactions are of particular importance – partial substitution of oxygen with nitrogen with the formation of oxynitrides, in which the band gap narrows making it possible to significantly expand the region of light absorption. A simplified representation of the nitridation reaction with ammonia using the example of the three-layer Dion-Jacobson niobate can be represented as:

$$KCa_2Nb_3O_{10} + xNH_3 = KCa_2Nb_3O_{10-1.5x}N_x + 1.5xH_2O$$

During this process, the initially colorless niobate acquires a pronounced color, and its bandgap energy decreases from approximately 3.5 to 2.5 eV [114]. Oxynitrides have also been successfully obtained based on other oxides, in particular $KCa_2NaNb_4O_{13}$ [115], $A'LaTa_2O_7$ (A' = K, Rb) [116], $CsCa_2Ta_3O_{10}$ [117], $NaLaTiO_4$ [118], $KLaTiO_4$ [119] and $K_2La_2Ti_3O_{10}$ [120]. That being said, in the works on the nitridation of niobates it was noted that the process is accompanied by partial niobium reduction to the oxidation state +4. At the same time, cationic substitution in a perovskite block as a post-modification reaction is usually not possible, and therefore the required cationic composition is specified at the stage of synthesis of the initial compound.

However, the main interest when working with layered perovskite-like oxides is the chemical processes involving their interlayer space – ion exchange (including protonation), hydration, intercalation and grafting of organic compounds, as well as exfoliation into nanosheets, most of which can be carried out using «soft chemistry» approaches. It should immediately be noted that these reactions are mainly typical of the so-called ion-exchangeable layered perovskite-like oxides – Dion-Jacobson and Ruddlesden-Popper phases with alkali interlayer cations. Interlayer ion exchange in Aurivillius phases is also possible, however, after substituting the bismuth-oxygen layer with cations, the corresponding compounds cease to be Aurivillius phases as such.

Ion exchange in layered perovskite-like oxides consists in the replacement of the initial interlayer cations with other cations or cationic structural units, occurring in solutions or melts. That being said, the difference in the size of the cations leads to a change in the interlayer distance *d*, which is directly related to the lattice parameter *c* (Fig. 19, a). The possibility of ion exchange significantly depends on the ratio of the sizes of the substituting and substituted

cations, as well as on the charge of the latter, which determines the strength of its Coulomb interaction with negatively charged perovskite blocks. All other things being equal, the substitution of relatively large cations with smaller ones proceeds faster. Singly charged cations are usually substituted relatively easily, while multiply charged cations may not undergo the substitution at all.

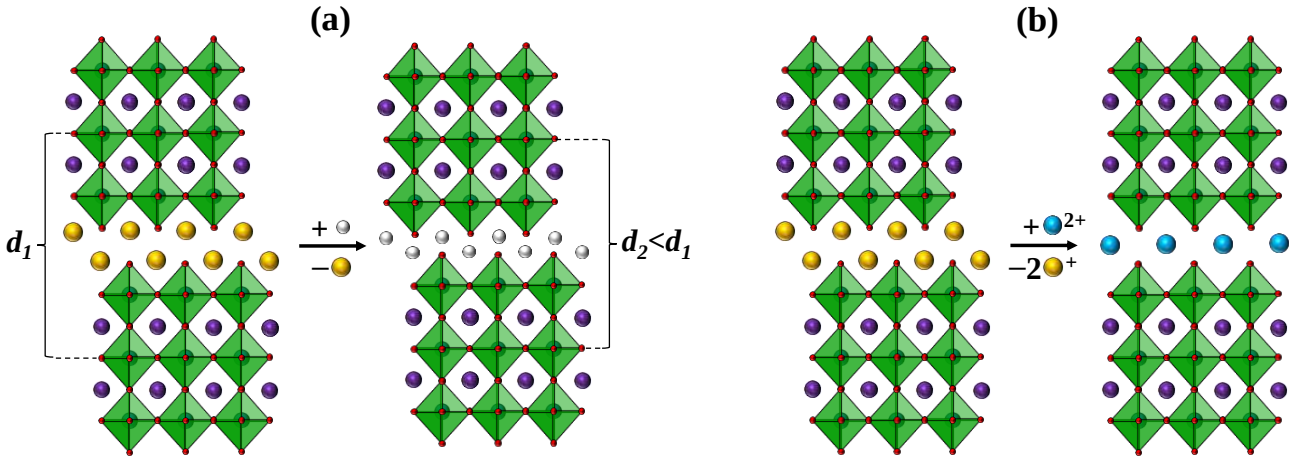


Fig. 19. Interlayer ion exchange in the Ruddlesden-Popper phase with preservation of the structural type (a) and with transformation into the Dion-Jacobson phase (b)

Interlayer ion exchange reactions serve as an important tool for managing the photocatalytic properties of layered perovskite-like oxides. Thus, in the study [121], it was found that partial substitution of interlayer potassium cations in the titanate $K_2La_2Ti_3O_{10}$ with cations of alkaline earth metals (calcium, strontium, barium) in molten salts leads to an increase in the photocatalytic activity of the titanate in the reactions of methyl orange decomposition and hydrogen evolution from aqueous methanol up to 4 times. In [122], a similar method was used to partially substitute interlayer lithium and potassium cations in tantalates $LiCa_2Ta_3O_{10}$ and $KCa_2Ta_3O_{10}$ with sodium, which made it possible to increase the efficiency of the photocatalytic splitting of water into simple substances up to 3.5 times. In addition, interlayer ion exchange can be used to carry out transformations between layered phases of different structural types. In particular, the authors of the study [123] replaced sodium cations in the Ruddlesden-Popper titanate $Na_2La_2Ti_3O_{10}$ with cations of cobalt, copper and zinc, which led to the transition of the staggered conformation to the eclipsed one and, accordingly, the transformation of the titanate into the Dion-Jacobson phase $MLa_2Ti_3O_{10}$ (M = Co, Cu, Zn), as shown in Fig. 19, b, while in [124], by reacting the titanate $K_2La_2Ti_3O_{10}$ with bismuthyl chloride BiOCl, the Aurivillius phase $(Bi_2O_2)La_2Ti_3O_{10}$ was successfully obtained.

A special case of ion exchange processes are the protonation reactions of layered perovskite-like oxides, during which interlayer metal cations are replaced by protons in aqueous solutions of Arrhenius acids. In this case, the initial alkaline forms of oxides are transformed into the so-called protonated forms [125]. The latter, being solid acids, are of great interest as precursors for the further production of hybrid organic-inorganic materials, as well as perovskite nanosheets via liquid-phase exfoliation [112,113]. In some cases, based on protonated forms, new alkaline forms can be obtained that are not amenable to direct ceramic synthesis due to thermal instability or other reasons. In particular, a series of single-layer titanates $KLnTiO_4$ (Ln = La or lanthanide) was synthesized by treating protonated compounds $HLnTiO_4$ with potassium hydroxide, obtained, in turn, from ceramically synthesized precursors $NaLnTiO_4$ [126]. Protonation with the preservation of the oxide's belongingness to the structural class is possible only in the case of the Dion-Jacobson and Ruddlesden-Popper phases. The interaction of Aurivillius phases with protic acids (usually hydrochloric acid) is called acid leaching and is accompanied by their transformation into Ruddlesden-Popper phases [127].

Protonation of layered perovskite-like oxides is often accompanied by their hydration – intercalation of water molecules into the interlayer space, promoting its expansion in the direction of stacking of perovskite blocks (increasing the interlayer distance *d*). That being said, protonation and hydration significantly depend on the structural features of specific compounds. For instance, a high degree of protonation of the well-known three-layer Dion-Jacobson niobate $KCa_2Nb_3O_{10}$ is achieved only in sufficiently concentrated acid solutions [128], while the three-layer Ruddlesden-Popper titanate $K_2La_2Ti_3O_{10}$ is intensively protonated even in pure water [129]. Hydrates of the alkaline form of the niobate $KCa_2Nb_3O_{10}$ with a large amount of interlayer water are currently unknown, while the titanate $K_2La_2Ti_3O_{10}$ forms them already in an atmosphere of humid air. However, when going to the protonated forms of these oxides, the opposite situation is observed: protonated niobate exists in a highly hydrated state $HCa_2Nb_3O_{10}\cdot 1.5H_2O$ [130], while protonated titanate $H_2La_2Ti_3O_{10}$ contains less than 0.5 molecules of water per formula unit [129].

Of particular interest in the light of the creation of new functional materials are also the reactions of intercalation and grafting of organic compounds into the interlayer space, as well

as the exfoliation of layered perovskite-like oxides into separate nanosheets, discussed in detail in subsections 1.2.4 and 1.2.5, respectively.

### 1.2.3. The role of interlayer space in photocatalysis

The increased photocatalytic activity of ion-exchangeable layered perovskite-like oxides compared to non-layered materials is largely due to the unique structure of perovskite blocks, which ensures effective separation of photogenerated charge carriers, as well as the existence of a chemically active interlayer space, considered as an additional reaction zone in the photocatalytic process. These compounds have great potential for further modification through topochemical transformations involving the interlayer zone, which is especially important in view of the approaching exhaustion of the possibilities for increasing the activity of traditional non-layered photocatalysts.

Intensive study of photocatalytically active materials based on layered perovskite-like oxides began in 1990 from the paper [131], in which Dion-Jacobson niobates $A'LaNb_2O_7$ and $A'Ca_2Nb_3O_{10}$ (A' = K, Rb, Cs, H) were tested in the reactions of hydrogen and oxygen generation from aqueous solutions of methanol and silver nitrate, respectively, for the first time. The study showed that the activity of the niobates increases sharply after protonation of their interlayer space, which is also accompanied by its pronounced hydration. This experimental fact led the authors to think about the possible functioning of the interlayer space as an additional reaction zone along with the external surface of the photocatalyst, into which water and methanol molecules can penetrate. Indirect confirmation of this hypothesis was the decrease in the rate of photocatalytic hydrogen evolution on the layered niobates with increasing the length of alcohol molecules in an aqueous solution (methanol, ethanol, *n*-propanol, *n*-butanol), which may be caused by steric hindrance of their transport into the interlayer zone. When titanium dioxide $TiO_2$, which is deprived of the possibility of interlayer intercalation, was used as a photocatalyst, this decrease in the activity was not observed [131]. A similar trend was also revealed in [132] using the example of the $HCa_2Nb_3O_{10}/SiO_2$ composite with a developed microporous structure between the perovskite layers. The study showed that in the case of the initial niobate, the rate of hydrogen generation drops sharply with increasing length of the alcohol molecule in an aqueous solution (in particular, by more than two orders of magnitude when replacing methanol with *n*-propanol), while in the case of the composite with increased accessibility of the interlayer space, the multiplicity of the

activity decrease does not exceed 8 times. In article [133], it was found that the three-layer tantalate $NaCa_2Ta_3O_{10}$, which forms a hydrate in an aqueous medium with an intercalated water content of 1.86 molecules per formula unit, is significantly superior in photocatalytic activity in the reaction of water decomposition to the $CsCa_2Ta_3O_{10}$ phase, practically not subject to hydration at all. As part of the same work, photocatalytic experiments were also carried out in heavy water, the results of which led to the conclusion that water molecules in the interlayer space of $NaCa_2Ta_3O_{10}$ actually participate in the photocatalytic process. The authors of the article [134] carried out hydrothermal treatment with water of the initially anhydrous composite $LiCa_2Ta_3O_{10}/NiO_x$ at 160 °C, which made it possible to obtain a hydrate that was approximately 2 times superior to the initial compound in photocatalytic activity in the water splitting reaction. In the already mentioned work [122], a series of tantalates $Na_xK_{1-x}Ca_2Ta_3O_{10}$ was studied, in which there was a monotonous increase in photocatalytic activity with an increase in the degree of interlayer hydration.

Similar patterns were observed in the case of Ruddlesden-Popper phases, which have been intensively studied as photocatalysts since 1997 [135]. Particularly, it was found that among three-layer titanates $A'_2La_2Ti_3O_{10}$ (A' = Li, Na, K, Rb), the most active in hydrogen generation reactions representatives are the compounds with A' = K, Rb, which undergo partial protonation and hydration in an aqueous medium, while their analogues with A' = Li, Na are significantly less active under the same conditions, practically do not experience protonation and water intercalation [136,137]. When titanium is partially substituted by niobium in the titanate $Rb_2La_2Ti_3O_{10}$ with the formation of titanoniobate $RbLa_2Ti_2NbO_{10}$, the photocatalytic activity in the water splitting reaction drops by almost an order of magnitude, which can mainly be associated with the loss of the ability of the interlayer space to hydrate, while the bandgap width and morphology of the compound are generally preserved [138].

The above experimental facts indicate that the composition of the interlayer space is one of the most important factors determining the photocatalytic activity of ion-exchangeable layered perovskite-like oxides, and targeted control of it can serve as a powerful tool for increasing the activity.

### 1.2.4. Organic-inorganic derivatives of layered perovskite-like oxides

Organic-inorganic derivatives of layered perovskite-like oxides are hybrid compounds consisting of chemically bonded inorganic perovskite matrix and organic molecules or their

fragments in the interlayer space [139,140]. Unlike composites, which by definition consist of several individual phases, organic-inorganic derivatives are solid materials with a single crystal lattice. Interest in the creation of the latter is due to the possibility of combining practically significant properties of inorganic and organic parts in one material. Moreover, the interaction between these parts can lead to the appearance of new unique properties that are not characteristic of the initial compounds taken separately.

1.2.4.1. Intercalation and grafting of organic compounds

The initial compounds for the synthesis of most organic-inorganic derivatives are protonated forms of oxides, which, being solid acids, are capable of reacting with a number of organic substances via their binding in the interlayer space. Depending on the type of a chemical bond between the inorganic matrix and the organic component, ionic and covalent organic-inorganic derivatives are distinguished, formed during intercalation and grafting reactions, respectively (Fig. 20) [141].

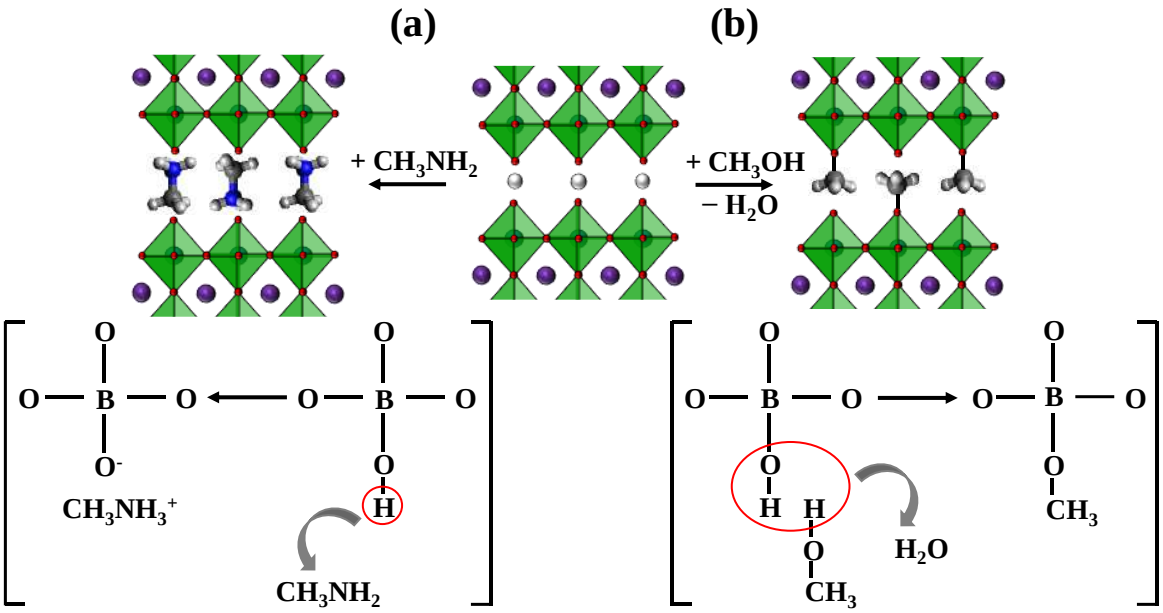


Fig. 20. Reactions of methylamine intercalation (a) and methanol grafting (b)

Intercalation is the process of non-covalent introduction of organic molecules into the interlayer space, usually proceeding according to an acid-base mechanism (Fig. 20, a) [142]. A pronounced tendency to intercalation is usually shown by organic bases (in particular, amines) – compounds that easily transform into a cationic form by binding interlayer protons. In this case, the intercalation products formally represent organic-inorganic salts. Grafting of organic compounds involves the covalent binding of their structural fragments to an inorganic matrix through the interlayer oxygen vertices of perovskite octahedra $BO_6$. It usually proceeds as a

condensation reaction, i.e. is accompanied by the formation of a low-molecular-weight by-product, the continuous removal of which from the reaction medium can contribute to a shift in the equilibrium towards the target grafted derivative. Alcohols [143], carbohydrates [144], carboxylic [145] and phosphonic acids [155], as well as other organic and organoelement compounds with a hydroxyl group can act as grafting modifiers. The most well-known grafting reactions of alcohols into protonated layered perovskite-like oxides proceed according to the gross scheme (Fig. 20, b), similar to the acylation of alcohols with acids in organic chemistry (esterification), and the resulting hybrid compounds are formally organic-inorganic esters. In a simplified manner, the reactions of amine intercalation and alcohol grafting using the example of niobate $HCa_2Nb_3O_{10}$ can be written in the form of the equations:

$$HCa_2Nb_3O_{10} + xRNH_2 = (RNH_2)_xHCa_2Nb_3O_{10}$$

$$HCa_2Nb_3O_{10} + xROH = (RO)_xH_{1-x}Ca_2Nb_3O_{10-x} + xH_2O$$

The preparation of organic-inorganic derivatives can be carried out both via standard laboratory synthesis [146] and using solvothermal [147] and solvothermal-microwave [148] methods. That being said, intercalation, as a rule, requires somewhat milder conditions than grafting, and the use of microwave heating can significantly reduce the synthesis time. The preparation of many organic-inorganic derivatives is multi-stage, since the initial protonated forms are able to directly accommodate only relatively small organic structures in the interlayer space, which can later be replaced by larger ones [147]. The practice of synthesizing grafted derivatives based on amine intercalation products is also common, since not all protonated oxides are able to directly participate in the grafting reaction [149]. The presence of water molecules in the system (including in trace amounts or located in the interlayer space) is of great importance for the intercalation and grafting of organic compounds. In particular, some studies note the impossibility of intercalation of amines and grafting of alcohols under absolutely anhydrous conditions [149], as well as the increased reactivity of the hydrated protonated forms [150,151]. These facts indicate that small amounts of water in the system can perform a catalytic function, increasing the chemical activity of the interlayer space.

Historically, the study of organic-inorganic derivatives of layered perovskite-like oxides began in 1987 [146], when a series of primary amines with different hydrocarbon chain lengths were first intercalated into the three-layer Dion-Jacobson niobate $HCa_2Nb_3O_{10}$. Subsequently, based on oxides of this structural type (primarily, niobates $HLaNb_2O_7$, $HCa_2Nb_3O_{10}$, and

$HSr_2Nb_3O_{10}$), numerous organic-inorganic materials with various aliphatic amines [152] and diamines were synthesized [153], as well as with aniline [154], ethanolamine [155], aminoacetic [155] and aminoundecanoic acids [156], pyridine [157] and other modifiers. The preparation of covalent organic-inorganic derivatives of layered perovskite-like oxides began with grafting of primary alcohols with different chain lengths, first described using the example of niobate $HCa_2Nb_3O_{10}$ in 2003 [151]. In subsequent studies, isopropanol [147], *tert*-butanol [147], 4-penten-1-ol [158], ethylene glycol [147], glucose [159], trifluoroacetic acid [145], alkyl and phenylphosphonic acids [160], polyesters [161], and organosilicon compounds [158]. At the same time, the formation of organic-inorganic derivatives based on Ruddlesden-Popper phases has been studied to a much lesser extent. In particular, some amine derivatives of tantalates $H_2CaNaTa_3O_{10}$ [162], $H_2SrTa_2O_7$ and $H_2La_{2/3}Ta_2O_7$ [163], as well as amine and alcohol derivatives of titanates $H_2K_{0.5}Bi_{2.5}Ti_4O_{13}$ [164,165] and $H_2La_2Ti_3O_{10}$ with unbranched organic modifiers were successfully obtained [149,166]. For tantalate $H_2CaTa_2O_7$, in addition to the reactions of intercalation of primary amines and grafting of alcohols [167], covalent introduction of glucose into the interlayer space is also mentioned [144].

The significantly greater number of known organic-inorganic derivatives based on Dion-Jacobson niobates is mainly due to the higher reactivity of the latter in the processes of intercalation and grafting compared to the Ruddlesden-Popper titanates. For instance, protonated niobate $HCa_2Nb_3O_{10}$ is able to directly intercalate long-chain amines (in particular, octadecylamine) [146] and enter into grafting reactions with the simplest alcohols (methanol, ethanol) [151] while protonated titanate $H_2La_2Ti_3O_{10}$, according to literature data [149,166], is capable of quantitative incorporation of *n*-propyl- and *n*-butylamine, and does not react directly with alcohols at all. These differences in the reactivity of the interlayer space are explained by the structural and chemical characteristics of the different classes of phases. In particular, protonated niobates and tantalates exhibit greater acidity than titanates [168,169], which has a beneficial effect on the chemical activity of the former as solid acids in intercalation and grafting reactions. Also, protonated Dion-Jacobson phases usually differ from Ruddlesden-Popper phases in a large number of interlayer water molecules, which, according to experimental data presented in the literature, are necessary for the quantitative occurrence of these reactions. In addition, Dion-Jacobson phases are more characterized by an eclipsed

conformation of perovskite blocks, which may provide better transport of reactants into the interlayer space compared to the staggered conformation typical of Ruddlesden-Popper phases.

The maximum theoretically possible amount of an intercalated or grafted organic component is determined by the number of interlayer protons per formula unit of the oxide. However, in practice it is limited by steric factors, since the organic component chemically bound to the interlayer vertex of the octahedron can spatially block the neighboring vertex [149]. The greatest completeness of intercalation and grafting is achieved in the case of Dion-Jacobson phases containing a smaller specific amount of interlayer protons; Ruddlesden-Popper phases usually bind about half the organic component of the theoretically possible amount.

1.2.4.2. Organic-inorganic derivatives as photocatalysts

As was shown earlier, the interlayer space of ion-exchange layered perovskite-like oxides can serve as an additional reaction zone in photocatalysis, and its composition and steric accessibility to reactants significantly affect the photocatalytic activity in hydrogen production reactions. In this regard, its targeted modification with the aim of further improving its photocatalytic properties is of particular interest. One type of such modification may be the introduction of organic components into the interlayer space, leading to its significant expansion and the production of hybrid organic-inorganic photocatalysts. However, despite the large number of currently known organic-inorganic derivatives of layered perovskite-like oxides, there is practically no data on their photocatalytic properties beyond the work of the applicant. One of the main reasons for this, apparently, is the instability of such compounds under photocatalysis, expected by many researchers.

The only work that mentioned the photocatalytic activity of an organic-inorganic derivative in the reaction of hydrogen production, until the publication of the applicant's articles, was the study [133], published in 2005. It was shown that after the intercalation of *n*-hexylamine into a three-layer Dion-Jacobson tantalate $HCa_2Ta_3O_{10}$, the rate of photocatalytic hydrogen evolution from pure water under ultraviolet radiation increases many times, reaching a value of 0.55 $mmol \cdot h^{-1} \cdot g^{-1}$, which is 42 and 9 times more than in the case of $HCa_2Ta_3O_{10}$ and $NaCa_2Ta_3O_{10}$, respectively. However, the authors noticed a significant decrease in the activity of the organically modified sample several hours after the start of irradiation, associated with the oxidation of intercalated *n*-hexylamine and the subsequent narrowing of the interlayer

space. It should be noted that organically modified tantalate was only one of several research objects in this article, which is why little attention was paid to the analysis of its photocatalytic properties.

At the same time, there are several works in the literature that consider the photocatalytic activity of organic-inorganic derivatives of layered oxides in relation to the processes of purification of aqueous media from model organic pollutants. In particular, the authors of the study [167] found that grafting of primary alcohols (methanol, *n*-propanol, *n*-decanol and *n*-octadecanol) into double-layer Ruddlesden-Popper tantalate $H_2CaTa_2O_7$ affects its photocatalytic activity in decomposition reactions rhodamine B and methyl orange under ultraviolet radiation, and the reaction rate in the presence of organically modified samples increases monotonically with increasing length of the hydrocarbon chain of interlayer *n*-alkoxy groups. Other examples of organic-inorganic photocatalysts include polyaniline-modified layered niobates and titanates, which do not possess a perovskite structure, but have also proven their effectiveness in the decomposition of methylene blue under visible light [170–172].

The above examples indicate that organic modification of the interlayer space can serve as an effective approach to improving photocatalytic properties of layered materials and therefore deserves detailed study.

### 1.2.5. Nanosheets of layered perovskite-like oxides

One of the leading trends in modern chemical science is the creation of nanomaterials, which in many cases have significantly superior functional properties to their bulk counterparts. A variety of such materials are nanosheets with a perovskite structure – plate-like particles characterized by a thickness of several nanometers and linear dimensions from tens to hundreds of nanometers. While retaining the practically significant properties of the initial compounds, perovskite nanosheets compare favorably with their developed surface and small specific volume, which provides an increased number of active centers, promotes effective adsorption of reactants and suppression of volume electron-hole recombination [48]. As a consequence, photocatalysts based on one nanosheets are significantly superior in activity to the initial bulk compounds. In addition, perovskite nanosheets can serve as building blocks for creating new nanostructured photocatalysts via their self-assembly with the layers of other materials [173].

1.2.5.1. Exfoliation of layered perovskite-like oxides into nanosheets

The main method for producing perovskite nanosheets is liquid-phase exfoliation (delamination, splitting) of the protonated forms of layered perovskite-like oxides. This process consists in separating their structure along the interlayer space into individual non-layered parts (monolayers) – perovskite blocks of the original thickness with counterions compensating their negative charge (Fig. 21). However, in practice, the exfoliation process may not proceed completely and may be accompanied by the formation of layered nanosized particles containing several perovskite blocks separated by interlayer spaces. In this regard, here and below, the equivalent concepts of «nanosheets» and «exfoliated forms» are used to designate the exfoliation products of both types.

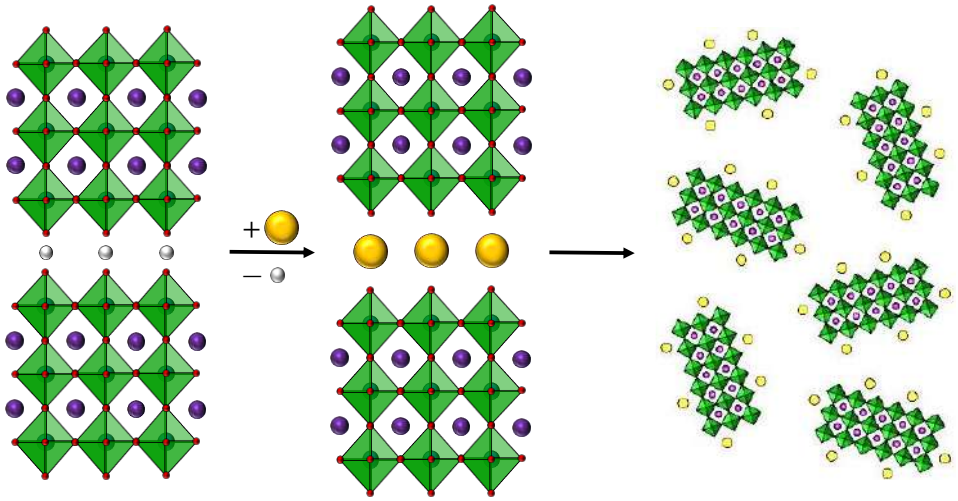


Fig. 21. Liquid-phase exfoliation of layered perovskite-like oxide into nanosheets

The modern strategy for the liquid-phase production of perovskite nanosheets dates back to the work of 1990 [174], in which it was shown that intercalation of protonated Dion-Jacobson niobates $HCa_2Na_{n-3}Nb_nO_{3n+1}$ (n = 3–5) by surfactants with an amino group leads to partial delamination of the bulk structure, and after ultrasonic treatment of the resulting intercalation products in a liquid medium, suspensions of their nano-sized layers are formed. Currently, to exfoliate layered perovskite-like oxides, as a rule, their interlayer space is first expanded by introducing large organic cations (in particular, tetrabutylammonium $TBA^+$), which leads to intense intercalation of water molecules from the solution and, as a consequence, pronounced swelling of the layered structure, which, during subsequent ultrasonic treatment, delaminates to form a suspension of nanosheets [104]. That being said, the exfoliation process can be carried out under the influence of not only ultrasound, but also other physical factors – for example, microwave heating [175].

Alternative strategies for the liquid-phase exfoliation of layered perovskite-like oxides without the use of tetraalkylammonium cations are also known in the literature. In particular, in the study [176], protonated tantalate $H_2Bi_{0.1}Sr_{0.85}Ta_2O_7$ was preliminarily modified with covalently bonded *n*-decylphosphonic acid to neutralize the interlayer charge and was subsequently successfully exfoliated into nanosheets using a special high-shear disperser. In the paper [156], the exfoliation of protonated niobate $HCa_2Nb_3O_{10}$ was achieved due to the intercalation of aminoundecanoic acid into the interlayer space, which, through subsequent alkalization of the medium, was converted into an anionic form, which caused the delamination of the sample under the influence of electrostatic repulsion forces from negatively charged perovskite blocks.

1.2.5.2. Perovskite nanosheets as photocatalysts

As noted earlier, exfoliation into nanosheets is one of the promising approaches to creating perovskite-like photocatalysts with a developed specific surface area. At the same time, the most studied at the moment are photocatalysts based on the nanosheets of three-layer Dion-Jacobson niobates – compounds that are relatively easy to liquid-phase exfoliation in aqueous solutions of tetrabutylammonium hydroxide TBAOH [177]. In particular, it was shown that the reassembled nanosheets of $HCa_2Nb_3O_{10}$ and $HSr_2Nb_3O_{10}$ are 2–4 times superior to the non-exfoliated precursors in their photocatalytic activity in hydrogen production reactions [178,179]. After modifying the surface with Pt nanoparticles as a cocatalyst, they provide a rate of hydrogen evolution from aqueous solutions of methanol [178], isopropanol [180], and triethanolamine [179] of up to 9, 0.9, and 0.53 $mmol \cdot h^{-1} \cdot g^{-1}$, respectively. In these studies, the radiation source is a xenon lamp, the power of which in the first work is 500 W, and in the second and third – 300 W. To improve the efficiency of spatial separation of photogenerated charge carriers and expand the light absorption region, the perovskite nanosheets were successfully used to yield composite photocatalysts with g-$C_3N_4$ [181], CdS [182–184], $Co_xP$ [185], $Mo_2C$ [186], $CaNb_2O_6$ [187], graphene oxide [188], ruthenium complexes [189–191] and other modifiers. Many of the resulting nanostructured photocatalysts showed stable maintenance of their activity during cyclic operation at a level of at least 80–90% of the initial value. However, many studies lack information on the quantum yields or efficiencies of photocatalytic reactions, and also do not compare the activity of the resulting

composites with the activity of the initial nanosheets under the same conditions, which makes it difficult to analyze the presented data.

At the same time, the photocatalytic properties of the exfoliated forms of Ruddlesden-Popper titanates (in particular, $HLnTiO_4$ and $H_2Ln_2Ti_3O_{10}$ considered in this work) remain practically unstudied. In particular, the liquid-phase exfoliation of protonated single-layer compounds $HLnTiO_4$ has not been reported in principle outside the applicant's publications, while the preparation of nanosheets of three-layer titanate $H_2La_2Ti_3O_{10}$ was mentioned in the literature [162,192,193], but they were not tested as photocatalysts. The reason for this, apparently, is the lower reactivity of Ruddlesden-Popper titanates compared to Dion-Jacobson niobates, which limits the possibility of introducing $TBA^+$ cations into the interlayer space and, accordingly, complicates the quantitative preparation of the nanosheets.

In addition, the fundamentally important question about the relationship between the used form of perovskite nanosheets (initial without reassembly, reassembled by various methods) and the exhibited photocatalytic activity remains unexamined in the available literature. In particular, nanosheets can be studied directly after liquid-phase exfoliation in the resulting suspensions, the composition of which, if necessary, can be adjusted by dialytic purification of the dispersion medium from TBAOH, changing pH, introducing the required amount of a sacrificial agent, etc. Alternatively, nanosheets can be isolated from suspensions (by filtration, electrolyte precipitation, freeze-drying, ultracentrifugation, etc.) and then redispersed in the desired reaction solution. It is obvious that the reassembly of nanosheets and the specific method of its implementation will affect their physical-chemical properties and photocatalytic activity. However, an analysis of the available literature indicates that perovskite nanosheets in the vast majority of cases are studied as photocatalysts not in their initial form, but after reassembly. The latter is usually carried out by precipitation of the layers from suspensions under the influence of strong electrolytes (salts [185,186,188,194–196], acids [179,182,184,187,189–191,197,198] alkalis [178]), leading to the contraction of their double electrical layer and, accordingly, loss of aggregation-sedimentation stability. The described approach turns out to be convenient from the point of view of practical implementation, since it does not require the use of complex or expensive equipment and allows one to quickly separate nanosheets from a suspension and then work with them as with standard powder photocatalysts. However, the available literature data do not allow us to

establish whether the precipitation of the nanosheets by electrolytes is the optimal method for their isolation from the point of view of the photocatalytic activity of the final samples.

### 1.2.6. Structural-chemical features and photocatalytic properties of titanates $A'LnTiO_4$ and $A'_2Ln_2Ti_3O_{10}$

#### 1.2.6.1. Single-layer titanates $A'LnTiO_4$

Layered perovskite-like titanates of the $A'LnTiO_4$ type (A' = singly charged metal or proton, Ln = La or lanthanide), belonging to the Ruddlesden-Popper phases, differ significantly from other representatives of this class of phases. In their unique structure (Fig. 22, a) complete ordering of nine-coordinated cations $A'^{+}$ and $Ln^{3+}$ is realized between two nonequivalent interlayer spaces separating perovskite blocks with a thickness of n = 1, due to significant differences in the size, charge and polarizing ability of these cations [199]. In this case, the titanium-oxygen octahedra $TiO_6$ are strongly distorted vertically, and the $A'^{+}$ cations have significant mobility in their interlayer space, which is therefore chemically active. In contrast, $Ln^{3+}$ cations are firmly bound to perovskite blocks via Coulomb interaction, which explains the inertness of the interlayer space containing them.

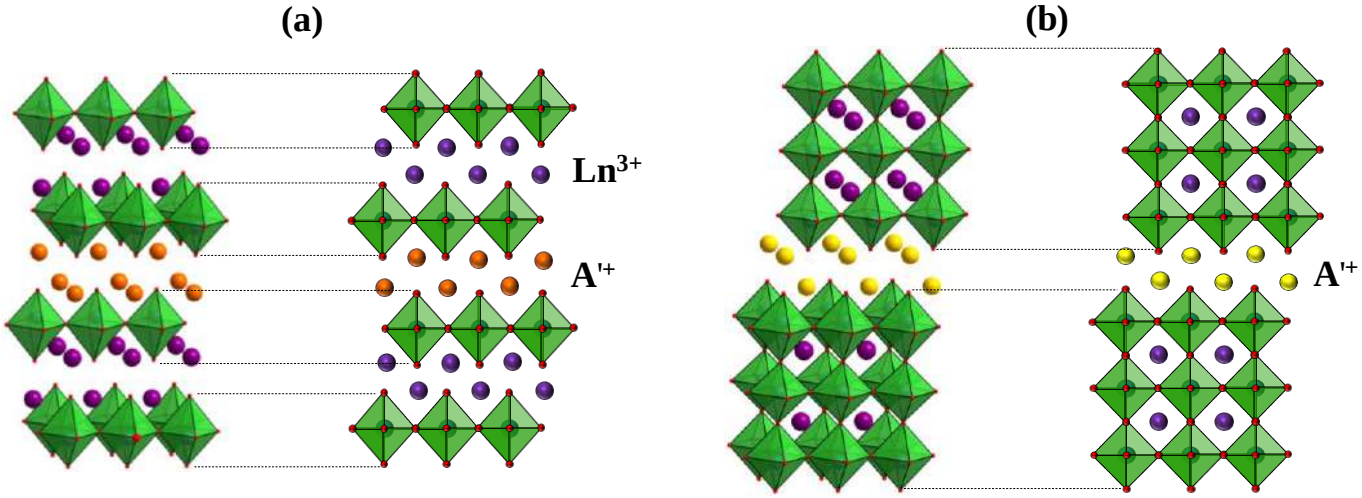


Fig. 22. Structure of titanates $A'LnTiO_4$ (a) and $A'_2Ln_2Ti_3O_{10}$ (b)

The described structural features determine the pronounced ionic conductivity of the titanates under consideration [200–203], as well as high activity in ion exchange reactions, including those involving doubly charged substituting cations, which is purposefully used for the synthesis of new compounds [204–207].

When alkaline forms of $A'LnTiO_4$ come into contact with aqueous solutions, the process of protonation begins, accompanied by the simultaneous intercalation of water into the

interlayer space [208]. The degree of substitution of alkali cations by protons for each specific titanate is determined by the pH value of the solution, and at a fixed pH it increases in the order $A'^{+} = K^{+}, Na^{+}, Li^{+}$. The amount of intercalated water depends significantly on the nature of interlayer cations of both types and can range from tenths to several molecules per formula unit of titanate [126]; when the degree of protonation increases, it usually decreases. According to the data of [209], interlayer water exists in both neutral and cationic (hydroxonium) forms. In aqueous suspensions with $pH > 3$, the existence of partially protonated hydrated forms is usually observed with the general formula $H_xA_{1-x}LnTiO_4 \cdot yH_2O$, where x is the degree of protonation and y is the amount of intercalated water. Upon greater acidification ($pH \leq 1$) complete protonation is achieved ($x = 1$), that is, the formation of compounds of the form $HLnTiO_4 \cdot yH_2O$ [210]. In practice, the protonation of single-layer titanates $A'LnTiO_4$ is complicated by the relatively low stability of their perovskite blocks to acidic decomposition, which manifests itself at $pH < 1$, long-term exposure of the oxide to an acid solution, and heating. However, despite the high level of knowledge of the ion-exchange properties of the considered single-layer titanates, the preparation of their organic-inorganic derivatives, as well as the exfoliation of their protonated forms into nanosheets, has not been reported outside the work of the applicant.

The number of publications devoted to the catalytic and photocatalytic properties of single-layer titanates $A'LnTiO_4$ is relatively small. Thus, in a study [211], it was demonstrated that titanates $NaLaTiO_4$ and $HLaTiO_4$ can serve as effective catalysts for the selective O-*tert*-butoxycarbonylation of alcohols and phenols. In the case of 4-methoxybenzyl alcohol, the catalytic activity of both titanates is almost the same and exceeds that exhibited by titanium dioxide $TiO_2$ and lanthanum oxide $La_2O_3$ by 2.5 and 4.5 times, respectively. In [212], the photocatalytic decomposition of methyl orange as a model pollutant of aqueous media was studied using titanates $A'NdTiO_4$ under ultraviolet radiation, the rate of which increased in the series of compounds with interlayer cations $A'^{+} = H^{+}, Na^{+}, Li^{+}$. Article [213] considered the possibility of photocatalytic hydrogen generation from an aqueous solution of isopropanol in a similar spectral region using protonated titanates $HLnTiO_4$ (Ln = La, Nd) and a number of products of their thermal destruction. It was shown that La-containing compounds exhibit 2–4 times greater activity compared to Nd-containing ones, and thermolysis products have up to 3 times higher activity compared to the initial protonated forms, which rises with increasing

calcination temperature. In [119], the activity of composite photocatalysts $KLaTiO_4$/Pt, $HLaTiO_4$/Pt, as well as their nitrided derivatives $KLaTiO_{4-x}N_x$/Pt, $HLaTiO_{4-x}N_x$/Pt was studied in the reaction of producing hydrogen from an aqueous solution of methanol under a full spectrum xenon lamp. Despite the fact that nitridation made it possible to shift the long-wave absorption edge from 350 to 586 nm, the nitrided samples showed lower photocatalytic activity compared to the initial compounds. This fact was explained by the authors by the intense recombination of photogenerated charge carriers on $Ti^{3+}$ cations and oxygen defects. Moreover, it was observed that the alkaline nitrided form $KLaTiO_{4-x}N_x$/Pt undergoes degradation during photocatalysis, as evidenced by the release of molecular nitrogen during the experiment. However, later the authors of another work [118] obtained oxynitride $NaLaTiO_{4-x}N_x$, over which, after surface modification with Pt nanoparticles, the photocatalytic evolution of hydrogen and oxygen from aqueous solutions of sacrificial agents under purely visible light was successfully realized. In article [214], it was shown that the photocatalytic activity of titanate $KLaTiO_4$ in the reaction of pure water splitting can be increased by partially replacing titanium with zirconium with the formation of highly crystalline phases of the form $KLaTi_{1-x}Zr_xO_4$. The dependence of activity, measured ceteris paribus, on the substitution degree passes through a maximum at x = 0.3 and further declines, which is associated with an increase in the bandgap energy. At the same time, modification of the photocatalyst surface with Ni particles makes it possible to further increase the activity by 2 times.

1.2.6.2. Three-layer titanates $A'_2Ln_2Ti_3O_{10}$

Layered perovskite-like titanates $A'_2Ln_2Ti_3O_{10}$ (A' = singly charged metal or proton, Ln = La or lanthanide), also belonging to the Ruddlesden-Popper phases, are significantly more studied compounds than $A'LnTiO_4$. Structure of titanates $A'_2Ln_2Ti_3O_{10}$ (Fig. 22) represents an alternation of perovskite blocks with a thickness of n = 3 with interlayer spaces containing $A'^+$ cations, located in a nine-coordinated oxygen surrounding, and $Ln^{3+}$ cations in a twelve-coordinated one [215]. In contrast to the case of single-layer titanates $A'LnTiO_4$, titanium-oxygen octahedra of $A'_2Ln_2Ti_3O_{10}$ compounds have greater asymmetry, and interlayer $A'^+$ cations are more strongly associated with perovskite blocks, which causes lower ionic conductivity of the three-layer compounds [200].

Like the $A'LnTiO_4$ phases, three-layer titanates can participate in ion exchange reactions, which are widely used for synthetic purposes [123,124,216,217]. The trends in

protonation and hydration of compounds $A'_2Ln_2Ti_3O_{10}$ are quite complex, manifested in the existence of a number of partially and fully protonated forms $H_{2x}A'_{2-2x}Ln_2Ti_3O_{10}\cdot yH_2O$ existing at different pH values of an aqueous solution and containing unequal amounts of intercalated water molecules [129]. In addition, for these compounds, the existence of hydrated alkaline forms $A'_2Ln_2Ti_3O_{10}\cdot yH_2O$, stable in an atmosphere of humid air, was established, and a change from the staggered conformation of perovskite blocks to an eclipsed one was revealed at the degree of protonation $x \approx 0.7$ [218,219]. The literature also mentions the possibility of obtaining nanosheets [162,192,193] and some organic-inorganic derivatives of the protonated titanate $H_2La_2Ti_3O_{10}$. In particular, the products of intercalation of *n*-propylamine [166], *n*-butylamine, as well as grafting of *n*-propanol, *n*-butanol, *n*-octanol, *n*-decanol and *n*-dodecanol [149] were characterized.

Titanates $A'_2Ln_2Ti_3O_{10}$ represent one of the most promising subclasses of photocatalysts with a layered perovskite structure for producing hydrogen from aqueous media. The photocatalytic activity of these compounds increases in the series of interlayer cations $A'^+ = Li^+$, $Na^+$, $K^+$, $Rb^+$, which is apparently due to an increase in the accessibility of the interlayer space for water molecules and sacrificial agents [136,137,218,220]. One of the most efficient photocatalysts is the $Rb_2La_2Ti_3O_{10}/NiO_x$ composite, on the example of which a quantum yield of ≈ 5% at a wavelength of 330 nm was achieved for the first time in the reaction of pure water splitting [138]. It should, however, be understood that the photocatalytic activity of the alkaline forms $A'_2Ln_2Ti_3O_{10}$ in aqueous media actually means the activity of partially protonated compounds $H_{2x}A'_{2-2x}Ln_2Ti_3O_{10}\cdot yH_2O$, formed as a result of ion exchange and hydration, which is not always explicitly indicated in the literature.

The main attention in the studies of recent decades has been paid to increasing the photocatalytic activity of titanates $A'_2Ln_2Ti_3O_{10}$ by creating composite materials based on them and partial ion substitution in perovskite blocks. In particular, the products of $K_2La_2Ti_3O_{10}$ modification with metal cocatalysts Ni, Pt, Au, as well as particles of oxides $TiO_2$, $Cr_2O_3$, $Fe_2O_3$, NiO and sulfides CdS, PbS were investigated in the reactions of hydrogen production from pure water and water-organic mixtures; the possibility of expanding the light absorption range by introducing impurity elements into the perovskite sublattice – boron, nitrogen, aluminum, vanadium, chromium, iron, nickel, zinc, gallium, niobium, indium, tin, cerium, tungsten – was studied [12]. Based on the protonated form $H_2La_2Ti_3O_{10}$, photocatalytically

active materials with $Fe_2O_3$ and $TiO_2$ nanoparticles in the interlayer space were successfully obtained [221,222]. In addition, the study [223] demonstrated the possibility of using titanates $A'_2Ln_2Ti_3O_{10}$ (A' = K, Rb; Ln = La, Nd, Sm, Gd, Dy) as standard heterogeneous catalysts for the oxidative conversion of methane.

### 1.3. Conclusion based on results of the literature review

The literature review showed that ion-exchangeable layered perovskite-like oxides are promising materials for the creation of new highly efficient photocatalysts for hydrogen generation. One of their unique features is the presence of a chemically active interlayer space, which serves as an additional reaction zone in photocatalytic processes along with the external surface, and the composition and steric accessibility of this zone for reactants significantly affect the photocatalytic activity. In view of this, special attention should be paid to the targeted topochemical modification of the interlayer zone using «soft chemistry» methods to further improve photocatalytic properties, as well as a comparative analysis of the resulting photocatalysts with materials in which the interlayer reaction zone is transformed into the external surface via the exfoliation of the layered structure into individual nanosheets.

However, there exist a number of significant gaps in the available literature on the development of this type of photocatalysts. Firstly, outside the applicant's publications, the articles do not cover the issue of creating layered perovskite-like photocatalysts with the organically modified interlayer space, which, as will be shown below, can outperform in the photocatalytic activity the initial unmodified compounds by more than two orders of magnitude. At the same time, questions remain open about the relationship between the composition of the interlayer reaction zone and the activity exhibited, as well as about the potential transformations of interlayer modifiers under photocatalysis conditions. Secondly, the creation of photocatalysts based on perovskite nanosheets, despite the known efficiency of this approach, has been sufficiently studied only for a narrow range of layered oxides that are relatively easy to liquid-phase exfoliation (in particular, Dion-Jacobson niobates $HA_2Nb_3O_{10}$ (A = Ca, Sr)). However, information on the activity of nanosheets of other promising photocatalysts, such as Ruddlesden-Popper titanates $HLnTiO_4$ and $H_2Ln_2Ti_3O_{10}$, is practically absent in the literature. In addition, the existing articles do not address the fundamentally important issue of the relationship between the used form of perovskite nanosheets (initial ones without reassembly and those reassembled by different methods) and their photocatalytic

activity. As will be shown below, the form of such photocatalysts used greatly influences the efficiency of hydrogen generation, and the nature of this influence depends, among other things, on the composition of the reaction solution. Thirdly, the photocatalytic activity of layered perovskite-like oxides has practically not been studied in the processes of hydrogen production from carbohydrate solutions, which are one of the key components of plant biomass.

Thus, despite a large number of known layered perovskite-like photocatalysts, some promising approaches to managing their photocatalytic activity (in particular, interlayer organic modification and exfoliation into nanosheets) require a separate detailed study, which is the focus of this work.

# 2. Experimental section

This work can be divided into two large logical blocks. The first of them examines in detail a new highly effective approach to improving the photocatalytic activity of layered perovskite-like oxides, which practically has not been covered in the literature – modification of their interlayer space with ionic and covalently bound organic components (creation of hybrid organic-inorganic derivatives). In this case, Ruddlesden-Popper titanates $HLnTiO_4$ and $H_2Ln_2Ti_3O_{10}$ (Ln = La, Nd) were selected as starting objects, and the modifiers were primary aliphatic amines and alcohols with different hydrocarbon chain lengths, as well as aromatic compounds capable of photosensitizing a layered photocatalyst, ensuring its functioning not only under ultraviolet, but also under visible radiation. The resulting compounds are studied in the reactions of photocatalytic hydrogen production from aqueous solutions of typical products of plant biomass processing – methanol, D-glucose and D-xylose, as well as from pure water. In addition to studying the photocatalytic activity itself, the work pays special attention to the comprehensive characterization of the obtained objects using a wide range of modern physical-chemical methods, as well as to the issue of their stability and potential transformations under photocatalysis conditions. The corresponding data are extremely important for a correct explanation of the observed photocatalytic properties, since most of the organic-inorganic derivatives obtained have not been previously described in the literature.

The second logical block of this work is devoted to photocatalysts based on nanosheets of the above-mentioned titanates. Despite the fact that exfoliation of layered photocatalysts into nanosheets is well known as an effective method for increasing their activity, information on the photocatalytic properties of nanosheets of the selected objects is practically absent in the literature. At the same time, the present work pays special attention to the previously unconsidered issue of the influence of reassembly and its specific method on the physical-chemical properties and photocatalytic activity of the nanosheets in the reactions of hydrogen production from various media, being of great importance.

## 2.1. Abbreviations

Here and below, the protonated forms of titanates $HLaTiO_4$, $HNdTiO_4$, $H_2La_2Ti_3O_{10}$ and $H_2Nd_2Ti_3O_{10}$ are designated as HLT, HNT, $HLT_3$ and $HNT_3$, respectively.

For the amine intercalation products (amine derivatives), designations of the form HLT×$RNH_2$, HNT×$RNH_2$, $HLT_3$×$RNH_2$ and $HNT_3$×$RNH_2$ are used, and for alcohol grafting products (alcohol derivatives) – HLT×ROH, HNT×ROH, $HLT_3$×ROH and $HNT_3$×ROH, where R = methyl Me, ethyl Et, *n*-propyl Pr, *n*-butyl Bu, *n*-hexyl Hx, *n*-octyl Oc and *n*-decyl Dc.

The products of grafting of aromatic modifiers into titanate $H_2La_2Ti_3O_{10}$ ($HLT_3$) are designated as $HLT_3$×Ar, where Ar = phenol PhOH, catechol Cat, resorcinol Res, hydroquinone Hyd, pyrogallol Pyr, salicylic acid SA, 2-allylphenol APhOH, 4-phenylphenol PhPhOH, 2-naphthol Nph, 8-hydroxyquinoline Oxy and alizarin Ali.

For perovskite nanosheets studied without reassembly, the designation NSs is used, for those reassembled by filtering – filtered NSs, for reassembled by precipitation with hydrochloric acid – HCl-restacked NSs.

A symbol /Pt is added to the end of the designations of photocatalysts modified with platinum nanoparticles as a cocatalyst.

### 2.2. Synthesis of protonated titanates $HLnTiO_4$ and $H_2Ln_2Ti_3O_{10}$

Protonated titanates HLT (HNT) and $HLT_3$ ($HNT_3$), were obtained by ion exchange from the corresponding alkaline forms $NaLnTiO_4$ and $K_2Ln_2Ti_3O_{10}$ (Ln = La, Nd), synthesized, in turn, using the high-temperature ceramic technology in air at atmospheric pressure in accordance with the reaction equations:

$$2TiO_2 + Ln_2O_3 + Na_3CO_3 \rightarrow 2NaLnTiO_4 + CO_2$$

$$3TiO_2 + Ln_2O_3 + K_3CO_3 \rightarrow K_2Ln_2Ti_3O_{10} + CO_2$$

All the reactants were subjected to preliminary calcination in order to remove traces of moisture. Oxides were taken in stoichiometric quantities, carbonates – with an excess of 30% to compensate for losses during calcination. A mixture of reactants (batch), calculated to obtain 20 g of the target product, was placed in a grinding bowl with silicon nitride balls, filled with *n*-heptane and ground in a Fritsch Pulverisette 7 planetary micro mill at a rotation speed of 600 rpm for 2 h. After drying, the final batch was pressed on an Omec PI 88.00 hydraulic press under a pressure of 50 atm into cylindrical tablets with a diameter of 1.5 cm and a weight of 2 g, which were then placed in corundum crucibles with lids at the rate of 3 tablets per crucible and calcined in a Nabertherm L-011K2RN muffle furnace at a temperature 825 °C (in

the case of $NaLnTiO_4$) or 1100 °C (in the case of $K_2Ln_2Ti_3O_{10}$) for 12 h. After cooling, the tablets were thoroughly ground in an agate mortar to a fine crystalline powder.

Protonation of the alkaline forms of the titanates was carried out in accordance with the overall reaction equations:

$$NaLnTiO_4 + HCl + yH_2O \rightarrow HLnTiO_4 \cdot yH_2O + NaCl$$

$$K_2Ln_2Ti_3O_{10} + 2HCl + yH_2O \rightarrow H_2Ln_2Ti_3O_{10} \cdot yH_2O + 2KCl$$

In the case of single-layer $NaLnTiO_4$ titanates, a one-step protonation technique was used. To do this, powders of their alkaline forms were treated with a 0.1 M aqueous solution of hydrochloric acid, taken at a rate of 200 mL of solution per 1 g of oxide, with stirring for 24 h, after which the solid phases were separated by centrifugation and dried in a desiccator over calcium oxide at room temperature and atmospheric pressure for 2 d. Then the resulting protonated titanates were further ground in a Fritsch Pulverisette 7 planetary micro mill at a rotation speed of 600 rpm for 2 h. In the case of three-layer titanates $K_2Ln_2Ti_3O_{10}$, a three-stage protonation technique was used. At the first stage, the powders of their alkaline forms were kept in an atmosphere of humid air for 24 h. The hydrated alkaline forms thus obtained were converted at the second stage to partially protonated ones by treatment with water at the rate of 200 mL of water per 1 g of oxide with stirring for 1 h. In the third stage, the partially protonated forms were treated with a 0.1 M aqueous solution of hydrochloric acid, taken at a rate of 200 mL of solution per 1 g of oxide, with stirring for 24 h. After this, the solid phases were separated by centrifugation and dried in a desiccator over calcium oxide at room temperature and atmospheric pressure within 2 d. The resulting protonated titanates were then further ground in a Fritsch Pulverisette 7 planetary micro mill at a rotation speed of 600 rpm for 2 h.

## 2.3. Synthesis of organic-inorganic derivatives of the titanates

### 2.3.1. Synthesis of amine and alcohol derivatives

Synthesis of amine and alcohol derivatives of the titanates was carried out according to the methods developed and optimized by the applicant on the basis of experimental data obtained during research work, as well as available literature information. The optimization of methods consisted in searching for schemes and conditions for synthesis of the derivatives that ensure the production of pure single-phase products with the maximum possible content of organic modifiers using the equipment available in the scientific group. This issue is discussed

in detail in the applicant's publications [224–226]. The general strategy for obtaining organic-inorganic compounds was to successively substitute smaller interlayer organic modifiers with larger ones, as shown in Fig. 23.

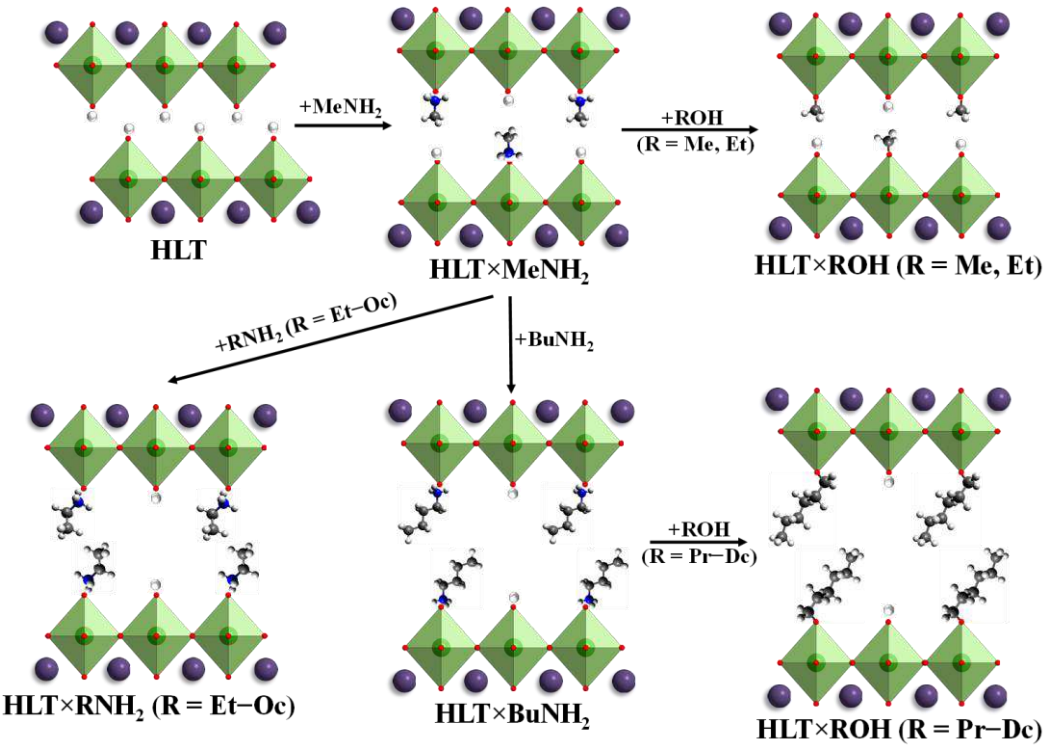


Fig. 23. Scheme for synthesis of amine and alcohol derivatives using the example of the single-layer titanate HLT

The methylamine derivatives HLT(HNT)×$MeNH_2$ and $HLT_3(HNT_3)$×$MeNH_2$ were synthesized directly from the protonated titanates. To do this, 3 g of each protonated form was placed in a glass tube with 30 mL of a 38% aqueous solution of methylamine, after which the reaction mixture was subjected to ultrasonic treatment on a Hielscher UP200St disperser (200 W) at half ultrasonic power for 5 min. The tube was then sealed with a cap and the suspension was stirred on an isothermal rotary shaker at 60 °C for 10 d. To obtain the other amine derivatives HLT(HNT)×$RNH_2$ and $HLT_3(HNT_3)$×$RNH_2$ (R = Et, Pr, Bu, Hx, Oc), the methylamine compounds HLT(HNT)×$MeNH_2$ and $HLT_3(HNT_3)$×$MeNH_2$ were used as precursors. In each case, 1 g of the methylamine derivative was loaded into a hermetically sealed glass tube with 10 mL of the intercalated amine solution, after which the reaction mixture was stirred at a given temperature T for a given time D (Table 1). In a simplified manner, the processes for obtaining amine derivatives using single-layer titanates as an example are described by the equations:

$$HLnTiO_4 + xMeNH_2 = (MeNH_2)_xHLnTiO_4$$

$$(MeNH_2)_xHLnTiO_4 + x'RNH_2 = (RNH_2)_{x'}HLnTiO_4 + xMeNH_2\ (R \neq Me)$$

Synthesis of alcohol derivatives HLT(HNT)×ROH and $HLT_3$ ($HNT_3$)×ROH (R = Me, Et, Pr, Bu, Hx, Dc) was carried out on the basis of the amine derivatives in solvothermal conditions. In each case, 1 g of the amine derivative was poured into a sealed Teflon vessel of a steel laboratory autoclave containing 35 mL of the grafted alcohol or its solution, which corresponds to 70% volume filling, and the resulting mixture was purged with a stream of argon. After assembly and thorough shaking, the autoclave was installed in a special cylindrical casing and kept on a laboratory hotplate with an external thermocouple at a given temperature T for a given time D (Table 1). In this case, the general reaction scheme using the example of single-layer titanates has the form:

$$(RNH_2)_xHLnTiO_4 + x'R'OH = (R'O)_{x'}H_{1-x'}LnTiO_{4-x'} + xRNH_2 + x'H_2O$$

Afterwards the reaction mixtures were cooled to room temperature and the target solid products were separated from the solution by vacuum filtration with washing with a suitable solvent to remove residual adsorbed alcohols, after which they were dried on a filter at room temperature and transferred for storage into plastic tubes with sealed lids.

Table 1. Conditions for synthesis of amine and alcohol derivatives of the titanates

<table>
<tr><td colspan="6">Amine derivatives</td></tr>
<tr><td>Amine</td><td>Precursors</td><td>Amine concentration, mass. %</td><td>T, ° C</td><td>D, d</td><td>Wash solvent</td></tr>
<tr><td>$MeNH_2$</td><td>HLT, HNT, $HLT_3$, $HNT_3$</td><td>38 (in water)</td><td>60</td><td>10</td><td rowspan="4">acetone</td></tr>
<tr><td>$EtNH_2$</td><td rowspan="5">HLT(HNT)×$MeNH_2$, $HLT_3$ ($HNT_3$)×$MeNH_2$</td><td>70 (in water)</td><td rowspan="3">25</td><td rowspan="3">1</td></tr>
<tr><td>$PrNH_2$</td><td rowspan="2">90 (in water)</td></tr>
<tr><td>$BuNH_2$</td></tr>
<tr><td>$HxNH_2$</td><td rowspan="2">30 (in n -heptane)</td><td rowspan="2">60</td><td rowspan="2">7</td><td rowspan="2">n-hexane</td></tr>
<tr><td>$OcNH_2$</td></tr>
<tr><td colspan="6">Alcohol derivatives</td></tr>
<tr><td>Alcohol</td><td>Precursors</td><td>Alcohol concentration, mass. %</td><td>T, ° C</td><td>D, d</td><td>Wash solvent</td></tr>
<tr><td>MeOH</td><td>HLT(HNT)×$MeNH_2$, $HLT_3$ ($HNT_3$)×$MeNH_2$</td><td>100</td><td rowspan="2">100</td><td rowspan="5">7</td><td rowspan="4">acetone</td></tr>
<tr><td rowspan="2">EtOH</td><td>HLT(HNT)×$MeNH_2$,</td><td rowspan="2">96 (in water)</td></tr>
<tr><td>$HLT_3$ ($HNT_3$)×$BuNH_2$</td><td rowspan="4">180</td></tr>
<tr><td>PrOH</td><td rowspan="4">HLT(HNT)×$BuNH_2$, $HLT_3$($HNT_3$)×$BuNH_2$</td><td rowspan="3">100</td></tr>
<tr><td>BuOH</td></tr>
<tr><td>HxOH</td><td rowspan="2">n-hexane</td></tr>
<tr><td>DcOH</td><td>30 (in n-heptane)</td><td>10</td></tr>
</table>

2.3.2. Synthesis of derivatives with aromatic modifiers

Synthesis of the three-layer titanate derivatives with aromatic modifiers $HLT_3$×Ar was carried out by Ph.D. Minich I. A. according to the methods developed by her. The precursor in all cases was the *n*-butylamine derivative $HLT_3$×$BuNH_2$ weighing 0.5 g. Grafting reactions were carried out in a laboratory solvothermal microwave setting Milestone Ethos Easy using Teflon reactors with a total volume of 100 mL, filled to 25%. The duration of microwave heating was 3 h. Upon completion of the syntheses, the target solid products were separated from the solution by centrifugation, washed with tetrahydrofuran and acetone, and then dried in air at room temperature. The other conditions for the preparation of $HLT_3$×Ar derivatives are given in Table 2.

Table 2. Conditions for synthesis of $HLT_3$ derivatives with aromatic modifiers

<table>
<tr><th colspan="2">Modifier</th><th>Modifier concentration, mass. %</th><th>Solvent</th><th>T, °C</th></tr>
<tr><td>PhOH</td><td>phenol</td><td rowspan="6">3.5</td><td rowspan="6">tetrahydrofuran</td><td>100</td></tr>
<tr><td>Cat</td><td>catechol</td><td rowspan="8">130</td></tr>
<tr><td>Res</td><td>resorcinol</td></tr>
<tr><td>Hyd</td><td>hydroquinone</td></tr>
<tr><td>Pyr</td><td>pyrogallol</td></tr>
<tr><td>S.A.</td><td>salicylic acid</td></tr>
<tr><td>APhOH</td><td>2-allylphenol</td><td>100</td><td>–</td></tr>
<tr><td>PhPhOH</td><td>4-phenylphenol</td><td rowspan="3">3.5</td><td rowspan="2">methyl ethyl ketone</td></tr>
<tr><td>Nph</td><td>2-naphthol</td></tr>
<tr><td>Oxy</td><td>8-hydroxyquinoline</td><td rowspan="2">tetrahydrofuran</td></tr>
<tr><td>Ali</td><td>alizarin</td><td>1.7</td></tr>
</table>

## 2.4. Liquid-phase exfoliation of the titanates into nanosheets

2.4.1. Development and optimization of the liquid-phase exfoliation procedure

Since the literature does not describe the quantitative exfoliation of the titanates HLT (HNT) and $HLT_3$ ($HNT_3$) into nanosheets with yields sufficient for photocatalytic studies, the applicant tested the efficiency of liquid-phase exfoliation by varying a wide range of conditions.

The possibility of quantitative liquid-phase exfoliation on nanosheets was studied using so-called physical, chemical and physical-chemical strategies. The physical exfoliation method involved sonication of the layered precursor in water without addition of TBAOH or any other exfoliating agents. The chemical approach consisted in stirring the initial compound in an

aqueous solution of TBAOH for a specified time without the use of ultrasound. The combined physical-chemical approach included ultrasonic treatment of the precursor in a TBAOH solution, followed by stirring the suspension for a given time and repeated ultrasonic treatment in the same mode. That being said, it was decided to use not only protonated forms of the titanates, but also their amine derivatives with different hydrocarbon chain lengths as layered precursors.

Ultrasonic treatment was carried out on a Hielscher disperser UP 200 St (200 W) via immersing a 7 mm diameter sonotrode in a glass test tube containing the initial suspension of the precursor for exfoliation. At the end of all experiments, the resulting mixture was centrifuged on a laboratory centrifuge Elmi CM-6 MT to sediment large non-exfoliated particles, and the supernatant suspension of the nanosheets was carefully collected using a glass pipette. The following conditions for physical-chemical exfoliation were used as standard ones: precursor weight (weight of the inorganic part excluding intercalated amine and water) m = 30 mg, volume of TBAOH solution $V_{TBAOH}$ = 30 mL, its concentration $c_{TBAOH}$ = 0.004 M, ultrasonic power P = 50% of the nominal, duration of single ultrasonic treatment $D_{US}$ = 5 min, stirring duration $D_{st}$ = 1 d, centrifuging separation factor F = 1000, centrifuging duration $D_{centr}$ = 1 h. Subsequently, the composition of the layered precursor and the specified experimental conditions were varied in order to establish the optimal method of liquid-phase exfoliation, providing the highest concentration and yield of perovskite nanosheets in the final suspensions (Table 3).

Table 3. Studied conditions for liquid-phase exfoliation of the titanates into nanosheets

| Exfoliation approach | Precursor | m, mg | $c_{TBAOH}$, M | Ultrasonic treatment | | $D_{st}$, d | F |
|---|---|---|---|---|---|---|---|
| | | | | P, % | $D_{US}$, min | | |
| Physical | HLT (HNT), $HLT_3$ ($HNT_3$) ×$MeNH_2$ | 30 | – | 100 | 5 | 1 | 1000 |
| Chemical | HLT (HNT), $HLT_3$ ($HNT_3$) ×$MeNH_2$ | 30 | 0.004 | – | – | 1 | 1000 |
| Physical-chemical (variable parameters are given below) | HLT (HNT), $HLT_3$ ($HNT_3$) ×$MeNH_2$ ×$EtNH_2$ ×$PrNH_2$ ×$BuNH_2$ ×$HxNH_2$ ×$OcNH_2$ | 30 | 0.004 | 50 | 5 | 1 | 1000 |
| Precursor weight | ×$EtNH_2$ | 30 | 0.004 | 50 | 5 | 1 | 1000 |
| | | 90 | 0.012 | | | | |
| | | 150 | 0.02 | | | | |
| TBAOH concentration | | 30 | 0.002 | 50 | 5 | 1 | 1000 |
| | | | 0.004 | | | | |
| | | | 0.008 | | | | |
| Ultrasound power | | 30 | 0.004 | 25 | 5 | 1 | 1000 |
| | | | | 50 | | | |
| | | | | 100 | | | |
| Ultrasound duration | | 30 | 0.004 | 50 | 1 | 1 | 1000 |
| | | | | | 5 | | |
| | | | | | 10 | | |
| Stirring duration | | 30 | 0.004 | 50 | 5 | 1 | 1000 |
| | | | | | | 7 | |
| | | | | | | 21 | |
| Separation factor | | 30 | 0.004 | 50 | 5 | 1 | 100 |
| | | | | | | | 500 |
| | | | | | | | 1000 |

Further investigation of the perovskite nanosheets was carried out using the example of suspensions obtained via exfoliation of the ethylamine derivatives under the above standard conditions.

2.4.2. Construction of spectrophotometric calibration dependencies

Concentration of the nanosheets in the final suspensions was controlled by spectrophotometry. It was found that the general appearance of the spectrum for a particular titanate is generally maintained over the entire range of conditions tested, and the optical

density A increases linearly with the volume concentration c of the nanosheets in the suspension. This fact makes it possible to construct spectrophotometric calibration dependences of the form A = A(c) based on some standard suspensions, the concentration of the nanosheets in which is determined by another independent method, and then use them to calculate concentrations in other cases.

Before constructing the indicated calibration dependences, concentrations of the nanosheets in the suspensions obtained via exfoliation of the ethylamine titanate derivatives under standard conditions were determined by inductively coupled plasma atomic emission spectroscopy after microwave homogenization of the samples in 12 M hydrochloric acid. Then, by diluting the initial suspensions with a 0.004 M aqueous solution of TBAOH, a series of suspensions with different nanosheet concentrations was prepared for each of the titanates and their spectrophotometric analysis was carried out. The analytical wavelengths chosen were $\lambda$ = 240 nm for HLT, $\lambda$ = 225 nm for HNT, $\lambda$ = 230 nm for $HLT_3$ and $HNT_3$, using the optical density values at which the experimental dependences $A_\lambda = A_\lambda(c)$ were obtained and further approximated by linear functions of the form $A_\lambda = kc$ using the least squares method (Fig. 24).

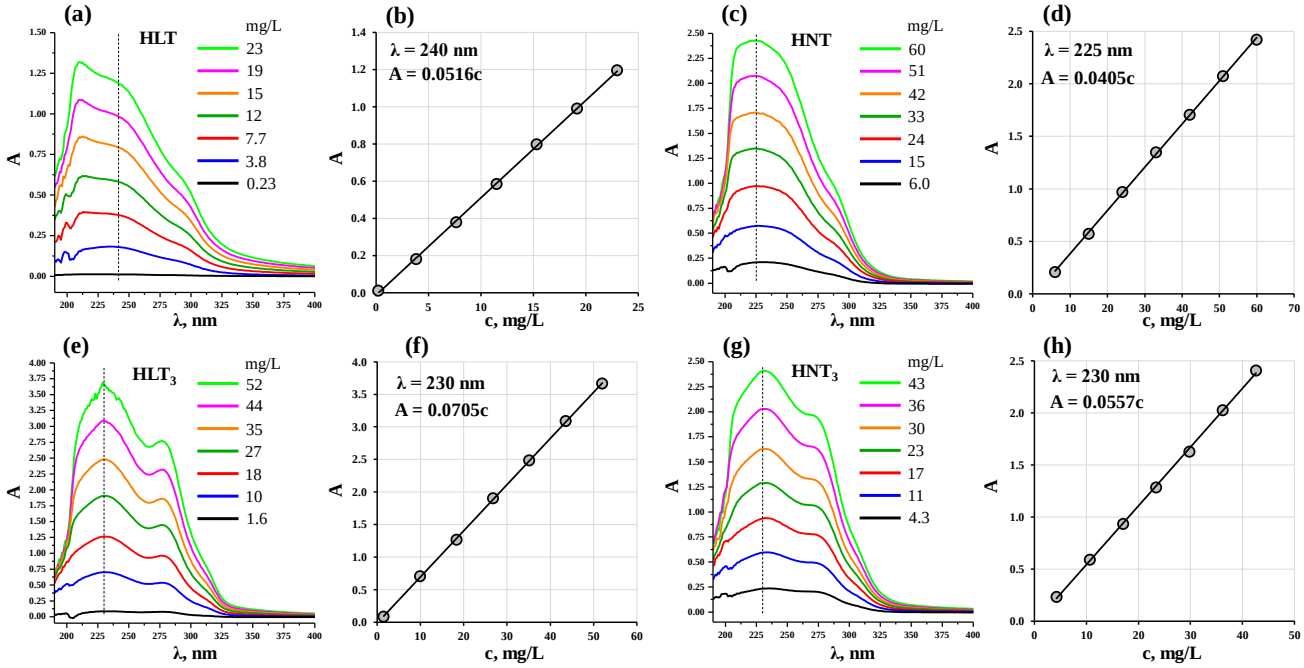


Fig. 24. Spectrophotometric calibration plots for determining concentrations of the titanate nanosheets HLT (a, b), HNT (c, d), $HLT_3$ (e, f) and $HNT_3$ (g, h)

### 2.4.3. Investigation of the nanosheet suspension stability upon changing pH

Suspensions of the nanosheets obtained in a 0.004 M aqueous solution of TBAOH are characterized by a sufficiently high pH value $\approx$ 11.7, which may be undesirable for

photocatalytic applications. In this regard, the issue of stability of these suspensions when changing the pH of the dispersion medium was separately studied.

The approximate range of pH values corresponding to the stability of the nanosheet suspensions relative to rapid coagulation and sedimentation was determined visually during their gradual alkalization or acidification. To do this, in each case, an aqueous solution of sodium hydroxide or hydrochloric acid was added dropwise to the continuously stirred suspension in the amount necessary to change the pH of the dispersion medium by 0.25 units. After stabilization of the pH value, the inhomogeneity of the scattered light (Tyndall effect) was visually assessed when the nanosheet suspension was transmitted through with a red laser ($\lambda = 633$ nm). Then the addition of alkali or acid was continued. The experiment was completed at a pH corresponding to intense coagulation of the nanoparticles with the subsequent formation of a flocculent sediment that precipitated when stirring was turned off. For the suspensions falling within the stability range determined in this way, the ζ-potential values were additionally measured at a pH change interval of 0.5 units.

### 2.4.4. Deposition of the nanosheets on substrates for microscopy

To study the morphology of individual nanosheets without their preliminary coagulation, the latter were deposited on silicon substrates by the electrostatic method. The corresponding experiments were directly carried out by Ph.D. Minich I. A. Prior to the deposition, the substrates were treated with a mixture of concentrated hydrochloric acid and methanol, taken in a volume ratio of 1 : 1, at a temperature of 60 °C for 30 min, washed with distilled water, acetone and dried in a stream of argon. The surface of the substrates was then hydroxylated by treatment with concentrated sulfuric acid at 60 °C for 30 min. After washing and drying, the substrates were immersed in an aqueous solution of polyethylenimine with a concentration of 2.5 g/L, acidified to pH ≈ 9, for 20 min to obtain a positively charged film required for subsequent electrostatic deposition of the negative perovskite nanosheets. Next, the substrates were immersed in dilute suspensions of the nanosheets with a concentration of the latter ≈ 25 mg/L and pH ≈ 11 for 20 min, after which they were washed with distilled water and dried in an oven at 250 °C for 30 min.

2.4.5. Preparation and reassembly of the nanosheets for photocatalytic studies

For a comparative study of photocatalytic properties, it was necessary to obtain three forms of the nanosheets for each of the titanates –initial nanosheets in the suspension without reassembly (NSs), as well as those reassembled by two methods – vacuum filtering (filtered NSs) and precipitation with hydrochloric acid (HCl-restacked NSs) (Fig. 25).

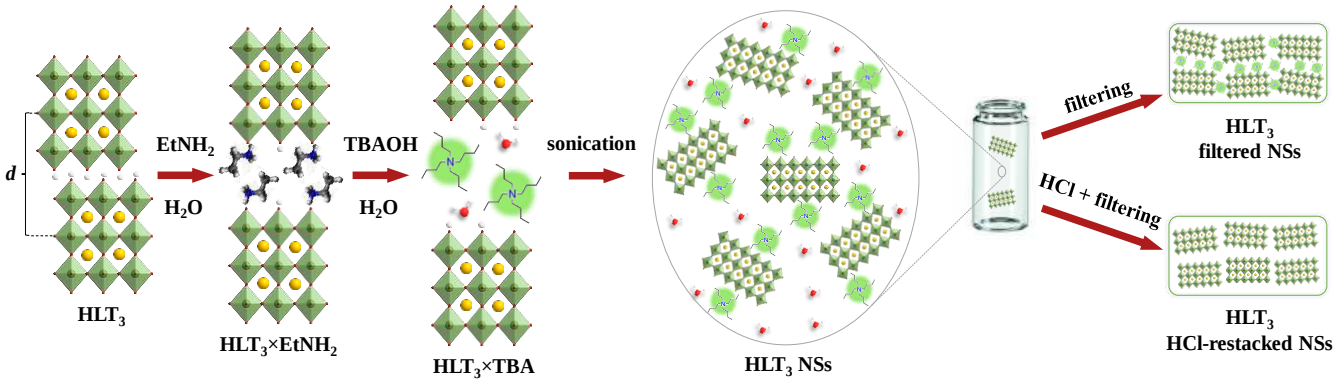


Fig. 25. Scheme for obtaining three forms of the nanosheets for photocatalytic studies using the example of the titanate $HLT_3$

To obtain suspensions of the initial titanate nanosheets (NSs), a liquid-phase exfoliation technique was used, optimized and scaled up in accordance with the approaches from subsection 2.4.1. In each case, 63 mg of the ethylamine derivative was loaded into a tube with 50 mL of a 0.004 M aqueous solution of TBAOH and processed using a Hielscher disperser UP 200 St (200 W) at half ultrasonic power for 5 min. After stirring for 7 d, the resulting mixture was again subjected to the ultrasonic treatment for 5 min. Bulk non-exfoliated titanate particles were then precipitated using a centrifuge Elmi CM-6 MT at a separation factor F = 1000 for 1 h and the target nanosheet-containing supernatants were collected using a glass pipette. The liquid-phase exfoliation procedure was repeated the required number of times to accumulate the required suspension volumes. The nanosheet concentrations in the final suspensions were determined spectrophotometrically using the calibration dependencies presented in subsection 2.4.2 (Fig. 24).

Preparation of the filtered nanosheets (filtered NSs) was carried out by vacuum filtration of the above suspensions on hydrophilic Teflon membrane filters with pores of 200 nm at a rate of 50 mL of suspension per filter. The filtered nanosheets were washed with an excess of hot (≈ 75 °C) water, dried in air, and removed from the filters using a spatula.

To obtain the nanosheets precipitated by hydrochloric acid (HCl-restacked NSs), the suspension was acidified with its 1 M aqueous solution under continuous stirring until

flocculent agglomerates formed (pH < 7), which were then filtered, washed and separated from the filters as described above.

## 2.5. Investigation of photocatalytic activity in hydrogen generation reactions

### 2.5.1. Design and operation principle of the photocatalytic setting

Kinetics of photocatalytic hydrogen evolution from water-organic mixtures was studied on a laboratory photocatalytic setting, the design of which was developed by Ph.D. Rodionov I. A. The main components of this setting are a replaceable radiation source, a two-section reaction cell with the possibility of light filtering and thermostatting, an online gas chromatograph, as well as a closed gas circulation system connecting the last two components (Fig. 26).

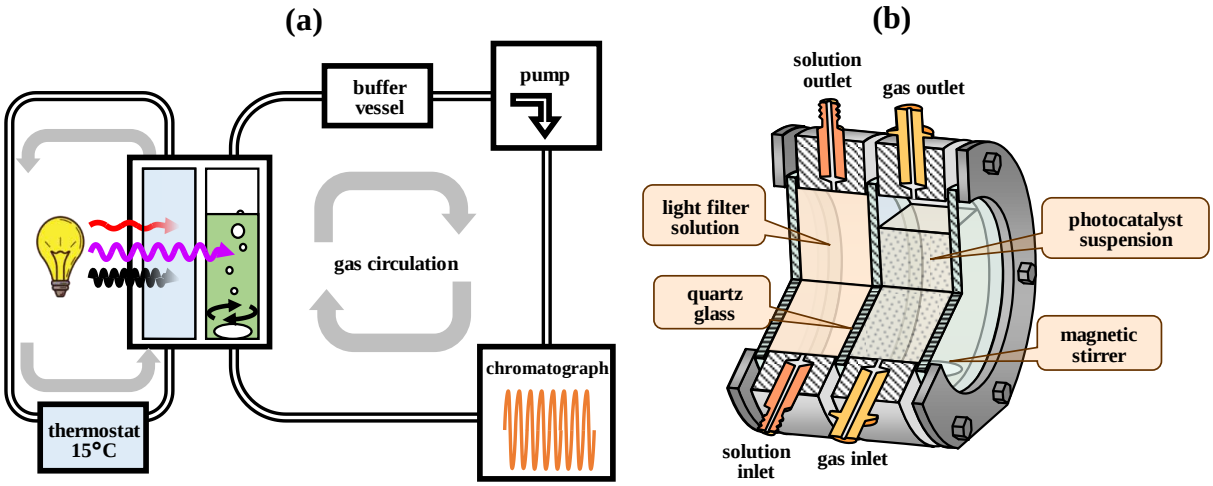


Fig. 26. Scheme of the photocatalytic setting (a) and reaction cell (b)

The light emitters used in this work are a DRT-125 mercury lamp (125 W), an Osram xenon lamp XBO-150 (150 W) and LED source designated as LED-425 (100 W). Spectra of the light emitters taken using a portable spectrometer Ocean Optics USB 2000+ are shown in Fig. 27. The DRT-125 mercury lamp has a line emission spectrum and is used mainly as a source of ultraviolet radiation. The xenon lamp Osram XBO-150 is characterized by a continuous emission spectrum, conditionally close to the solar one. The LED-425 source has an emission maximum at a wavelength of 425 nm and, thus, gives purely visible light.

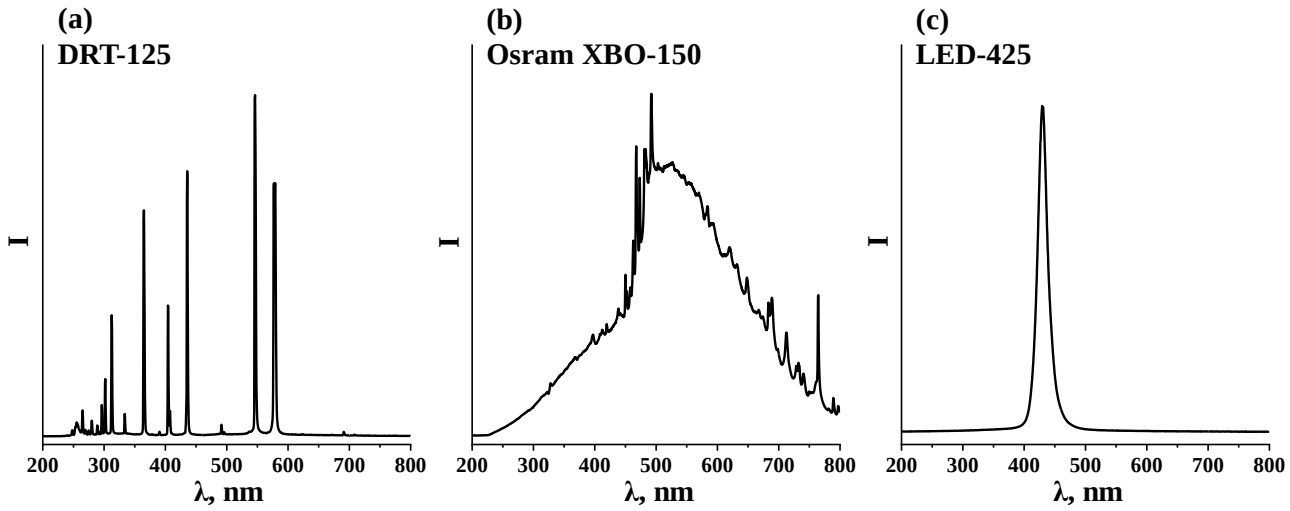


Fig. 27. Spectra of the light emitters used: mercury lamp DRT-125 (a), xenon lamp Osram XBO-150 (b) and LED-425 (c)

The photocatalytic cell used represents an external irradiation reactor, consisting of two compartments equipped with pipes for supplying and removing solutions and gases. The volume of each compartment is 60 mL, and the length of the optical path in each compartment is 2 cm. Through the compartment closest to the lamp, a pump continuously circulates a liquid filter from an external reservoir installed in a refrigeration thermostat and maintained at a set temperature of 15 °C. An aqueous solution of NaBr + KCl salts with a concentration of each 6 g/L is used as a light filter when carrying out photocatalytic experiments, which cuts off the high-energy part of ultraviolet radiation from mercury and xenon lamps ($\lambda < 220$ nm), which can lead to an undesirable reaction of direct photolysis of organic compounds, and also serves to cool the photocatalytic cell. The compartment farthest from the lamp is intended for the reaction suspension, being intensively stirred by a magnetic stirrer placed directly under the cell.

When the suspension is irradiated through a light filter, gaseous products of the photocatalytic reaction flow from the cell into the gas circulation system. The latter has a total volume of 120 mL and consists of two closed circuits, a circulation membrane pump, two taps, as well as a buffer vessel that prevents the photocatalytic suspension from entering the pump in the case of an emergency release into the gas circuit through the upper pipe of the reaction compartment of the cell. Switching the taps serves to transfer the system from one mode to another: accumulation of gaseous products in a closed circuit, supplying a gas sample to the chromatograph, purging the system with argon to remove gaseous products into the atmosphere.

To detect gaseous products of a photocatalytic reaction, a Shimadzu GC-2014 online gas chromatograph connected to a computer is used, equipped with a 30 m long Rt-Msieve 5A capillary column with molecular sieves and a thermal conductivity detector. Argon is used as a carrier gas. Chromatographic analysis of the gas phase is carried out automatically in accordance with a specified program at certain time intervals, and the recorded chromatogram is displayed in real time in the Shimadzu GCsolution program on the computer.

2.5.2. Determination of photon flux of the radiation sources

In this work, the photon flux of the light sources was understood as the rate of entry of photons of a certain energy range (mmol·h$^{-1}$) into a reaction mixture with a volume of 50 mL, located in the corresponding compartment of the photocatalytic cell. The light flux was measured using the ferrioxalate actinometry method, adapted from GOST 16948-79. As an actinometer within the framework of this method, a light-sensitive solution of potassium ferrioxalate $K_3[Fe(C_2O_4)_3]$ is used, in which, under the influence of ultraviolet and visible radiation with wavelengths $\lambda < 480$ nm, the photochemical reduction of $Fe^{II}$ to $Fe^{III}$ proceeds with quantum yield being close to unity:

$$[Fe(C_2O_4)_3]^{3-} + h\nu = Fe^{2+} + 2.5{C_2O_4}^{2-} + CO_2$$

Thus, each absorbed photon leads to the formation of one $Fe^{II}$ ion, and the increase in the $Fe^{II}$ concentration over a certain irradiation time is equal to the number of photons entered the system, which makes it possible to calculate the photon flux.

The photon flux of a light source in different spectral areas, corresponding to the absorption regions of specific photocatalysts, can be determined using a series of light filters with different light absorption edges (Fig. 28). Thus, the photon flux in the range of 220–340 nm will be equal to the difference in photon fluxes measured when the photosensitive solution is irradiated through NaBr + KCl liquid filters (transmission $\lambda > 220$ nm) and $KNO_3$ (transmittance $\lambda > 340$ nm), and in the range of 220–400 nm – to the difference in fluxes determined through NaBr + KCl and $NaNO_2$ filters (transmission $\lambda > 400$ nm).

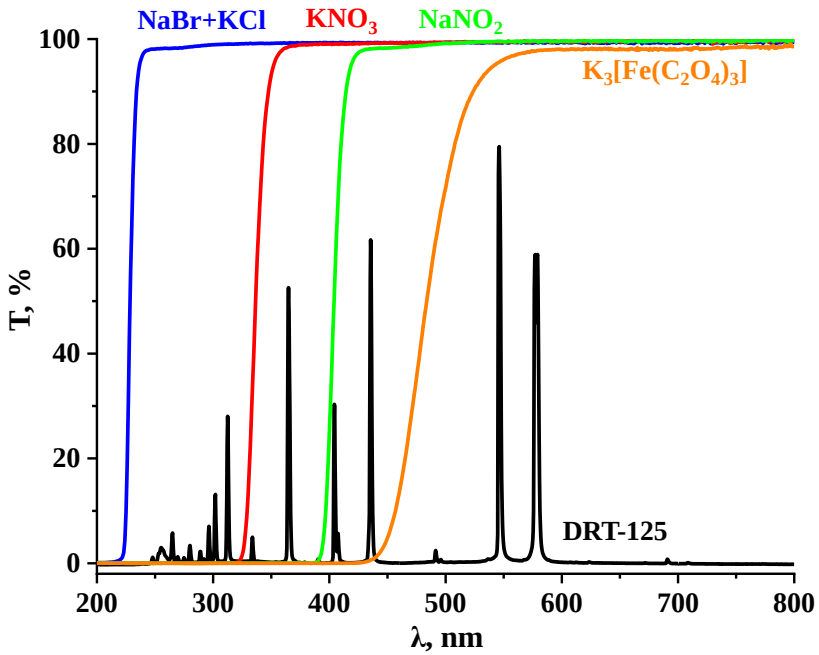


Fig. 28. Transmission spectra of liquid light filters and a light-sensitive actinometer solution against the background of the DRT-125 mercury lamp emission spectrum

In this work, actinometry experiments were carried out in a darkened room under the light of a red lamp. To prepare the photosensitive solution, 6.74 g of potassium ferrioxalate $K_3[Fe(C_2O_4)_3]\cdot 3H_2O$, which corresponds to 6 g of the anhydrous complex, was dissolved in 1 L of 0.05 M sulfuric acid. Next, 50 mL of the resulting solution was pumped into the reaction compartment of the photocatalytic cell, and the light filtering compartment was filled with an aqueous solution of NaBr + KCl with a concentration of each salt of 6 g/L. Before turning on the radiation source, a metal screen was installed between it and the cell, preventing light from entering the cell while the source reached a stationary mode (≈ 5 min). Then the screen was removed and the photosensitive solution was irradiated through the specified light filter for a given time. The concentration of $Fe^{II}$ formed during irradiation was determined spectrophotometrically after its binding into a colored complex with 1,10-phenanthroline. To do this, 1 mL of the solution from the cell, 5 mL of 1 M acetate buffer with pH ≈ 4.8 and 5 mL of 0.1% aqueous 1,10-phenanthroline were mixed in a 25 mL volumetric flask, after which the mixture was brought to the mark with distilled water. After shaking and holding for 10 min, the absorption spectrum of the final solution in the visible region was recorded. A similar experiment was carried out for the initial photosensitive solution that was not irradiated. The concentration of $Fe^{II}$ formed during irradiation (mmol/L) was calculated from a previously constructed calibration dependence, taking into account the dilution of the solutions during the analysis process, using the formula

$$c_{Fe^{II}} = 2.233 \cdot (A_{510} - A^0_{510})$$

where $A_{510}$ and $A^0_{510}$ are the optical densities at the maximum of the absorption spectrum $\lambda$ = 510 nm when analyzing the irradiated and initial photosensitive solution, respectively. In a general case, this concentration corresponds to the radiation entering the photosensitive solution in the range from 220 nm to the absorption edge of the actinometer (≈ 480 nm) and allows one to calculate the photon flux $\Phi$ (mmol·h$^{-1}$) of the source LED-425, the emission spectrum of which falls entirely within the specified range, according to the formula

$$\Phi = \frac{V \cdot c_{Fe^{II}}}{t}$$

where V = 0.05 L is the volume of the irradiated photosensitive solution and t is the duration of irradiation (h).

To determine the photon flux of the DRT-125 and Osram XBO-150 lamps in the ranges of 220–340 nm and 220–400 nm, the experiments similar to those described above were carried out on irradiation of a light-sensitive solution through liquid light filters $KNO_3$ and $NaNO_2$ with a salt concentration of 6 g/L. Light fluxes in the indicated spectral ranges were calculated using the formula

$$\Phi = V \cdot \left( \frac{c_{Fe^{II}}}{t} - \frac{c'_{Fe^{II}}}{t'} \right)$$

where $c_{Fe^{II}}$ is the concentration of $Fe^{II}$ (mmol/L) formed when the light-sensitive solution is irradiated through a NaBr + KCl light filter for time t (h), $c'_{Fe^{II}}$ is when irradiated through a $KNO_3$ or $NaNO_2$ light filter for time t′ (h). Photon fluxes $\Phi'$ of the DRT-125 and Osram XBO-150 lamps in other regions of the spectrum that do not fall within the absorption edges of the used light filters were calculated by multiplying the experimentally determined fluxes $\Phi$ in the range of 220–340 nm or 220–400 nm by the ratio of the integral light intensities in the ranges of interest in accordance with the expression

$$\Phi' = \Phi \cdot \frac{\int_{220}^{\lambda_{max}} I(\lambda) d\lambda}{\int_{220}^{\lambda'} I(\lambda) d\lambda}$$

in which $\lambda'$ = 340 or 400 nm, $\lambda_{max}$ is a long-wave absorption edge of a particular photocatalyst, I is the emission intensity along the source spectrum (Fig. 27).

The irradiation times were selected so that $Fe^{II}$ was formed in a sufficient amount for reliable spectrophotometric detection in the range of linearity of the calibration dependence

and, at the same time, the concentration of the actinometer in the light-sensitive solution remained at the end of irradiation sufficient for complete light absorption in the spectral area of interest. The experiments on determination of the photon flux of each source were carried out 3 times, after which the values obtained were averaged. The irradiation times used with different light filters, as well as the found values of light fluxes, are presented in Table 4.

Table 4. Durations of irradiation of the photosensitive solution through different light filters and photon fluxes of the sources used

| Mercury and xenon lamps | | | | | | |
|---|---|---|---|---|---|---|
| | t, s | t′, s | | Φ, mmol·h$^{-1}$ | | |
| | NaBr + KCl | KNO $_3$ | NaNO2 | 220–340 nm | 220–400 nm | 220–600 nm |
| DRT-125 | 20 | thirty | 120 | 12.1 | 19.4 | 34.2 |
| Osram XBO-150 | 300 | 600 | 1200 | 0.254 | 0.683 | 2.27 |
| LED emitter | | | | | | |
| | t, s | | | Φ, mmol·h$^{-1}$ (425 ± 25 nm) | | |
| LED-425 | 5 | | | ≈ 100 | | |

2.5.3. Methodology of the photocatalytic experiments

The resulting photocatalysts were systematically studied in the reactions of hydrogen production from aqueous solutions of typical products of plant biomass processing – methanol, D-glucose and D-xylose, as well as pure distilled water. The amine and alcohol derivatives, as well as titanate nanosheets, were tested under mid- and near-ultraviolet radiation of a DRT-125 mercury lamp. The derivatives with aromatic modifiers were also studied under the radiation of an Osram XBO-150 xenon lamp, approximately corresponding to solar, and LED-425, generating purely visible light with a maximum at a wavelength of 425 nm. The activity of the photocatalysts obtained was measured both without a cocatalyst and after surface modification with Pt nanoparticles, and compared with the activity of the initial protonated titanates HLT (HNT) and $HLT_3$ ($HNT_3$), as well as titanium dioxide $TiO_2$ P25 Degussa – a «gold standard» in the field of heterogeneous photocatalysis, measured by the applicant under identical conditions.

2.5.3.1. Measurement of photocatalytic activity without cocatalyst

Experiments on studying the activity of powdered photocatalysts (that is, all photocatalysts in this work, with the exception of the initial titanate nanosheets without

reassembly – NSs) were carried out as follows. In a typical experiment, 27 mg of the sample was loaded into a round-bottom flask with 54 mL of a 1% (mol.) aqueous solution of the selected organic compound or distilled water, which corresponds to a volume concentration of the photocatalyst of 500 mg/L. The flask with the specified mixture was sealed with a laboratory film Parafilm M and was subjected to ultrasonic treatment in an Elmasonic S10H bath (60 W) for 10 min. After starting the circulation of the NaBr + KCl light filter and turning on the magnetic stirrer, the resulting suspension was completely pumped into the reaction compartment of the photocatalytic cell through the lower pipe by creating a vacuum in the compartment with a running membrane pump. Then the radiation source was turned on and, at the same time, the system was purged with argon to remove air. After 15 min, 4 mL of the suspension was taken through the upper pipe of the reaction compartment using a syringe to establish the actual volume concentration of the photocatalyst and the pH of the medium before starting the photocatalytic experiment ($c_1$, $pH_1$). After 15 min from the moment of sampling, the argon purge was stopped, and the accumulation of gaseous products of the photocatalytic reaction began in a closed gas circulation system for a total duration of 2 h, during which the composition of the gas phase was analyzed chromatographically at fixed time intervals of 15 min. After this, the radiation source was turned off, and the potential activity of the catalyst was monitored in the dark mode over the next 45 min. After the dark stage, 4 mL of the suspension was sampled to establish the actual concentration of the photocatalyst and the pH of the medium at the end of the photocatalytic experiment ($c_2$, $pH_2$). When testing the amine and alcohol derivatives, their potential exfoliation into nanosheets during photocatalysis was additionally monitored. For this purpose, 30 mL of the remaining suspension was poured through the lower pipe of the reaction compartment into a glass tube and centrifuged on an Elmi CM-6MT laboratory centrifuge at a separation factor F = 1000 for 1 h to sediment large non-exfoliated particles, after which the concentration of the photocatalyst, potentially exfoliated into nanosheets, was determined in the supernatant and pH of the medium was measured ($c_3$, $pH_3$).

Pristine titanate nanosheets without reassembly (NSs) were studied as photocatalysts in TBAOH-containing suspensions obtained via the liquid-phase exfoliation. Concentration of the HLT nanosheets was initially ≈ 250 mg/L; suspensions of HNT, $HLT_3$ and $HNT_3$ ones were diluted with a 0.004 M aqueous solution of TBAOH to ≈ 500 mg/L. All the nanosheet

suspensions were acidified with 1 M hydrochloric acid under intense stirring to pH ≈ 6, corresponding to suspensions of the protonated titanates. When studying the photocatalytic hydrogen production from methanol, D-glucose and D-xylose, the required amounts of these organic compounds were introduced into the suspension to achieve the same volume concentration as when working with powdered photocatalysts. Otherwise, the procedure for conducting photocatalytic experiments with the initial nanosheets corresponded to that described above.

2.5.3.2. Measurement of photocatalytic activity with Pt as a cocatalyst

In order to increase the efficiency of the spatial separation of photogenerated charge carriers, as well as to reduce the overpotential during the hydrogen formation, the surface of the studied photocatalysts was additionally modified with Pt nanoparticles as a cocatalyst with a calculated content of the latter in the final composites of 1% (mass). Platinization was carried out by the photocatalytic method in situ under the radiation of the DRT-125 mercury lamp through a NaBr + KCl light filter using hexachloroplatinic acid $H_2PtCl_6$ as a Pt source, which is reduced by conduction electrons reaching the semiconductor surface:

$$H_2PtCl_6 + 4H^+ + 4e^- = Pt + 6HCl$$

The volume of the suspension loaded into the reaction compartment was 53 mL. 15 min after the lamp was turned on and the system was purged with argon, 1.1 mL of a 1.28 mM $H_2PtCl_6$ solution was injected into the cell with a syringe. After 15 min, 4 mL of the suspension was sampled for analysis ($c_1$, $pH_1$). After 15 min from the moment of sampling, argon purging was finished, and the accumulation of gaseous products of the photocatalytic reaction began in a closed gas circulation system with chromatographic analysis of the gas phase every 5 min. At the hydrogen generation rate $\omega > 500$ μmol·h$^{-1}$, the program for measuring photocatalytic activity was divided into 3–4 stages, separated by purging the system with argon for 10 min to reduce hydrogen pressure in the system and prevent undesirable reverse reactions. The duration of the dark stage at the end of the measurement was 20 min.

When studying the photocatalytic activity of organic-inorganic derivatives in aqueous solutions of carbohydrates, two platinization methods were tested – carried out directly in the carbohydrate medium, as described above, and carried out separately in a 1% (mol.) methanol solution, followed by isolation of the platinized photocatalyst from the suspension by filtration and dispersing in the selected carbohydrate solution. Platinization of the photocatalysts, further

tested under radiation of the Osram XBO-150 xenon lamp or LED-425, was performed under the DRT-125 lamp, after which it was replaced with the required light emitter, and the system was purged with argon. Otherwise, the experimental procedure coincided with that described previously for the samples without a cocatalyst.

2.5.3.3. Calculation of the reaction rate and apparent quantum efficiency

The main indicators of photocatalytic activity in this work were the rate of hydrogen generation (absolute ω in μmol·h$^{-1}$ and normalized per unit mass of the photocatalyst ω′ in μmol·h$^{-1}$·g$^{-1}$), apparent quantum efficiency φ (%), as well as the factor of increase in the reaction rate during platinization of the photocatalyst $k_{Pt}$.

Primary processing of the chromatograms obtained during each photocatalytic experiment was carried out using Shimadzu GCsolution software. First, the integration of the chromatographic peaks corresponding to hydrogen was performed, and the resulting areas under the peaks S were recalculated into the amount of hydrogen n (μmol) using the formula

$$n = kS$$

where k = 1.79·10$^{-4}$ is a proportionality coefficient, established experimentally during the process of calibrating the system using known quantities of introduced hydrogen. Based on the obtained values of n, a kinetic curve n = n (t) was constructed, which was then approximated by a linear function. The reaction rate for hydrogen (μmol·h$^{-1}$ ) was determined as a slope of this function:

$$\omega = \frac{dn(t)}{dt}$$

If the kinetic curve deviated significantly from the linear course, the latter was divided into 2–3 conditionally linear sections, and the reaction rate was calculated for each of them separately. The normalized rate of hydrogen evolution (mmol·h$^{-1}$·g$^{-1}$) was found according to the formula

$$\omega' = \frac{\omega}{1000 \cdot m}$$

in which m is the mass of the photocatalyst in the cell (g).

The apparent quantum efficiency of hydrogen generation (%) was calculated according to the formula

$$\varphi = \frac{2\omega}{\Phi} \cdot 100\%$$

where Φ is the photon flux of the source (μmol·h$^{-1}$) in the light absorption range of a particular photocatalyst. The coefficient $k_{Pt}$, which serves as a measure of the efficiency of the photocatalyst platinization, was calculated by definition

$$k_{Pt} = \frac{\omega_{Pt}}{\omega}$$

where $\omega_{Pt}$ and ω are the reaction rates for hydrogen after and before reduction of 1% Pt on the surface as a cocatalyst.

2.5.3.4. Monitoring stability and composition of the reaction suspensions

To assess the dispersibility of the photocatalysts obtained in aqueous-organic media, as well as to control the stability of their reaction suspensions with respect to precipitation during photocatalysis, the spectrophotometric method was used. When working with amine and alcohol derivatives of the titanates, the actual volume concentrations of the samples at the beginning ($c_1$) and ending ($c_2$) of photocatalytic measurements were determined using previously constructed spectrophotometric calibration dependencies of the form

$$A_{550} = kc_n \ (n = 1, 2)$$

where $A_{550}$ is the optical density at a wavelength of 550 nm, k is the experimentally determined coefficient equal to 0.0056, 0.0061, 0.0043 and 0.0045 for derivatives of the titanates HLT, HNT, $HLT_3$ and $HNT_3$, respectively. The potential exfoliation of the derivatives into nanosheets during the process of photocatalysis was also controlled, for which, using the calibration dependencies from subsection 2.4.2 (Fig. 24) the concentration $c_3$ of fine fractions of the particles remaining in the volume of the solution after centrifugation of the reaction suspensions was calculated.

Stability of suspensions of the photocatalysts based on perovskite nanosheets was assessed by the ratio of their volume concentrations at the ending and beginning of each photocatalytic measurement $c_2/c_1$, determined from the ratio of the corresponding optical densities $A_2/A_1$, measured spectrophotometrically at wavelengths of 240 nm for HLT, 225 nm for HNT, 230 nm for $HLT_3$ and $HNT_3$:

$$\frac{c_2}{c_1} = \frac{A_2}{A_1}$$

In this case, the ratio $c_2/c_1$ corresponds to the fraction of the photocatalyst remaining in the volume of the reaction suspension at the end of the experiment, while the difference $1–c_2/c_1$ gives the fraction of the photocatalyst precipitated on the walls of the cell.

A pH value of the suspension medium served an indirect parameter indicating changes in the composition of the reaction solutions during the photocatalytic hydrogen generation and was determined before the start of each measurement of photocatalytic activity ($pH_1$), at its end ($pH_2$) and, in the case of the amine and alcohol derivatives, after centrifuging the final suspension ($pH_3$). In some cases, Raman spectroscopy and other methods were used to analyze the composition of the reaction solutions, with the dispersed photocatalyst previously separated from the solution by filtration.

2.5.3.5. Investigation of the photocatalytic activity dependence on the reaction conditions

The activity of selected photocatalysts in aqueous methanol was further studied depending on the reaction conditions: methanol concentration (0–30 mol. %), photocatalyst concentration (0.1–2 g/L) and mass fraction of Pt as a cocatalyst (0–5%). The corresponding experiments were carried out with the direct participation of undergraduate students Maksimova E. A. and Gruzdeva E. O. Each reaction suspension was prepared anew, and in each series of experiments only one parameter was varied, keeping other conditions constant, which corresponded to the standard method of photocatalytic experiment: methanol concentration 1% (mol.), photocatalyst loading concentration 0.5 g/L, cocatalyst mass fraction 1%. When changing the loading of the photocatalyst, the concentration of the hexachloroplatinic acid solution $H_2PtCl_6$ introduced into the cell was proportionally changed to ensure the same mass fraction of Pt in the final samples. The mass fraction of Pt as a cocatalyst was varied by introducing 1 mL of $H_2PtCl_6$ solutions of various concentrations into 49 mL of the irradiated reaction suspension at a fixed photocatalyst loading.

## 2.6. Investigation of stability of the photocatalysts

Stability of the photocatalysts obtained was studied in two aspects – kinetic and chemical. In the first case, the subject of the study was the constancy of photocatalytic activity during long-term operation of the catalyst, and in the second, its potential structural-chemical transformations during photocatalysis, mainly affecting the interlayer space.

2.6.1. Measuring activity under long-term operating conditions

The most active photocatalysts based on organic-inorganic derivatives and nanosheets of the titanates were additionally tested in experiments with increased duration (12–24 h). Activity measurements were carried out in a 1% (mol.) aqueous solution of methanol, and the

radiation source was a DRT-125 mercury lamp with a NaBr + KCl filter. In this case, the rate of hydrogen generation was monitored every 2 h for 30 min, and the rest of the time the system operated in the argon purging mode with the liberation of the released hydrogen into the atmosphere. Every 4 h, using a microdispenser, the required amount of methanol was introduced into the cell to restore its concentration to the initial value, and the cell was thoroughly shaken to transfer the photocatalyst particles precipitated on the walls into the suspension volume.

2.6.2. Analysis of the structure and composition after photocatalysis

Chemical stability of the organic-inorganic photocatalysts was studied using the example of derivatives with extreme hydrocarbon chain lengths of interlayer modifiers (methylamine, *n*-octylamine, methanol, *n*-decanol), as well as those exhibiting the greatest activity in each series of organically modified single-layer and three-layer titanates. For this purpose, standard photocatalytic experiments were carried out with the indicated samples in a 1% (mol.) aqueous solution of methanol. The source of radiation in all cases (including when studying derivatives with aromatic modifiers) was a DRT-125 mercury lamp with a NaBr + KCl filter. After 2.5 h of irradiation, the photocatalysts were isolated from the reaction suspension by filtration and dried in air. To determine possible changes in structure, composition, light absorption and morphology, the final samples were examined using X-ray diffraction analysis, Raman spectroscopy, elemental CHN-analysis, thermogravimetry, diffuse reflectance spectroscopy and scanning electron microscopy.

## 2.7. Physical-chemical characterization of the samples

2.7.1. Instrumentation

2.7.1.1. X-ray diffraction analysis

Powder X-ray diffraction analysis served as the main method for primary characterization of the photocatalysts at all stages of their preparation. Using this method, the synthesized samples were identified by their crystal structure as well as the phase composition, structural parameters and their changes were determined in the course of topochemical modification of the interlayer space. X-ray diffraction patterns of the samples were recorded on a desktop X-ray diffractometer Rigaku Miniflex II («Center for X-ray diffraction studies»)

using Cu $K_\alpha$ radiation ($h\nu$ = 8.0478 keV) in the range of diffraction angles $2\theta$ = 3–60° at a scanning rate of 10°/min.

2.7.1.2. Raman spectroscopy

Raman spectroscopy was used to identify organic components in the composition of the organic-inorganic derivatives and reassembled titanate nanosheets by the characteristic frequencies of vibrations of their chemical bonds, to identify shifts in the vibrational modes of the perovskite lattice during organic modification, exfoliation into nanosheets and other topochemical transformations and also, in some cases, to analyze the composition of the reaction solutions after photocatalytic experiments. Raman spectra were recorded on a Bruker Senterra spectrometer («Center for optical and laser research») in the Raman shift range of 100–4000 $cm^{-1}$. When studying protonated titanates, amine and methanol derivatives, as well as reassembled nanosheets, a 488 nm laser (power 0.1–20 mW) was used as a radiation source; the spectra of other alcohol derivatives, those with aromatic modifiers and reaction solutions were collected with a 785 nm laser (power 1–100 mW). The laser power was selected in each case individually, taking into account the intensity of side luminescence. The duration of a single signal accumulation was 10–120 s, depending on the wavelength and power mode of the laser. The accumulation was repeated 4–8 times, after which the resulting spectra were averaged and the luminescent background was subtracted.

2.7.1.3. Nuclear magnetic resonance spectroscopy

Nuclear magnetic resonance (NMR) spectroscopy on $^{13}C$ nuclei was used to determine the type of chemical bonding between the organic modifier and perovskite matrix in the organic-inorganic derivatives, as well as to establish the completeness of the substitution of some organic modifiers by others during multi-stage syntheses. $^{13}C$ NMR spectra of La-containing samples were recorded on a Bruker Avance III 400 WB spectrometer («Center for magnetic resonance») at an operating frequency of 100.64 MHz using tetramethylsilane as a standard. Each sample was placed in a zirconium oxide rotor with an outer diameter of 4 mm and rotated at a frequency of 12.5 kHz at a magic angle to the direction of the constant magnetic field. To obtain the spectra, a cross-polarization sequence of exciting pulses was used with a contact time of 2 ms, a relaxation delay time of 5 s, and a number of repetitions of

12000. The study of Nd-containing compounds by NMR was not possible due to their paramagnetic nature.

2.7.1.4. Thermogravimetry

The thermogravimetry (TG) method was used to study thermal stability of the samples obtained, as well as to partially determine their quantitative composition (degrees of protonation and hydration) based on the mass losses observed during thermolysis. The analysis was carried out on a Netzsch TG 209 F1 Libra thermomicrobalance («Center for thermogravimetric and calorimetric research») in an atmosphere of synthetic air. The temperature program included heating ≈ 10–15 mg of each sample from room temperature to 950 °C at a rate of 10 °C/min, followed by keeping at the maximum temperature for 20 min for the completion of the hindered processes of thermal destruction and establishment of a constant mass.

2.7.1.5. Elemental CHN-analysis

The method of CHN-analysis was used to determine the mass fractions of these elements in the organically modified samples, which were used in conjunction with TG data for further calculation of their quantitative compositions. The studies were carried out on a Euro EA3028-HT elemental analyzer («Center for chemical analysis and materials research»). In each case, a sample weighed ≈ 1 mg was placed in a miniature container made of aluminum foil and subjected to oxidative flash pyrolysis in a high-temperature chamber at 980 °C, the gaseous products of which ($CO_2$, $H_2O$, $N_2$) were analyzed chromatographically using previously constructed calibration dependencies.

2.7.1.6. Energy dispersive X-ray spectroscopy

Energy dispersive X-ray spectroscopy was used to confirm the elemental composition of the protonated titanates as well as their nanosheets. The samples were irradiated with a high-energy electron beam under vacuum in a Zeiss Merlin electron microscope, and the resulting X-ray radiation was detected by an Oxford Instruments INCAx-act energy-dispersive microanalyzer («Interdisciplinary center for nanotechnology»). The quantitative elemental composition was calculated on the basis of the spectra obtained using previously constructed calibration dependencies.

2.7.1.7. Atomic emission spectroscopy

Inductively coupled plasma atomic emission spectroscopy (ICP-AES) was used to determine the concentration of the titanate nanosheets in standard suspensions used to construct spectrophotometric calibration curves. Before this, the suspensions were subjected to microwave homogenization in 12 M hydrochloric acid, and the resulting solutions were diluted with distilled water 100 times. Analysis of the solutions was carried out on a Shimadzu ICPE-9000 spectrometer («Center for chemical analysis and materials research») in an axial mode with a mini-burner and included the determination of the elements Ln and Ti. The concentrations of the latter were calculated from calibration curves constructed using Merck monocomponent standards in 0.1 M nitric acid.

2.7.1.8. Diffuse reflectance spectroscopy

Diffuse reflectance spectroscopy was used to determine the intrinsic light absorption region of the photocatalysts and subsequently calculate the optical bandgap energy. The spectra of all the studied samples, with the exception of the derivatives with aromatic modifiers, were recorded on a Shimadzu UV-2550 spectrophotometer with an ISR-2200 integrating sphere («Center for chemical analysis and materials research») in the range of 220–800 nm. The spectra of the derivatives with aromatic modifiers were recorded on a Perkin Elmer Lambda 1050 spectrophotometer with an integrating sphere 150 mm InGaAs («Center for optical and laser research») in the range of 200–2500 nm. In all cases, barium sulfate $BaSO_4$ was used as a substrate to fix the samples in the holders, the signal of which was subtracted as a baseline.

2.7.1.9. Photoelectron spectroscopy

Based on ultraviolet and X-ray photoelectron spectroscopy (UPS and XPS) data, the position of the valence band top of the photocatalysts obtained was assessed. The studies were carried out using a Thermo Fisher Scientific Escalab 250Xi spectrometer («Center for studies in surface science») under high vacuum after depositing the samples on a conductive substrate. Ultraviolet spectra were recorded under He $I_\alpha$ radiation ($h\nu$ = 21.2 eV) with the application of an external potential of −5 V, which was subtracted during further data processing, X-ray spectra were measured under Al $K_\alpha$ radiation ($h\nu$ = 1486.6 eV).

2.7.1.10. Time-resolved luminescence spectroscopy

Time-resolved luminescence spectroscopy was used to indirectly estimate the average lifetime of photogenerated charge carriers in the samples, which, in physical terms, is the reciprocal of the recombination rate. It was assumed that the recombination is predominantly radiative, and the directly determined value was the average lifetime of luminescence upon excitation in the region of the photocatalyst intrinsic absorption. The work was carried out on a modular spectrofluorometer Horiba Jobin Yvon Fluorolog-3 («Center for optical and laser research»). First, standard luminescence spectra of the samples were recorded upon excitation at a wavelength of 265 nm, and the position of the emission maxima was determined. Then the luminescence was excited using a pulsed LED source with the specified wavelength and the kinetics of its decay was monitored – the dependence of the intensity on time $I_\lambda = I_\lambda(t)$ at the predetermined emission maximum.

2.7.1.11. Scanning electron microscopy

Using scanning electron microscopy (SEM), the particle morphology of the samples obtained was studied, including, in particular, monitoring changes in their shape and size, potential partial delamination during the process of topochemical modification, as well as the reduction of the platinum cocatalyst nanoparticles on the surface. The samples were deposited on a carbon tape and analyzed on a Zeiss Merlin microscope equipped with a field emission cathode, a Gemini-II electron optics column, and an oil-free vacuum system («Interdisciplinary center for nanotechnology»).

2.7.1.12. Transmission electron microscopy

Morphology of the titanate nanosheets was studied using transmission electron microscopy (TEM), and the main interplanar distances in their structure were assessed based on selected area electron diffraction (SAED) data. The studies were carried out using a Zeiss Libra 200FE high-resolution microscope («Interdisciplinary center for nanotechnology»). Before depositing on the sample holder, the nanosheet suspensions were diluted with methanol to a concentration of ≈ 15–20 mg/L.

2.7.1.13. Atomic force microscopy

Atomic force microscopy (AFM) was used to determine the thickness of the titanate nanosheets deposited on silicon substrates. The work was carried out using the Integra Spectra

research complex («Center for diagnostics of functional materials for medicine, pharmacology and nanoelectronics»).

2.7.1.14. Specific surface area measurement

The specific surface area of the photocatalysts was determined using the Brunauer, Emmett and Teller (BET) multipoint method on a Quadrasorb SI sorption analyzer («Center for diagnostics of functional materials for medicine, pharmacology and nanoelectronics»). Before the study, weighed samples of ≈ 250 mg were subjected to vacuum degassing at 25 °C for 12 h. Nitrogen $N_2$ was used as an adsorbate. Adsorption isotherms were measured at −196 °C.

2.7.1.15. Dynamic light scattering

Size distribution of the titanate nanosheets in suspensions after liquid-phase exfoliation, as well as values of the particle ζ-potentials at different pH of the dispersion medium, were studied using the dynamic light scattering method. The work was performed on a Photocor Compact-Z analyzer («Center for diagnostics of functional materials for medicine, pharmacology and nanoelectronics»). The radiation source was a thermally stabilized diode laser with a wavelength of 659 nm. Scattered light detection was carried out at angles of 90° and 20° when studying particle sizes and ζ-potentials, respectively.

2.7.1.16. Laser granulometry

Laser granulometry was used to comparatively evaluate particle sizes in the samples of titanate nanosheets reassembled by various methods. The studies were carried out on a Malvern Mastersizer 3000 laser diffraction analyzer («Center for innovative technologies of composite nanomaterials»), equipped with two radiation sources with wavelengths of 470 and 633 nm, after dispersing the samples in distilled water using a proprietary Hydro MW ultrasonic module. Particle sizes were estimated using the Mie light scattering model using refractive and absorption indices of 2.51 and 0.01, respectively.

2.7.1.17. Spectrophotometry

Spectrophotometry was used in determining the concentrations of dispersed samples in suspensions, monitoring the stability of the latter during photocatalytic experiments, as well as in measuring photon fluxes using ferrioxalate actinometry and preparing liquid light filters.

The analysis was carried out on a Thermo Scientific Genesys 10S UV-Vis single-beam spectrophotometer in the wavelength range 190–1100 nm and at optical densities A < 2. Since this spectrophotometer is not equipped with an integrating sphere, the optical densities observed when working with suspensions corresponded to the superposition of scattering and absorption by the suspended particles. However, this fact did not interfere with the analysis due to the linear dependence of the experimental optical density on the volume concentration of dispersed samples, which made it possible to construct spectrophotometric calibration graphs.

2.7.1.18. pH-metry

pH values of solutions and suspensions were controlled during their preparation, as well as during photocatalytic experiments, serving as an indirect indicator of changes in the composition of reaction systems. pH measurements were carried out using a Mettler Toledo SevenCompact S220 laboratory pH-meter equipped with an InLab Expert Pro-ISM combination electrode, under conditions of continuous stirring with a magnetic stirrer.

2.7.2. Methods for processing experimental data

2.7.2.1. Processing of diffraction patterns and calculation of structural parameters

The phase composition of the initial alkaline and protonated forms of the titanates was confirmed by comparing the X-ray diffraction patterns obtained with those presented in the literature and the database of the International Center for Diffraction Data (ICDD), work with which was carried out through a Rigaku PDXL 2 software. Indexing of diffraction patterns and calculation of lattice parameters in the tetragonal system (*a, c)* were performed based on all the observed diffraction maxima using Bruker DiffracPlus Topas software. An additional structural parameter when characterizing the samples was the interlayer distance *d* (Fig. 19), equal to the *c* parameter or half of it, depending on the conformation of perovskite blocks in a particular sample.

Additionally, based on X-ray diffraction analysis, the average angle α between the hydrocarbon chains of interlayer organic modifiers and the plane of perovskite blocks in the amine and alcohol derivatives was estimated. It was assumed that all hydrocarbon chains are completely in the *all-trans*-conformation and parallel to each other, and the overlap of the modifier chains associated with opposite perovskite blocks is absent or constant in magnitude.

First, the experimental dependence of the interlayer distance on the number of carbon atoms in the chain $d = d(n_C)$ was approximated by a linear function with an angular coefficient $l_1$, after which the desired chain tilt angle α was calculated using the formula

$$\alpha = \arcsin\frac{l_1}{2l_2}$$

where $l_2$ = 1.27 Å is a theoretical chain elongation upon insertion of the homologous difference –$CH_2$–.

2.7.2.2. Calculation of quantitative composition of the photocatalysts

Cationic composition of the initial protonated titanates, which served as precursors for the creation of new photocatalysts, was controlled by X-ray energy-dispersive spectroscopy. The degrees of protonation x and hydration y were calculated from thermogravimetry data. During thermolysis of samples of these compounds with a mass of $m_0$, two main areas of mass loss are observed, corresponding to the deintercalation of interlayer water molecules and the subsequent decomposition of the anhydrous protonated form of the titanate, respectively:

$$\begin{cases} H_xNa_{1-x}LnTiO_4 \cdot yH_2O = H_xNa_{1-x}LnTiO_4 + yH_2O \\ H_xNa_{1-x}LnTiO_4 = Na_{1-x}LnTiO_{4-0.5x} + 0.5xH_2O \end{cases}$$

$$\begin{cases} H_{2x}K_{2-2x}Ln_2Ti_3O_{10} \cdot yH_2O = H_{2x}K_{2-2x}Ln_2Ti_3O_{10} + yH_2O \\ H_{2x}K_{2-2x}Ln_2Ti_3O_{10} = K_{2-2x}Ln_2Ti_3O_{10-x} + xH_2O \end{cases}$$

Using the notation $m_1$ for the mass of the sample after the first section of mass loss and $m_2$ for that after the second, the degree of protonation of single-layer and three-layer titanates was found by solving for x the following equations

$$\frac{M(Na_{1-x}LnTiO_{4-0.5x})}{M(H_xNa_{1-x}LnTiO_4)} = \frac{m_2}{m_1}$$

$$\frac{M(K_{2-2x}Ln_2Ti_3O_{10-x})}{M(H_{2x}K_{2-2x}Ln_2Ti_3O_{10})} = \frac{m_2}{m_1}$$

in which M are the molar masses of the compounds indicated in brackets, presented in a general form. Taking into account the obtained x values, the degrees of hydration were then calculated by solving the following equations for y:

$$\frac{M(H_xNa_{1-x}LnTiO_4)}{M(H_xNa_{1-x}LnTiO_4 \cdot yH_2O)} = \frac{m_1}{m_0}$$

$$\frac{M(H_{2x}K_{2-2x}Ln_2Ti_3O_{10})}{M(H_{2x}K_{2-2x}Ln_2Ti_3O_{10} \cdot yH_2O)} = \frac{m_1}{m_0}$$

Quantitative compositions of the amine derivatives were sought in the form of $HLnTiO_4 \cdot xRNH_2 \cdot yH_2O$ and $H_2Ln_2Ti_3O_{10} \cdot xRNH_2 \cdot yH_2O$, those of the alcohol derivatives and derivatives with aromatic modifiers – in the form of $H_{1-x}LnTiO_{4-x} \cdot xRO \cdot yH_2O$ and $H_{2-x}Ln_2Ti_3O_{10-x} \cdot xRO \cdot yH_2O$. The initial data for the calculation were the mass fractions of nitrogen $\eta_N$ and carbon $\eta_C$ in the samples, determined by the CHN-analysis method, as well as the total mass loss during thermolysis, determined during thermogravimetry. First, the amount of the organic component x per formula unit of titanate was calculated, assuming that the derivative does not contain intercalated water (y = 0):

$$x_{RNH_2} = \frac{\eta_N M}{A_N}$$

$$x_{RO} = \frac{\eta_C M}{A_C}$$

Here M is the molar mass of the formula unit of a hypothetical anhydrous organic-inorganic derivative, $A_N$ and $A_C$ are the atomic masses of nitrogen and carbon, respectively. For the resulting composition, the theoretical mass loss $\Delta m_{theor}$ (%) was calculated under the assumption that the final thermolysis product has the form $LnTiO_{3.5}$ or $Ln_2Ti_3O_9$ in the case of single-layer and three-layer titanates, respectively. Then, using the difference between the experimental and theoretical mass losses (%), the amount of intercalated water y was determined:

$$y = \frac{M(\Delta m_{exp} - \Delta m_{theor})}{M_{H_2O}(100 - \Delta m_{exp} + \Delta m_{theor})}$$

where $M_{H_2O}$ is the molar mass of water.

Calculation of the quantitative composition of the reassembled nanosheets, containing firmly adsorbed tetrabutylammonium cations and water molecules, was performed in a similar way.

2.7.2.3. Calculation of bandgap energy and band edge potentials

To determine the optical bandgap energy $E_g$, diffuse reflectance spectra of the photocatalysts were converted into coordinates

$$(F \cdot h\nu)^{1/2} = f(h\nu)$$

where F is the Kubelka-Munk function of the reflection coefficient R:

$$F = \frac{(1-R)^2}{2R}$$

Linear sections in the low-energy region of the Kubelka-Munk plots were extrapolated to the intersection point, the abscissa of which was the value of $E_g$.

Potentials of the valence band top $E_V$ and conduction band bottom $E_C$ relative to the SHE were estimated using photoelectron spectroscopy data and the obtained $E_g$ values. First, according to UPS data, the work function W was found using the formula

$$W = E_B^1 - E_B^2 + 21.2$$

in which $E_B^1$ and $E_B^2$ are the edges of photoelectron emission (minimum and maximum binding energy, respectively), 21.2 eV is the energy of the radiation source [227]. The edge $E_B^1$ was determined by the abscissa of the point on the spectrum, starting from which the derivative of the signal intensity with respect to the binding energy $dI(E_B)/dE_B$ becomes positive. The $E_B^2$ edge was determined by linearly extrapolating the corresponding shoulder on the spectrum to the intersection with the baseline. Then, from the valence band XPS spectra, the energy $E_V'$ corresponding to the band top was found as the abscissa of the point of intersection of the linearly extrapolated photoelectron emission shoulder with the baseline, after which the desired band edge potentials relative to the SHE were calculated using the formulae

$$\begin{cases} E_V = E_V' + W - 4.44 \\ E_C = E_V - E_g \end{cases}$$

where 4.44 is the shift of the physical energy scale relative to the electrochemical potential scale.

2.7.2.4. Calculation of average luminescence lifetime

In each case, the luminescence decay curves were approximated by a biexponential function of the form

$$I_\lambda(t) = A_1 \cdot e^{-t/t_1} + A_2 \cdot e^{-t/t_2} + I_0$$

after which the average luminescence lifetime τ was calculated using the formula:

$$\tau = \frac{A_1 \cdot t_1^2 + A_2 \cdot t_2^2}{A_1 \cdot t_1 + A_2 \cdot t_2}$$

# 3. Discussion of the results

## 3.1. Identification of protonated titanates $HLnTiO_4$ and $H_2Ln_2Ti_3O_{10}$

Identification of protonated titanates HLT (HNT) and $HLT_3$ ($HNT_3$), which served as initial materials for the preparation of organic-inorganic derivatives and nanosheets, was carried out using X-ray diffraction, X-ray energy-dispersive spectroscopy and thermogravimetry methods.

Results of X-ray diffraction analysis (Fig. 29) indicate the successful preparation of single-phase protonated forms of the four titanates under study, which do not contain noticeable amounts of any crystalline impurities. All the observed diffraction maxima can be indexed, and the calculated lattice parameters in the tetragonal system (Table 5) are in good agreement with the available literature data [208,228]. That being said, the parameters of La-containing compounds are slightly greater than those of Nd-containing ones, which is explained by the larger crystallographic radius of the first cation. In the case of both alkali and protonated three-layer titanates, the lattice parameter *c* is doubled compared to the interlayer distance *d* due to the relative displacement of adjacent perovskite blocks (staggered conformation). The process of protonation of all the alkaline forms is accompanied by a slight decrease in the value of *d* due to the substitution of large alkaline cations by relatively small protons, which is manifested in the characteristic shift of reflections (00x) to the region of large diffraction angles 2θ.

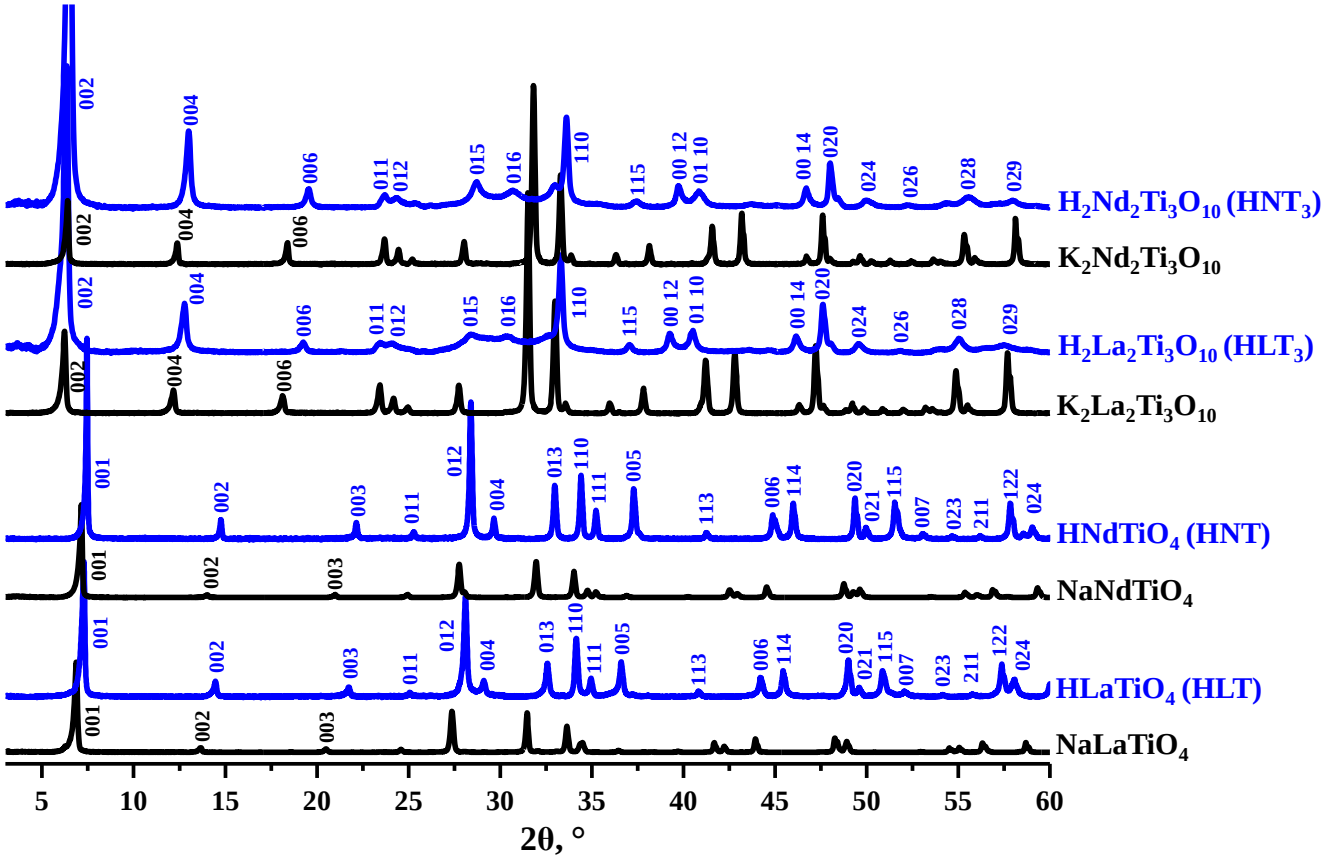


Fig. 29. X-ray diffraction patterns of alkaline and protonated forms of the titanates

Table 5. Lattice parameters in the tetragonal system, interlayer distances *d* and quantitative compositions of the protonated titanates (x is the degree of protonation, y is the degree of hydration)

| Titanate | Structural parameters, Å | | | Compound | | |
|---|---|---|---|---|---|---|
| | *a* | *c* | *d* | Formula | x | y |
| HLT | 3.71 | 12.2 | 12.2 | $HLaTiO_4 \cdot 0.1H_2O$ | 1.00 | 0.10 |
| HNT | 3.68 | 12.1 | 12.1 | $HNdTiO_4 \cdot 0.1H_2O$ | 1.00 | 0.10 |
| $HLT_3$ | 3.79 | 27.2 | 13.6 | $H_{1.9}K_{0.1}La_2Ti_3O_{10} \cdot 0.2H_2O$ | 0.95 | 0.20 |
| $HNT_3$ | 3.78 | 27.2 | 13.6 | $H_{1.9}K_{0.1}Nd_2Ti_3O_{10} \cdot 0.2H_2O$ | 0.95 | 0.20 |

Using X-ray energy-dispersive spectroscopy it was established that the ratio of Ln : Ti cations in the protonated titanates obtained (1 : 1 for HLT, HNT and 2 : 3 for $HLT_3$, $HNT_3$) corresponds to the theoretical one, and residual sodium and potassium are practically absent in the samples. To more accurately determine the degree of protonation, as well as calculate the amount of intercalated water, a thermogravimetric analysis of the protonated titanates was carried out. On the thermogravimetric curves obtained (Fig. 30) two main areas of mass loss can be distinguished. On the first of them, related to the temperature range up to 250–300 °C, deintercalation of interlayer water molecules occurs with the formation of a dehydrated protonated form, which has slightly greater thermal stability in the case of the three-layer

compounds. In the second section, its decomposition takes place, which consists in the binding of interlayer oxygen anions by protons with the release of water and the closure of the vertices of titanium-oxygen octahedra of adjacent perovskite blocks.

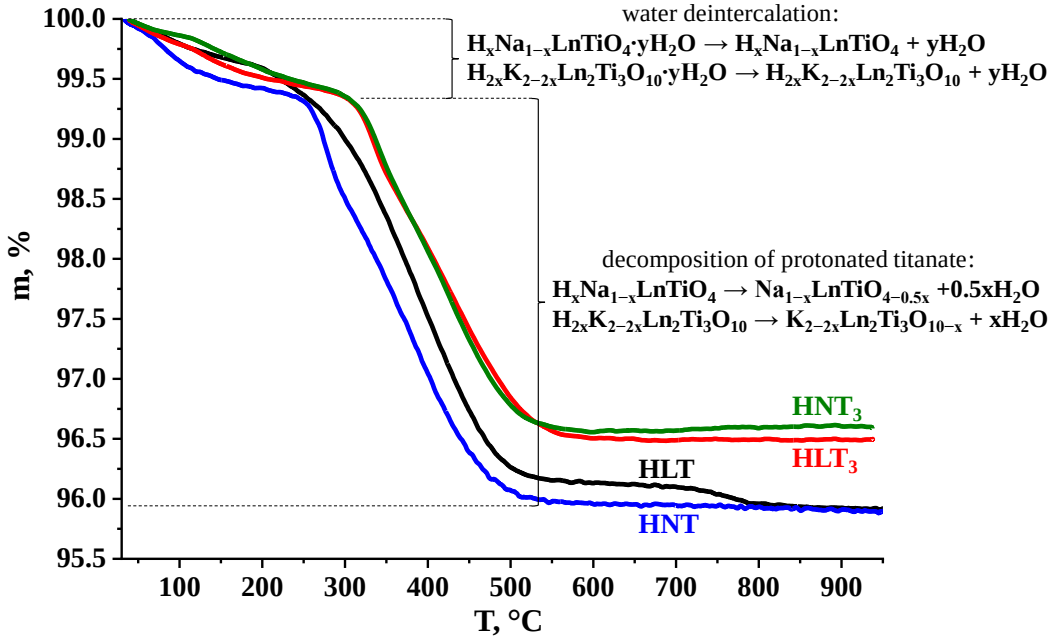


Fig. 30. Thermogravimetric curves of the protonated titanates

The true compositions of the protonated forms, calculated from the aforementioned mass losses, are given in Table 5. In the resulting compounds, complete or almost complete substitution of alkali cations with protons was achieved. The degree of hydration of their interlayer space is quite low, which is generally typical of the Ruddlesden-Popper titanates.

### 3.2. Amine and alcohol derivatives of the titanates as photocatalysts for hydrogen generation

For photocatalytic studies, two series of derivatives were obtained based on each of the titanates: amine ones (with a chain length from methyl Me to *n*-octyl Oc) and alcohol ones (with a chain length from methyl Me to *n*-decyl Dc), which were then systematically studied in the reactions of hydrogen generation from aqueous solutions of methanol, D-glucose, D-xylose, as well as pure water under medium and near ultraviolet radiation. Data on the development and optimization of methods for the synthesis of these compounds were published in the applicant's articles [224–226], and those on photocatalytic properties – in works [229–233].

### 3.2.1. Characterization of the amine and alcohol derivatives

#### 3.2.1.1. Structure and composition of the amine and alcohol derivatives

Successful preparation of amine and alcohol derivatives of the titanates was confirmed by X-ray diffraction analysis data (Fig. 31). Like the initial protonated forms, the organically modified titanates are single-phase crystalline compounds, and all the observed diffraction maxima are indexed in the tetragonal system (hereinafter, only selected indices necessary for discussion are labeled in the figures).

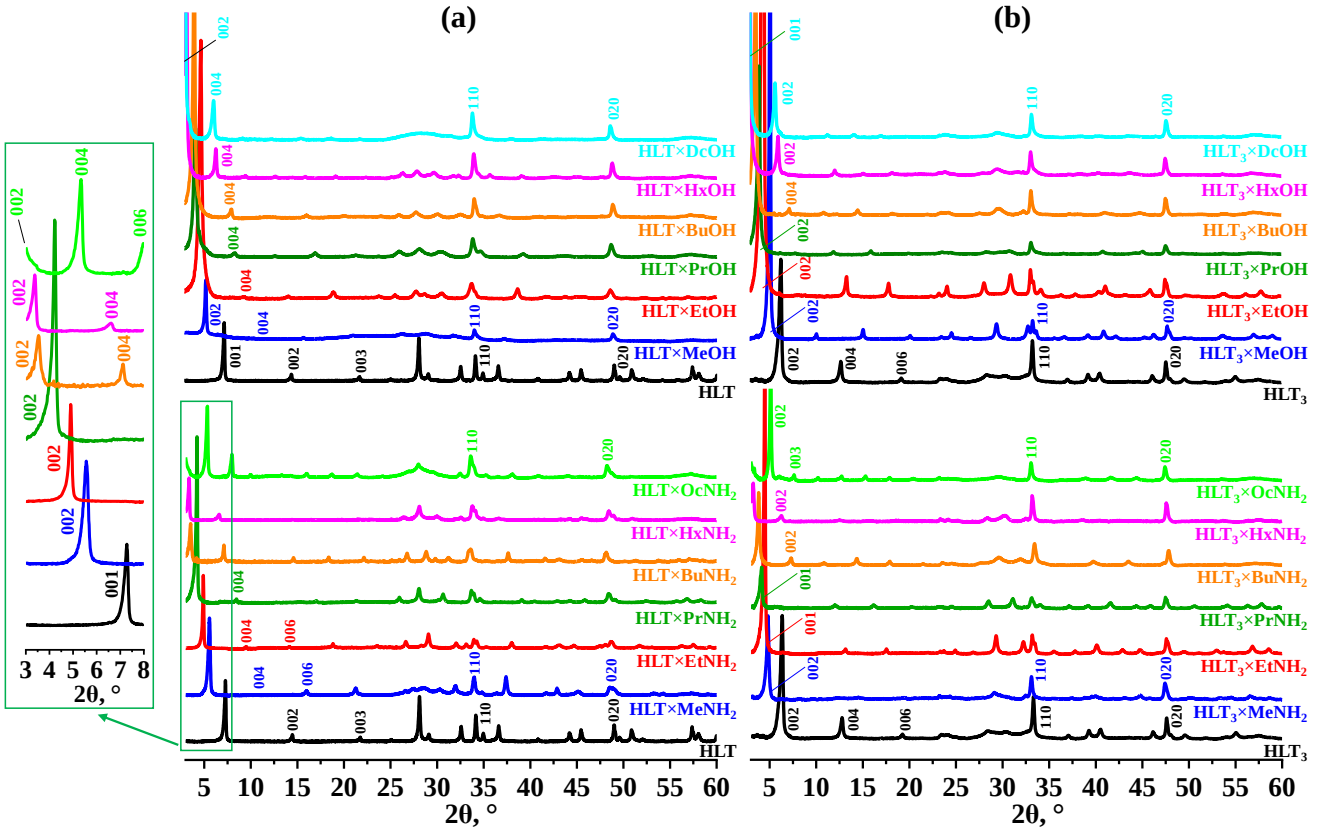


Fig. 31. X-ray diffraction patterns of protonated forms, amine and alcohol derivatives of the titanates HLT (a) and $HLT_3$ (b)

Intercalation of amines and grafting of alcohols in the interlayer space are accompanied by its pronounced expansion, observed by the characteristic shift of reflections (00x) to the low-angle region, proportional to the length of the hydrocarbon chain. This shift corresponds to an increase in the lattice parameter *c* and the directly related interlayer distance *d* (Table 6). At the same time, the position of reflections corresponding to perovskite blocks (in particular, (110), (020)), and, accordingly, the value of the lattice parameter *a* remain practically unchanged, which indicates the preservation of the structure of titanium-oxygen octahedra. In the case of single-layer titanates, all the amine and alcohol derivatives are characterized by a

doubling of the parameter *c* relative to the interlayer distance *d*, whereas for the initial protonated forms these parameters are the same. This fact indicates a probable transition of perovskite blocks, separated by a chemically active interlayer space, from a staggered conformation to eclipsed one. In the case of three-layer titanates, the doubling of the parameter *c* relative to the value of *d*, characteristic of the initial protonated forms, is preserved in the case of methylamine, methanol, ethanol, *n*-propanol and *n*-butanol derivatives, which apparently have a staggered conformation. The diffraction patterns of the other organically modified compounds are fully indexed without doubling the *c* parameter, which indicates a probable eclipsed conformation of their perovskite blocks.

Table 6. Characterization of protonated forms, amine and alcohol derivatives of the titanates: lattice parameters in the tetragonal system *a*, *c*, interlayer distances *d*, average tilt angles of interlayer hydrocarbon chains α, quantitative compositions (presented as $HLnTiO_4 \cdot xRNH_2 \cdot yH_2O$, $H_{1-x}LnTiO_{4-x} \cdot xRO \cdot yH_2O$, $H_2Ln_2Ti_3O_{10} \cdot xRO \cdot yH_2O$ and $H_{2-x}Ln_2Ti_3O_{10-x} \cdot xRO \cdot yH_2O$), specific surface areas S

| Sample | Structure | | | | Composition | | S, $m^2/g$ |
|---|---|---|---|---|---|---|---|
| | *a*, Å | *c*, Å | *d*, Å | α,° | x | y | |
| HLT | 3.71 | 12.2 | 12.2 | – | – | 0.10 | 9.7 |
| HLT×$MeNH_2$ | 3.77 | 33.3 | 16.7 | 77 | 0.35 | 0.45 | 4.0 |
| HLT×$EtNH_2$ | 3.75 | 37.7 | 18.9 | | 0.35 | 0.50 | – |
| HLT×$PrNH_2$ | 3.76 | 41.2 | 20.6 | | 0.35 | 0.30 | – |
| HLT×$BuNH_2$ | 3.76 | 47.8 | 23.9 | | 0.40 | 0.25 | 2.6 |
| HLT×$HxNH_2$ | 3.76 | 54.9 | 27.5 | | 0.35 | 0.45 | – |
| HLT×$OcNH_2$ | 3.78 | 66.3 | 33.2 | | 0.45 | 0.40 | 15 |
| HLT×MeOH | 3.72 | 32.3 | 16.2 | 78 | 0.70 | 0.45 | 17 |
| HLT×EtOH | 3.72 | 36.6 | 18.3 | | 0.40 | 0.50 | – |
| HLT×PrOH | 3.73 | 41.6 | 20.8 | | 0.45 | 0.35 | – |
| HLT×BuOH | 3.73 | 45.6 | 22.8 | | 0.40 | 0.25 | 1.6 |
| HLT×HxOH | 3.74 | 55.4 | 27.7 | | 0.40 | 0.10 | – |
| HLT×DcOH | 3.73 | 56.8 | 28.4 | – | 0.35 | 0.05 | 6.4 |
| HNT | 3.68 | 12.1 | 12.1 | – | – | 0.10 | 8. 5 |
| HNT×$MeNH_2$ | 3.74 | 33.1 | 16.6 | 72 | 0.35 | 0.40 | 5.6 |
| HNT×$EtNH_2$ | 3.74 | 37.6 | 18.8 | | 0.45 | 0.20 | – |
| HNT×$PrNH_2$ | 3.74 | 40.4 | 20.2 | | 0.45 | 0.40 | – |
| HNT×$BuNH_2$ | 3.74 | 47.7 | 23.9 | | 0.45 | 0.30 | 5.6 |
| HNT×$HxNH_2$ | 3.72 | 54.0 | 27.0 | | 0.45 | 0.35 | – |
| HNT×$OcNH_2$ | 3.81 | 65.4 | 32.7 | | 0.45 | 0.40 | 7.7 |
| HNT×MeOH | 3.71 | 32.0 | 16.0 | 75 | 0.75 | 0.40 | 5.0 |
| HNT×EtOH | 3.70 | 36.4 | 18.2 | | 0.50 | 0.30 | – |
| HNT×PrOH | 3.72 | 41.1 | 20.6 | | 0.40 | 0.15 | – |
| HNT×BuOH | 3.71 | 44.5 | 22.3 | | 0.40 | 0.15 | 4.0 |
| HNT×HxOH | 3.71 | 54.9 | 27.5 | | 0.40 | 0.10 | – |
| HNT×DcOH | 3.71 | 58.0 | 29.0 | – | 0.35 | 0.10 | 15 |
| $HLT_3$ | 3.79 | 27.2 | 13.6 | – | – | 0.20 | 3.2 |
| $HLT_3$×$MeNH_2$ | 3.83 | 36.7 | 18.4 | 74 | 0.70 | 0.30 | 3.9 |

| Sample | Structure | | | | Composition | | S, $m^2/g$ |
|---|---|---|---|---|---|---|---|
| | *a*, Å | *c*, Å | *d*, Å | α,° | x | y | |
| $HLT_3$×$EtNH_2$ | 3.82 | 20.2 | 20.2 | | 0.70 | 0.35 | – |
| $HLT_3$×$PrNH_2$ | 3.82 | 21.7 | 21.7 | | 0.65 | 0.20 | – |
| $HLT_3$×$BuNH_2$ | 3.81 | 24.7 | 24.7 | | 0.70 | 0.35 | 4.1 |
| $HLT_3$×$HxNH_2$ | 3.87 | 29.4 | 29.4 | | 0.80 | 0.10 | – |
| $HLT_3$×$OcNH_2$ | 3.85 | 34.2 | 34.2 | | 0.80 | 0.10 | 4.4 |
| $HLT_3$×MeOH | 3.81 | 35.1 | 17.6 | | 1.30 | 0.20 | 5.7 |
| $HLT_3$×EtOH | 3.83 | 39.5 | 19.8 | | 0.85 | 0.40 | – |
| $HLT_3$×PrOH | 3.83 | 44.2 | 22.1 | 79 | 0.75 | 0.20 | – |
| $HLT_3$×BuOH | 3.82 | 48.5 | 24.3 | | 0.70 | 0.20 | 4.2 |
| $HLT_3$×HxOH | 3.82 | 29.2 | 29.2 | | 0.65 | 0.15 | – |
| $HLT_3$×DcOH | 3.82 | 31.3 | 31.3 | – | 0.65 | 0.05 | 5.5 |
| $HNT_3$ | 3.78 | 27.2 | 13.6 | – | – | 0.20 | 3.1 |
| $HNT_3$×$MeNH_2$ | 3.81 | 35.4 | 17.7 | | 0.70 | 0.30 | 3.7 |
| $HNT_3$×$EtNH_2$ | 3.80 | 19.9 | 19.9 | | 0.70 | 0.35 | – |
| $HNT_3$×$PrNH_2$ | 3.78 | 21.5 | 21.5 | | 0.70 | 0.20 | – |
| $HNT_3$×$BuNH_2$ | 3.78 | 24.4 | 24.4 | 71 | 0.75 | 0.35 | 3.9 |
| $HNT_3$×$HxNH_2$ | 3.80 | 29.2 | 29.2 | | 0.90 | 0.10 | – |
| $HNT_3$×$OcNH_2$ | 3.80 | 33.4 | 33.4 | | 0.85 | 0.15 | 4.4 |
| $HNT_3$×MeOH | 3.76 | 34.1 | 17.1 | | 0.95 | 0.25 | 4.5 |
| $HNT_3$×EtOH | 3.77 | 40.9 | 20.5 | | 0.85 | 0.35 | – |
| $HNT_3$×PrOH | 3.79 | 43.8 | 21.9 | 67 | 0.75 | 0.30 | – |
| $HNT_3$×BuOH | 3.78 | 47.3 | 23.7 | | 1.10 | 0.25 | 3.9 |
| $HNT_3$×HxOH | 3.81 | 28.3 | 28.3 | | 0.80 | 0.10 | – |
| $HNT_3$×DcOH | 3.74 | 30.8 | 30.8 | – | 0.65 | 0.05 | 4.7 |

Approximate tilt angles α between the interlayer organic chains and the perovskite block in amine and alcohol derivatives of the titanates were estimated from data on the dependence of the interlayer distance on the number of carbon atoms in the chains (Fig. 32). It was assumed that the chains are in *all-trans*-conformation and parallel to each other. The dependences obtained are conditionally linear for all the studied lengths of organic chains with the exception of R = Dc. That being said, the average increase in the interlayer distance with the insertion of the homologous difference $–CH_2–$ exceeds the theoretically expected increase in the chain length (1.27 Å), which indicates probable formation a bilayer of organic chains in the interlayer space. The calculated tilt angles of the chains (Table 6) fall in the range of 67–79° and are consistent with the literature value α = 75°, found previously for the alcohol derivatives of titanate $HLT_3$ [149]. When moving to the *n*-decanol derivatives, the dependence of the interlayer distance on the hydrocarbon chain length significantly deviates from linearity in a smaller direction, which may indicate both a decrease in the tilt angle relative to the

average value for the series of the alcohol derivatives, and a change in the conformation of the chain.

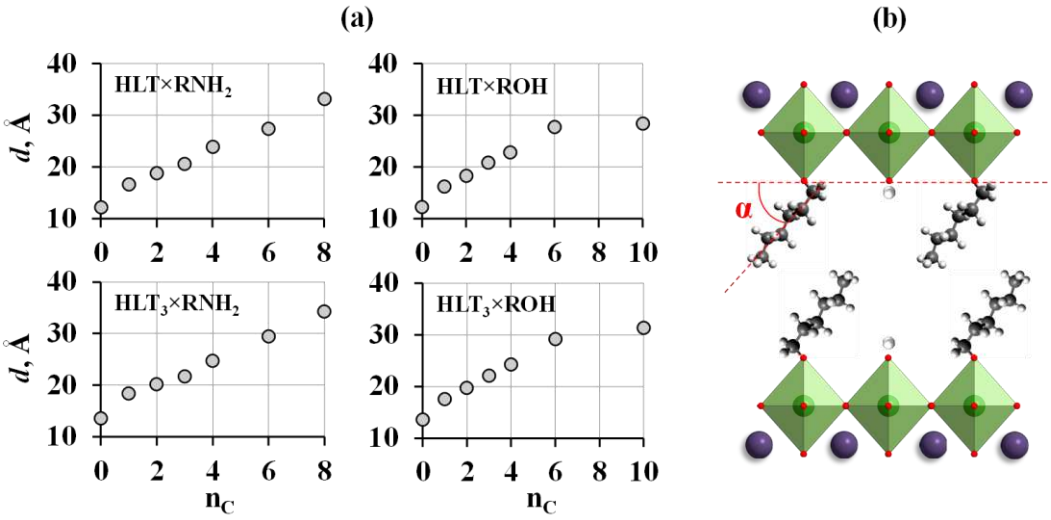


Fig. 32. Dependence of interlayer distance of the amine and alcohol derivatives of the titanates HLT and $HLT_3$ on number of carbon atoms in the modifier chain (a) and a model of the organic bilayer with tilt angle α (b)

The fact of successful preparation of amine and alcohol derivatives of the titanates is also confirmed by the appearance of characteristic signals of incorporated organic components in the Raman spectra of the samples (Fig. 33). In particular, one can observe bands related to bending vibrations of the fragments H–C–O (1170–1180 $cm^{-1}$), C–C–H (1330–1340 $cm^{-1}$), $CH_2$ (1450–1460 $cm^{-1}$) and $NH_2$ (1570–1580 $cm^{-1}$), as well as to stretching of the C–N (1030–1070 $cm^{-1}$), C–O (1040–1070 $cm^{-1}$) and C–H bonds (2800–3050 $cm^{-1}$). At the same time, there are no vibrational bands of hydroxyl groups in the spectra of the alcohol derivatives, which indicates the presence in the interlayer space not of molecular alcohols, but of their covalently bonded alkoxy fragments. The introduction of organic modifiers is also accompanied by a change in the vibrational modes of the terminal (bordering the chemically active interlayer space) titanium-oxygen octahedra. In particular, the vibration band of axial Ti–O bonds directed into the interlayer space (≈ 835 $cm^{-1}$ in single-layer titanates and ≈ 820 $cm^{-1}$ in three-layer titanates) splits into two new ones, located in the region of 720–790 $cm^{-1}$ and 870–910 $cm^{-1}$. The position of the first strongly depends on the specific organic component and shifts to the low-frequency range with increasing length of the hydrocarbon chain. This splitting is apparently explained by the presence in the amine and alcohol derivatives of two types of terminal octahedra with unequal lengths of axial Ti–O bonds containing organic components at the interlayer vertices ($Ti–O^-RNH_3^+$ or Ti−O−R, first band)

and residual protons (Ti–O$^{-}$H$^{+}$, second band). Moreover, in the case of the methanol derivatives, the first band has a significantly higher intensity and is shifted to a greater extent to the low-frequency range (670–690 cm$^{-1}$), while the second is practically invisible. At the same time, the vibrational modes of other Ti–O bonds, not directed into the interlayer space or located in the central octahedra, as well as vibrations in the $(LnO)_2$ layer of single-layer titanates practically do not change.

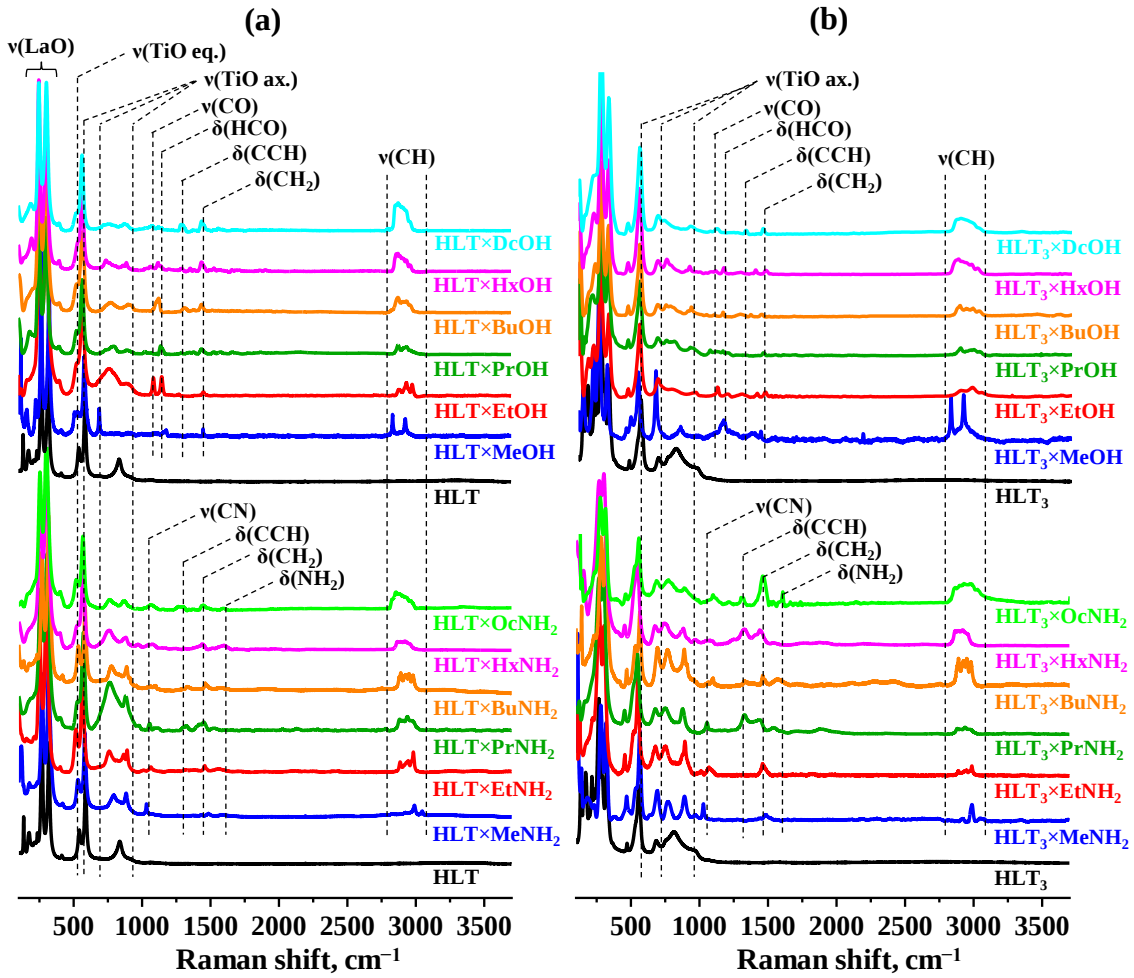


Fig. 33. Raman spectra of protonated forms, amine and alcohol derivatives of the titanates HLT (a) and $HLT_3$ (b)

To confirm the completeness of the substitution of the initial organic modifiers with others during multi-stage syntheses, as well as the nature of their binding to the perovskite matrix, the amine and alcohol derivatives were studied by solid-state $^{13}$C NMR spectroscopy (Fig. 34). It was found that when obtaining derivatives based on methyl- and *n*-butylamine samples, these interlayer amines are completely substituted by the target organic components. In all the amine derivatives, positions of the bands corresponding to the carbon atoms closest to the amino group are shifted by an average of 2 ppm in the high field region compared to the

signals of similar atoms in molecular amines, which indicates the existence of the intercalated compounds in a cationic (alkylammonium) form. In the case of the alcohol derivatives, evidence of the covalent binding of modifiers to the inorganic matrix is the shift of the bands corresponding to the carbon atoms closest to oxygen to the weak field region by 16–19 ppm compared to the bands of similar atoms in molecular alcohols shown in Fig. 34 by a blue dotted line.

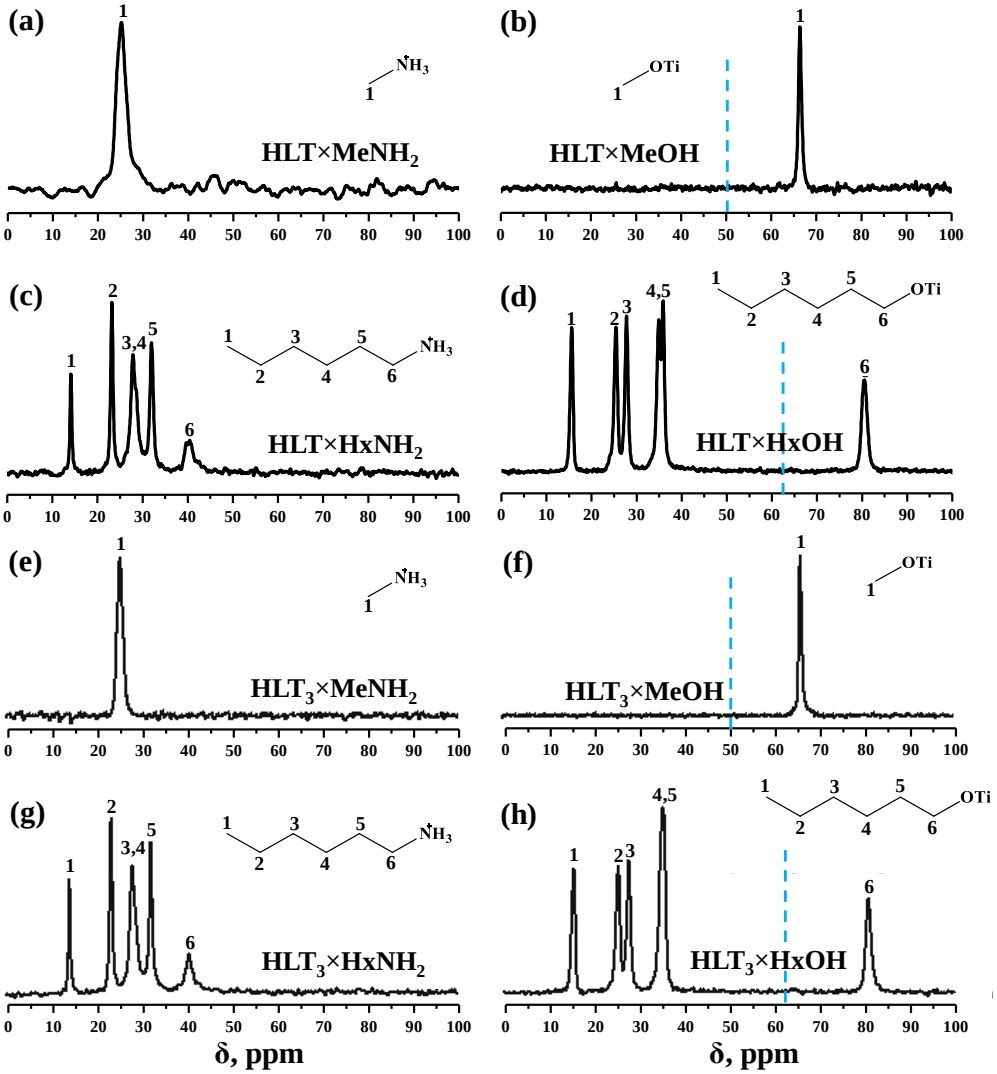


Fig. 34. $^{13}C$ NMR spectra of selected amine and alcohol derivatives of the titanates HLT (a–d) and $HLT_3$ (e–h)

Quantitative compositions of the amine and alcohol derivatives were calculated based on the results of elemental CHN-analysis and thermogravimetry (Table 6). It was found that the total mass loss during thermolysis of the samples is proportional to the chain length (molecular weight) of the organic modifier and most of the resulting derivatives contain on average 0.4–0.5 units of it per proton of the initial titanate. At the same time, no residual nitrogen was detected in the alcohol derivatives, which, along with NMR spectroscopy data,

confirms the complete displacement of the interlayer amines during grafting reactions. The participation of not all interlayer protons in the binding of organic components is explained by the steric blocking of the vertex of the adjacent titanium-oxygen octahedron by the already introduced modifier, noted in the literature [149], and is consistent with the splitting of vibration bands of axial Ti–O bonds, directed into the interlayer space, observed in the Raman spectra (Fig. 33). The exception is methanol derivatives containing up to 0.75 units of the organic component per proton of the initial compound. Apparently, a small size of the methoxy group makes it possible to graft an increased amount of methanol per the titanate formula unit, which may also be one of the reasons for the high intensity of the vibrational bands of Ti–O–Me bonds in the Raman spectra compared to the Ti–$O^-H^+$ bands (Fig. 33). Along with the target organic modifiers, the interlayer space of the amine and alcohol derivatives obtained also contains a certain amount of intercalated water, and the degree of hydration of most organically modified samples, with the exception of the long-chain derivatives of three-layer titanates, exceeds that observed in the case of the initial protonated forms (Table 6).

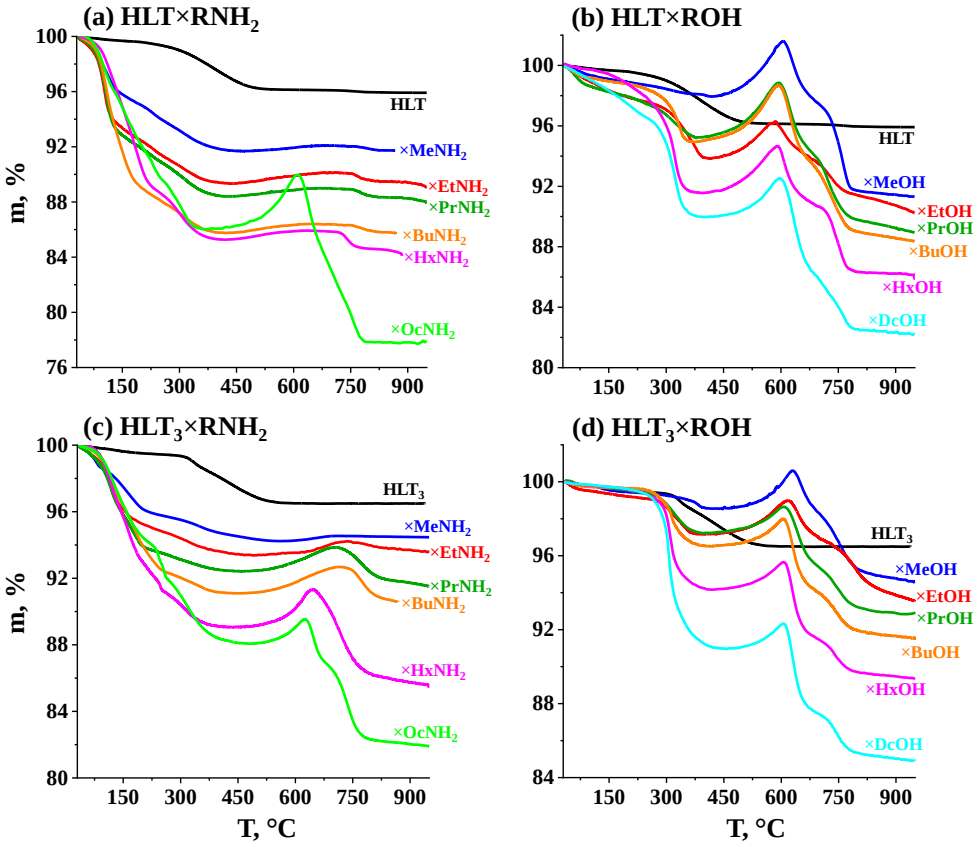


Fig. 35. Thermogravimetric curves of protonated forms, amine and alcohol derivatives of the titanates HLT (a, b) and HLT $_3$ (c, d) measured in an atmosphere of synthetic air

3.2.1.2. Light absorption region and band edge potentials

The range of intrinsic light absorption of the photocatalysts synthesized was studied by diffuse reflectance spectroscopy with the transformation of the recorded spectra into Kubelka-Munk coordinates (Fig. 36). As follows from the data obtained (Table 7), the optical bandgap energy $E_g$ of the initial protonated titanates is 3.45–3.48 eV, which allows them to use mid- and partly near-ultraviolet radiation in photocatalytic reactions. That being said, the light absorption of the La-containing titanates is due exclusively to the interband transition, and the corresponding compounds are uncolored (white) powders. The Nd-containing titanates additionally exhibit a number of absorption bands in the visible spectrum region associated with the partial filling of the 4f-orbitals, which explains a lilac color of the samples.

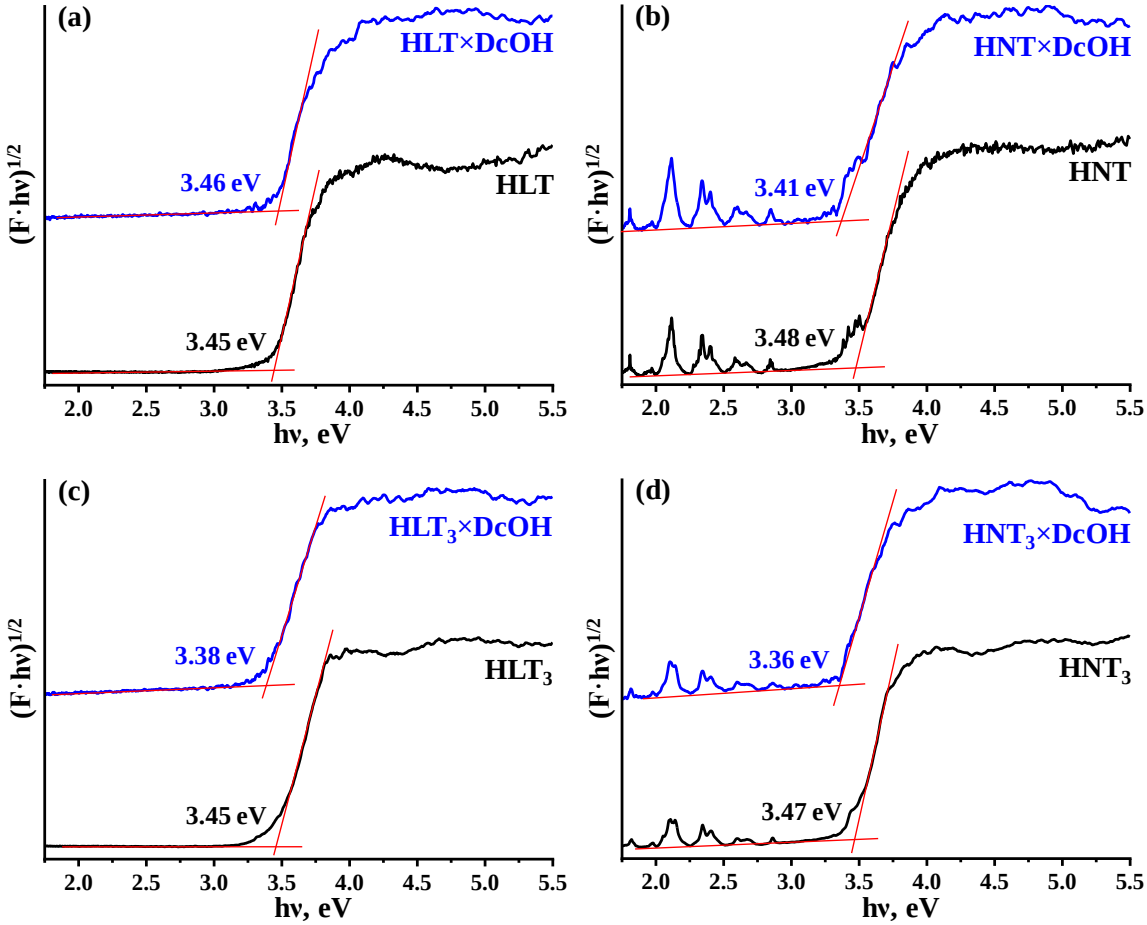


Fig. 36. Kubelka-Munk plots for protonated forms and *n*-decanol derivatives of the titanates

Formation of amine and alcohol derivatives of the titanates is accompanied by neither a change in the general appearance of the spectra nor manifestation of new absorption bands (Fig. 36). The observed change in the optical bandgap energy does not exceed 0.16 eV in absolute value and does not clearly correlate with the length of the interlayer organic modifier.

However, in the case of three-layer titanates, all the products of organic modification are characterized by a slightly lower $E_g$ value compared to the initial protonated forms. That being said, the long-wavelength edges of the intrinsic light absorption of amine and alcohol derivatives of the same titanate turn out to be quite close with equal chain lengths of the organic components (Table 7). In general, the spectral region of functioning of the amine and alcohol derivatives, as well as the initial protonated compounds, remains the middle and near ultraviolet.

Table 7. Characterization of protonated forms, amine and alcohol derivatives of the titanates: range of intrinsic absorption (optical bandgap energy $E_g$, long-wave absorption edge $\lambda_{max}$), approximate potentials of the energy band edges (valence band top $E_V$ and conduction band bottom $E_C$) relative to the SHE, maxima $\lambda_{lum}$ and average luminescence lifetimes $\tau$ upon excitation at a wavelength of 265 nm

| Sample | Light absorption | | Band edges (≈) | | Luminescence | |
|---|---|---|---|---|---|---|
| | $E_g$, eV | $\lambda_{max}$, nm | $E_V$, V | $E_C$, V | $\lambda_{lum}$, nm | $\tau$, μs |
| HLT | 3.45 | 359 | 3.0 | −0.5 | 360 | 4.70 |
| HLT×$MeNH_2$ | 3.58 | 346 | | | | |
| HLT×$EtNH_2$ | 3.48 | 356 | | | | |
| HLT×$PrNH_2$ | 3.50 | 354 | | | | |
| HLT×$BuNH_2$ | 3.61 | 343 | | | | |
| HLT×$HxNH_2$ | 3.47 | 357 | | | | |
| HLT×$OcNH_2$ | 3.49 | 355 | | | | |
| HLT×MeOH | 3.47 | 357 | – | – | – | – |
| HLT×EtOH | 3.47 | 357 | | | | |
| HLT×PrOH | 3.45 | 359 | | | | |
| HLT×BuOH | 3.45 | 359 | | | | |
| HLT×HxOH | 3.46 | 358 | | | | |
| HLT×DcOH | 3.46 | 358 | | | | |
| HNT | 3.48 | 356 | 2.9 | -0.6 | 360 | 4.77 |
| HNT×$MeNH_2$ | 3.41 | 364 | | | | |
| HNT×$EtNH_2$ | 3.50 | 354 | | | | |
| HNT×$PrNH_2$ | 3.43 | 362 | | | | |
| HNT×$BuNH_2$ | 3.50 | 354 | | | | |
| HNT×$HxNH_2$ | 3.42 | 363 | | | | |
| HNT×$OcNH_2$ | 3.45 | 359 | | | | |
| HNT×MeOH | 3.42 | 363 | – | – | – | – |
| HNT×EtOH | 3.39 | 366 | | | | |
| HNT×PrOH | 3.45 | 359 | | | | |
| HNT×BuOH | 3.45 | 359 | | | | |
| HNT×HxOH | 3.41 | 364 | | | | |
| HNT×DcOH | 3.41 | 364 | | | | |
| $HLT_3$ | 3.45 | 359 | 3.0 | −0.5 | 370 | 4.73 |
| $HLT_3$×$MeNH_2$ | 3.34 | 371 | | | | |
| $HLT_3$×$EtNH_2$ | 3.39 | 366 | | | | |
| $HLT_3$×$PrNH_2$ | 3.40 | 365 | – | – | – | – |
| $HLT_3$×$BuNH_2$ | 3.42 | 363 | | | | |
| $HLT_3$×$HxNH_2$ | 3.41 | 364 | | | | |

| Sample | Light absorption | | Band edges (≈) | | Luminescence | |
|---|---|---|---|---|---|---|
| | $E_g$, eV | $\lambda_{max}$, nm | $E_V$, V | $E_C$, V | $\lambda_{lum}$, nm | τ, μs |
| $HLT_3$×$OcNH_2$ | 3.40 | 365 | 2.9 | −0.5 | 410 | 5.65 |
| $HLT_3$×MeOH | 3.33 | 372 | – | – | – | – |
| $HLT_3$×EtOH | 3.41 | 364 | | | | |
| $HLT_3$×PrOH | 3.38 | 367 | | | | |
| $HLT_3$×BuOH | 3.40 | 365 | | | | |
| $HLT_3$×HxOH | 3.40 | 365 | | | | |
| $HLT_3$×DcOH | 3.38 | 367 | 2.9 | −0.5 | 410 | 5.30 |
| $HNT_3$ | 3.47 | 357 | 2.9 | −0. 6 | 370 | 5.42 |
| $HNT_3$×$MeNH_2$ | 3.40 | 365 | – | – | – | – |
| $HNT_3$×$EtNH_2$ | 3.32 | 373 | | | | |
| $HNT_3$×$PrNH_2$ | 3.33 | 372 | | | | |
| $HNT_3$×$BuNH_2$ | 3.33 | 372 | | | | |
| $HNT_3$×$HxNH_2$ | 3.35 | 370 | | | | |
| $HNT_3$×$OcNH_2$ | 3.36 | 369 | 2.8 | −0.6 | 410 | 6.39 |
| $HNT_3$×MeOH | 3.33 | 372 | – | – | – | – |
| $HNT_3$×EtOH | 3.33 | 372 | | | | |
| $HNT_3$×PrOH | 3.32 | 373 | | | | |
| $HNT_3$×BuOH | 3.33 | 372 | | | | |
| $HNT_3$×HxOH | 3.35 | 370 | | | | |
| $HNT_3$×DcOH | 3.36 | 369 | 2.8 | −0.6 | 410 | 6.18 |

To confirm the fact of the thermodynamic allowance of hydrogen evolution reactions on the photocatalysts synthesized, the approximate potentials of the energy bands edges relative to the SHE were assessed using UPS and XPS data (Fig. 37). As a result, it was established (Table 7) that the conduction band bottom $E_C$ of the samples lies significantly higher (is more negative) than the standard potential for the reduction of protons to hydrogen, which makes the corresponding photocatalytic process allowed from a thermodynamic point of view. At the same time, the valence band top $E_V$ lies significantly lower (is more positive) than the reduction potential of the half-reaction of oxygen formation from water, and even lower than the oxidation potentials of most organic compounds (in particular, bioalcohols and carbohydrates). Thus, the resulting photocatalysts fully satisfy the thermodynamic criteria for the feasibility of the reactions of pure water splitting and dehydrogenation of organic compounds isolated from plant biomass.

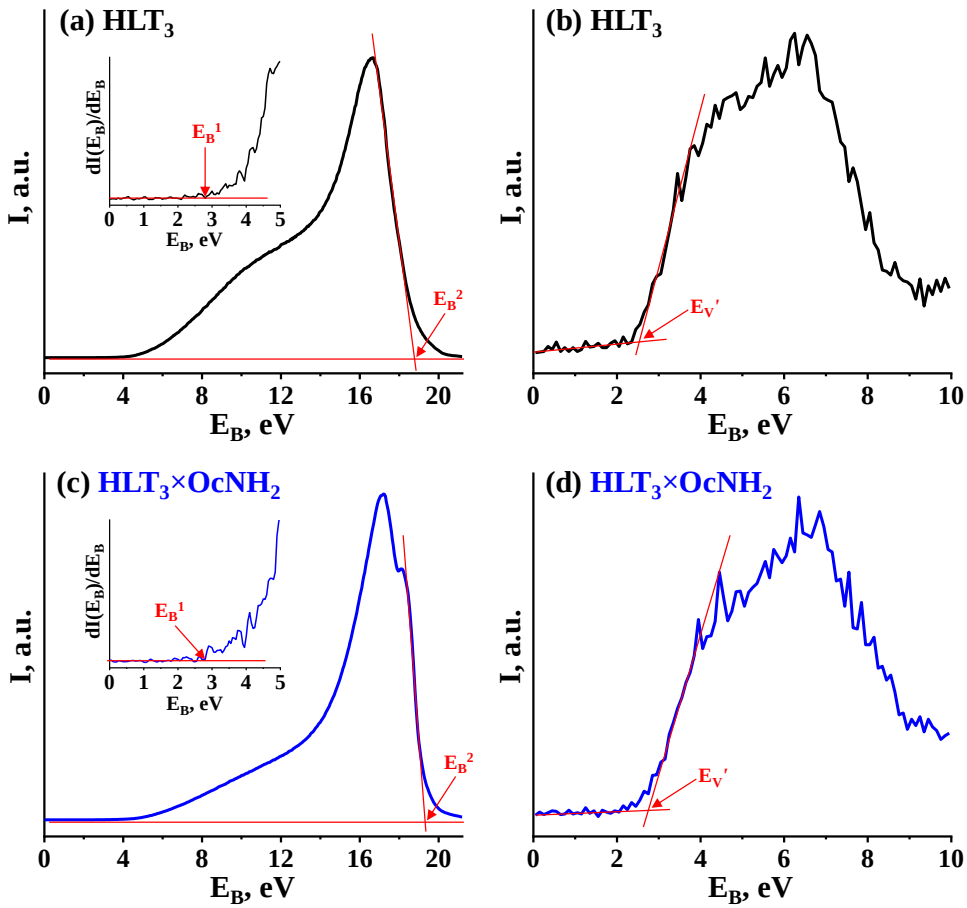


Fig. 37. UPS and XPS of the valence band of the protonated titanate $HLT_3$ (a, b) and its *n*-octylamine derivative (c, d)

The slight narrowing of the band gap observed during the formation of a number of amine and alcohol derivatives of the titanates is apparently explained by a corresponding increase in energy of the valence band top, formed predominantly by 2p-orbitals of oxygen [234], due to the electronic effects of the organic modifiers associated with the perovskite matrix. At the same time, the position of the conduction band bottom, formed mainly by vacant 3d-orbitals of titanium [234], remains practically unchanged.

### 3.2.1.3. Average luminescence lifetimes

An average lifetime of luminescence excited in the intrinsic light absorption range of photocatalysts may serve as an indirect measure of the lifetime of photogenerated electron-hole pairs under the assumption that their recombination is predominantly radiative [235]. In the framework of this study, the luminescence spectra and its decay curves (Fig. 38) were recorded upon excitation at a wavelength of 265 nm, which falls within the intrinsic absorption region of all the samples under consideration. The studies were carried out using the example of the initial protonated titanates and their selected derivatives with the longest interlayer modifiers.

It was shown that protonated titanates have a luminescence maximum at 360–370 nm, which shifts to ≈ 410 nm during the intercalation of n-octylamine and grafting of n-decanol (Table 7), and its decay curves are well approximated by a decreasing biexponential function. The average luminescence lifetime of the protonated titanates is 4.73–5.42 μs, significantly exceeding that observed in the case of the reference photocatalyst $TiO_2$ P25 Degussa (1.94 μs). After organic modification of the titanates, it increases by 1.1–1.2 times, reaching a value of 6.39 μs. The data obtained indicate that the structure of layered perovskites provides more efficient separation and, accordingly, a lower recombination rate of photogenerated charge carriers, and the introduction of the above-mentioned organic modifiers also has a beneficial effect on their average lifetime.

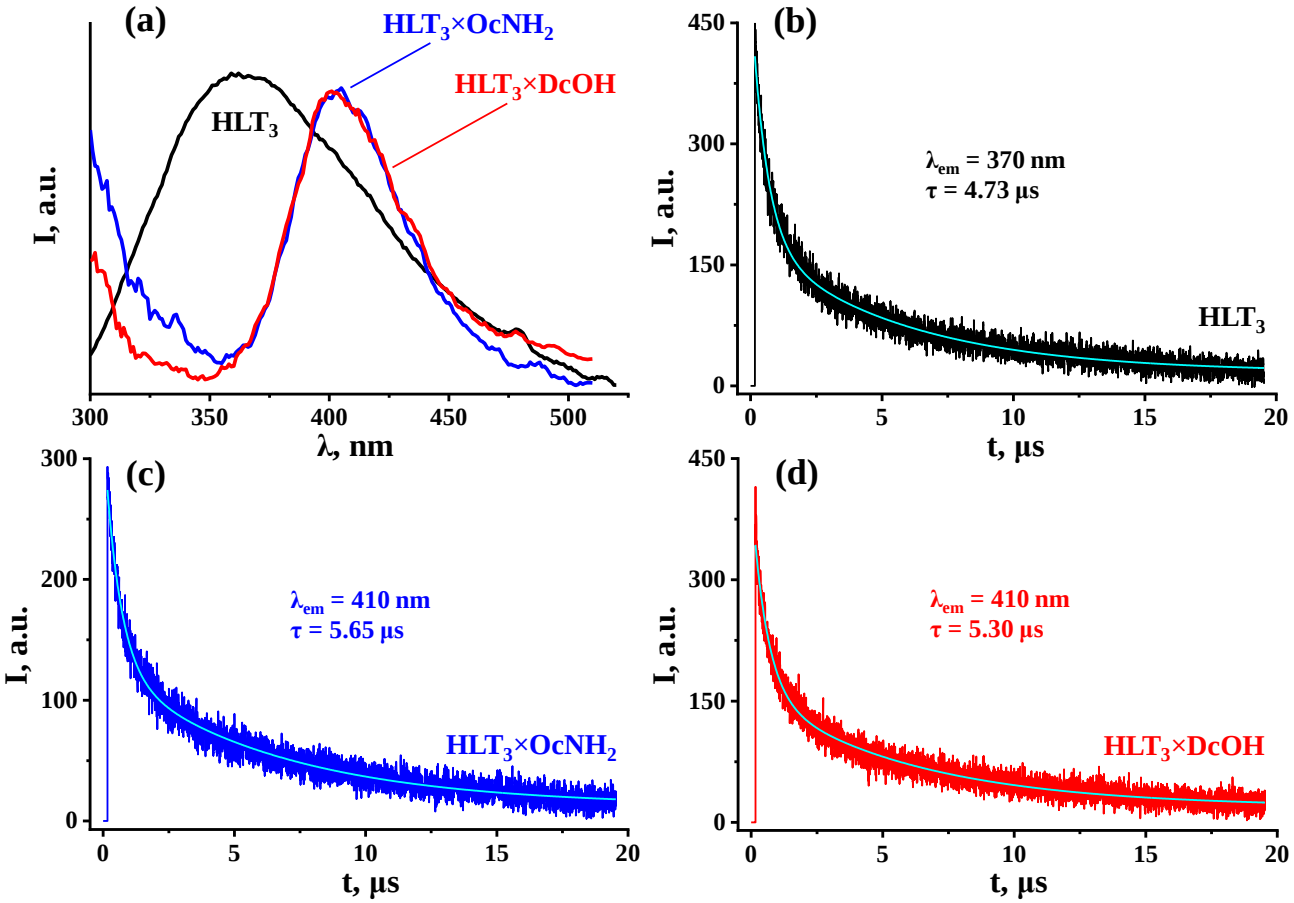


Fig. 38. Luminescence spectra (a) and its decay curves (b–d) for the protonated titanate $HLT_3$, its *n*-octylamine and *n*-decanol derivatives upon excitation at a wavelength of 265 nm

3.2.1.4. Morphology and specific surface area

Study of the morphology of the photocatalysts obtained by means of SEM (Fig. 39) showed that the particles of both the initial protonated titanates and the products of their organic modification have a predominantly lamellar shape, being typical of layered materials.

Moreover, the samples show pronounced polydispersity: the linear sizes of the particles are in the range of 0.5–4 μm, and their thickness is 200–600 nm. Upon the introduction of organic components, the proportion of relatively small particles (up to 1 μm) increases, which is probably a result of their separation from larger ones during ultrasonic treatment of the precursors in an aqueous solution of methylamine and subsequent chemical transformations. In the case of several amine and alcohol derivatives, partial delamination of polycrystals with the formation of noticeable slits is also observed.

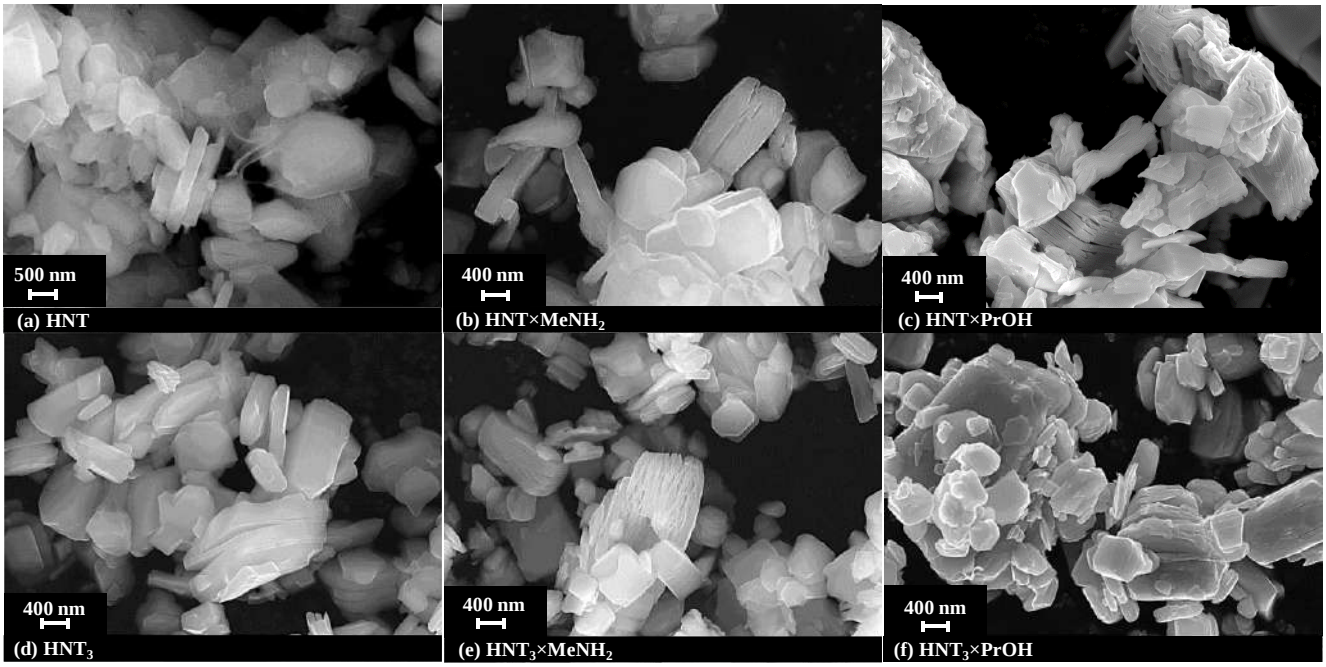


Fig. 39. SEM images of protonated forms, methylamine and *n*-propanol derivatives of the titanates HNT (a–c) and $HNT_3$ (d–f)

Specific surface area of the protonated single-layer and three-layer titanates, measured by the BET method, is ≈ 9 $m^2/g$ and ≈ 3 $m^2/g$, respectively (Table 6), which is a relatively low value for heterogeneous photocatalysts (in particular, $TiO_2$ P 25 Degussa has a specific surface area of ≈ 50 $m^2/g$). The small specific surface area of the compounds under consideration is largely determined by the high-temperature ceramic technology for the synthesis of their alkaline precursors $NaLnTiO_4$ and $K_2Ln_2Ti_3O_{10}$, which makes it possible to achieve high crystallinity, but causes intense particle intergrowth. At the same time, the single-layer protonated titanates have a specific surface area exceeding that of their three-layer analogues by almost 3 times, which may be due, among other things, to the lower temperature of the synthesis of their precursors $NaLnTiO_4$ (825 °C) compared to $K_2Ln_2Ti_3O_{10}$ (1100 °C). The organic modification in some cases leads to an increase in the specific surface area by 1.5–1.8

times, however, this increase does not occur for all the derivatives studied and its obvious correlation with the chain length of the organic modifier is not seen. At the same time, among both the single-layer and three-layer compounds, the most developed surface is observed in the case of the methanol samples (17 $m^2/g$ for HLT×MeOH and 5.7 $m^2/g$ for $HLT_3$×MeOH).

3.2.2. Photocatalytic activity of the amine and alcohol derivatives in hydrogen generation reactions

Photocatalytic activity of all the obtained amine and alcohol derivatives was studied in the reaction of hydrogen evolution from a 1% (mol.) aqueous solution of methanol under the radiation of a DRT-125 mercury lamp ($\lambda > 220$ nm) both without additional modification and with the reduction of 1% Pt nanoparticles on the surface as a cocatalyst. Using several samples as an example, the dependence of the activity on methanol concentration, photocatalyst loading, and mass fraction of the cocatalyst was studied. Selected derivatives were also tested in 1 % (mol.) aqueous solutions of D-glucose, D-xylose and in pure water. In all cases, the quantitative indicators of photocatalytic activity were the absolute ω and normalized per unit photocatalyst mass hydrogen evolution rate ω′, apparent quantum efficiency φ, as well as the factor of increase in the reaction rate upon platinization of the surface $k_{Pt}$. Additionally, during photocatalytic measurements, the actual volume concentration of the photocatalysts in suspensions, pH of the medium, and, in some cases, the chemical composition of the reaction solutions were also monitored.

3.2.2.1. Activity of $HLnTiO_4$ derivatives in a 1% (mol.) aqueous methanol solution

Kinetic curves of photocatalytic hydrogen generation in the presence of the single-layer titanates and their amine and alcohol derivatives are presented in Fig. 40, the values of their photocatalytic activity are summarized in Table 8 and visualized as bar graphs in Fig. 41. As can be seen from the data in Fig. 40, the kinetic curves of hydrogen production are in most cases linear or deviate slightly from linearity, indicating the maintenance of a relatively constant rate of the target reaction. When the radiation source is turned off (dark stage), all the curves reach a plateau, corresponding to a zero hydrogen generation rate.

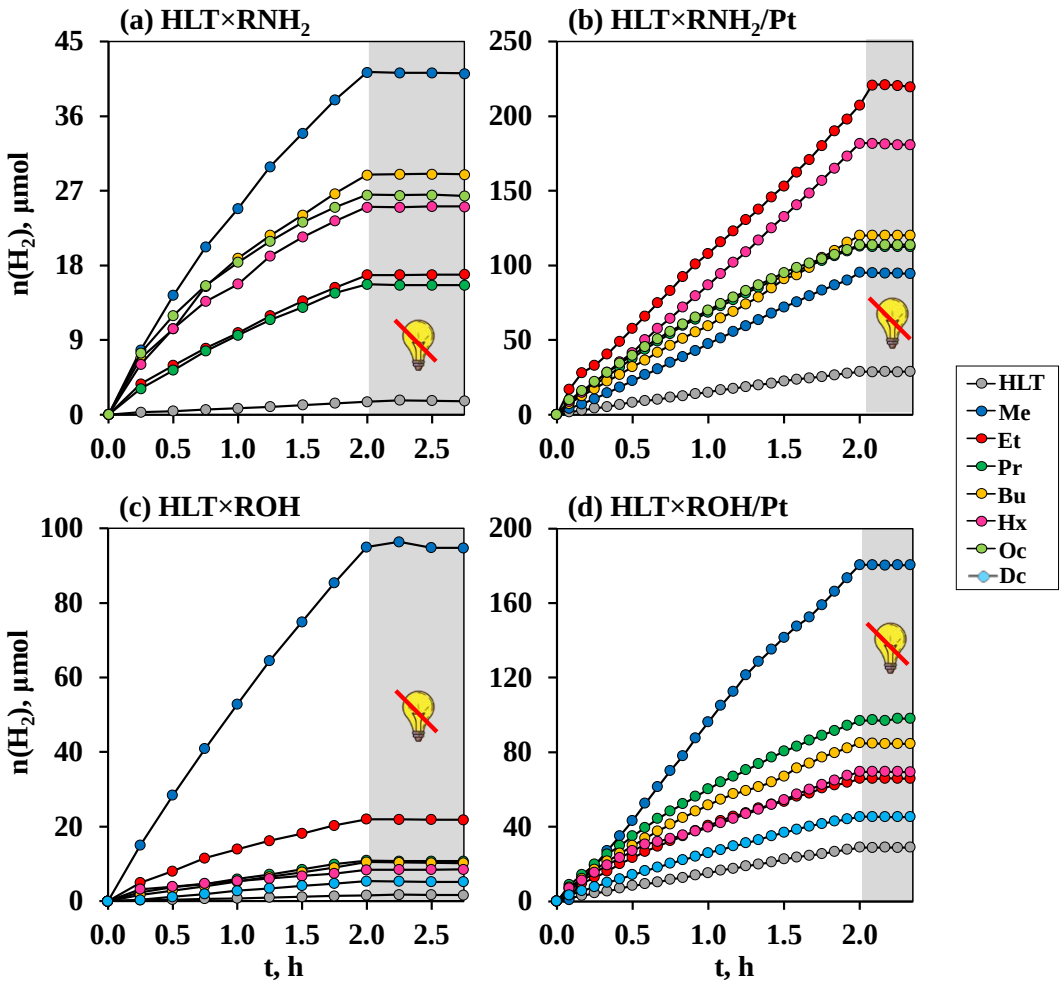


Fig. 40. Kinetic curves of photocatalytic hydrogen evolution from a 1% (mol.) aqueous solution of methanol in the presence of protonated form, amine and alcohol derivatives of the titanate HLT

The efficiency of hydrogen generation in the presence of the protonated titanates is relatively low (φ = 0.01%) and is equal in the case of the both samples. However, when the surface is modified with a platinum cocatalyst, the La-containing titanate (φ = 0.19%) proves to be more than 2 times more active than the Nd-containing analogue (φ = 0.083%). The role of the cocatalyst in this case is to reduce the overpotential of hydrogen evolution, as well as to decrease the intensity of surface recombination of photogenerated charge carriers and prevent the occurrence of undesirable reverse reactions due to the spatial separation of reducing and oxidizing centers between Pt nanoparticles and the unmodified titanate surface, respectively.

All amine and alcohol derivatives of the single-layer titanates demonstrate a significantly higher rate of photocatalytic hydrogen evolution from the aqueous solution of methanol compared to the initial protonated forms (Table 8, Fig. 41), and after organic modification the difference in the activity of La- and Nd-containing samples becomes more pronounced. This difference is consistent with the literature data on the photocatalytic activity

of the titanates HLT, HNT and their thermolysis products in the reaction of hydrogen evolution from an aqueous solution of isopropanol, according to which the La-containing samples are 2–4 times superior to the Nd-containing analogues [213].

Table 8. Photocatalytic activity of protonated forms, amine and alcohol derivatives of the titanates HLT and HNT in the reaction of hydrogen evolution from a 1% (mol.) aqueous solution of methanol: absolute and normalized rates of hydrogen generation ω and ω′, apparent quantum efficiency φ, factor of increase in the rate after platinization $k_{Pt}$

| Photocatalyst | ω, μmol·h$^{-1}$ | ω′, mmol·h$^{-1}$·g$^{-1}$ | φ, % | $k_{Pt}$ |
|---|---|---|---|---|
| HLT | 0.73 | 0.029 | 0.010 | – |
| HLT/Pt | 14.2 | 0.57 | 0.19 | 19 |
| HLT×$MeNH_2$ | 22.8 | 0.91 | 0.31 | – |
| HLT×$MeNH_2$/Pt | 48.2 | 1.93 | 0.65 | 2.1 |
| HLT×$EtNH_2$ | 8.20 | 0.33 | 0.11 | – |
| HLT×$EtNH_2$/Pt | 97.9 | 3.92 | 1.31 | 12 |
| HLT×$PrNH_2$ | 7.26 | 0.29 | 0.10 | – |
| HLT×$PrNH_2$/Pt | 69.6 | 2.78 | 0.93 | 9.6 |
| HLT×$BuNH_2$ | 12.6 | 0.50 | 0.17 | – |
| HLT×$BuNH_2$/Pt | 56.6 | 2.26 | 0.76 | 4.5 |
| HLT×$HxNH_2$ | 15.2 | 0.61 | 0.20 | – |
| HLT×$HxNH_2$/Pt | 90.6 | 3.62 | 1.21 | 6.0 |
| HLT×$OcNH_2$ | 18.1 | 0.72 | 0.24 | – |
| HLT×$OcNH_2$/Pt | 72.1 | 2.88 | 0.96 | 4.0 |
| HLT×MeOH | 50.3 | 2.01 | 0.67 | – |
| HLT×MeOH/Pt | 102 | 4.08 | 1.37 | 2.0 |
| HLT×EtOH | 13.2 | 0.53 | 0.18 | – |
| HLT×EtOH/Pt | 37.7 | 1.51 | 0.50 | 2.9 |
| HLT×PrOH | 4.92 | 0.20 | 0.066 | – |
| HLT×PrOH/Pt | 59.4 | 2.38 | 0.80 | 12 |
| HLT×BuOH | 4.98 | 0.20 | 0.067 | – |
| HLT×BuOH/Pt | 52.5 | 2.10 | 0.70 | 10 |
| HLT×HxOH | 2.89 | 0.12 | 0.039 | – |
| HLT×HxOH/Pt | 47.2 | 1.89 | 0.63 | 16 |
| HLT×DcOH | 3.25 | 0.13 | 0.043 | – |
| HLT×DcOH/Pt | 24.6 | 0.98 | 0.33 | 7.6 |
| HNT | 0.73 | 0.029 | 0.010 | – |
| HNT/Pt | 6.23 | 0.25 | 0.083 | 8.5 |
| HNT×$MeNH_2$ | 1.10 | 0.044 | 0.014 | – |
| HNT×$MeNH_2$/Pt | 16.3 | 0.65 | 0.22 | 15 |
| HNT×$EtNH_2$ | 1.14 | 0.046 | 0.015 | – |
| HNT×$EtNH_2$/Pt | 10.9 | 0.44 | 0.15 | 10 |
| HNT×$PrNH_2$ | 2.23 | 0.089 | 0.030 | – |
| HNT×$PrNH_2$/Pt | 23.3 | 0.93 | 0.31 | 10 |
| HNT×$BuNH_2$ | 1.14 | 0.046 | 0.015 | – |
| HNT×$BuNH_2$/Pt | 12.3 | 0.49 | 0.16 | 11 |
| HNT×$HxNH_2$ | 1.15 | 0.046 | 0.015 | – |
| HNT×$HxNH_2$/Pt | 22.2 | 0.89 | 0.30 | 20 |
| HNT×$OcNH_2$ | 1.14 | 0.046 | 0.015 | – |

| Photocatalyst | ω, μmol·h$^{-1}$ | ω′, mmol·h$^{-1}$·g$^{-1}$ | φ, % | $k_{Pt}$ |
|---|---|---|---|---|
| HNT×OcNH$_2$/Pt | 28.2 | 1.13 | 0.38 | 25 |
| HNT×MeOH | 12.6 | 0.50 | 0.17 | – |
| HNT×MeOH/Pt | 40.1 | 1.60 | 0.54 | 3.2 |
| HNT×EtOH | 6.72 | 0.27 | 0.090 | – |
| HNT×EtOH/Pt | 16.4 | 0.66 | 0.22 | 2.4 |
| HNT×PrOH | 3.26 | 0.13 | 0.043 | – |
| HNT×PrOH/Pt | 34.5 | 1.38 | 0.46 | 11 |
| HNT×BuOH | 3.00 | 0.12 | 0.040 | – |
| HNT×BuOH/Pt | 27.0 | 1.08 | 0.36 | 9.0 |
| HNT×HxOH | 1.62 | 0.065 | 0.022 | – |
| HNT×HxOH/Pt | 21.2 | 0.85 | 0.28 | 14 |
| HNT×DcOH | 9.28 | 0.37 | 0.12 | – |
| HNT×DcOH/Pt | 35.3 | 1.41 | 0.47 | 3.8 |

The most photocatalytically active in the series of non-platinized amine derivatives HLT×RNH$_2$ is the methylamine titanate (φ = 0.31%) and in the HNT×RNH$_2$ series – *n*-propylamine one (φ = 0.030%). After modifying the surface of the samples with Pt nanoparticles as a cocatalyst, the dependence of photocatalytic activity on the interlayer amine changes, and in the HLT×RNH$_2$/Pt series the ethylamine derivative becomes the most active (φ = 1.31%), while in the HNT×RNH$_2$/Pt series – *n*-octylamine one (φ = 0.38%). Among the non-platinized alcohol derivatives HLT×ROH and HNT×ROH, the methanol titanates provide the maximum efficiency of hydrogen generation (φ = 0.67% and 0.17%, respectively). When the surface is modified with a platinum cocatalyst, the activity maxima in both series of the alcohol derivatives do not shift and still correspond to the methanol samples (φ = 1.37% for La-containing and φ = 0.54% for Nd-containing). In general, according to the data obtained, the most promising of the considered photocatalytic materials based on the single-layer titanates are the platinized ethylamine and methanol derivatives HLT×EtNH$_2$/Pt and HLT×MeOH/Pt, the activity of which in 1% (mol.) aqueous methanol is 3.92 mmol·h$^{-1}$·g$^{-1}$ (1.31%) and 4.08 mmol·h$^{-1}$·g$^{-1}$ (1.37%), respectively.

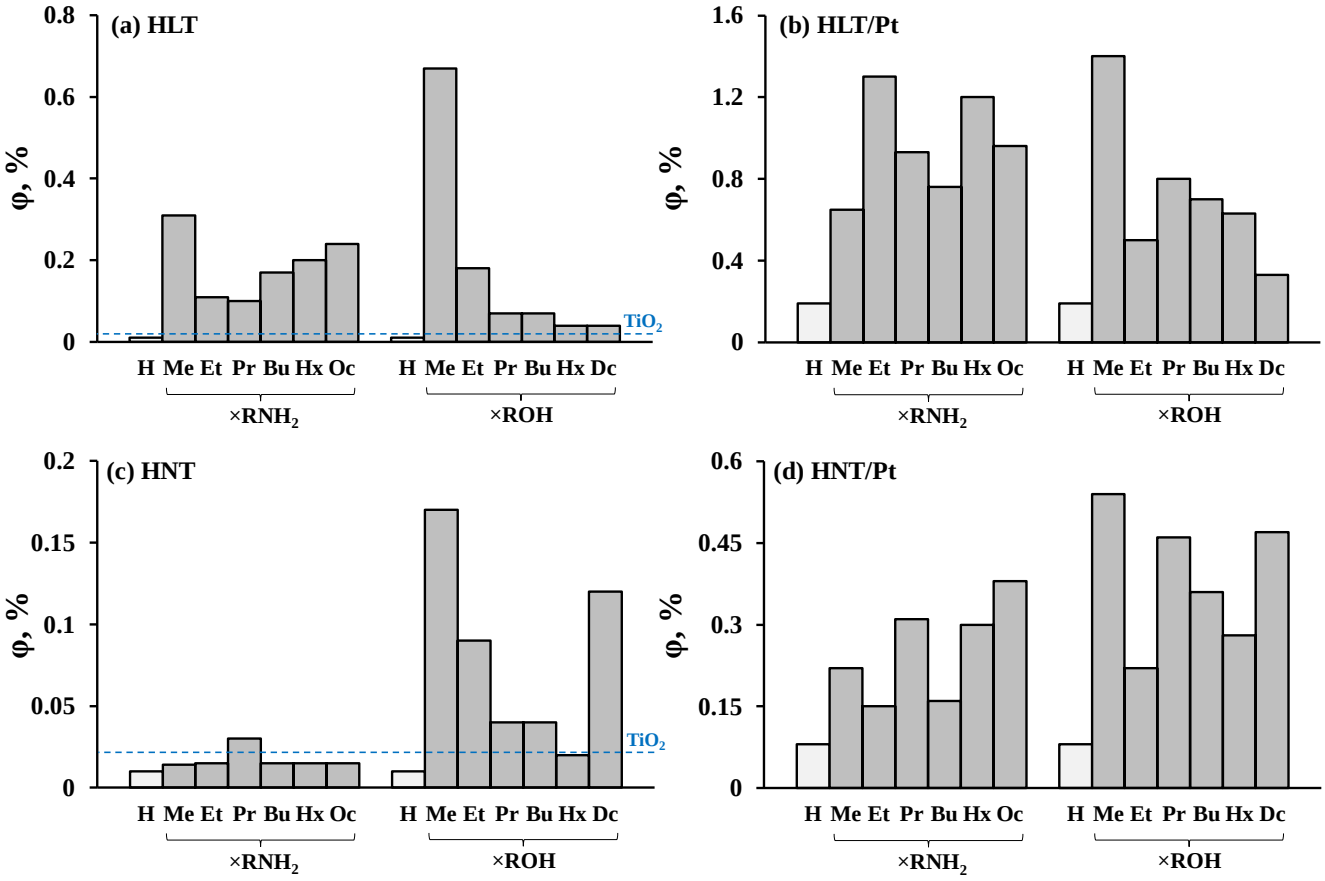


Fig. 41. Comparison of apparent quantum efficiency of photocatalytic hydrogen evolution from a 1 mol. % aqueous methanol solution in the presence of protonated forms, amine and alcohol derivatives of the titanates HLT and HNT

Thus, the organic modification of the single-layer titanates turned out to be an effective approach to increasing their photocatalytic activity in the reactions of hydrogen evolution from aqueous methanol solutions: the resulting derivatives are up to 68 times more active than the initial protonated compounds, as well as up to 29 times – than a «gold standard» in photocatalysis $TiO_2$ P25 Degussa, demonstrating under the same conditions an apparent quantum efficiency of $\varphi = 0.023\%$.

At the same time, photocatalytic activity of the amine and alcohol derivatives does not clearly correlate with the chain length of the interlayer organic modifiers (Fig. 41) and, apparently, is predetermined by the simultaneous influence of a number of different structural-chemical factors. The increased activity of several compounds (in particular, HLT×MeOH and HNT×DcOH) may be due, among other things, to the relatively large specific surface area (Table 6), however, the value of the latter does not explain the experimental trends in the activity changes in general. A more probable reason for the multiple increase in the activity after organic modification is associated with the presumed functioning of the interlayer space

as an additional reaction zone in the photocatalytic process along with the external surface of the sample. Organic modifiers significantly increase the interlayer distance, facilitating the supply of methanol and water molecules to the interlayer reaction centers, which in the case of the initial protonated titanates remain practically unused for steric reasons. This hypothesis may also partly explain the increased activity of La-containing photocatalysts, which have a slightly larger interlayer distance compared to the Nd-containing analogues (Table 6).

3.2.2.2. Activity of $H_2Ln_2Ti_3O_{10}$ derivatives in a 1% (mol.) aqueous methanol solution

Kinetic curves of hydrogen evolution from a 1% (mol.) aqueous solution of methanol in the presence of photocatalysts based on the three-layer titanates are shown in Fig. 42, the activities observed in this case are presented in Table 9 and visualized in Fig. 43. It was shown that the activity of the samples obtained was stably maintained throughout the entire measurement time, as evidenced by the linear course of the kinetic graphs. After the light emitter is turned off (dark stage), the evolution of hydrogen stops.

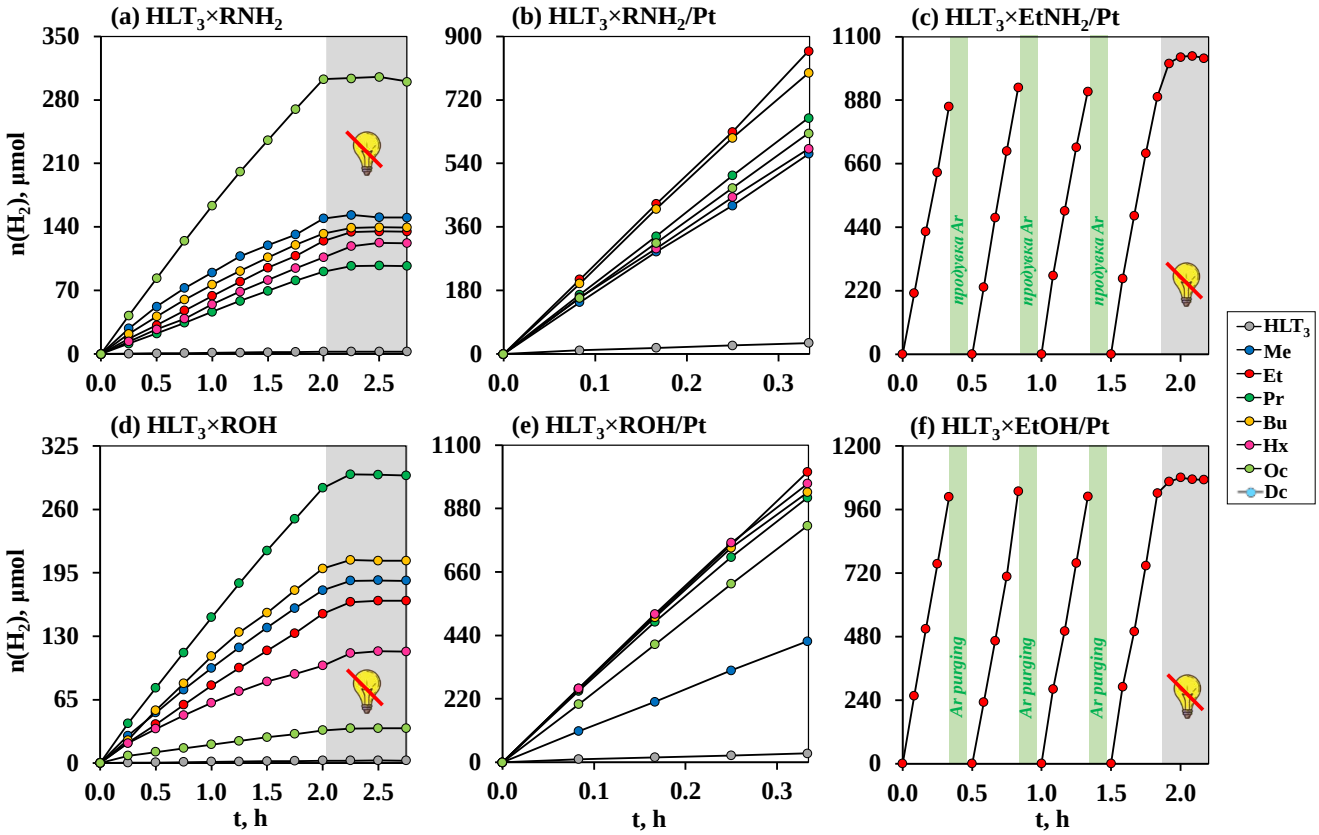


Fig. 42. Kinetic curves of photocatalytic hydrogen evolution from a 1% (mol.) aqueous methanol solution in the presence of protonated form, amine and alcohol derivatives of the titanate $HLT_3$

The efficiency of photocatalytic hydrogen generation in the presence of the protonated three-layer titanates is relatively low (φ = 0.017% for La-containing and φ = 0.027% for Nd-

containing), but is somewhat higher than that achieved when using the single-layer compounds discussed above. After surface modification with a platinum cocatalyst, the photocatalytic activity of the protonated titanates increases several tens of times, with La-containing titanate (φ = 1.14%) becoming more active than the Nd-containing one (φ = 0.92%).

Without exception, all the amine and alcohol derivatives of three-layer titanates demonstrate a high quantum efficiency of hydrogen generation from the aqueous solution of methanol, up to 117 times higher than the initial protonated forms and up to 87 times higher than a standard photocatalyst $TiO_2$ P25 Degussa (φ = 0.023%). That being said, the La-containing samples in most cases turn out to be more active than the Nd-containing analogues (Table 9), however, this difference is expressed much less clearly than in the case of the single-layer titanates.

Table 9. Photocatalytic activity of protonated forms, amine and alcohol derivatives of the titanates $HLT_3$ and $HNT_3$ in the reaction of hydrogen evolution from a 1% (mol.) aqueous solution of methanol: absolute and normalized rates of hydrogen generation ω and ω′, apparent quantum efficiency φ, factor of increase in the rate after platinization $k_{Pt}$

| Photocatalyst | ω, μmol·h$^{-1}$ | ω′, mmol·h$^{-1}$·g$^{-1}$ | φ, % | $k_{Pt}$ |
|---|---|---|---|---|
| $HLT_3$ | 1.27 | 0.051 | 0.017 | – |
| $HLT_3$/Pt | 85.1 | 3.40 | 1.14 | 67 |
| $HLT_3$×$MeNH_2$ | 81.9 | 3.28 | 1.10 | – |
| $HLT_3$×$MeNH_2$/Pt | 1650 | 66.0 | 22.0 | 20 |
| $HLT_3$×$EtNH_2$ | 61.6 | 2.46 | 0.82 | – |
| $HLT_3$×$EtNH_2$/Pt | 2390 | 95.6 | 31.9 | 39 |
| $HLT_3$×$PrNH_2$ | 45.9 | 1.84 | 0.61 | – |
| $HLT_3$×$PrNH_2$/Pt | 1990 | 79.6 | 26.6 | 43 |
| $HLT_3$×$BuNH_2$ | 72.3 | 2.89 | 0.97 | – |
| $HLT_3$×$BuNH_2$/Pt | 2180 | 87.2 | 29.2 | 30 |
| $HLT_3$×$HxNH_2$ | 53.8 | 2.15 | 0.72 | – |
| $HLT_3$×$HxNH_2$/Pt | 1660 | 66.4 | 22.1 | 31 |
| $HLT_3$×$OcNH_2$ | 149 | 5.96 | 1.99 | – |
| $HLT_3$×$OcNH_2$/Pt | 1840 | 73.6 | 24.5 | 12 |
| $HLT_3$×MeOH | 92.8 | 3.71 | 1.24 | – |
| $HLT_3$ ×MeOH/Pt | 1200 | 48.0 | 16.0 | 13 |
| $HLT_3$×EtOH | 78.5 | 3.14 | 1.05 | – |
| $HLT_3$×EtOH/Pt | 3000 | 120 | 40.1 | 38 |
| $HLT_3$×PrOH | 138 | 5.52 | 1.85 | – |
| $HLT_3$×PrOH/Pt | 2780 | 111 | 37.2 | 20 |
| $HLT_3$×BuOH | 114 | 4.56 | 1.52 | – |
| $HLT_3$×BuOH/Pt | 2750 | 110 | 36.8 | 24 |
| $HLT_3$×HxOH | 55.1 | 2.20 | 0.74 | – |
| $HLT_3$×HxOH/Pt | 2850 | 114 | 38.1 | 52 |
| $HLT_3$×DcOH | 14.9 | 0.60 | 0.20 | – |
| $HLT_3$×DcOH/Pt | 2160 | 86.4 | 28.8 | 145 |

| Photocatalyst | ω, μmol·h$^{-1}$ | ω′, mmol·h$^{-1}$·g$^{-1}$ | φ, % | $k_{Pt}$ |
|---|---|---|---|---|
| $HNT_3$ | 2.00 | 0.080 | 0.027 | – |
| $HNT_3$/Pt | 69.0 | 2.76 | 0.92 | 35 |
| $HNT_3$×$MeNH_2$ | 130 | 5.20 | 1.74 | – |
| $HNT_3$×$MeNH_2$/Pt | 1480 | 59.2 | 19.7 | 11 |
| $HNT_3$×$EtNH_2$ | 106 | 4.24 | 1.42 | – |
| $HNT_3$×$EtNH_2$/Pt | 1480 | 59.2 | 19.8 | 14 |
| $HNT_3$×$PrNH_2$ | 128 | 5.12 | 1.71 | – |
| $HNT_3$×$PrNH_2$/Pt | 1470 | 58.8 | 19.7 | 12 |
| $HNT_3$×$BuNH_2$ | 147 | 5.88 | 1.97 | – |
| $HNT_3$×$BuNH_2$/Pt | 2080 | 83.2 | 27.8 | 14 |
| $HNT_3$×$HxNH_2$ | 42.0 | 1.68 | 0.56 | – |
| $HNT_3$×$HxNH_2$/Pt | 965 | 38.6 | 12.9 | 23 |
| $HNT_3$×$OcNH_2$ | 54.6 | 2.18 | 0.73 | – |
| $HNT_3$×$OcNH_2$/Pt | 1030 | 41.2 | 13.7 | 19 |
| $HNT_3$×MeOH | 115 | 4.60 | 1.54 | – |
| $HNT_3$×MeOH/Pt | 1790 | 71.6 | 23.9 | 16 |
| $HNT_3$×EtOH | 75.8 | 3.03 | 1.01 | – |
| $HNT_3$×EtOH/Pt | 2270 | 90.8 | 30.3 | 30 |
| $HNT_3$×PrOH | 112 | 4.48 | 1.49 | – |
| $HNT_3$×PrOH/Pt | 2430 | 97.2 | 32.5 | 22 |
| $HNT_3$×BuOH | 83.5 | 3.34 | 1.12 | – |
| $HNT_3$×BuOH/Pt | 2580 | 103 | 34.5 | 31 |
| $HNT_3$×HxOH | 97.9 | 3.92 | 1.31 | – |
| $HNT_3$×HxOH/Pt | 2290 | 91.6 | 30.6 | 23 |
| $HNT_3$×DcOH | 42.0 | 1.68 | 0.56 | – |
| $HNT_3$×DcOH/Pt | 2040 | 81.6 | 27.3 | 49 |

The most photocatalytically active in the series of non-platinized three-layer amine derivatives $HLT_3$×$RNH_2$ is the *n*-octylamine titanate (φ = 1.99%), and in the $HNT_3$×$RNH_2$ series – *n*-butylamine one (φ = 1.97%). Among the amine derivatives modified with a platinum cocatalyst $HLT_3$×$RNH_2$/Pt, the highest hydrogen generation efficiencies are provided by the ethyl (φ = 31.9%) and *n*-butylamine (φ = 29.2%) derivatives, while the activity of the other samples lies in the range φ = 22–27%. In the $HNT_3$×$RNH_2$/Pt series, the activities of the titanates are generally proportional to those observed in the absence of the cocatalyst, and the maximum one is demonstrated by the *n*-butylamine compound (φ = 27.8%). Among the non-platinized alcohol derivatives $HLT_3$×ROH and $HNT_3$×ROH, the maximum efficiency of hydrogen generation is demonstrated by the *n*-propanol derivatives (φ = 1.85% and φ = 1.49%, respectively). After modification with the cocatalyst, the maximum activity in the series $HLT_3$×ROH/Pt is exhibited by the ethanol derivative (φ = 40.1%), while the *n*-propanol, *n*-butanol and *n*-hexanol samples are slightly less active (φ = 36–38%). In the $HNT_3$×ROH/Pt

series, an increase in the photocatalytic activity is observed when moving from the methanol titanate to *n*-butanol one (φ = 34.5%) with a further decrease with the increasing alkoxy chain length.

Thus, the organic modification of the three-layer titanates has made it possible to create a number of new highly efficient photocatalysts for hydrogen generation, some representatives of which outperform the initial protonated forms by more than two orders of magnitude. The most active of them is the platinized ethanol derivative $HLT_3$×EtOH/Pt, which provides a hydrogen evolution rate from a 1% (mol.) aqueous solution of methanol of 120 $mmol \cdot h^{-1} \cdot g^{-1}$ and an apparent quantum efficiency of 40.1%. At the same time, the organically modified three-layer titanates exhibit significantly greater photocatalytic performance than their single-layer analogues, despite the fact that the introduction of organic components has a beneficial effect on the activity of both. This difference may be due to the unequal efficiency of spatial separation of photogenerated charge carriers in the titanate perovskite blocks of different thicknesses. Moreover, it becomes more pronounced after the reduction of Pt nanoparticles as a cocatalyst on the surface: the typical factor of the increase in the reaction rate during the platinization of the derivatives of single-layer titanates ($k_{Pt}$ = 5–15) turns out to be noticeably smaller than in the case of the derivatives of three-layer compounds ($k_{Pt}$ = 20–30). Moreover, the lowest values of $k_{Pt}$ are observed for the most active single-layer photocatalysts (in particular, HLT×MeOH/Pt). In other words, photocatalytic activity of the single-layer samples can be significantly less enhanced by surface modification with the cocatalyst than that of the three-layer ones. Such a difference may be due to the difference in the relative position of the Fermi levels of the titanates and platinum under consideration, which determines the efficiency of the transfer of photogenerated electrons from the semiconductor to the metal. However, this issue requires a separate detailed study. In general, the advantage in the photocatalytic activity of layered perovskite-like oxides with a larger thickness of the perovskite block has already been noted in the literature previously using the example of double- and three-layer niobates [131] and tantalates [133].

It was also found that the photocatalytic activity of three-layer titanates, when going from one sample to another, in many cases changes symbatically with the degree of hydration of their interlayer space (Fig. 43), which indicates the probable participation of water molecules in the target reaction of hydrogen formation. In particular, under the influence of

photogenerated holes, interlayer water can form highly active hydroxyl radicals, which are also involved in the oxidation of methanol, leading to an increase in the observed rate of hydrogen production [236,237].

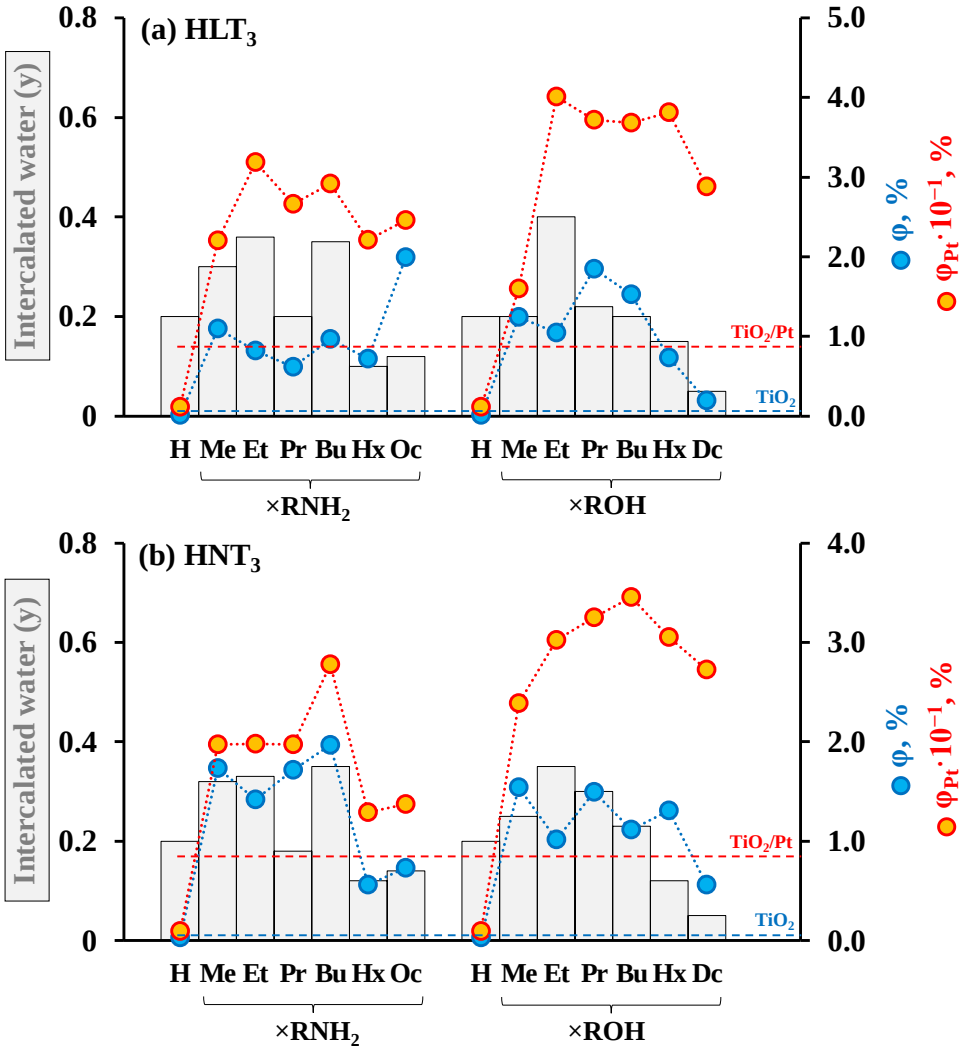


Fig. 43. Correlation of the photocatalytic activity of protonated forms, amine and alcohol derivatives of the titanates $HLT_3$ and $HNT_3$ in the reaction of hydrogen evolution from a 1% (mol.) aqueous solution of methanol with the amount of intercalated water

### 3.2.2.3. Dependence of the activity of $H_2Ln_2Ti_3O_{10}$ derivatives in aqueous methanol solutions on the reaction conditions

Using the example of platinized *n*-butylamine derivatives of the three-layer titanates $HLT_3{\times}BuNH_2/Pt$ and $HNT_3{\times}BuNH_2/Pt$, the dependence of the activity on the methanol concentration, photocatalyst concentration and the mass fraction of the cocatalyst was studied (Fig. 44).

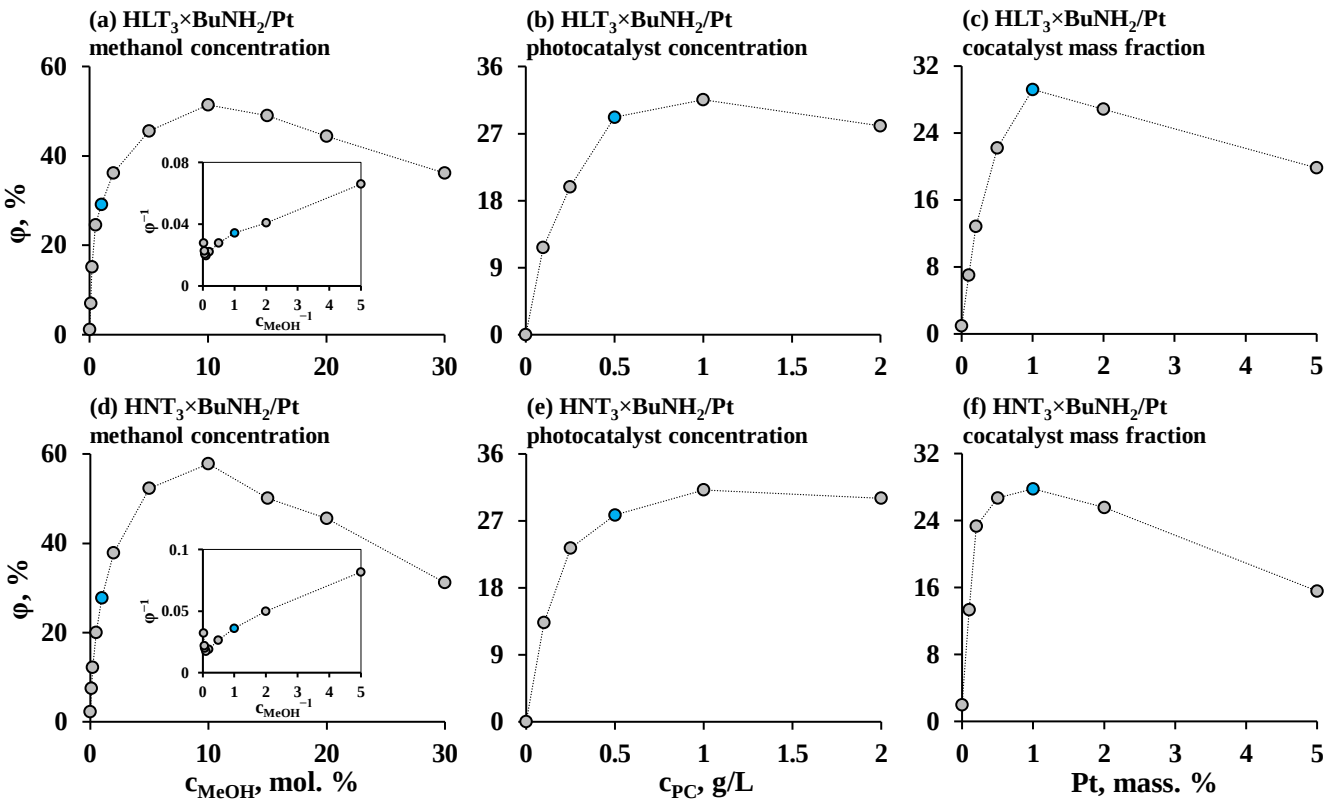


Fig. 44. Dependence of apparent quantum efficiency of photocatalytic hydrogen evolution from aqueous solutions of methanol in the presence of *n*-butylamine derivatives of the titanates $HLT_3$ (a–c) and $HNT_3$ (d–f) on the reaction conditions. Blue dots correspond to standard experimental conditions

As already noted in section 1.1.5.1, the dependence of the rate (quantum efficiency) of a heterogeneous photocatalytic reaction on the concentration of the reactant is usually described by the Langmuir-Hinshelwood kinetic model, borrowed from the field of standard heterogeneous catalysis. Within this model, the reaction rate increases linearly with the content of the reactant in solution until the majority of the active sites on the surface of the catalyst remain free and, accordingly, the catalyst has the potential to the further activity increase due to the adsorption of more reactant molecules, which is usually observed in the region of low concentrations of the reaction solution. With a further increase in the concentration, the dependence deviates from linearity towards lower reaction rates and gradually reaches a plateau due to the involvement of all available active centers in the catalytic process. The described dependence is linearized by converting it into inverse rate – inverse concentration coordinates. The experimentally obtained concentration dependences of the photocatalytic activity of the *n*-butylamine derivatives generally correspond to the Langmuir-Hinshelwood model in the range of methanol contents in an aqueous solution from 0.2 to 10 mol. %, and the corresponding sections of the graphs can be satisfactorily linearized when going to the reverse

coordinates (Fig. 44, a, d). At a methanol concentration of 10 mol. %, an unprecedentedly high photocatalytic activity of the samples $HLT_3{\times}BuNH_2$/Pt and $HNT_3{\times}BuNH_2$/Pt is achieved, equal to 155 mmol·$h^{-1}$·$g^{-1}$ (φ = 52%) and 175 mmol·$h^{-1}$·$g^{-1}$ (φ = 58%), respectively. At the same time, the Langmuir-Hinshelwood model does not adequately describe the methanol concentration ranges below 0.2 and above 10 mol. %. In the first case, the deviation of the experimental points from those expected according to the model is due to the fact that the photocatalytic activity of the samples when the methanol concentration tends to zero (in pure water) remains non-zero. In other words, water in the system under consideration is not an inert solvent, but a participant in the reaction along with methanol, which is not taken into account by the model. In the second case, in the region of high concentrations, the observed activity decreases with increasing methanol content in the solution, while the model predicts that the dependence will reach a plateau. One of the possible reasons for this, apparently, is also that water is an indispensable participant in the photocatalytic process necessary for the effective dehydrogenation of methanol. This hypothesis is further supported by the previously noted correlation of the photocatalytic activity of organic-inorganic derivatives with the degree of hydration of their interlayer space (Fig. 43), as well as literature data on the relationship between the activity of the three-layer titanates and the content of intercalated water in the absence of organic modifiers [129,218,220]. In addition, methanol concentration may also affect the process of in situ platinization of photocatalysts (in particular, the size and distribution of the cocatalyst particles on the surface), which, in turn, can affect the activity of the final samples.

It was found that the efficiency of hydrogen generation increases monotonically with increasing photocatalyst concentration in the range from 0 to 1 g/L (Fig. 44, b, d), which is explained by an increase in the active surface in the system. The maximum activity achieved at the point of 1 g/L is ≈ 93 mmol·$h^{-1}$·$g^{-1}$ (φ ≈ 31%) in the case of both photocatalysts under study and exceeds that observed with a standard sample loading of 0.5 g/L by no more than 1.1 times. However, with a further increase in the concentration of photocatalysts to 2 g/L, their activity begins to slowly go down. The reason for this may be a strong increase in light scattering by a concentrated reaction suspension to the detriment of absorption, as well as a slowdown in the diffusion of reactants and products in the liquid phase. It should be noted that the described type of the activity dependence on the concentration of the photocatalyst,

according to literature data, was also observed in the case of other photocatalytic systems [57,58].

A study of the photocatalytic activity dependence on the mass fraction of Pt as a cocatalyst showed that the latter value of 1% chosen as a standard value is optimal, providing the greatest efficiency of hydrogen generation (Fig. 44, c, f). A further increase in the Pt content is accompanied by a decrease in the photocatalytic activity, which is apparently explained by the screening of the main photocatalyst material by its particles, making it difficult to absorb light. The presence of a maximum in similar dependences was previously noted in the literature for other oxide materials, and its position is determined by the nature of both a photocatalyst and a cocatalyst [101,238,239].

### 3.2.2.4. Activity of $H_2Ln_2Ti_3O_{10}$ derivatives in 1% (mol.) aqueous solutions of glucose and xylose

Photocatalytic hydrogen generation from 1% (mol.) aqueous solutions of glucose and xylose was studied using the example of the protonated three-layer titanate $HLT_3$ as well as its ethylamine and ethanol derivatives $HLT_3{\times}EtNH_2$ and $HLT_3{\times}EtOH$, which demonstrated the highest activity values in aqueous methanol solutions after platinization. At the same time, two approaches to modifying their surface with Pt nanoparticles as a cocatalyst were tested: direct platinization in situ in an aqueous solution of carbohydrate, as well as preliminary platinization in aqueous methanol, followed by isolation of the final photocatalyst and redispersion in the required reaction medium.

The kinetic curves of photocatalytic hydrogen evolution from aqueous solutions of glucose and xylose obtained (Fig. 45) generally maintain a constant slope throughout the entire measurement time, indicating a stable rate of the target reaction, and after turning off the radiation source (dark stage) they reach a plateau.

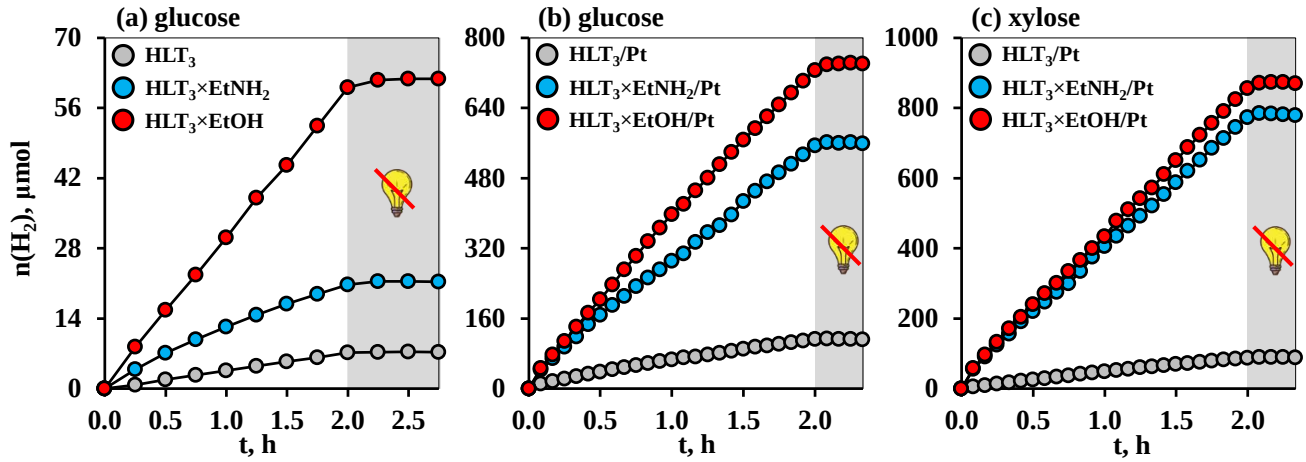


Fig. 45. Kinetic curves of photocatalytic hydrogen evolution from 1% (mol.) aqueous solutions of glucose and xylose in the presence of protonated form, ethylamine and ethanol derivatives of the titanate $HLT_3$

It was shown that the organic modification of the titanate $HLT_3$ leads to a significant increase in the efficiency of hydrogen generation from aqueous solutions of carbohydrates, reaching 9 times (Table 10). That being said, as in aqueous solutions of methanol, the ethanol derivative is superior in photocatalytic activity to the ethylamine derivative, which is more noticeable in the absence of a cocatalyst. After modification of the surface with Pt nanoparticles, the ethanol titanate demonstrates the activity in solutions of glucose and xylose of 14.3 $mmol \cdot h^{-1} \cdot g^{-1}$ (5.95%) and 16.8 $mmol \cdot h^{-1} \cdot g^{-1}$ (7.01%), respectively, surpassing in quantum efficiency a similarly platinized photocatalyst-standard $TiO_2$ P25 Degussa approximately by 3 times. However, it should be noted that the latter has a 10 times greater specific surface area ($\approx 50$ $m^2/g$) compared to the organic-inorganic derivatives of the titanate $HLT_3$ ($\approx 5$ $m^2/g$), due to which, when normalizing the activity per unit surface area, the derivatives will exceed $TiO_2$ in the efficiency of hydrogen generation by more than an order of magnitude. Thus, selected organic-inorganic derivatives of the titanate can serve as efficient photocatalysts for hydrogen generation not only from aqueous methanol, but also from glucose and xylose solutions, which are one of the key components of plant biomass.

Table 10. Photocatalytic activity of protonated form, ethylamine and ethanol derivatives of the titanate $HLT_3$ in the reactions of hydrogen evolution from 1% (mol.) aqueous solutions of glucose and xylose. Platinization method: /Pt – directly in a carbohydrate solution, /Pt(MeOH) – in a methanol solution with isolation and subsequent dispersion of the resulting photocatalyst in the required carbohydrate solution

| Solution | Photocatalyst | ω, μmol·h$^{-1}$ | ω′, mmol·h$^{-1}$·g$^{-1}$ | φ, % | $k_{Pt}$ |
|---|---|---|---|---|---|
| 1% (mol.) glucose | $HLT_3$ | 3.60 | 0.14 | 0.060 | – |
| | $HLT_3$/Pt | 60.5 | 2.42 | 1.01 | 17 |
| | $HLT_3$/Pt(MeOH) | 110 | 4.4 | 1.83 | 31 |
| | $HLT_3$×$EtNH_2$ | 9.56 | 0.38 | 0.16 | – |
| | $HLT_3$×$EtNH_2$/Pt | 270 | 10.8 | 4.50 | 28 |
| | $HLT_3$×$EtNH_2$/Pt(MeOH) | 239 | 9.56 | 3.98 | 25 |
| | $HLT_3$×EtOH | 29.8 | 1.19 | 0.50 | – |
| | $HLT_3$×EtOH/Pt | 357 | 14.3 | 5.95 | 12 |
| | $HLT_3$×EtOH/Pt(MeOH) | 118 | 4.72 | 1.96 | 4.0 |
| 1% (mol.) xylose | $HLT_3$/Pt | 47.7 | 1.91 | 0.79 | – |
| | $HLT_3$×$EtNH_2$/Pt | 376 | 15.0 | 6.27 | – |
| | $HLT_3$×EtOH/Pt | 421 | 16.8 | 7.01 | – |

It was also found that for the protonated titanate, preliminary platinization in an aqueous solution of methanol is preferable, providing a 1.8 times greater activity of the final photocatalyst compared to that achieved by direct platinization in a glucose solution (Table 10). At the same time, direct platinization in the aqueous solution of glucose turned out to be more effective in relation to the organically modified titanates and, in particular, the ethanol derivative, the activity of which was 3 times higher than after the preliminary reduction of the cocatalyst in aqueous methanol. The lower activity of the final photocatalyst in the latter case may indicate irreversible changes in the composition of its interlayer space during the platinization procedure (in particular, partial loss of intercalated water during isolation and drying with an inevitable decrease in the interlayer distance).

The ratio of the photocatalytic activity of the protonated form and organic-inorganic derivatives of the titanate $HLT_3$ in aqueous solutions of methanol, glucose and xylose allows one to indirectly assess the degree of participation of the interlayer space in the occurrence of the corresponding photocatalytic reactions (Fig. 46). In particular, the efficiency of hydrogen generation from solutions of the three above-mentioned organic compounds in the presence of the protonated titanate differs slightly, while the activity of the organic-inorganic derivatives when moving from carbohydrates to methanol increases 5–7 times. The latter experimental fact indicates that the interlayer space of the derivatives indeed functions as an additional reaction zone in the photocatalytic process, but the contribution of this zone to the overall

activity, other things being equal, significantly depends on the steric characteristics of the reactants. In particular, relatively small methanol molecules can easily penetrate into the interlayer space and undergo dehydrogenation there, while the access of relatively large carbohydrate molecules into the interlayer zone is difficult, which is why they probably undergo chemical transformations mainly at the boundaries of the interlayer space and the external photocatalyst surface. This hypothesis is also supported by the slightly greater activity of the organic-inorganic derivatives in a solution of xylose, which is characterized by a slightly smaller molecule size compared to glucose. At the same time, the relatively narrow interlayer space of the protonated titanate, apparently, is practically not involved in the photocatalytic process, due to which the chemical transformations of the reactants occur predominantly on the external surface and the reactant size has a lesser effect on the kinetics of the corresponding reactions.

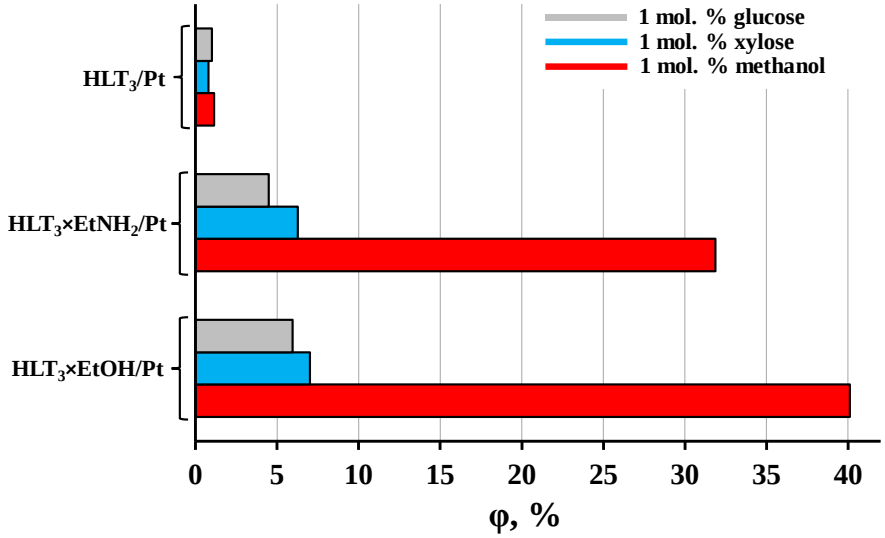


Fig. 46. Comparison of apparent quantum efficiency of photocatalytic hydrogen evolution from 1 mol. % aqueous solutions of glucose, xylose and methanol in the presence of platinized protonated form, ethylamine and ethanol derivatives of the titanate $HLT_3$

### 3.2.2.5. Activity of $H_2Ln_2Ti_3O_{10}$ derivatives in water

Photocatalytic activity of the ethylamine and ethanol derivatives $HLT_3{\times}EtNH_2$ and $HLT_3{\times}EtOH$ was also tested in the reaction of hydrogen generation from pure water (Fig. 47, Table 11). As can be seen from the presented data, the interlayer organic modification led to an increase in the rate of the target reaction up to 40 times, and after platinization of the surface, the activity of 3.59 $mmol{\cdot}h^{-1}{\cdot}g^{-1}$ (1.50%) and 3.42 $mmol{\cdot}h^{-1}{\cdot}g^{-1}$ (1.42%) was achieved in the case of the ethylamine and ethanol titanates, respectively. A significant decrease in the efficiency of hydrogen generation when moving from aqueous solutions of organic compounds

(bioalcohols, carbohydrates) to pure water is a common trend for most heterogeneous photocatalysts due to the kinetically hindered four-electron half-reaction of the oxidative water decomposition, as well as the high overpotential during the formation of two gaseous products [87].

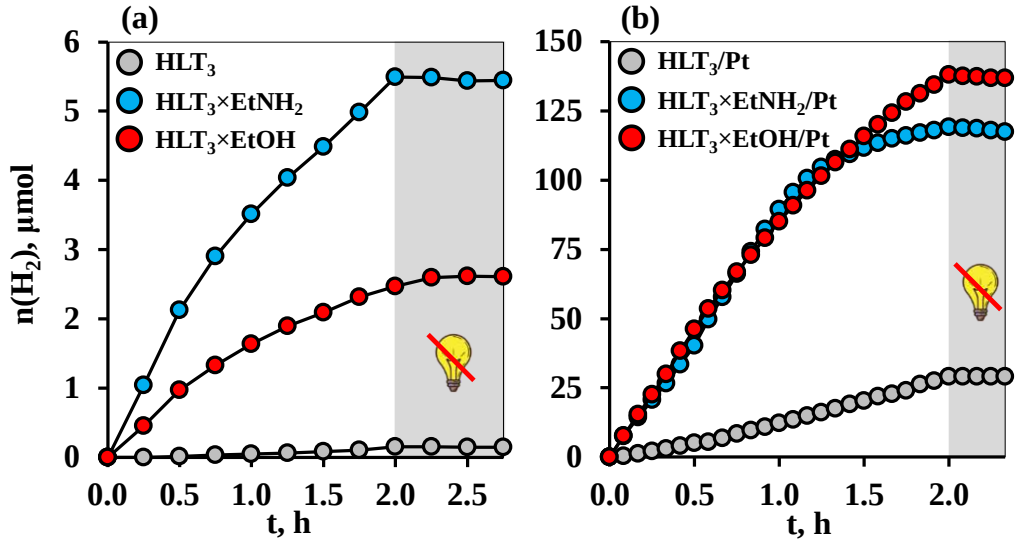


Fig. 47. Kinetic curves of photocatalytic hydrogen evolution from water in the presence of protonated form, ethylamine and ethanol derivatives of the titanate $HLT_3$

Table 11. Photocatalytic activity of protonated form, ethylamine and ethanol derivatives of the titanate $HLT_3$ in the reaction of hydrogen evolution from water

| Photocatalyst | ω, μmol·h$^{-1}$ | ω′, mmol·h$^{-1}$·g$^{-1}$ | φ, % | $k_{Pt}$ |
|---|---|---|---|---|
| $HLT_3$ | 0.08 | 0.003 | 0.002 | – |
| $HLT_3$/Pt | 19.7 | 0.79 | 0.32 | 246 |
| $HLT_3$×$EtNH_2$ | 3.28 | 0.13 | 0.055 | – |
| $HLT_3$×$EtNH_2$/Pt | 89.8 | 3.59 | 1.50 | 27 |
| $HLT_3$×EtOH | 1.56 | 0.062 | 0.026 | – |
| $HLT_3$×EtOH/Pt | 85.4 | 3.42 | 1.42 | 55 |

However, during photocatalytic measurements, it was noticed that the activity of the ethylamine and ethanol derivatives in pure water decreases slightly with time, which is seen from a noticeable decrease in the slope of the kinetic curves (Fig. 47) not observed for most of the studied organic-inorganic derivatives when working in aqueous solutions of methanol and carbohydrates. This fact may indicate some irreversible changes in the composition of the interlayer reaction zone of the photocatalysts during operation – in particular, the oxidation of introduced organic modifiers in the absence of other easily oxidized components (methanol or carbohydrates) in the system, followed by a narrowing of the interlayer space and, accordingly, a decrease in its availability for water molecules.

3.2.3. Stability of the amine and alcohol derivatives under photocatalysis conditions

Stability of selected photocatalysts based on organic-inorganic derivatives of the titanates during hydrogen generation from a 1% (mol.) aqueous solution of methanol was studied in kinetic and structural-chemical aspects. In the first case, the subject of the study was the stability of maintaining photocatalytic activity over time during long-term operation, and in the second, the potential transformations of the interlayer space during photocatalysis.

It was shown that the amounts of hydrogen released during photocatalytic experiments in the presence of the most active organic-inorganic derivatives are many times higher than its content in interlayer organic modifiers. Thus, in 3 h of the photocatalytic reaction involving the platinized ethanol titanate $HLT_3$×EtOH/Pt, ≈ 9 mmol of hydrogen is released – an amount being more than two orders of magnitude greater than the amount that could hypothetically be formed by complete dehydrogenation of all the interlayer ethoxy groups of the photocatalyst (0.0865 mmol), and the reaction rate remains almost unchanged. Accordingly, hydrogen evolution reactions in the presence of highly active organic-inorganic derivatives of the titanates actually proceed catalytically, and hydrogen is generated from the reaction solution.

During photocatalytic experiments of extended duration, it was found that the rate of hydrogen evolution in the presence of the most active amine and alcohol derivatives $HLT_3$×$EtNH_2$/Pt and $HLT_3$×EtOH/Pt is maintained for a long time (Fig. 48) provided that the concentration of methanol in the solution is kept relatively constant. Similar experiments were also carried out with the participation of the applicant's colleagues in the scientific group with the derivative $HLT_3$×$BuNH_2$/Pt, the activity of which not only did not decrease over time, but also increased slightly, possible reasons for which were additional hydration of the interlayer space and a decrease in the pH of the medium during photocatalysis [232].

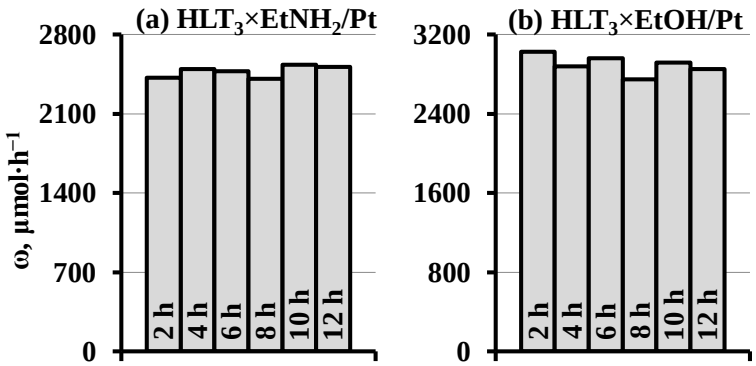


Fig. 48. Activity of the platinized ethylamine and ethanol derivatives of $HLT_3$ in a 1% (mol.) aqueous solution of methanol under long-term operating conditions

The study of structural-chemical stability of the organically modified photocatalysts was carried out using the example of derivatives of the titanates HLT and $HLT_3$ with extreme modifier chain lengths, and also demonstrating the greatest activity after platinization. For this purpose, these samples were isolated after standard photocatalytic experiments with a total duration of ≈ 2.5 h by vacuum filtration, dried in air and analyzed using a number of physical-chemical methods. X-ray diffraction patterns and Raman spectra of the samples studied for stability before and after photocatalysis are presented in Fig. 49 and 50, interlayer distances and quantitative compositions are given in Table 12. It was found that the composition and width of the interlayer space of most of the tested derivatives changes in one way or another during the photocatalytic generation of hydrogen, despite the consistently high photocatalytic activity throughout the entire measurement time. In particular, diffraction patterns of the organically modified single-layer titanates after photocatalysis differ from those of the initial derivatives by the shift of reflections (00x) to the region of large diffraction angles (HLT×$MeNH_2$, HLT×$EtNH_2$), their broadening (HLT×$OcNH_2$, HLT×DcOH) or the appearance of impurity phases (HLT×MeOH) (Fig. 49, a). The noted structural transformations may be due to partial degradation of the embedded organic components, a decrease in the degree of ordering of the layered structure along the crystallographic *c* axis and secondary hydration of the interlayer zone, respectively. It is important to note that the diffraction pattern of none of the final derivatives coincides with that observed in the case of the initial protonated titanate, which indicates at least partial retention of the interlayer modifiers.

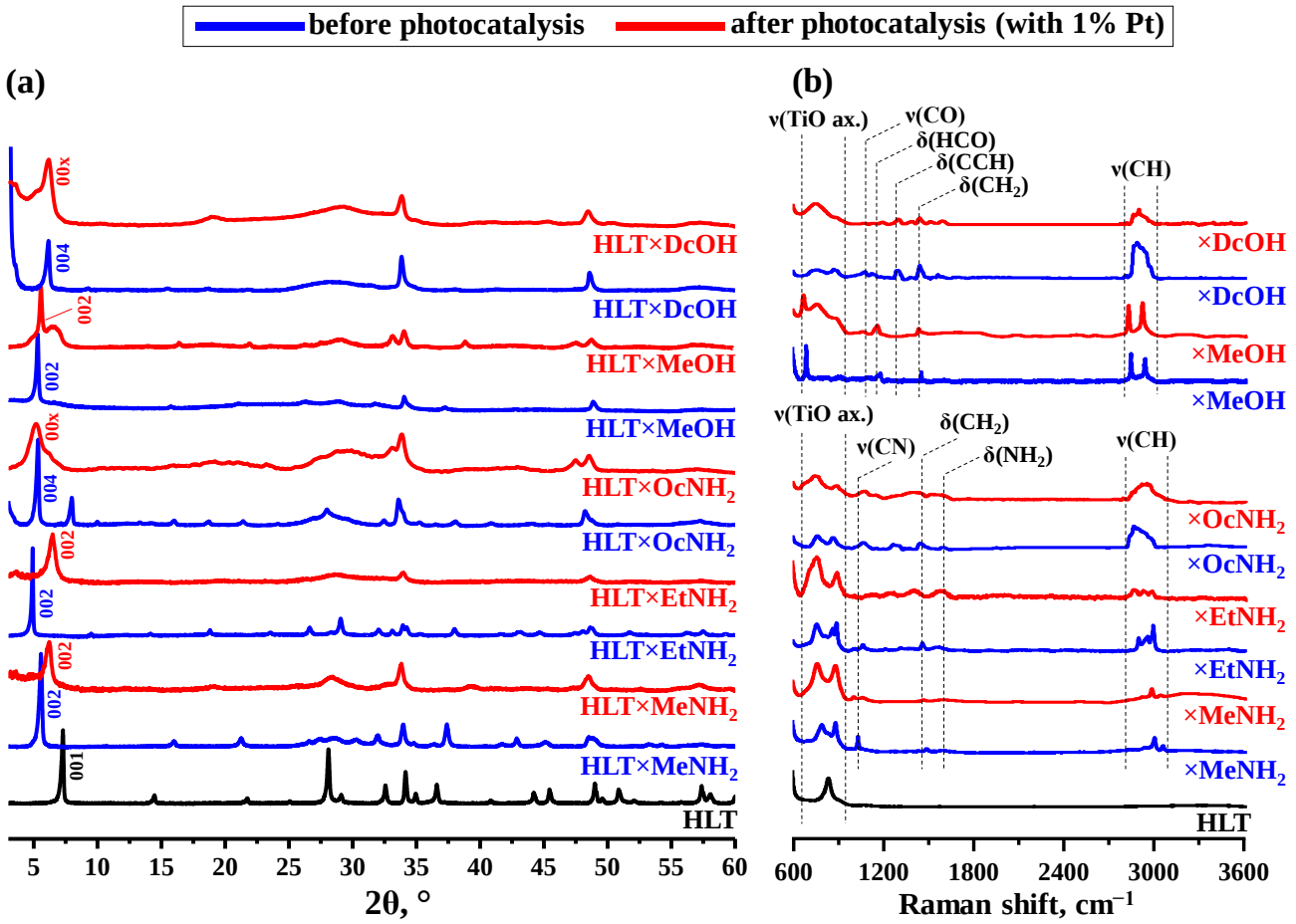


Fig. 49. X-ray diffraction patterns (a) and Raman spectra (b) of selected amine and alcohol derivatives of the titanate HLT before and after standard photocatalytic experiments in a 1% (mol.) aqueous methanol solution

The latter fact is confirmed by Raman spectra of the final samples (Fig. 49, b), in which vibrational bands of the organic modifiers in the perovskite matrix are observed. In this case, the intensity of the corresponding signals in the spectra of the compounds HLT×$MeNH_2$ and HLT×MeOH after photocatalysis changes slightly, while in the case of the derivatives HLT×$EtNH_2$, HLT×$OcNH_2$ and HLT×DcOH noticeably decreases, which is apparently due to decreasing the content of the organic component in these samples. The presented results of X-ray diffraction analysis and Raman spectroscopy are in full agreement with the quantitative compositions of the interlayer space of the final samples, calculated on the basis of elemental CHN-analysis and thermogravimetry data (Table 12). In particular, the derivatives HLT×$MeNH_2$ and HLT×MeOH retain the main part of the interlayer organic modifier during photocatalysis, while in the case of the other compounds (HLT×$EtNH_2$, HLT×$OcNH_2$ and HLT×DcOH) its content decreases by an average of 4 times.

Organic-inorganic derivatives of the three-layer titanate $HLT_3$, despite their unprecedentedly high and stable activity, undergo significantly more pronounced structural-chemical changes in the interlayer zone during photocatalysis than their single-layer analogues. Thus, the X-ray diffraction patterns of the derivatives with short-chain modifiers ($HLT_3$×$MeNH_2$, $HLT_3$×$EtNH_2$, $HLT_3$×MeOH, $HLT_3$×EtOH) after photocatalysis turn out to be close to those of the protonated titanate $HLT_3$ (Fig. 50), and the interlayer distance of the aforementioned samples is only 0.2–0.7 Å higher than that observed in the case of $HLT_3$ (Table 12). A strong contraction of the interlayer space indicates that during photocatalysis, the main part of the introduced organic modifier most probably leaves this zone or decomposes in it, which is why the final compounds are structurally close to the initial protonated titanate. This fact is confirmed by the Raman spectra of the final samples (Fig. 50, b), in which the vibration bands of organic components are practically invisible, as well as the quantitative compositions calculated from the data of CHN-analysis and thermogravimetry (Table12). It was also found that the interlayer organic modifiers of the above derivatives are retained in significant quantities at least during the first 40–50 min of the photocatalytic reaction, and after 12–24 h, the interlayer distance of the samples still remains somewhat larger than in the case of the initial protonated titanates. At the same time, a certain amount of carbon remains in the samples, the exact form of existence of which is not possible to establish based on the available data. At the same time, the derivatives with long-chain modifiers ($HLT_3$×$OcNH_2$, $HLT_3$×DcOH) demonstrate higher chemical stability under photocatalysis conditions, although they do not fully retain the initial interlayer composition. Their X-ray diffraction patterns recorded after photocatalysis (Fig. 50, a), are characterized by broadening of reflections (00x) and do not allow one to unambiguously determine the value of the interlayer distance. If we assume that the initial reflections (001) of the derivatives are preserved, but go beyond the working range of the diffractometer ($2\theta < 3°$), then from the position of the observed reflections (002) we can calculate $d \approx 29$ Å for $HLT_3$×$OcNH_2$ and $d \approx 31$ Å for $HLT_3$×DcOH, respectively. In the Raman spectra of these samples, bands corresponding to the organic modifiers are observed, but their intensity is approximately two times lower than in the case of the initial derivatives (Fig. 50, b). This fact is consistent with the calculated quantitative compositions of the samples (Table 12), according to which the latter retain only half of the initial amount of interlayer organic components during photocatalysis.

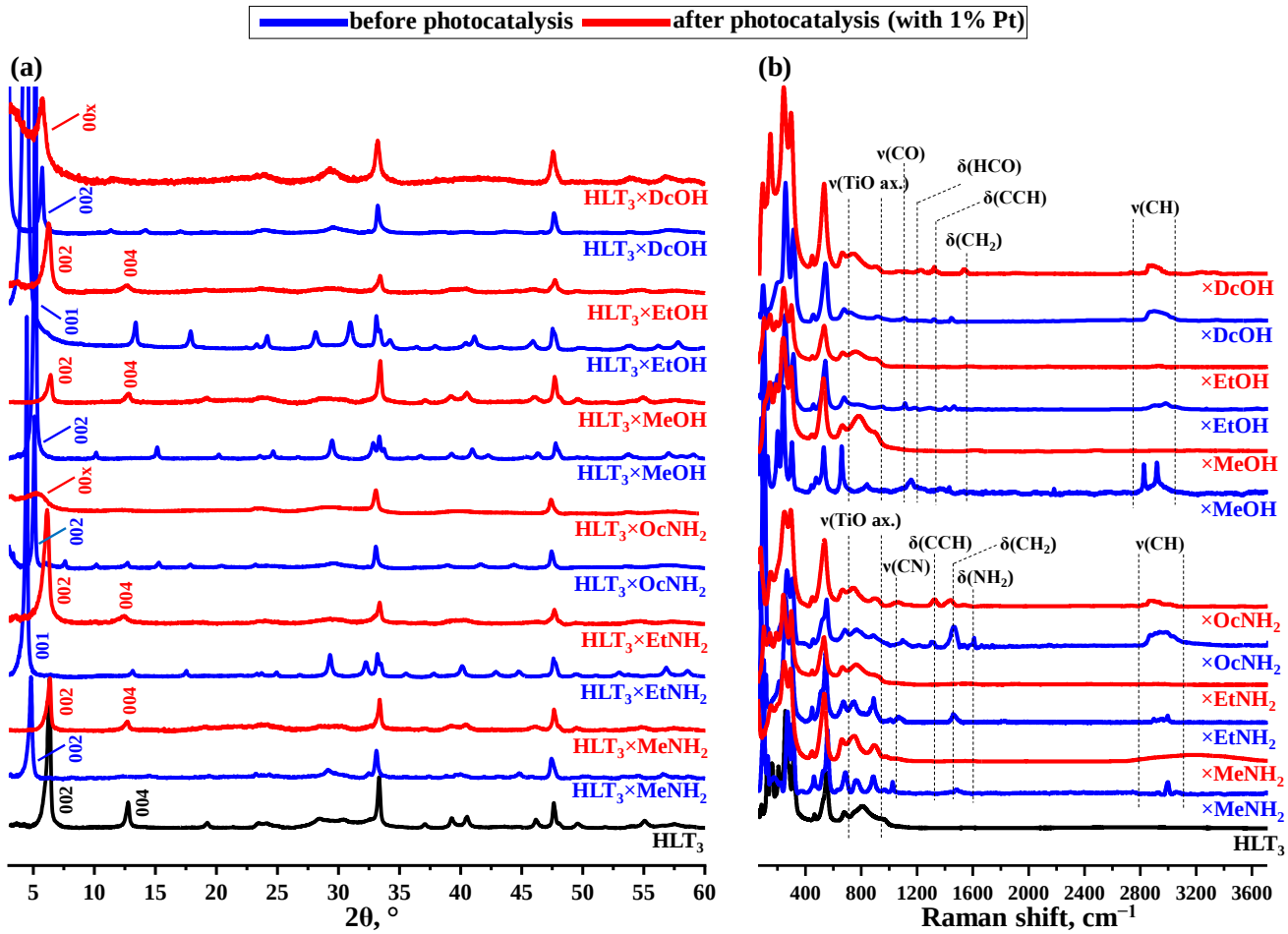


Fig. 50. X-ray diffraction patterns (a) and Raman spectra (b) of selected amine and alcohol derivatives of the titanate $HLT_3$ before and after standard photocatalytic experiments in a 1% (mol.) aqueous solution of methanol

Table 12. Interlayer distances *d*, amounts of organic modifier x and intercalated water y per formula unit for selected amine and alcohol derivatives of the titanates HLT and $HLT_3$ before and after standard photocatalytic experiments in a 1% (mol.) aqueous methanol solution

| Sample | | *d*, Å | x | y | Sample | | *d*, Å | x | y |
|---|---|---|---|---|---|---|---|---|---|
| HLT | | 12.2 | – | 0.10 | $HLT_3$ | | 13.6 | – | 0.20 |
| $HLT×MeNH_2$ | before | 16.7 | 0.35 | 0.45 | $HLT_3×MeNH_2$ | before | 18.4 | 0.70 | 0.30 |
| | after | 14.4 | 0.30 | 0.20 | | after | 13.9 | 0.15 | 0.25 |
| $HLT×EtNH_2$ | to | 18.9 | 0.35 | 0.50 | $HLT_3×EtNH_2$ | to | 20.2 | 0.70 | 0.35 |
| | after | 13.6 | 0.10 | 0.60 | | after | 14.3 | 0.25 | 0.45 |
| $HLT×OcNH_2$ | to | 33.2 | 0.45 | 0.40 | $HLT_3×OcNH_2$ | to | 34.2 | 0.80 | 0.10 |
| | after | – | 0.10 | 0.25 | | after | – | 0.40 | 0.15 |
| HLT×MeOH | to | 16.2 | 0.70 | 0.45 | $HLT_3×MeOH$ | to | 17.6 | 1.30 | 0.20 |
| | after | 15.4 | 0.50 | 0.35 | | after | 13.8 | 0.05 | 0.10 |
| HLT×DcOH | to | 28.4 | 0.35 | 0.05 | $HLT_3×EtOH$ | to | 19.8 | 0.85 | 0.40 |
| | after | – | 0.10 | 0.20 | | after | 13.9 | 0.15 | 0.35 |
| | | | | | $HLT_3×DcOH$ | to | 31.3 | 0.65 | 0.05 |
| | | | | | | after | – | 0.30 | 0.10 |

In the SEM images of the organic-inorganic derivatives isolated after photocatalysis (Fig. 51), bright dots are clearly visible – nanoparticles of the platinum cocatalyst with a size of 5–7 nm. In addition, in the case of the *n*-octylamine derivative shown, partial delamination of the crystals is observed, which probably occurred during the release of the organic modifier from the interlayer space. This feature of the sample morphology is consistent with the pronounced broadening of the reflections (00x) in its diffraction pattern (Fig. 50, a), associated with a decrease in order in the stacking of perovskite layers. Moreover, Fig. 51, d clearly shows the presence of Pt nanoparticles at the edges of the crystal delamination regions. This fact suggests a possible reduction of the cocatalyst not only on the external surface, but also in the interlayer zone, but the corresponding issue requires special study.

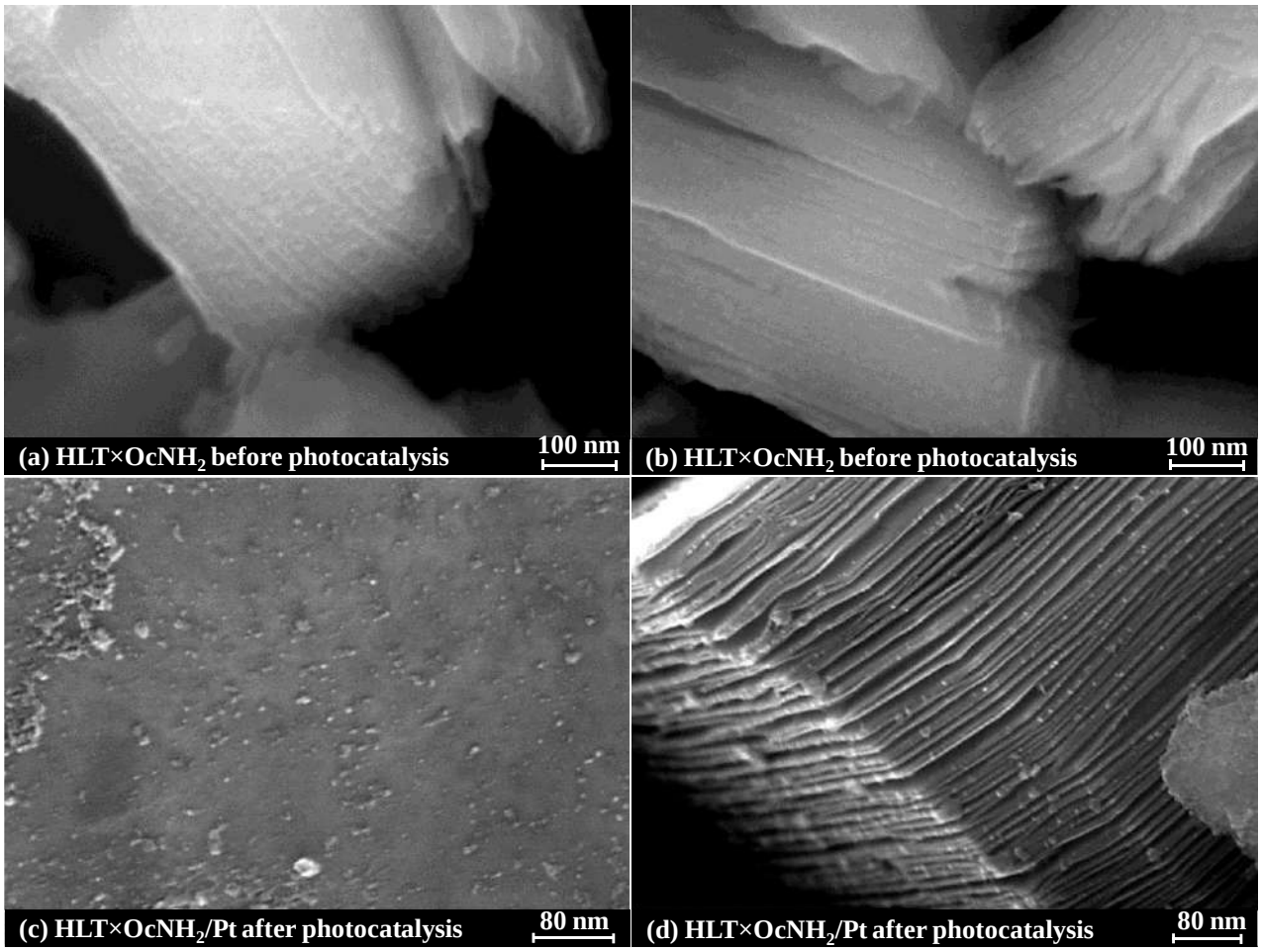


Fig. 51. SEM images of *n*-octylamine derivative of the titanate HLT before (a, b) and after (c, d) a standard photocatalytic experiment in a 1% (mol.) aqueous methanol solution

### 3.2.4. Stability and composition of reaction suspensions of the amine and alcohol derivatives

The actual volume concentration of photocatalysts in the reaction suspensions, which characterizes dispersibility of the samples and stability of the suspensions towards

sedimentation, was monitored spectrophotometrically at the beginning ($c_1$) and at the ending ($c_2$) of each photocatalytic experiment (Fig. 52). It was found that the initial titanates are inferior in stability with respect to sedimentation on the cell walls to most organically modified samples, which may be due to the large particle size of the protonated compounds. At the same time, dispersibility of the derivatives significantly depends on the interlayer organic component. Thus, the titanates modified with short-chain organic compounds (R = Me, Et, Pr, Bu) easily form suspensions in aqueous methanol, while the derivatives with long-chain modifiers (R = Hx, Oc, Dc) are difficult to disperse, forming films on the suspension surface and vessel walls due to poor solvability of low-polar organic components. This pattern is confirmed by dependences of actual volume concentrations of the photocatalysts in reaction suspensions on the interlayer modifier (Fig. 52), the maxima of which correspond to the materials with well-solvated organic components having a short hydrocarbon chain length. At the same time, the highest values of the photocatalytic activity in the series of amine and alcohol derivatives of the titanates in many cases are also demonstrated by compounds with relatively short-chain modifiers, which is why increased dispersibility and, accordingly, the greater actual volume concentration of these samples may be one of the factors responsible for their high activity.

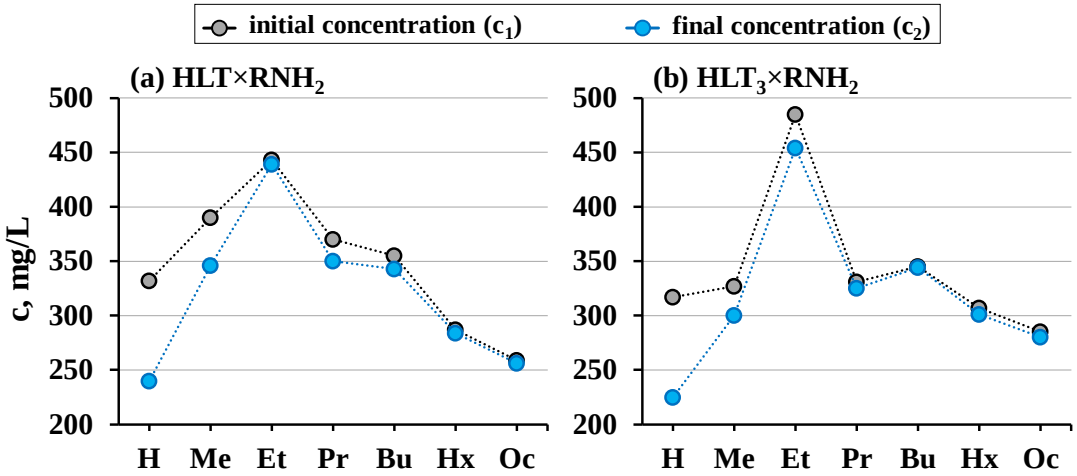


Fig. 52. Actual concentration of amine derivatives of the titanates HLT (a) and $HLT_3$ (b) in reaction suspensions at the beginning and ending of photocatalytic experiments in a 1% (mol.) aqueous solution of methanol

When studying the photocatalytic properties of the amine and alcohol derivatives, the question of the possibility of their partial exfoliation into nanosheets during the preparation of the reaction suspensions and conducting photocatalytic reactions, was separately considered since it could explain the high activity of the corresponding compounds. The concentration of

nanosheets and other fine fractions of the titanates ($c_3$) was estimated via spectrophotometric analysis of the supernatant solutions obtained after precipitation of relatively large particles by centrifugation of the suspensions. It was found that any noticeable concentrations of the nanosheets were present only in the suspensions of the amine derivatives HNT×$EtNH_2$ ($c_3 \approx 7$ mg/L) and HNT×$PrNH_2$ ($c_3 \approx 5$ mg/L), which are not leaders in the photocatalytic activity among the studied compounds. Thus, quantitative exfoliation of most organic-inorganic derivatives into nanosheets does not occur during photocatalytic studies, and this factor, accordingly, does not explain the multiple increase in the activity upon organic modification.

It was found that the pH value of the initial reaction suspensions is different and is determined by the nature of the photocatalyst. Thus, suspensions of the protonated titanates and alcohol derivatives are slightly acidic (pH ≈ 5–6) while those of the amine derivatives are slightly alkaline (pH ≈ 7.5–9). Previously, the authors of the paper [61] found that the photocatalytic activity of titanium dioxide $TiO_2$ in the reactions of hydrogen evolution from aqueous solutions of alcohols reaches maximum values in the region of pH ≈ 8–9. Taking this into account, one would expect an increased activity of the amine derivatives of the titanates compared to the alcohol derivatives due to the creation of optimal pH of the medium by the former. However, the data array obtained indicates that the amine derivatives do not demonstrate a clear advantage in the photocatalytic activity over the alcohol derivatives, and representatives of the latter are the most active samples among single-layer and three-layer titanates (HLT×MeOH/Pt, $HLT_3$×EtOH/Pt). Moreover, with the participation of the applicant's colleagues, it was shown that the photocatalytic activity of the *n*-butylamine derivative $HLT_3$×$BuNH_2$/Pt, in contrast to that of $TiO_2$, increases with decreasing pH [232].

A comparison of the pH values at the beginning ($pH_1$) and at the ending ($pH_2$) of photocatalytic experiments showed that hydrogen generation from aqueous solutions of methanol and carbohydrates in the presence of the highly active amine and alcohol derivatives is accompanied by a noticeable acidification of the medium to pH ≈ 3–3.5 already in the first hours of the reaction. This fact may indicate partial oxidation of methanol to formic acid, and carbohydrates to the corresponding aldonic and aldaric acids. To consider this issue using aqueous methanol as an example, Raman spectra of the reaction solutions were recorded after photocatalytic experiments of various durations carried out with the *n*-butylamine titanate $HLT_3$×$BuNH_2$/Pt (Fig. 53). It is easy to see that during the photocatalytic reaction there is a

decrease in the intensity of the bands corresponding to bond vibrations in the alcohol molecules (in particular, C–O at ≈ 1015 $cm^{-1}$) due to a decrease in its concentration in the solution. At the same time, new signals appear in the spectra, apparently corresponding to bending vibrations of the O–C–O (≈ 700 $cm^{-1}$) and H–C–O (≈ 1400 $cm^{-1}$) fragments in formic acid, as well as a new broadened band at 1695–1720 $cm^{-1}$, probably corresponding to stretching of the C=O bonds. In addition, a distinct peak appears in the spectra at ≈ 905 $cm^{-1}$, which cannot be attributed to the acid. Turning to the reference data made it possible to establish that the signals observed at ≈ 905 and ≈ 1710 $cm^{-1}$ coincide with the most intense bands in the spectrum of methyl formate (stretching of C–O and C=O in the ester group, respectively). In this case, the bending vibration of H–C–O (≈ 1400 $cm^{-1}$) is active in the spectra of both methyl formate and formic acid, while that of O–C–O (≈ 700 $cm^{-1}$) should be clearly observed only in the case of the latter.

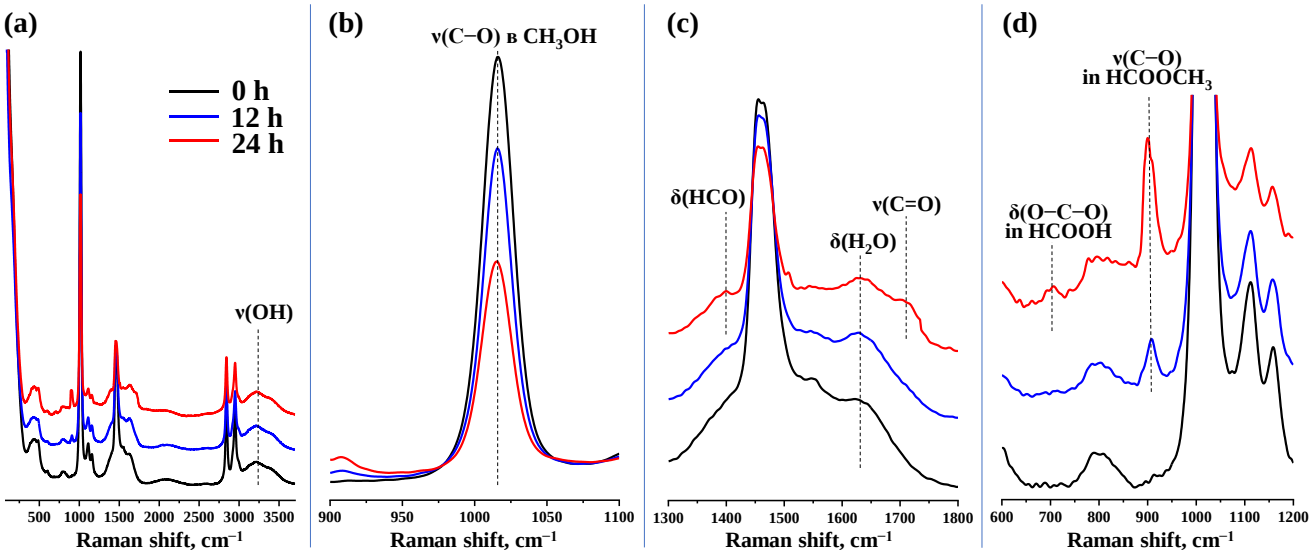


Fig. 53. Raman spectra of filtered 5% (mol.) aqueous methanol solutions before and after photocatalytic experiments of various durations with platinized *n*-butylamine derivative of the titanate $HLT_3$

Based on the presented data, it can be assumed that formic acid formed during the oxidation of methanol interacts with an excess of the latter under the conditions of a photocatalytic experiment, forming methyl formate. Meanwhile, the vibrational bands of both the acid and the ester remain relatively low-intensity even after almost half of the methanol in the solution has been consumed, which indirectly indicates the presence of other channels of the alcohol conversion that are not obvious from the Raman spectra (for example, complete oxidation to carbon dioxide and water with the release of the former from the solution). However, these issues require more detailed study.

3.2.5. Factors determining photocatalytic activity of the organic-inorganic derivatives

As was shown above, the organic modification of the interlayer space of the titanates under consideration made it possible to create new highly efficient photocatalytic materials for the processes of hydrogen production from aqueous organic solutions, which are many times superior in the activity to the initial titanates and the standard photocatalyst $TiO_2$ P25 Degussa. Moreover, the resulting compounds are interesting not only from an applied, but also from a fundamental point of view, since their physical-chemical behavior is extremely unusual both for heterogeneous photocatalysis in particular, and for catalysis as a field of chemical science in general. One of the general requirements for any catalysts is their stability under operating conditions, since irreversible changes in the structure and composition of a catalyst are usually accompanied by an inevitable deterioration in its catalytic activity and other functional properties. However, in the case of organic-inorganic derivatives of the titanates obtained in the framework of this study, this rule is formally violated: the most promising of them retain consistently high activity, despite partial or, in some cases, even almost complete degradation of the interlayer organic modifiers, and hydrogen is generated from the reaction solution truly catalytically. In other words, despite chemical instability (irreversible changes in the composition of the interlayer space), these materials are stable in the kinetic aspect (maintaining activity). In this case, interlayer organic modifiers of the least stable samples from a chemical point of view are retained in significant quantities at least during the first 40–50 min of the photocatalytic reaction, and after this time there is no noticeable decrease in the activity. Accordingly, at the initial stages of photocatalytic measurements, the observed activity corresponds to the organically modified sample, and at later stages, to the product of its in situ transformations occurring directly during photocatalysis, and the numerical activity data are almost identical. At the same time, a specific type of the introduced organic component affects the formation of the final photocatalyst during operation, since the photocatalytic activity of different derivatives is not the same. In general, the highest activities of the titanates under study were achieved after their modification with relatively short-chain components (ethylamine, ethoxy groups), however, this pattern requires testing on a wider range of objects.

Apparently, the key reason for the high photocatalytic activity of the organic-inorganic derivatives compared to the initial unmodified titanates is the increased accessibility of their

interlayer reaction zone for the reactant molecules due to the expansion of the latter with the introduced modifiers. In other words, the amines and alkoxy groups of alcohols significantly move apart adjacent perovskite blocks and thereby provide the possibility of diffusion of the reaction participants to interlayer active centers, which in the case of the initial titanates remain practically not involved in the photocatalytic process (Fig. 54, a). In this case, the efficiency of supplying reactants to the interlayer region is largely determined by the steric factor: in particular, relatively small methanol molecules diffuse more easily to the interlayer reaction centers than relatively large carbohydrate ones, which can be one of the key factors determining the greater activity of the samples in methanol solutions. Apparently, despite the partial or even almost complete degradation of the organic modifiers, the interlayer space remains sufficiently expanded and continues to fully function as an additional reaction zone at least as long as the photocatalyst is in the reaction medium, which explains the consistently high rate of the target reaction. In addition, the expanded interlayer space of the organic-inorganic derivatives can potentially serve as a site for the reduction of Pt nanoparticles along with the external surface (Fig. 54, b), thereby explaining the increased activity of the platinized organically modified samples due to the special properties of interlayer hydrogen evolution centers. This possibility is indicated by the presence of cocatalyst nanoparticles directly at the boundary of the crystal delamination regions (Fig. 51), however, the corresponding issue requires a separate detailed study.

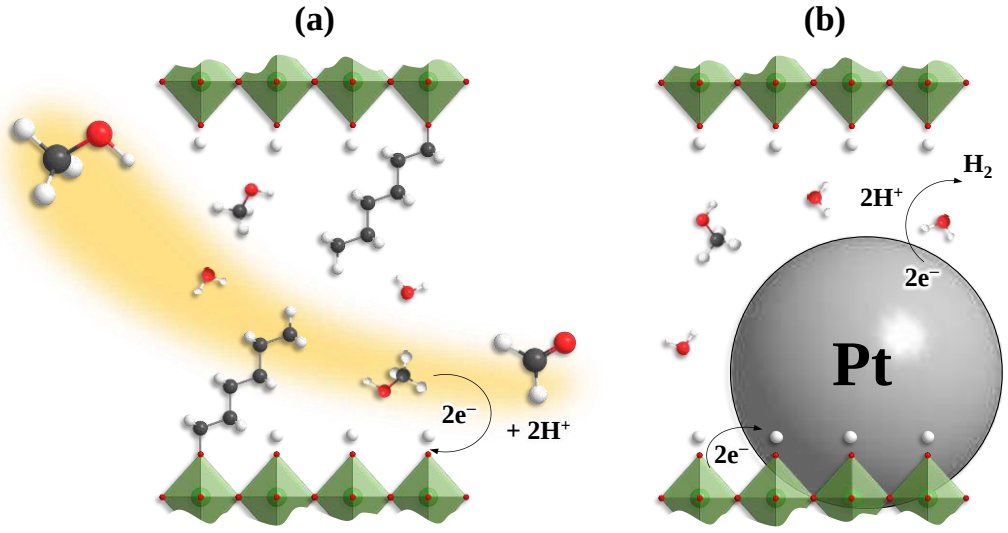


Fig. 54. Illustration of possible factors explaining photocatalytic properties of the organic-inorganic derivatives: increasing accessibility of the interlayer reaction zone for reactants (a) and reduction of the cocatalyst nanoparticles in this zone (b)

The increase in the hydrogen generation efficiency during the organic modification of the titanates may also be partly due to a slight increase in the average lifetime of photogenerated charge carriers, specific area of external surface, dispersibility in aqueous-organic media, and stability of the reaction suspensions towards sedimentation. However, the scale of changes in the aforementioned properties of the samples is not comparable with the multiplicity of increase in their photocatalytic activity, which is why these changes most probably have only a minor effect on it.

### 3.2.6. Comparison of organic-inorganic derivatives of the titanates with those of the niobates $HA_2Nb_3O_{10}$ (A = Ca, Sr)

With the direct participation of the applicant, series of amine and alcohol derivatives of three-layer Dion-Jacobson niobates $HCa_2Nb_3O_{10}$ ($HCN_3$) and $HSr_2Nb_3O_{10}$ ($HSN_3$) were also obtained and studied [240–242].

It was shown that organic modification of the niobates, like that of the titanates, leads to a significant increase in their interlayer distance from 16 to 35 Å, proportional to the length of the introduced modifiers. In this case, the optical band gap lies in the range of 3.45–3.62 eV for $HCN_3$ derivatives and 3.27–3.34 eV for $HSN_3$ ones, which is why the range of functioning of the corresponding compounds as photocatalysts is the middle and near ultraviolet. Specific surface area of the initial protonated niobates is 4–5 $m^2/g$ and its noticeable increase occurs only upon the formation of *n*-hexanol and *n*-decanol derivatives, in which case its value reaches 10–11 $m^2/g$.

Photocatalytic activity of protonated forms of the niobate $HCN_3$, titanate $HLT_3$ and their most highly active organic-inorganic derivatives in the platinized state is presented in Fig. 55. The key difference between the initial protonated niobates $HCN_3$ and $HSN_3$ and the protonated titanates considered in this work is high hydration of the niobates' interlayer space, which apparently explains their significantly higher photocatalytic activity. Thus, the niobate $HCN_3$ forms highly hydrated compounds containing up to 1.5 water molecules per formula unit, and when in an aqueous medium, the actual degree of its hydration can be even higher. At the same time, the titanates HLT (HNT) and $HLT_3$ ($HNT_3$) contain no more than 0.1–0.2 units of water in the interlayer space and practically do not undergo secondary hydration. At the same time, photocatalytic activity of $HCN_3$/Pt in 1% (mol.) aqueous solutions of methanol, glucose and xylose exceeds that exhibited by $HLT_3$/Pt by approximately 6, 1.5 and 1.8 times, respectively

(Fig. 55). Meanwhile, in the reaction of hydrogen evolution from pure water, $HLT_3$/Pt demonstrates 1.7 times greater efficiency than $HCN_3$/Pt.

Most organic-inorganic derivatives of the niobate $HCN_3$ noticeably outperform its initial protonated form in the photocatalytic performance (φ = 7.80% with Pt), however, due to the relatively high activity of the latter, this difference is less pronounced than in the case of the titanates. Among the platinized amine derivatives, the *n*-butylamine sample $HCN_3$×$BuNH_2$/Pt (φ = 14.2%) exhibits the greatest activity in a 1% (mol.) aqueous solution of methanol, and among the alcohol derivatives, the most active is the ethanol one $HCN_3$×EtOH/Pt (φ = 20.6%). When using organic-inorganic derivatives of the titanates $HLT_3$×$EtNH_2$/Pt and $HLT_3$×EtOH/Pt under the same conditions, twice the apparent quantum efficiency is achieved φ = 31.9% and 40.1%, respectively, which makes them significantly more promising photocatalytic materials for processing water-methanol mixtures to produce hydrogen fuel. Moreover, in series of the organically modified niobates, as in those of the titanates, there is generally a positive correlation of the activity with the amount of intercalated water, which indicates the participation of the latter in the photocatalytic process along with methanol. At the same time, the organically modified niobates have some advantage over the titanates in the reactions of hydrogen evolution from 1% (mol.) aqueous solutions of carbohydrates: in the presence of the most active derivative $HCN_3$×$BuNH_2$/Pt, quantum efficiency φ = 7.45% and 8.89% is achieved in glucose and xylose, respectively, while the most active titanate $HLT_3$×EtOH/Pt demonstrates φ = 6.05% and 7.13% under the same conditions (Fig. 55).

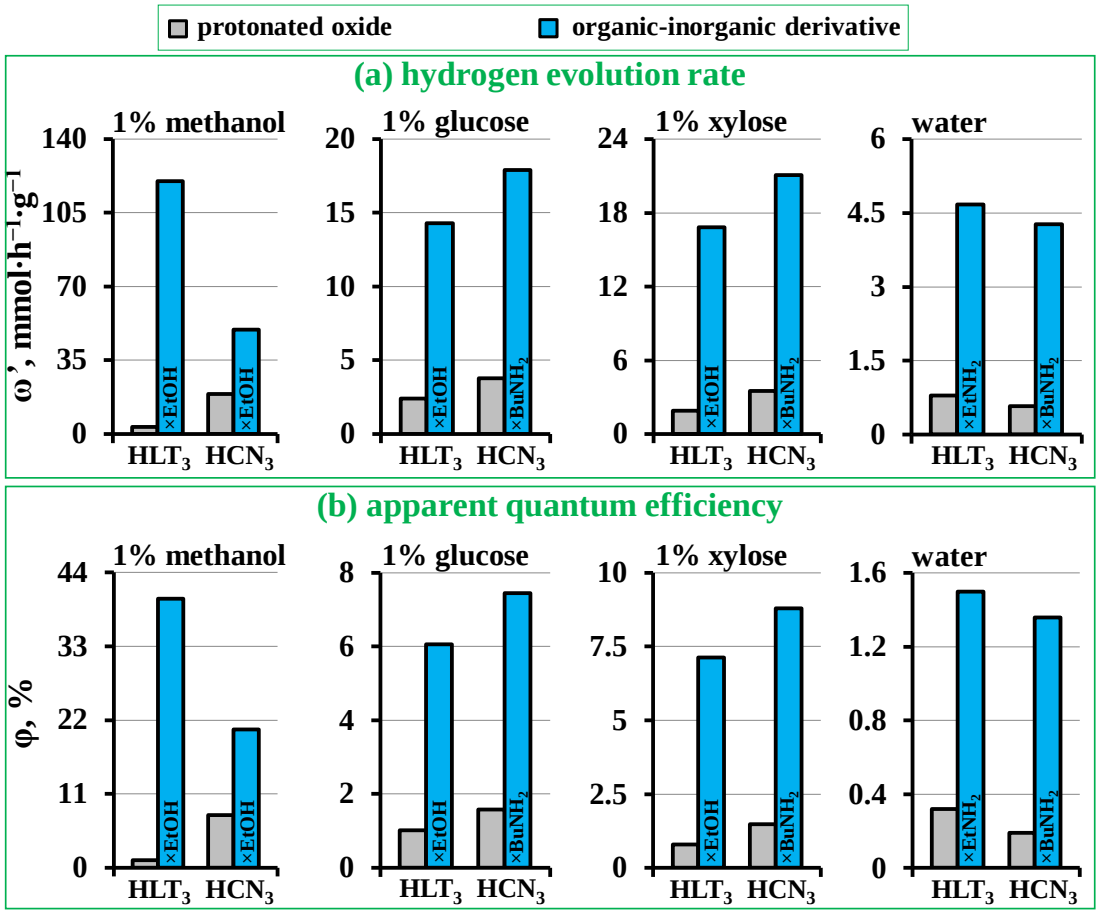


Fig. 55. Comparison of photocatalytic activity of platinized protonated forms and organic-inorganic derivatives of the titanate $HLT_3$ and niobate $HCN_3$ in hydrogen evolution reactions

When generating hydrogen from pure water, the most active organically modified titanates are approximately 1.1 times more efficient than the organic-inorganic niobates (Fig. 55), however, in the case of both, a gradual decrease in the activity is observed over time.

Analysis of selected platinized organic-inorganic derivatives of the niobate $HCN_3$ after standard photocatalytic experiments in aqueous methanol showed that, as in the case of titanates, partial ($HCN_3$×$MeNH_2$, $HCN_3$×$OcNH_2$, $HCN_3$×MeOH, $HCN_3$×DcOH) or almost complete ($HCN_3$×$BuNH_2$, $HCN_3$×EtOH) degradation of interlayer organic modifiers takes place, which practically does not affect the functioning efficiency of the most active samples.

Summarizing the above, we can conclude that the organic modification of the interlayer space of both the considered Ruddlesden-Popper titanates and Dion-Jacobson niobates is an effective approach to the creation of new efficient photocatalysts for hydrogen production processes. That being said, the greatest activities in the presence of the platinum cocatalyst are exhibited by the materials with relatively short-chain interlayer modifiers (ethylamine, *n*-butylamine, ethoxy groups). Materials based on the three-layer titanate $HLT_3$ seem more

promising for the photocatalytic processing of aqueous methanol solutions, and those based on the three-layer niobate $HCN_3$ – carbohydrate solutions. At the same time, the most active derivatives $HLT_3$ and $HCN_3$, despite the degradation of introduced modifiers under photocatalysis conditions, stably maintain high efficiency of hydrogen generation from aqueous methanol.

### 3.3. Derivatives of the titanates with aromatic modifiers as photocatalysts for hydrogen generation

In addition to the considered amine and alcohol derivatives, a series of hybrid organic-inorganic photocatalysts with covalently bonded aromatic modifiers were obtained and studied based on the three-layer titanate $HLT_3$. The modifiers were mono-, di- and triatomic phenols (phenol itself, catechol, resorcinol, hydroquinone, pyrogallol), phenol derivatives (salicylic acid, 2-allylphenol, 4-phenylphenol), as well as polycyclic aromatic hydroxy compounds (2-naphthol, 8-hydroxyquinoline, alizarin) (Fig. 56).

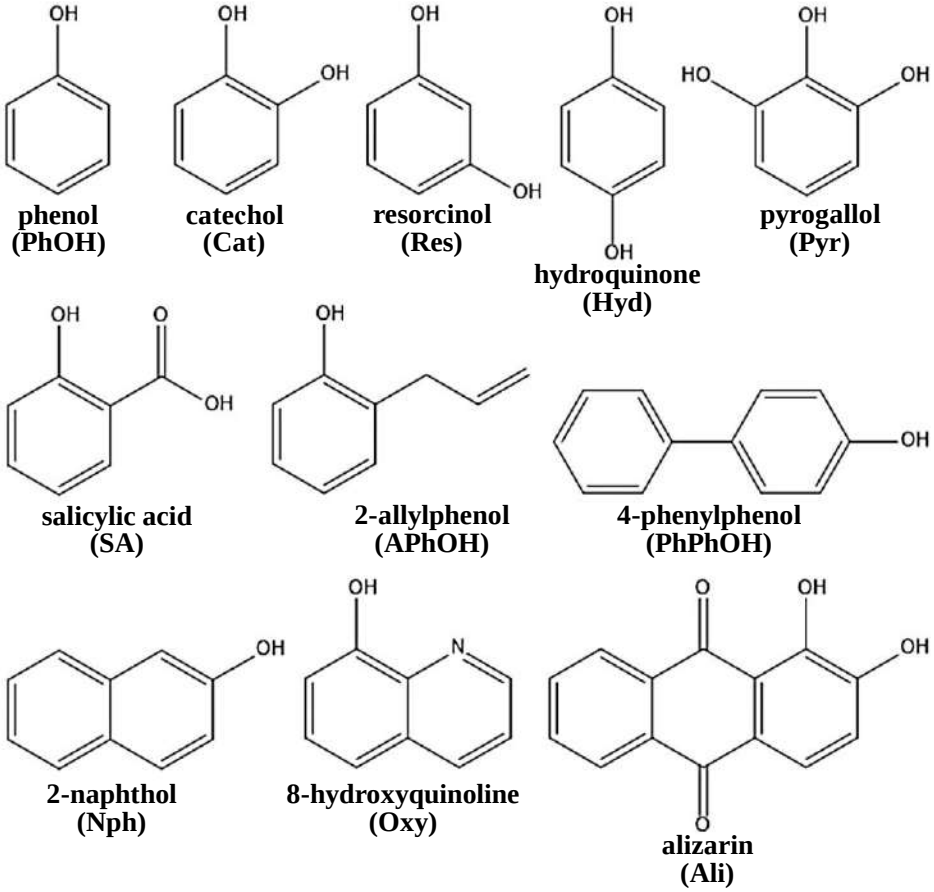


Fig. 56. Aromatic compounds used to modify the interlayer space of the titanate $HLT_3$

### 3.3.1. Characterization of the derivatives with aromatic modifiers

#### 3.3.1.1. Structure and composition of the derivatives with aromatic modifiers

X-ray diffraction analysis of the $HLT_3$ titanate derivatives with aromatic modifiers showed that the resulting compounds do not contain significant amounts of impurity crystalline phases and are characterized by a significantly expanded interlayer space compared to the initial protonated titanate while maintaining the lattice parameter *a* (Fig. 57, Table 13). The interlayer distance of most of the obtained samples lies in the range of 24–27 Å. The exception is the 4-phenylphenol derivative, whose large interlayer space width ($d$ = 31 Å) is caused by the presence of a large substituent in the para position of the grafted aromatic ring.

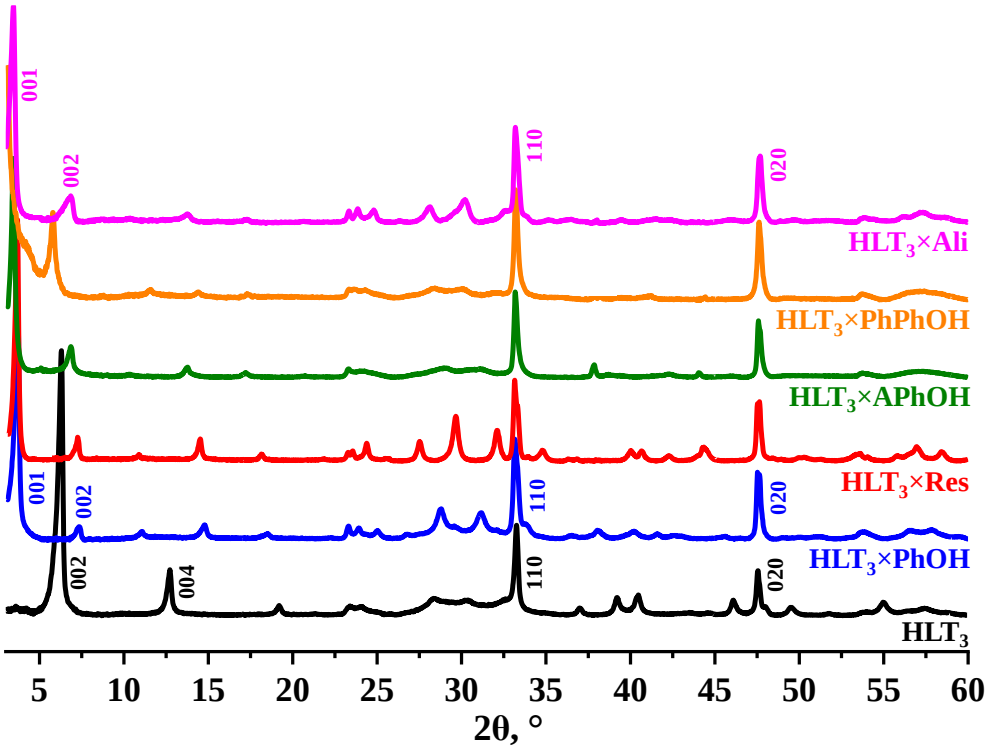


Fig. 57. X-ray diffraction patterns of the protonated titanate $HLT_3$ and its selected derivatives with aromatic modifiers

Table 13. Characterization of the protonated titanate $HLT_3$ and its selected derivatives with aromatic modifiers: lattice parameters in the tetragonal system *a*, *c*, interlayer distances *d*, quantitative compositions in the form $H_{2-x}Ln_2Ti_3O_{10-x}\cdot xRO\cdot yH_2O$

| Sample | Structure | | | Composition | |
|---|---|---|---|---|---|
| | *a*, Å | *c*, Å | *d*, Å | x | y |
| $HLT_3$ | 3.79 | 27.2 | 13.6 | – | 0.20 |
| $HLT_3$×PhOH | 3.83 | 24.3 | 24.3 | 0.70 | 0.25 |
| $HLT_3$×Cat | 3.84 | 24.4 | 24.4 | 0.85 | 0.40 |
| $HLT_3$×Res | 3.84 | 24.7 | 24.7 | 0.95 | 0.50 |
| $HLT_3$×Hyd | 3.83 | 25.3 | 25.3 | 0.85 | 0.30 |
| $HLT_3$×Pyr | 3.83 | 25.3 | 25.3 | 0.80 | 0.45 |
| $HLT_3$×SA | 3.83 | 26.3 | 26.3 | 0.95 | 0.30 |

| Sample | Structure | | | Composition | |
|---|---|---|---|---|---|
| | *a*, Å | *c*, Å | *d*, Å | x | y |
| $HLT_3$×APhOH | 3.83 | 26.1 | 26.1 | 0.60 | 0.85 |
| $HLT_3$×PhPhOH | 3.83 | 31.0 | 31.0 | 0.80 | 0.25 |
| $HLT_3$×Nph | 3.83 | 26.5 | 26.5 | 0.90 | 0.60 |
| $HLT_3$×Oxy | 3.83 | 25.1 | 25.1 | 0.55 | 0.35 |
| $HLT_3$×Ali | 3.82 | 25.8 | 25.8 | 0.55 | 0.15 |

The fact of the formation of derivatives with aromatic modifiers is confirmed by appearance of the bands in Raman spectra of the samples (Fig. 58, a) corresponding to bending vibrations of the aromatic ring (1000–1200 $cm^{-1}$) and stretching ones of the C–C (1440–1590 $cm^{-1}$) and C–H (3010–3070 $cm^{-1}$) bonds in it. Also bands of stretching modes of C–O (1280–1310 $cm^{-1}$), as well as C=C (1630 $cm^{-1}$ in the 2-allylphenol derivative) and C=O (1665 $cm^{-1}$ in the alizarin derivative) are observed. In addition, the spectra clearly show bands in the region of 2820–2980 $cm^{-1}$, which probably correspond to residual *n*-butylamine from $HLT_3$×$BuNH_2$, which was used as a precursor in the synthesis of all the derivatives with aromatic compounds. Grafting of aromatic compounds is also accompanied by pronounced changes in the Raman spectrum in the region of Ti–O vibrational modes in terminal perovskite octahedra (750–1000 $cm^{-1}$), which indicates a significant influence of the modifier on the inorganic matrix.

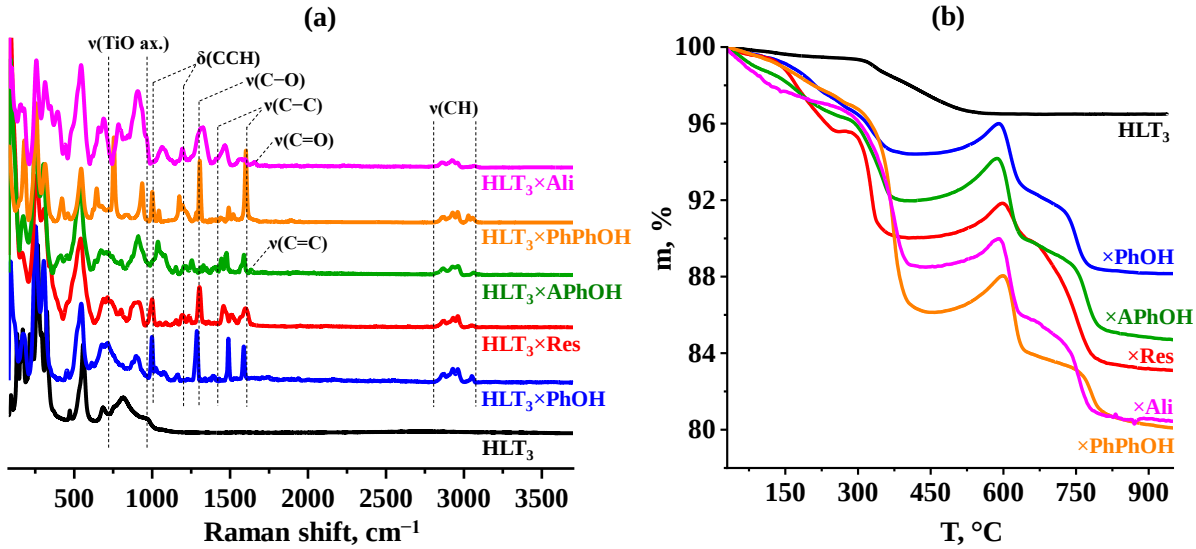


Fig. 58. Raman spectra (a) and thermogravimetric curves (b) of the protonated titanate $HLT_3$ and its selected derivatives with aromatic modifiers

Calculation of the quantitative composition of the derivatives with aromatic modifiers based on CHN-analysis and thermogravimetry data (Fig. 58, b) showed that the resulting compounds contain on average 0.4 units of an aromatic component and 0.1 units of residual *n*-

butylamine per proton of the initial titanate, as well as a certain amount of intercalated water (Table 13).

3.3.1.2. Light absorption region and band edge potentials

The main change in the properties of the titanate $HLT_3$ when grafting aromatic components, easily detectable with the naked eye, was the appearance of a pronounced color, the nature of which depends on the specific modifier. It is important to note that both the initial titanate and all the aromatic compounds used (Fig. 56), with the exception of alizarin, are themselves uncolored substances. Thus, the appearance of light absorption in the visible region of the spectrum occurs in the process of integration of the inorganic matrix and aromatic modifiers into a single hybrid organic-inorganic material, and is not a simple superposition of the properties of the individual components. A possible reason for the photosensitization that occurs in this case is the coupling of the electronic subsystems of the layered perovskite and aromatic structures, but the specific mechanism for its implementation requires further study. At the same time, the coloring of titanium dioxide $TiO_2$ colloids when catechol and hydroxybenzoic acids are bound to their surface was previously noted in the literature, explained by the authors through the formation of a ligand–metal charge transfer complex [243,244].

Diffuse reflectance spectra of the derivatives obtained, transformed into Kubelka-Munk coordinates (Fig. 59) indicate that the acquisition of color by the samples is due to a pronounced shift of the long-wavelength edge of their intrinsic light absorption into the visible range, and not the appearance of individual new bands. This trend also occurs in the case of the derivative with alizarin, which itself is a dye. However, the spectrum of the organic-inorganic sample does not represent a superposition of the spectra of the components: alizarin titanate is characterized by a longer wavelength position of the absorption edge than alizarin in its individual form, which indicates the coupling of the electronic subsystems of the perovskite matrix and the grafted modifier.

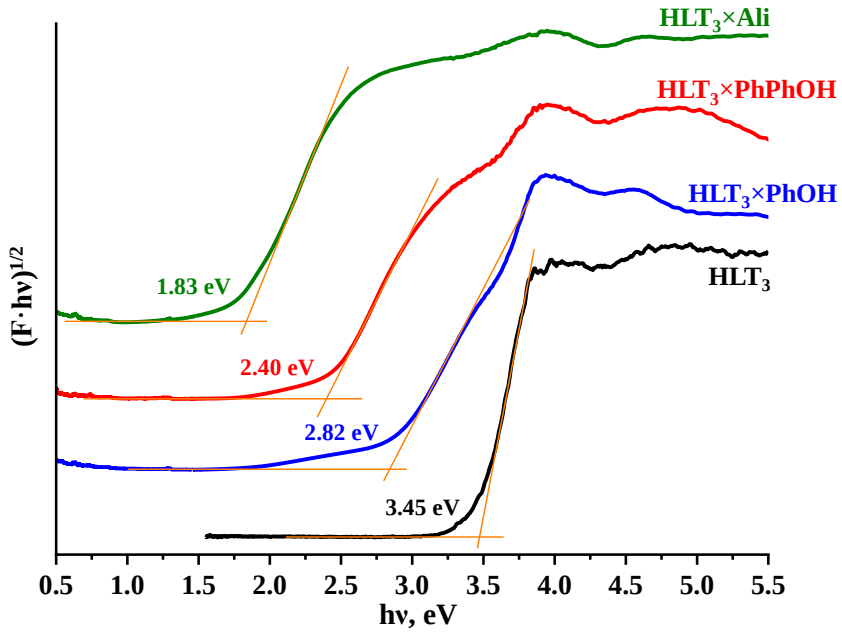


Fig. 59. Kubelka-Munk plots for the protonated titanate $HLT_3$ and its selected derivatives with aromatic modifiers

The greatest optical bandgap energy is observed in the case of the titanate derivative with phenol ($E_g$ = 2.82 eV), and the lowest – with pyrogallol ($E_g$ = 1.60 eV), in which the long-wave absorption edge reaches the near-infrared area. The $E_g$ value of the other derivatives, except for alizarin one, lies in the range of 2.2–2.7 eV (Table 14). That being said, the narrowing of the band gap of the samples is achieved mainly due to the rise of the valence band top $E_V$, while the position of the conduction band bottom $E_C$ does not change significantly. Due to the significant expansion of the absorption range, the derivatives with aromatic modifiers are potential photocatalysts, being active not only under ultraviolet, but also under visible radiation.

Table 14. Characterization of the protonated titanate $HLT_3$ and its derivatives with aromatic modifiers: intrinsic absorption range (optical bandgap energy $E_g$, long-wave absorption edge $\lambda_{max}$), approximate potentials of energy band edges (valence band top $E_V$ and conduction band bottom $E_C$) relative to SHE

| Sample | Light absorption | | Band edges (≈) | |
|---|---|---|---|---|
| | $E_g$, eV | $\lambda_{max}$, nm | $E_V$, V | $E_C$, V |
| $HLT_3$ | 3.45 | 359 | 3.0 | −0.5 |
| $HLT_3$×PhOH | 2.82 | 440 | 2.3 | −0.5 |
| $HLT_3$×Cat | 2.21 | 561 | – | – |
| $HLT_3$×Res | 2.48 | 500 | 2.0 | −0.5 |
| $HLT_3$×Hyd | 2.44 | 508 | – | – |
| $HLT_3$×Pyr | 1.60 | 775 | | |
| $HLT_3$×SA | 2.65 | 468 | | |
| $HLT_3$×APhOH | 2.42 | 512 | 2.0 | −0.4 |
| $HLT_3$×PhPhOH | 2.40 | 517 | 2.0 | −0.4 |
| $HLT_3$×Nph | 2.32 | 534 | – | – |

| Sample | Light absorption | | Band edges (≈) | |
|---|---|---|---|---|
| | $E_g$, eV | $\lambda_{max}$, nm | $E_V$, V | $E_C$, V |
| $HLT_3$×Oxy | 2.44 | 508 | | |
| $HLT_3$×Ali | 1.83 | 678 | 1.4 | −0.4 |

3.3.2. Photocatalytic activity of the derivatives with aromatic modifiers in hydrogen generation reactions

Photocatalytic activity of photosensitized derivatives of the three-layer titanate $HLT_3$ was tested in the reaction of hydrogen evolution from a 1% (mol.) aqueous solution of methanol using a DRT-125 mercury lamp, emitting predominantly in the ultraviolet region, an Osram xenon lamp XBO-150, which has a spectrum close to the solar one, as well as a source of purely visible light LED-425 with an emission maximum at 425 nm. When working with mercury and xenon lamps, a light filter with transmission $\lambda > 220$ nm was used. Kinetic curves of hydrogen evolution in the presence of selected photocatalysts are presented in Fig. 60, data on the photocatalytic activity of all the samples modified with aromatic components are summarized in Table 15 and for platinized compounds are visualized in the form of bar graphs in Fig. 61.

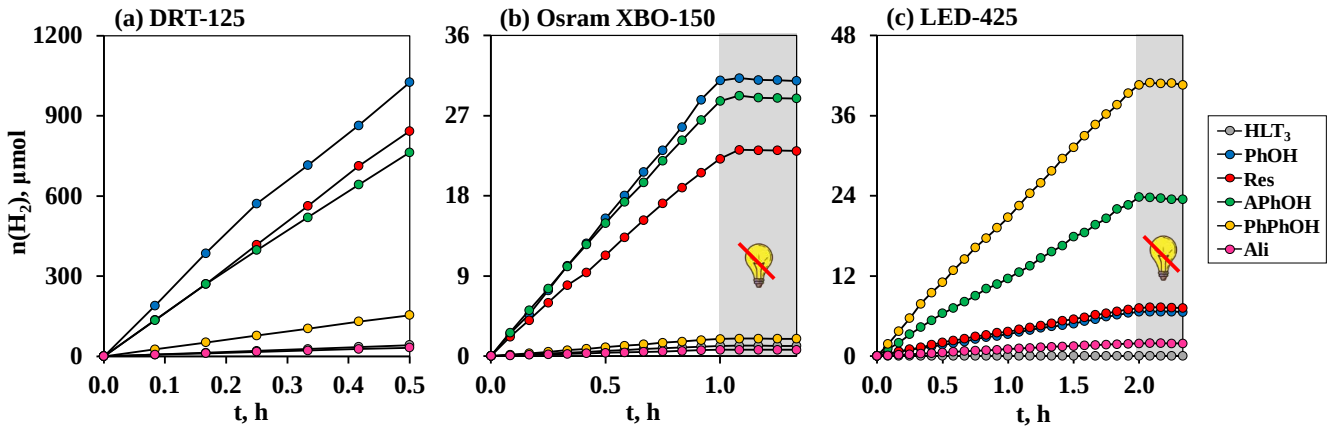


Fig. 60. Kinetic curves of photocatalytic hydrogen evolution from a 1% (mol.) aqueous solution of methanol in the presence of the platinized protonated titanate $HLT_3$ and its selected derivatives with aromatic modifiers

It was found that the introduction of aromatic modifiers into the interlayer space of the titanate $HLT_3$, like insertion of the aliphatic components considered previously, leads to a manifold increase in the hydrogen generation rate from aqueous methanol under the radiation of a DRT-125 lamp. Thus, when going from the protonated form $HLT_3$ to the 8-hydroxyquinoline derivative $HLT_3$×Oxy, the rate of the target reaction increases approximately 285 times, reaching the highest value among all non-platinized photocatalysts studied in this

work, 14.5 mmol·h$^{-1}$·g$^{-1}$ (φ = 2.16%). However, it should be noted that, despite the high rates of hydrogen evolution, most derivatives with aromatic modifiers are formally inferior to the amine and alcohol titanates in terms of the quantum efficiency of the process due to a wider range of light absorption. After reduction of the cocatalyst nanoparticles on the surface of the samples, the highest rate of 79.5 mmol·h$^{-1}$·g$^{-1}$ and quantum efficiency of the reaction of 12.5% are achieved in the case of the phenol titanate $HLT_3$×PhOH/Pt.

Table 15. Photocatalytic activity of the protonated titanate $HLT_3$ and its derivatives with aromatic modifiers in the reaction of hydrogen evolution from a 1% (mol.) aqueous solution of methanol under radiation from three different sources

| | Sample | Without cocatalyst | | | With 1% Pt cocatalyst | | |
|---|---|---|---|---|---|---|---|
| | | ω, μmol·h$^{-1}$ | ω′, mmol·h$^{-1}$·g$^{-1}$ | φ, % | ω, μmol·h$^{-1}$ | ω′, mmol·h$^{-1}$·g$^{-1}$ | φ, % |
| DRT-125 (λ > 220 nm) | $HLT_3$ | 1.27 | 0.051 | 0.017 | 85.1 | 3.40 | 1.14 |
| | ×PhOH | 176 | 7.02 | 1.10 | 1990 | 79.5 | 12.5 |
| | ×Cat | 34.0 | 1.36 | 0.14 | 371 | 14.8 | 1.50 |
| | ×Res | 235 | 9.39 | 1.41 | 1720 | 68.7 | 10.3 |
| | ×Hyd | 72.5 | 2.90 | 0.43 | 1350 | 53.8 | 8.01 |
| | ×Pyr | 30.8 | 1.23 | 0.089 | 80.0 | 3.20 | 0.23 |
| | ×SA | 74.5 | 2.98 | 0.46 | 1440 | 57.6 | 8.88 |
| | ×APhOH | 111 | 4.45 | 0.66 | 1500 | 60.1 | 8.95 |
| | ×PhPhOH | 20.2 | 0.81 | 0.12 | 303 | 12.1 | 1.79 |
| | ×Nph | 2.57 | 0.10 | 0.015 | 11.0 | 0.44 | 0.064 |
| | ×Oxy | 363 | 14.5 | 2.16 | 955 | 38.2 | 5.69 |
| | ×Ali | 6.38 | 0.26 | 0.019 | 63.7 | 2.55 | 0.19 |
| XBO-150 (λ > 220 nm) | $HLT_3$ | 0 | 0 | 0 | 1.19 | 0.048 | 0.93 |
| | ×PhOH | 13.0 | 0.52 | 2.40 | 31.5 | 1.26 | 5.83 |
| | ×Cat | 0.09 | 0.004 | 0.005 | 2.00 | 0.080 | 0.11 |
| | ×Res | 1.80 | 0.072 | 0.16 | 22.1 | 0.89 | 1.99 |
| | ×Hyd | 0.83 | 0.033 | 0.069 | 8.68 | 0.35 | 0.72 |
| | ×Pyr | 0.03 | 0.001 | 0.001 | 0.63 | 0.025 | 0.020 |
| | ×SA | 16.5 | 0.66 | 2.26 | 38.4 | 1.54 | 5.26 |
| | ×APhOH | 0.15 | 0.006 | 0.012 | 28.4 | 1.14 | 2.26 |
| | ×PhPhOH | 0.08 | 0.003 | 0.006 | 1.97 | 0.079 | 0.15 |
| | ×Nph | 0.05 | 0.002 | 0.003 | 0.22 | 0.009 | 0.014 |
| | ×Oxy | 4.54 | 0.18 | 0.37 | 13.5 | 0.54 | 1.11 |
| | ×Ali | 0.05 | 0.002 | 0.002 | 0.67 | 0.027 | 0.024 |
| LED-425 (λ = 425 nm) | $HLT_3$ | 0 | 0 | 0 | 0 | 0 | 0 |
| | ×PhOH | 0.04 | 0.001 | – | 3.24 | 0.13 | 0.006 |
| | ×Cat | 0.07 | 0.003 | | 3.02 | 0.12 | 0.006 |
| | ×Res | 0.06 | 0.002 | | 3.56 | 0.14 | 0.007 |
| | ×Hyd | 0.03 | 0.001 | | 1.65 | 0.066 | 0.003 |
| | ×Pyr | 0 | 0 | | 0.11 | 0.005 | 0.0002 |
| | ×SA | 0.11 | 0.004 | | 1.82 | 0.073 | 0.004 |
| | ×APhOH | 0.02 | 0.001 | | 11.7 | 0.47 | 0.023 |
| | ×PhPhOH | 0.02 | 0.001 | | 20.5 | 0.82 | 0.041 |

| | Sample | Without cocatalyst | | | With 1% Pt cocatalyst | | |
|---|---|---|---|---|---|---|---|
| | | ω, μmol·h$^{-1}$ | ω′, mmol·h$^{-1}$·g$^{-1}$ | φ, % | ω, μmol·h$^{-1}$ | ω′, mmol·h$^{-1}$·g$^{-1}$ | φ, % |
| | ×Nph | 0.06 | 0.002 | | 2.86 | 0.11 | 0.006 |
| | ×Oxy | 0.02 | 0.001 | | 8.34 | 0.33 | 0.017 |
| | ×Ali | 0.02 | 0.001 | | 1.04 | 0.041 | 0.002 |

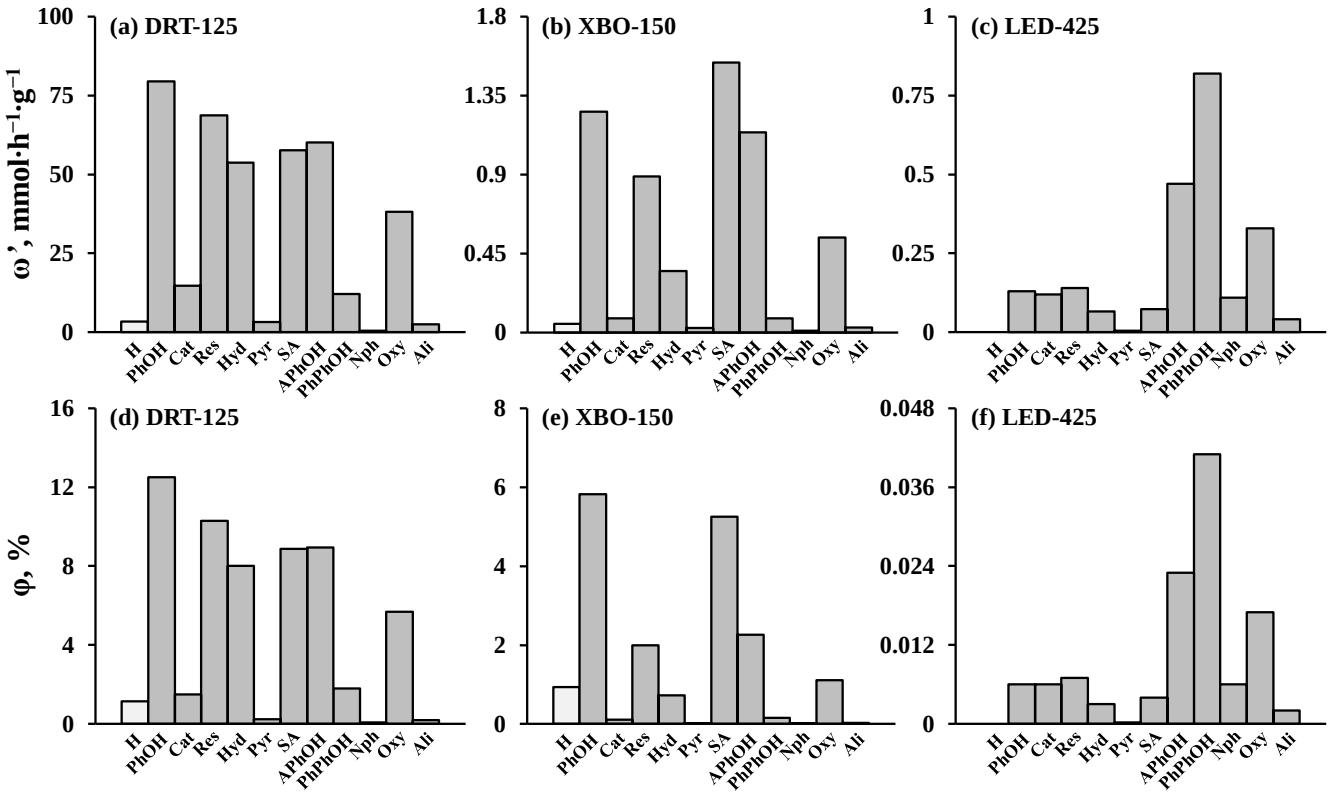


Fig. 61. Comparison of photocatalytic activity of the platinized protonated titanate $HLT_3$ and its derivatives with aromatic modifiers in the reaction of hydrogen evolution from a 1% (mol.) aqueous solution of methanol under radiation from three different sources

Photosensitization of the titanate $HLT_3$ by grafted aromatic components made it possible for the final materials to function effectively as photocatalysts under radiation from an Osram XBO-150 xenon lamp, which is conditionally close in spectral composition to sunlight. The most active sample in terms of the hydrogen generation rate was the derivative with salicylic acid $HLT_3$×SA (0.66 mmol·h$^{-1}$·g$^{-1}$, 2.26% without Pt and 1.54 mmol·h$^{-1}$·g$^{-1}$, 5.26% with Pt), and from the point of view of apparent quantum efficiency – the phenol derivative $HLT_3$×PhOH (0.52 mmol·h$^{-1}$·g$^{-1}$, 2.40% without Pt and 1.26 mmol·h$^{-1}$·g$^{-1}$, 5.83% with Pt). That being said, the initial protonated titanate $HLT_3$ without platinization does not exhibit photocatalytic activity at all under the same conditions, and in the presence of the cocatalyst, its activity does not exceed 0.048 mmol·h$^{-1}$·g$^{-1}$ (φ = 0.93%).

It was also found that most of the derivatives of $HLT_3$ with aromatic components obtained are capable of functioning as photocatalysts under purely visible radiation (LED-425 source), while the range of operation of the initial titanate is limited to ultraviolet radiation due to the relatively wide band gap ($E_g$ = 3.45 eV). In this case, the greatest activity is exhibited by the derivatives with 4-phenylphenol $HLT_3$×PhPhOH/Pt (0.82 $mmol \cdot h^{-1} \cdot g^{-1}$, 0.041%), 2-allylphenol $HLT_3$×APhOH/Pt (0.47 $mmol \cdot h^{-1} \cdot g^{-1}$, 0.023%) and 8-hydroxyquinoline $HLT_3$×Oxy/Pt (0.33 $mmol \cdot h^{-1} \cdot g^{-1}$, 0.017%). Although the currently achieved efficiencies of hydrogen generation under purely visible radiation are not very high, the strategy of modifying layered materials with photosensitizing aromatic components is of interest for the further development of new photocatalysts, since it allows expanding the spectral range of their operation while maintaining the functional advantages of the initial layered matrix.

It should also be noted that the highest rates of hydrogen generation from aqueous methanol, achieved when using three different radiation sources, occur with different photocatalysts (Fig. 61). In particular, under purely visible light from the LED-425 source, emitting in a narrow range with a maximum at 425 nm, the most active is the 4-phenylphenol titanate $HLT_3$×PhPhOH/Pt, while under the radiation of the DRT-125 lamp ($\lambda > 220$ nm) this sample is inferior in activity to many other derivatives. One of the possible reasons for this is that the photocatalytic activity of the samples when using the mercury lamp is predominantly determined by the absorption of the ultraviolet part of its emission spectrum, the possibility of which is mainly due to the perovskite matrix itself. In this case, the main role of aromatic modifiers is to expand the interlayer reaction zone and increase the accessibility of the active centers localized in it for reactant molecules. Smaller modifiers (for example, grafted phenol) provide, on average, better accessibility to the interlayer reaction centers than larger analogues (such as 4-phenylphenol), which can sterically limit the supply of reactants to the perovskite block. When using the LED-425 source, apparently, the decisive factor is the efficiency of absorption of light in a narrow spectral range with the formation of reactive electron-hole pairs, depending, among other things, on the specific coupling of the electronic subsystems of the perovskite matrix and the aromatic modifier, while the steric factor is somewhat less important.

### 3.3.3. Stability of the derivatives with aromatic modifiers under photocatalysis conditions

Stability of selected derivatives with grafted aromatic components $HLT_3$×Ar (Ar = PhOH, Res, APhOH, PhPhOH, Ali) was studied by analyzing the final samples isolated after standard photocatalytic measurements under the radiation of a DRT-125 mercury lamp ($\lambda > 220$ nm) for a duration of $\approx 2.5$ h. Since the operating conditions of the photocatalysts under a mercury lamp are more severe than when using a xenon lamp or an LED emitter, in the latter two cases one can expect a higher stability of the samples to photodegradation of the introduced aromatic components.

Using X-ray diffraction methods (Fig. 62, a), Raman spectroscopy (Fig. 62, b), CHN-analysis and thermogravimetry, it was found that the most stable under photocatalysis conditions are the 4-phenylphenol and alizarin derivatives: after 2.5 h of operation under ultraviolet and visible radiation, the aromatic modifier in these photocatalysts is retained in full, and the interlayer space is additionally expands due to secondary hydration (Table 16). During photocatalysis, the 2-allylphenol titanate retains at least two-thirds of the initial amount of the aromatic component, but the interlayer distance of the sample decreases by 5.8 Å, which may also be due to degradation or deintercalation of residual *n*-butylamine, initially contained in all the aromatic derivatives. At the same time, the phenol and resorcinol titanates turned out to be much less stable, having lost more than two-thirds of the grafted modifiers during photocatalytic hydrogen generation (Table 16).

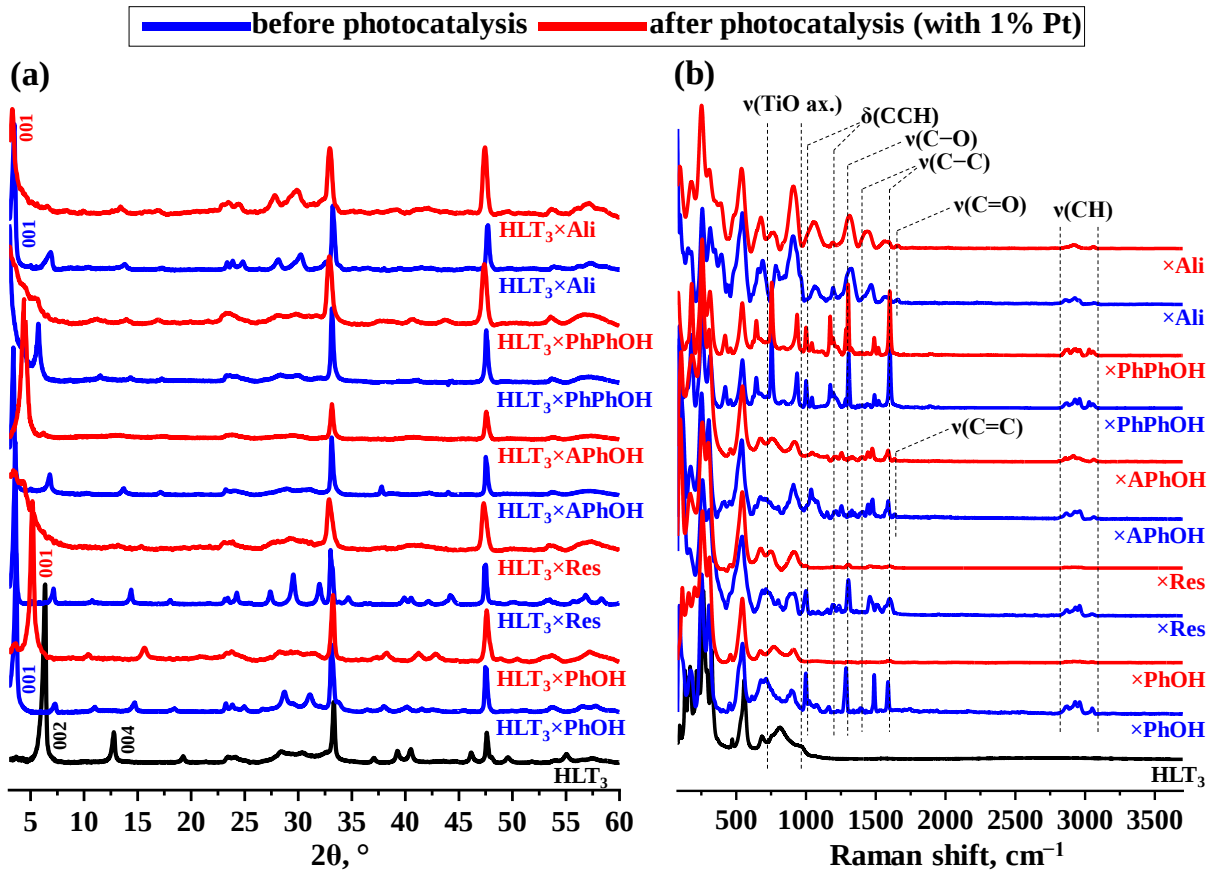


Fig. 62. X-ray diffraction patterns (a) and Raman spectra (b) of selected titanate derivatives $HLT_3$ with aromatic modifiers before and after photocatalytic experiments in a 1% (mol.) aqueous solution of methanol under radiation from a DRT-125 lamp (λ > 220 nm)

Table 16. Interlayer distances *d*, amounts of aromatic modifier x and intercalated water y per formula unit, optical bandgap energies $E_g$ and long-wavelength absorption edges $\lambda_{max}$ for selected titanate derivatives $HLT_3$ before and after photocatalytic experiments in 1% (mol.) aqueous methanol solution under radiation from a DRT-125 lamp (λ > 220 nm)

| Sample | | *d*, Å | x | y | $E_g$, eV | $\lambda_{max}$, nm |
|---|---|---|---|---|---|---|
| $HLT_3$ | | 13.6 | – | 0.20 | 3.45 | 359 |
| $HLT_3$×PhOH | before | 24.3 | 0.70 | 0.25 | 2.82 | 440 |
| | after | 17.1 | 0.20 | 0.70 | 3.30 | 376 |
| $HLT_3$×Res | to | 24.7 | 0.95 | 0.50 | 2.48 | 500 |
| | after | 17.4 | 0.30 | 1.00 | 3.11 | 399 |
| $HLT_3$×APhOH | to | 26.1 | 0.60 | 0.85 | 2.42 | 512 |
| | after | 20.3 | 0.40 | 1.10 | 2.42 | 512 |
| $HLT_3$×PhPhOH | to | 31.0 | 0.80 | 0.25 | 2.40 | 517 |
| | after | 31.5 | 0.80 | 0.50 | 2.40 | 517 |
| $HLT_3$×Ali | to | 25.8 | 0.55 | 0.15 | 1.83 | 678 |
| | after | 26.5 | 0.55 | 0.30 | 1.83 | 678 |

Study of the final samples using diffuse reflectance spectroscopy with the Kubelka-Munk transformation (Fig. 63, Table 16) showed that the position of the long-wavelength light absorption edge of 4-phenylphenol, 2-allylphenol and alizarin derivatives of the titanate is

stably maintained when these compounds are used as photocatalysts for hydrogen generation. At the same time, the degradation of grafted phenol and resorcinol is accompanied by an inevitable increase in the optical bandgap energy of the corresponding samples and a loss of light absorption in the visible region.

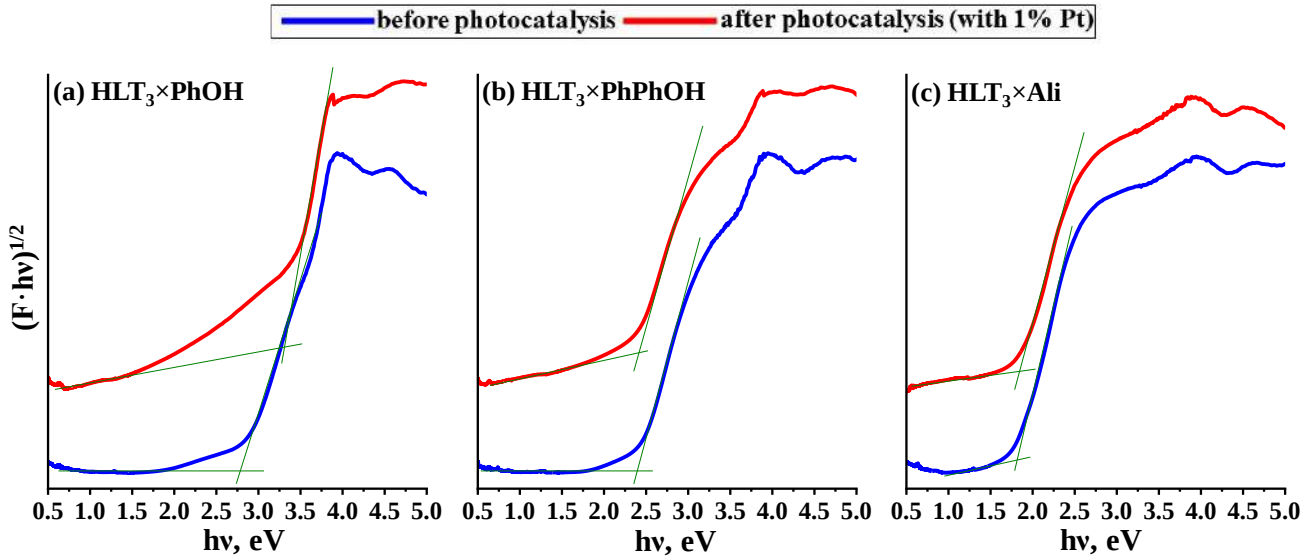


Fig. 63. Kubelka-Munk plots for selected titanate derivatives $HLT_3$ with aromatic modifiers before and after photocatalytic experiments in a 1% (mol.) aqueous solution of methanol under radiation from a DRT-125 lamp (λ > 220 nm)

However, it is important to note that the photocatalytic activity of the phenol and resorcinol titanates is stably maintained throughout the entire measurement time with each of the light emitters (Fig. 60). When using a mercury lamp, this is probably due to the fact that the observed activity is mainly caused by the absorption of ultraviolet radiation, which persists regardless of the state of the grafted component. That being said, despite the partial degradation of the latter, the interlayer reaction zone can remain expanded and continue functioning at least as long as the sample is in the reaction medium, as in the case of the previously considered derivatives with aliphatic modifiers. At the same time, the preservation of the activity by the phenol and resorcinol derivatives under radiation from a xenon lamp and LED-425 source probably indicates that these photocatalysts are chemically stable under corresponding relatively milder operating conditions and, thus, retain light absorption in the visible range.

### 3.4. Nanosheets of the titanates as photocatalysts for hydrogen generation

Along with hybrid organic-inorganic derivatives of the titanates HLT, HNT, $HLT_3$ and $HNT_3$, this study included preparation of the photocatalysts based on their nanosheets –

materials formed during the delamination of the titanates along their chemically active interlayer space, during which the interlayer area transforms into external surface. The corresponding photocatalysts were tested in hydrogen evolution reactions from aqueous solutions of methanol, glucose and xylose, as well as from pure water under mid- and near-ultraviolet radiation. That being said, special attention was paid to the influence of the form of nanosheets used (initial nanosheets without reassembly, those reassembled by different methods) on their photocatalytic activity. Data on the preparation and study of the titanate nanosheets are published in the applicant's articles [245,246].

3.4.1. Results of optimization of the liquid-phase exfoliation procedure

Due to the almost complete absence of data in the literature on the liquid-phase exfoliation of the titanates under study, the primary task was the development and optimization of the corresponding procedure in order to establish conditions that ensure nanosheet yields being sufficient for photocatalytic measurements. At the same time, it was decided to use not only protonated forms of the titanates, but also their amine derivatives, possessing an expanded interlayer space, as precursors for exfoliation. Liquid-phase exfoliation was carried out in accordance with physical, chemical and combined physical-chemical strategies, and quantitative measures of its efficiency were the concentration of nanosheets in final suspensions after precipitation of bulk non-exfoliated particles by centrifugation (c, mg/L) and their yield (η, %) from theoretically achievable upon complete exfoliation of the sample (Fig. 64). The efficiency of liquid-phase exfoliation, assessed in this way, is determined by two key factors: the ability of the selected precursor to undergo delamination as such and stability of the resulting nanosheet suspension to centrifugation.

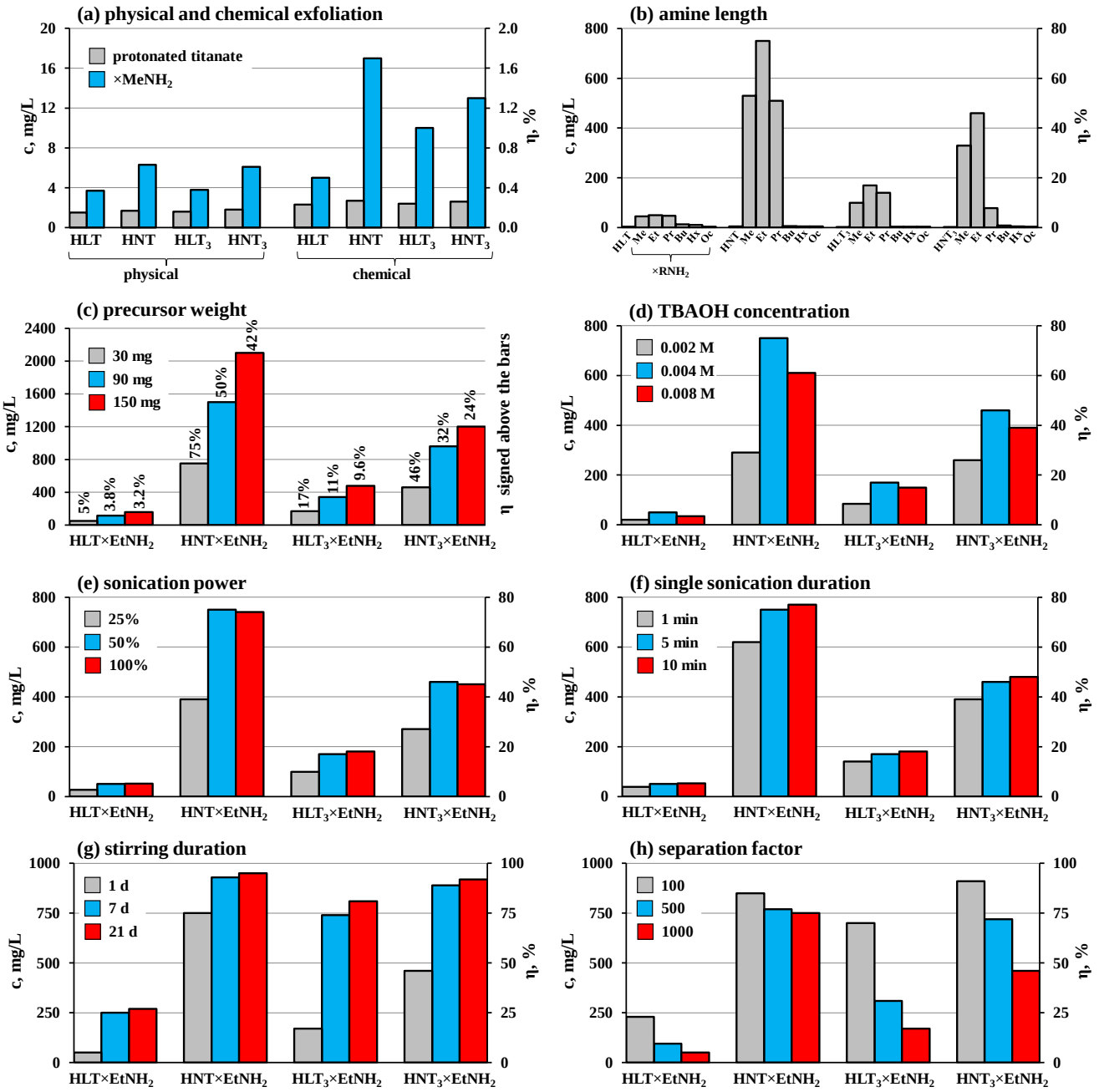


Fig. 64. Influence of conditions of liquid-phase exfoliation of the titanates on concentration and yield of nanosheets in the final suspensions

Physical exfoliation of the protonated titanates, consisting in their ultrasonic treatment in water (Fig. 64, a), turned out to be extremely ineffective: the final suspensions after centrifugation contained only trace amounts of the suspended solids ($c < 2$ mg/L, $\eta < 0.2\%$). The use of methylamine precursors made it possible to increase the yield of nanosheets by 2.5–3.5 times ($c < 6$ mg/L, $\eta < 0.6\%$), which is apparently due to their greater interlayer distance, which facilitates the delamination of the bulk structure.

Chemical exfoliation of the protonated titanates in an aqueous solution of tetrabutylammonium hydroxide TBAOH without the use of ultrasound (Fig. 64) also turned

out to be ineffective ($c < 3$ mg/L, $\eta < 0.3\%$). Meanwhile, when using the methylamine derivatives, it was possible to achieve noticeably better yields of nanosheets ($c < 17$ mg/L, $\eta < 1.7\%$) due to greater accessibility of their expanded interlayer space for $TBA^+$ cations and water molecules, providing higher completeness of swelling and subsequent delamination of the samples.

Physical-chemical exfoliation combining the use of TBAOH and ultrasound is known as a highly efficient method for producing nanosheets of Dion-Jacobson phases. Thus, the applicant found [247] that this approach makes it possible to obtain suspensions of exfoliated forms of the niobates $HA_2Nb_3O_{10}$ (A = Ca, Sr) with concentrations of approximately 500 and 950 mg/L, respectively, using the conditions of physical-chemical exfoliation, selected in this work as standard (Table 3). However, this approach turned out to be of little use for the Ruddlesden-Popper titanates under consideration, providing a relatively low yield of the nanosheets ($c < 5$ mg/L, $\eta < 0.5\%$). The probable reason for this is the sharply different chemical activity of the interlayer space of Dion-Jacobson niobates and Ruddlesden-Popper titanates. The former are easily hydrated and intercalate fairly large organic molecules under relatively mild conditions [146]. Taking this into account, they are able to quantitatively introduce $TBA^+$ cations into the interlayer space, which facilitates its hydration and subsequent delamination of the swollen structure under the influence of ultrasound. The latter, on the contrary, usually exist in a weakly hydrated or almost anhydrous state and directly intercalate only small molecules, such as methylamine [225]. At the same time, the penetration of bulk $TBA^+$ cations into their interlayer space is extremely difficult, which complicates the process of liquid-phase exfoliation.

To overcome this problem, amine derivatives of the titanates were used as precursors for exfoliation (Fig. 64, b). The corresponding approach turned out to be extremely effective and made it possible to achieve up to 160 times higher concentrations and yields of nanosheets than upon the exfoliation of the protonated forms under the same conditions: 50 mg/L (5.0%) for HLT, 750 mg/L (75%) for HNT, 170 mg/L (17%) for $HLT_3$ and 460 mg/L (46%) for $HNT_3$. It has been shown that the exfoliation efficiency is highly dependent on the chain length of the intercalated amine (Fig. 64, b): it increases many times when going from the protonated titanates to their methylamine derivatives, reaches a maximum in the case of the ethylamine derivatives, moderately decreases when going to the *n*-propylamine ones, and drops sharply

with further elongation of the interlayer amine. In particular, the *n*-hexylamine and *n*-octylamine samples undergo exfoliation reluctantly and provide practically the same yield of the nanosheets as the initial protonated titanates. Apparently, one of the main factors determining the ability of amine derivatives to experience delamination is the increased accessibility of their interlayer space for $TBA^+$ cations and water molecules. The highest efficiency of exfoliation is achieved in the case of the derivatives with short-chain amines (R = Me, Et, Pr), which, on the one hand, sufficiently expand the interlayer zone and, on the other hand, are polar enough for energetically favorable contact with water molecules coming from the solution. Despite the larger interlayer distance, the derivatives with long-chain amines (R = Hx, Oc) are probably less susceptible to hydration due to the need for water to come into contact with non-polar hydrocarbon chains and, accordingly, swell slightly. Moreover, these precursors can be stabilized by alkyl-alkyl interactions between the embedded amine chains, preventing the sample from separating into individual perovskite layers. In addition, the amines can partially remain on the surface of the nanosheets after direct delamination of the bulk structure and, accordingly, affect the stability of the final suspensions. In particular, aqueous suspensions of the nanosheets with adsorbed hydrophilic methylamine may be more stable to the precipitation of suspended particles on the walls of the vessel than those with hydrophobic *n*-octylamine.

Due to the greatest completeness of liquid-phase exfoliation, ethylamine derivatives of the titanates were used as precursors in all subsequent experiments. It was found that more concentrated suspensions of the nanosheets can be obtained by increasing the precursor weight with a proportional increase in the concentration of TBAOH (Fig. 64, c). In particular, a threefold increase in sample loading leads on average to a twofold increase in the nanosheet concentration, and a fivefold increase – to a threefold increase. That being said, the concentration of the exfoliated form reaches impressive values of 2100 mg/L in the case of HNT and 1200 mg/L in the case of $HNT_3$. However, the yield of nanosheets from the theoretically possible one decreases with increasing precursor loading due to the limited aggregation-sedimentation stability of overly concentrated suspensions. At the same time, the amounts of the precursor for exfoliation and TBAOH in this work were chosen in such a way as to ensure a ratio of $TBA^+$ cations to the number of interlayer vertices of perovskite octahedra equal to 1 : 1. This ratio turned out to be optimal, since both a twofold deficiency and a

twofold excess of TBAOH led to a decrease in the final concentration and yield of nanosheets (Fig. 64, d).

It has been shown that the efficiency of liquid-phase exfoliation doubles when the ultrasonic power is increased from 25% to 50% of the nominal value (200 W). Meanwhile, a further increase in the power has virtually no effect on the yield of nanosheets (Fig. 64, e), indicating that it is limited by other factors. Moreover, the use of high disperser power during ultrasonic treatment can negatively affect the morphology of the resulting nanoparticles, lead to rapid overheating of the suspension and premature corrosion of the sonotrode with contamination of the sample with its material. In view of this, an ultrasound power of 50% was chosen as optimal. It was also possible to establish that for the efficient exfoliation of the titanates into nanosheets, both stages of ultrasonic treatment are important – after mixing the components of the suspension and after stirring it for a given time. In the absence of the first ultrasound treatment, the final yield of nanosheets is on average 15% lower, and in the absence of the second, 25% lower than in the standard experiment. It is logical to assume that the first stage of ultrasonic exposure makes it possible to prepare the layered matrix for the introduction of $TBA^+$ cations and water molecules into the interlayer space. During further stirring of the resulting suspension, the interlayer space of the particles continues swelling, and the second stage of ultrasonic exposure serves for quantitative delamination of the already swollen precursor. In this case, too long an ultrasonic treatment is not required to achieve a high completeness of exfoliation of the titanates in question (Fig. 64, f). In particular, increasing the duration of ultrasonic exposure from 1 to 5 min really pays off, leading to an increase in the yield of nanosheets by 20–30%, while its subsequent extension to 10 min additionally increases the efficiency of the exfoliation by no more than 5%.

The completeness of liquid-phase exfoliation is also significantly influenced by the duration of the suspension stirring between ultrasonic treatments, which is especially noticeable in the case of titanates HLT and $HLT_3$ (Fig. 64, g). Thus, with an increase in duration from 1 to 7 d, the yield of nanosheets increases by 4–5 times. Upon a further extension of the sample treatment with TBAOH to 21 d, the additional increase in the concentration is less pronounced, however, the highest yields of the exfoliated forms of the titanates are achieved in this work: 270 mg/L (27%) for HLT, 950 mg/L (95%) for HNT, 810 mg/L (81%) for $HLT_3$ and 920 mg/L (92%) for $HNT_3$. Prolonged stirring of the suspensions

apparently ensures greater completeness of the reactions of $TBA^+$ insertion and hydration of the interlayer space, which can proceed slowly for steric reasons. Comparably high concentrations of the titanate nanosheets can formally be achieved in the experiments of standard duration (1 d) under milder centrifugation conditions (Fig. 64, h). However, the use of reduced separation factors (F = 100, 500) leads to the preservation, along with nanosheets, of relatively large fractions of non-exfoliated particles, which is why the final suspensions obtained in this way, strictly speaking, are not suspensions of nanosheets as such.

Thus, the optimal physical-chemical method for exfoliation of the titanates from the point of view of the nanosheet yield seems to be that including two stages of ultrasonic treatment (50% power, 5 min each) of their ethylamine derivatives (1 g/L) in a 0.004 M TBAOH solution with intermediate stirring for 7 d and centrifugation at a separation factor F = 1000 lasting 1 h, which was used further in this work. If it is necessary to obtain higher concentrations of the nanosheets (1–2 g/L), the precursor loading and, in proportion to it, the TBAOH concentration can be increased, however, this will reduce the yield of the exfoliated form from the theoretically possible one.

3.4.2. Stability of the nanosheet suspensions upon pH changes

The dispersion medium of the nanosheet suspensions in aqueous TBAOH has pH ≈ 11.7, which may be too high for photocatalytic reactions, and therefore the issue of stability of the corresponding suspensions when changing pH deserves separate consideration.

It was found that the nanosheets in the initial suspensions are characterized by a moderately negative ζ-potential, equal to −23.5 mV in the case of HLT and −26...−27 mV in the case of HNT, $HLT_3$ and $HNT_3$, lying in absolute value slightly below the value of ± 30 mV, conventionally accepted in colloid chemistry as the boundary between low-stable and highly stable disperse systems. The slightly less negative ζ-potential of the HLT nanosheets compared to that found for the other titanates indicates lower aggregation stability of the corresponding suspensions and is consistent with the lower efficiency of HLT exfoliation (Fig. 64). Both acidification and alkalization of the dispersion medium are accompanied by a decrease in the absolute value of the ζ-potential due to an increase in the ionic strength of the solution and the resulting contraction of the particle electrical double layer (Fig. 65, a). Corresponding weakening of the electrostatic barrier leads to coagulation of the nanosheets, observed visually when the suspension is illuminated with a laser beam (Fig. 65, b). When the nanosheet

suspension is relatively stable, the scattered laser light (Tyndall effect) appears uniform and individual scattering particles are indistinguishable to the naked eye. With intense coagulation, individual scattering centers in the laser beam become clearly visible. A further change in pH is accompanied by an increase in the number of the aggregated nanosheets, and at a certain critical pH value there is a sharp increase in the turbidity of the suspension, indicating rapid flocculation of the particles that begin to form a flocculent sediment when stirring is turned off. The single-layer titanates undergo rapid flocculation at pH below 8.0 or above 12.5, the three-layer ones – below 7.5 and above 12.0. The values of ζ-potentials measured at these critical pHs are individual for different titanates and fall in the range of −16…−10 mV. Meanwhile, the first signs of the nanosheets coagulation are observed already at pH ≤ 9.5, corresponding to ζ ≥ −15 mV for the single-layer titanates and ζ ≥ −20 mV for the three-layer ones. In general, suspensions of the exfoliated titanates are characterized by a narrower range of stability (≈ 4.5 pH units) compared to those of the exfoliated niobates $HA_2Nb_3O_{10}$ (A = Ca, Sr), studied by the applicant separately (≈ 6.5 pH units) [247].

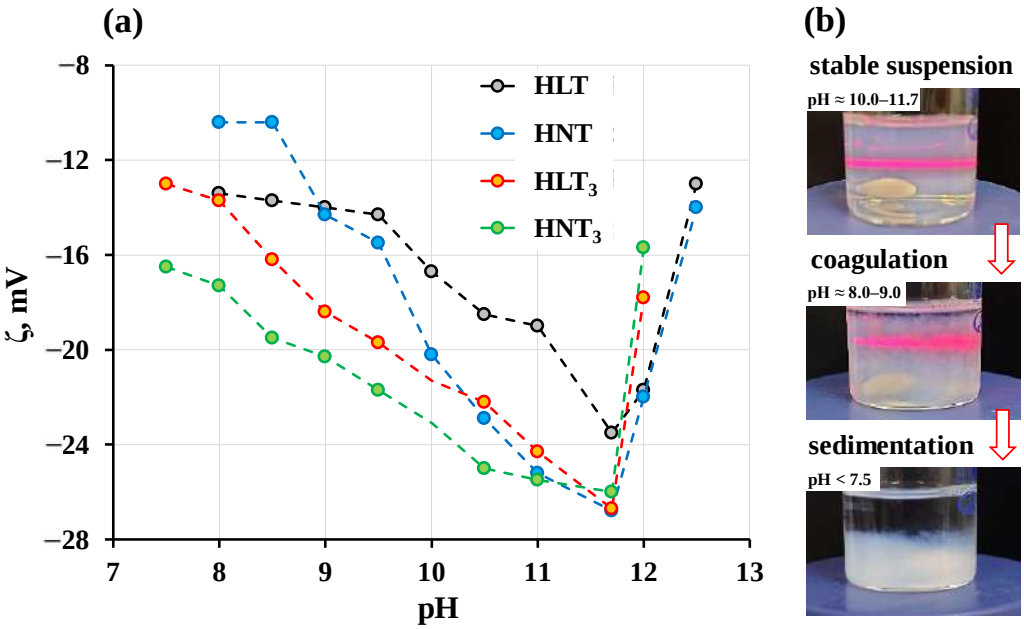


Fig. 65. Dependence of ζ-potential of the titanate nanosheets in suspensions on pH of the medium (a) and their coagulation during its acidification (b)

### 3.4.3. Characterization of the initial and reassembled nanosheets

#### 3.4.3.1. Structure, composition and morphology of the initial nanosheets

Hydrodynamic radii of the particles in standard suspensions of exfoliated forms of the titanates were assessed using the dynamic light scattering method (Fig. 66). It was found that the particle size distribution in the case of HLT has a maximum at ≈ 90 nm and is much

narrower than in the case of other titanates, covering the range 65–125 nm and having a width at half maximum of 40 nm. The distribution for HNT nanosheets with a maximum at ≈ 125 nm turns out to be wider (50–250 nm), has a width at half maximum of 120 nm and is characterized by pronounced asymmetry due to the shoulder extending into the region of large hydrodynamic radii. The distributions for the exfoliated forms of $HLT_3$ and $HNT_3$ are quite similar: both exhibit a predominant particle size of ≈ 120 nm, span a radius range of 50–210 nm, and have a width at half maximum of 100 nm. All the distributions also show an additional maximum in the region of 15–30 nm, which may relate to smaller fractions of the nanoparticles.

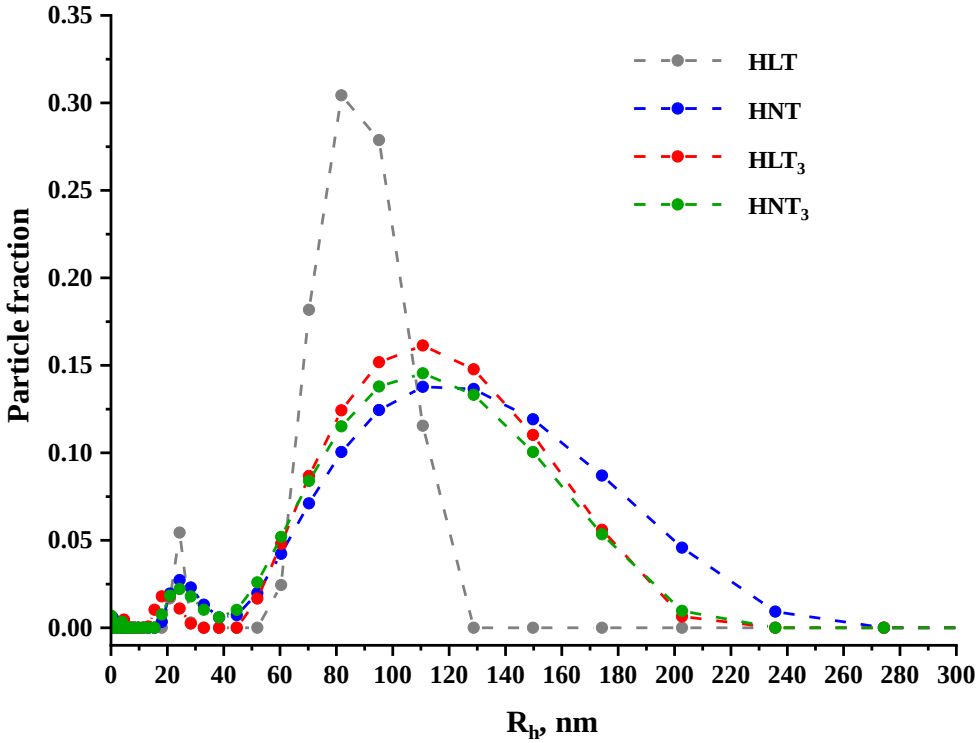


Fig. 66. Size distributions of the nanosheets in suspensions after liquid-phase exfoliation measured by dynamic light scattering

It should be noted that the data obtained by the dynamic light scattering method provide only an upper estimate of the actual sizes of the nanosheets in suspensions and do not allow us to draw strict conclusions, since the above distributions, due to software limitations, were calculated under the assumption of a spherical particle geometry, different from the real shape of perovskite nanosheets. Meanwhile, the dynamic light scattering data are consistent with the results of spectrophotometric analysis of suspensions of the exfoliated titanates (Fig. 24). In particular, the suspensions of HNT, $HLT_3$ and $HNT_3$ nanosheets show similar size distributions and almost identical spectra with a clearly pronounced maximum at 225–230 nm, while the

distribution for HLT is clearly different from the above, and the spectral maximum occurs at 217 nm. At the same time, the titanate HLT stands out among the other compounds exhibiting noticeably lower completeness of liquid-phase exfoliation (Fig. 64).

It was shown by TEM that the main part of the resulting nanosheets has a rectangular shape and linear dimensions of 30–250 nm (Fig. 67), which are generally consistent with the dynamic light scattering data. In this case, sizes of the titanate nanosheets turn out to be on average slightly smaller than those previously reported in the literature for other layered perovskite-like oxides [183,195,197,248–250], which may be due to both the structural-chemical features of specific objects and more stringent centrifugation conditions in this work, ensuring preservation in final suspensions of only relatively small fractions of the nanoparticles.

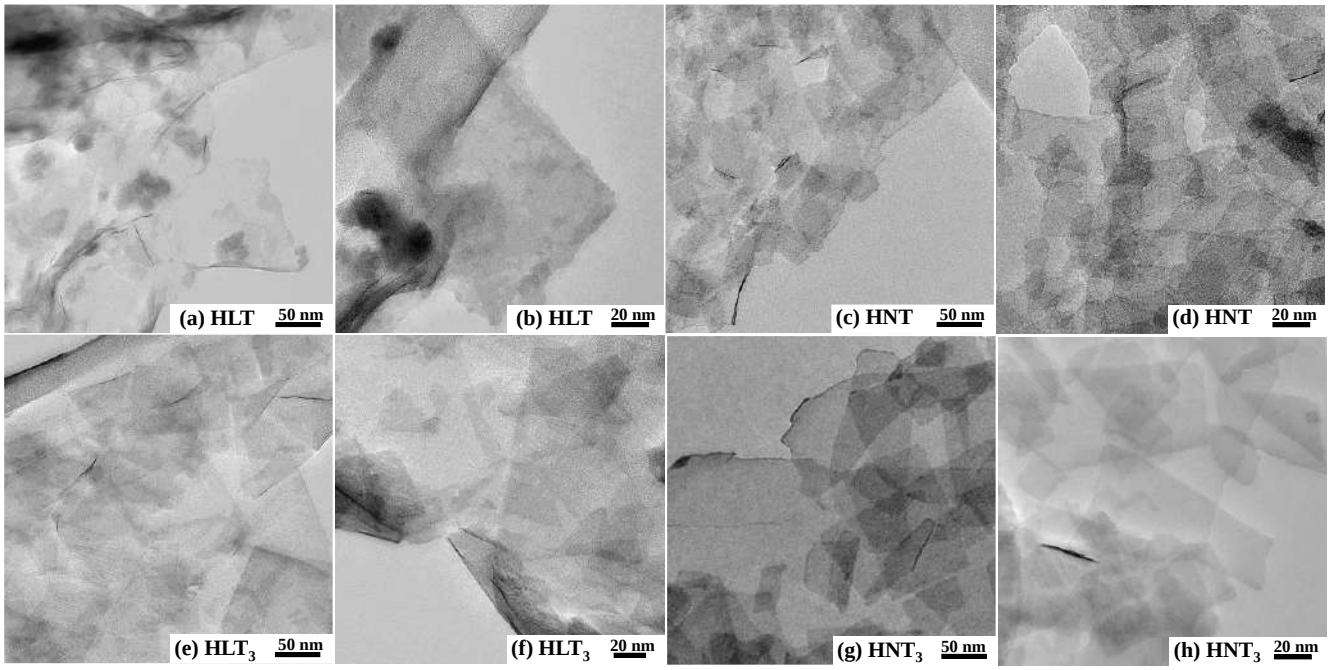


Fig. 67. TEM images of the titanate nanosheets

Study of the nanosheets by the SAED technique (Fig. 68) allowed us to identify the main interplanar distances in their structure, approximately equal to 2.62–2.74 Å, 1.86–1.94 Å, and 1.31–1.37 Å. Using the resources of the International Center for Diffraction Data (ICDD), it was determined that the distances found belong to the families of crystallographic planes with indices (110), (020) and (220), respectively. Also, using energy-dispersive X-ray microanalysis, the ratio of Ln : Ti cations in the nanosheets deposited on silicon substrates was confirmed to be 1 : 1 for the single-layer samples and 2 : 3 for the three-layer ones. Thus, the

structure and composition of perovskite blocks are preserved during the liquid-phase exfoliation of the titanates.

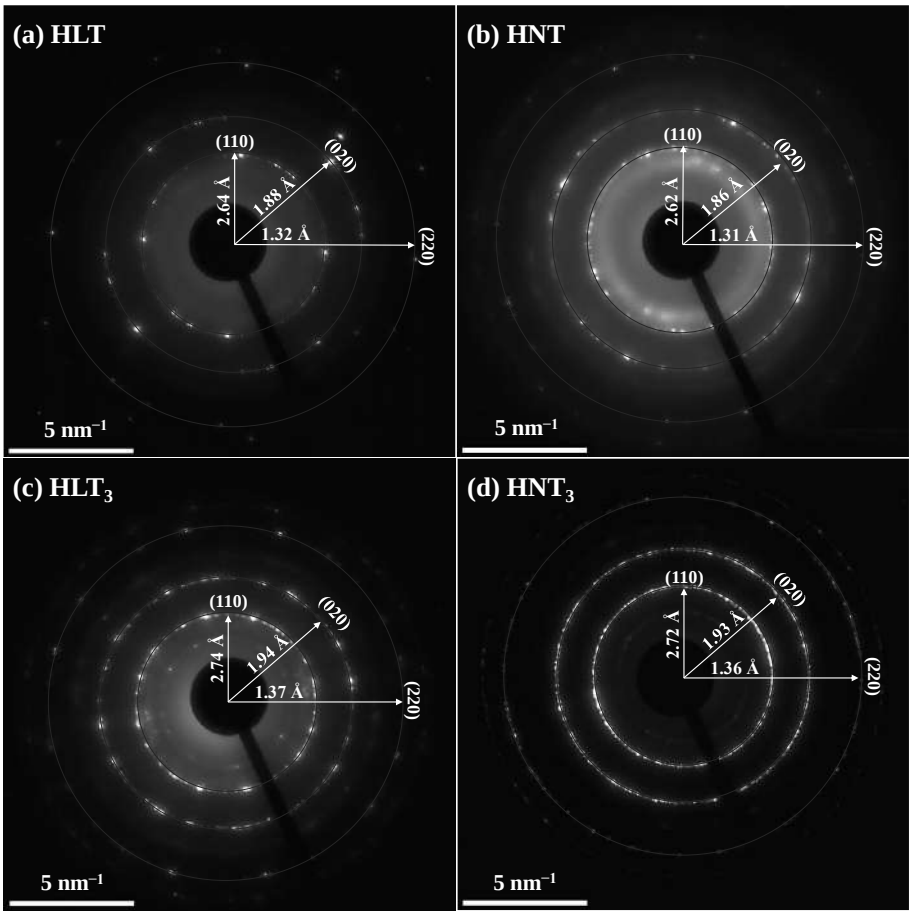


Fig. 68. SAED patterns of the titanate nanosheets

It was shown using the AFM method (Fig. 69), that a predominant thickness of the nanosheets deposited on substrates is 2.0–2.5 nm and approximately corresponds to the thickness of the titanate monolayer (two perovskite blocks with a thickness n = 1 octahedron separated by a Ln-containing space in the case of single-layer titanates and one perovskite block with thickness n = 3 octahedra in the case of three-layer ones). At the same time, bilayer nanoparticles with a thickness of 4.0–4.5 nm, containing an undivided interlayer space, were found in significantly smaller quantities.

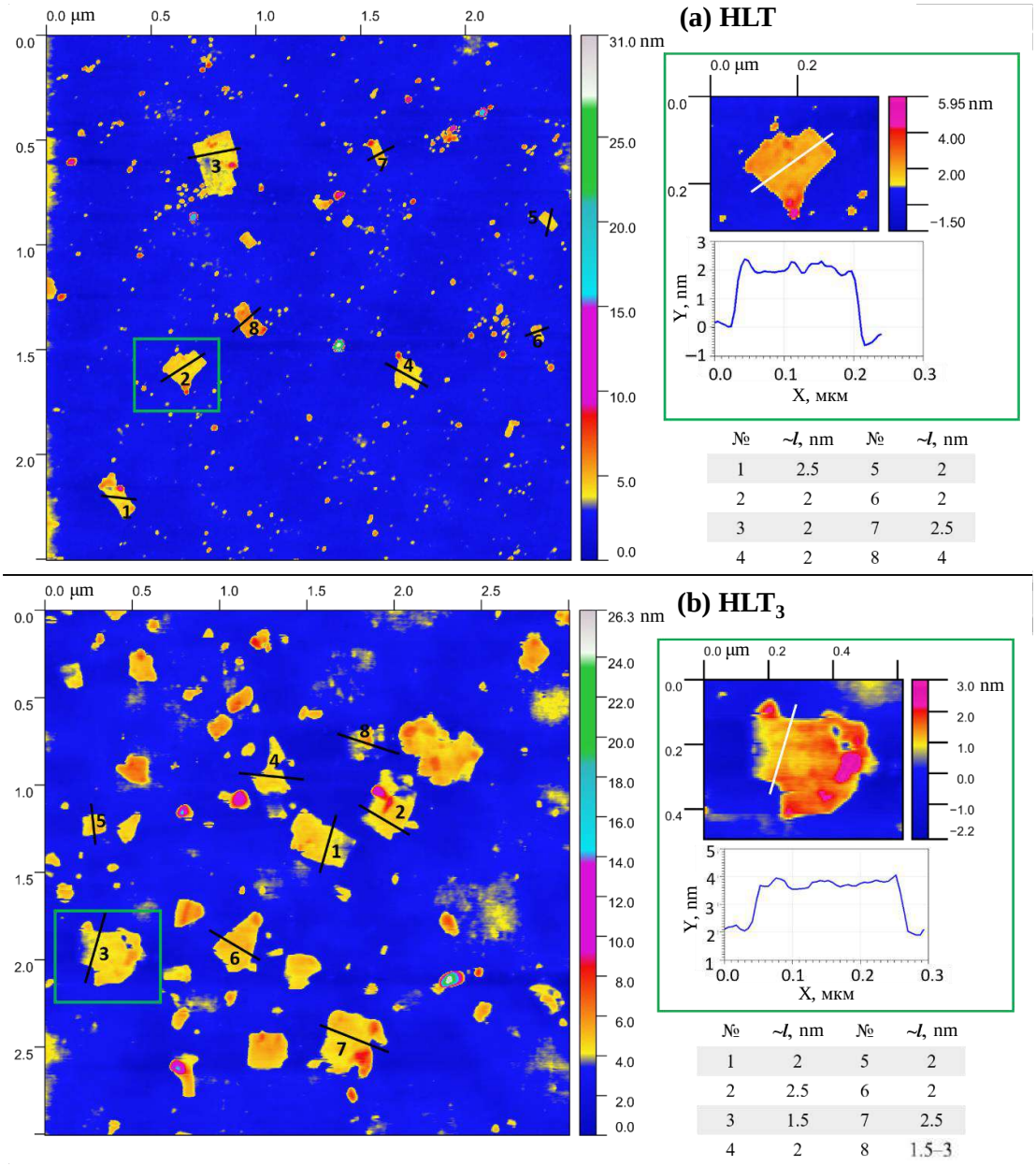


Fig. 69. AFM profiles of the titanate nanosheets on silicon substrates

3.4.3.2. Structure and composition of the reassembled nanosheets

In addition to the initial titanate nanosheets in TBAOH-containing suspensions (NSs), their reassembled forms were also obtained for photocatalytic studies. Reassembly was carried out by two methods: direct vacuum filtration of the initial suspensions (filtered NSs) and precipitation of the suspended particles via the medium acidification with hydrochloric acid (HCl-restacked NSs). That being said, the direct filtration turned out to be a much less time-consuming approach to isolating nanosheets than their flocculation under the action of acid. It was noted that in the first case, nanosheets quickly clog the pores of the membrane filter, causing a sharp decrease in the filtration rate already in the first minutes of the process. In the

second case, on the contrary, acidification of the suspension leads to the formation of flocculent aggregates of nanosheets, which quickly settle on the filter and at the same time practically do not reduce its permeability, which makes it possible to isolate a sufficient amount of the reassembled sample from the suspensions in a relatively short time. Apparently, this is the reason for the widespread use of the precipitation with strong electrolytes as a method for isolating perovskite nanosheets in the available literature. However, as will be shown below, the reassembly approach significantly affects the properties of the final samples, including their photocatalytic activity.

Primary characterization of the reassembled titanates was carried out using X-ray diffraction analysis (Fig. 70). It was found that in the process of exfoliation and reassembly by both methods, positions of the reflections (110) and (020), corresponding to the structure of the perovskite block, are preserved in the diffraction patterns of the samples, and the lattice parameter *a* also remains relatively unchanged (Table 17). At the same time, the reassembled titanates differ from the initial protonated compounds by the broadening of the diffraction maxima (mainly (00x)), which is caused by a significantly lower order in the stacking of perovskite layers, as well as smaller particle sizes. Additionally, both forms of the reassembled nanosheets are characterized by a pronounced shift of the reflections (00x) to the low-angle region and, accordingly, by a formally large interlayer distance compared to that of the protonated samples (Table 17). This observation indicates the existence of some factors that prevent the narrowing of the interlayer distance to a value characteristic of the protonated forms, such as the presence of $TBA^+$ cations and water molecules between the layers. Moreover, aggregates of the filtered nanosheets have a larger interlayer space width than their counterparts precipitated by hydrochloric acid, which is especially noticeable in the case of the three-layer titanates.

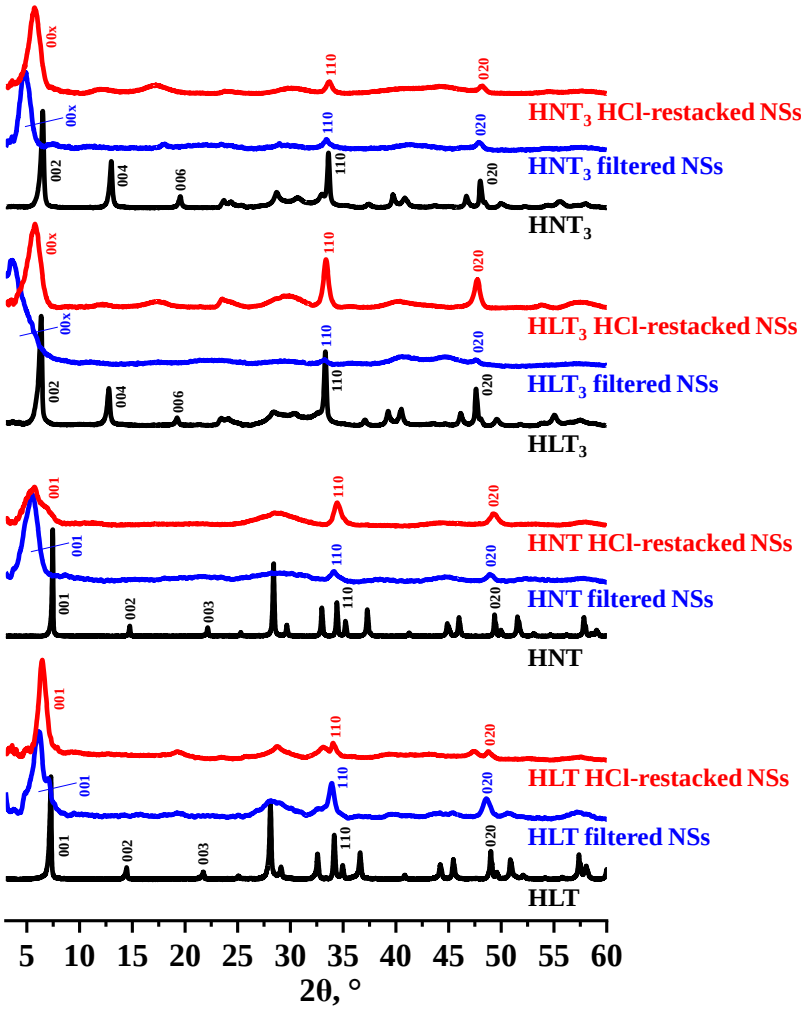


Fig. 70. X-ray diffraction patterns of the protonated titanates and their reassembled nanosheets

Table 17. Characterization of the protonated titanates and their reassembled nanosheets: lattice parameters in the tetragonal system *a*, *c*, interlayer distances *d*, quantitative compositions in the form $H_{1-x}LnTiO_4 \cdot xTBA \cdot yH_2O$ and $H_{2-x}Ln_2Ti_3O_{10} \cdot xTBA \cdot yH_2O$, specific surface areas S

| Sample | Structural parameters, Å | | | Composition | | S, $m^2/g$ |
|---|---|---|---|---|---|---|
| | *a* | *c* | *d* | x | y | |
| HLT | 3.71 | 12.2 | 12.2 | – | 0.10 | 9.7 |
| HLT filtered NSs | ≈3.7 | ≈14.5 | ≈14.5 | 0.05 | 0.40 | 54 |
| HLT HCl-restacked NSs | ≈3.7 | ≈14.0 | ≈14.0 | 0.02 | 0.40 | 73 |
| HNT | 3.68 | 12.1 | 12.1 | – | 0.10 | 8.6 |
| HNT filtered NSs | ≈3.7 | ≈16.5 | ≈16.5 | 0.05 | 0.45 | 64 |
| HNT HCl-restacked NSs | ≈3.7 | ≈16.0 | ≈16.0 | 0.01 | 0.75 | 85 |
| $HLT_3$ | 3.79 | 27.2 | 13.6 | – | 0.20 | 3.2 |
| $HLT_3$ filtered NSs | ≈3.8 | ≈24.0 | ≈24.0 | 0.20 | 0.60 | 21 |
| $HLT_3$ HCl-restacked NSs | ≈3.8 | ≈15.5 | ≈15.5 | 0.02 | 1.10 | 60 |
| $HNT_3$ | 3.78 | 27.2 | 13.6 | – | 0.20 | 3.1 |
| $HNT_3$ filtered NSs | ≈3.8 | ≈19.5 | ≈19.5 | 0.20 | 1.20 | 15 |
| $HNT_3$ HCl-restacked NSs | ≈3.8 | ≈15.5 | ≈15.5 | 0.02 | 1.20 | 47 |

Raman spectra of the reassembled nanosheets (Fig. 71) exhibit the main vibrational modes localized in the titanium-oxygen octahedra (400–750 $cm^{-1}$) and in the $(LnO)_2$ layer (270–320 $cm^{-1}$, only for the single-layer samples), which, together with the previously presented data on electronic and X-ray diffraction, confirms the preservation of the perovskite structure during liquid-phase exfoliation and reassembly. An exception is the vibrational band of Ti–O bonds directed into the chemically active interlayer space (≈ 835 $cm^{-1}$ for HLT, HNT and ≈ 820 $cm^{-1}$ for $HLT_3$, $HNT_3$), the frequency of which is most sensitive to the interlayer composition. When going from protonated titanates to their reassembled forms, this band splits into two new ones: ≈ 775 and ≈ 890 $cm^{-1}$ for filtered HLT (HNT) nanosheets, ≈ 780 and ≈ 905 $cm^{-1}$ for HCl-restacked HLT (HNT) nanosheets, ≈ 760 and ≈ 900 $cm^{-1}$ for filtered $HLT_3$ ($HNT_3$), ≈ 765 and ≈ 910 $cm^{-1}$ for HCl-restacked $HLT_3$ ($HNT_3$). This splitting is apparently associated with a change in the environment of the interlayer oxygen vertices of the perovskite octahedra. That being said, the corresponding bands of the filtered nanosheets are shifted by 5–15 $cm^{-1}$ to the low-frequency region relative to similar bands of the HCl-restacked samples, which may be due to a stronger association of oxygen vertices with interlayer components in the first case. Moreover, the Raman spectra confirm the presence of $TBA^+$ cations in the aggregates of the filtered nanosheets, causing the expansion of the interlayer space and, probably, the above-mentioned splitting of the Ti–O band. In particular, the spectra contain signals corresponding to stretching vibrations of C–N (≈ 1040 $cm^{-1}$) and C–H (2820–3050 $cm^{-1}$) bonds, as well as to bending vibrations of C–C–H (≈ 1130 $cm^{-1}$), C–N–C (≈ 1450 $cm^{-1}$) and H–C–H (≈ 1310 and ≈ 1450 $cm^{-1}$) fragments. Apparently, $TBA^+$ cations are quite strongly adsorbed on the perovskite nanosheets and remain in noticeable amounts even after thorough washing of the samples with an excess of hot water. Moreover, the above bands are more intense in the spectra of the filtered nanosheets of three-layer titanates, which indicates a higher content of $TBA^+$ cations in these samples. In the spectra of the HCl-restacked nanosheets, on the contrary, the vibration bands of the organic component are barely noticeable and are comparable in intensity to the bands of water, being a very weak Raman scatterer, which indicates significantly lower amounts of residual $TBA^+$ cations in the samples.

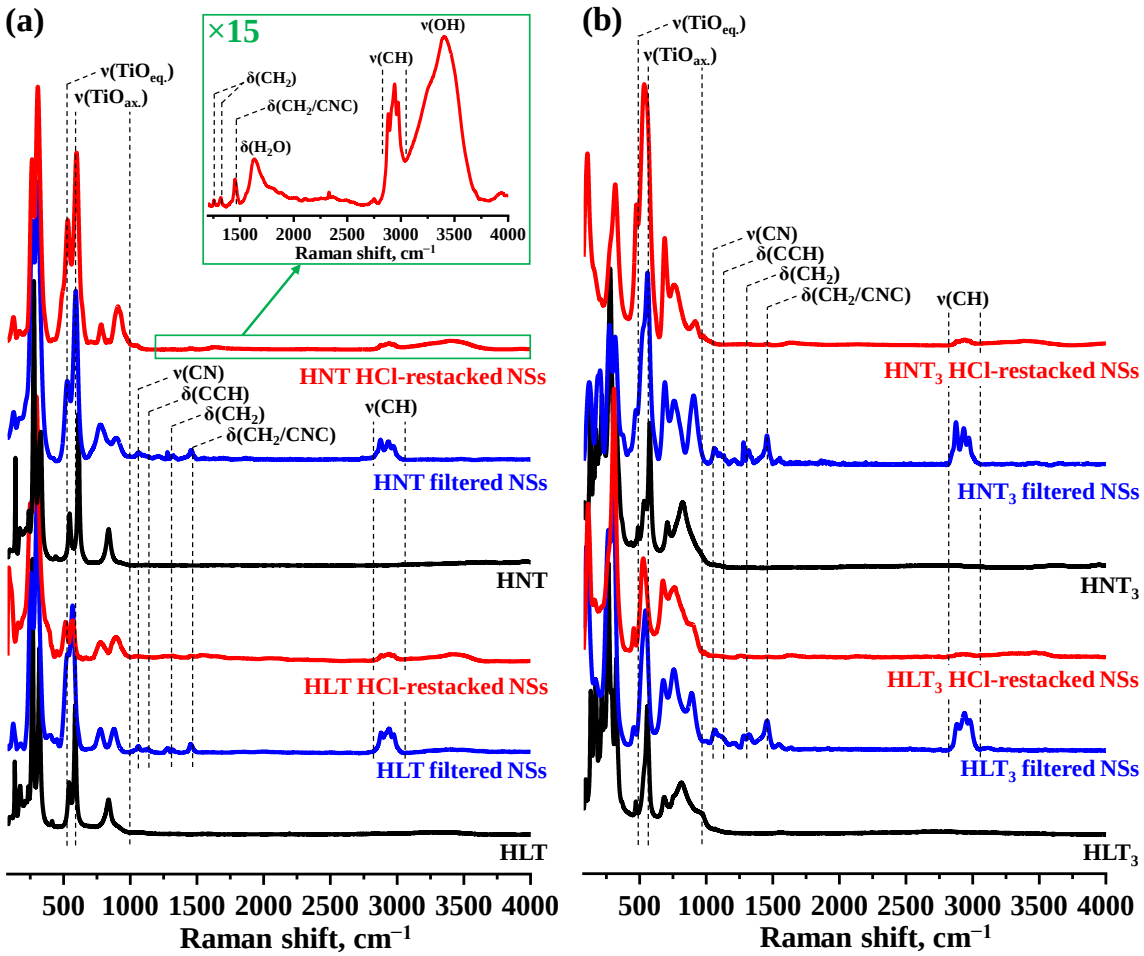


Fig. 71. Raman spectra of the protonated titanates and their reassembled nanosheets

The amounts of tetrabutylammonium and water in the reassembled titanates were determined via CHN-analysis and thermogravimetry. It was found that the filtered nanosheets exhibit noticeably greater mass losses during thermolysis than the HCl-restacked ones (Fig. 72). The content of $TBA^+$ cations per formula unit of the filtered nanosheets is 0.05 and 0.20 for the single-layer and three-layer titanates, respectively, while in the case of the HCl-restacked analogues it does not exceed 0.01–0.02 (Table 17), which is consistent with the previously noted difference in the interlayer distance and intensity of the $TBA^+$ vibration bands in the Raman spectra. Moreover, all the reassembled samples also contain noticeable amounts of water adsorbed and/or intercalated into the interlayer spaces (0.40–1.20 molecules per unit of the titanate). Thus, the filtered nanosheets, in a sense, can be considered as hybrid organic-inorganic materials with strongly bound $TBA^+$ cations in their composition. The HCl-restacked nanosheets, on the contrary, are practically devoid of the residual organic component, which, apparently, is washed out in the form of tetrabutylammonium chloride during acidification of the suspensions and subsequent rinsing of the samples.

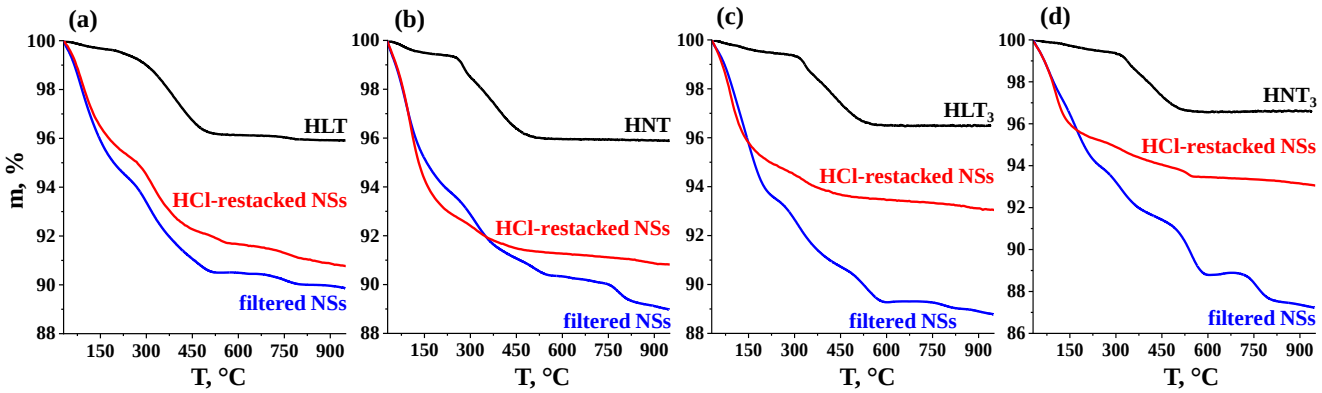


Fig. 72. Thermogravimetric curves of the protonated titanates and their reassembled nanosheets measured in a synthetic air atmosphere

3.4.3.3. Light absorption region and band edge potentials

Study of the reassembled titanates by diffuse reflectance spectroscopy with the Kubelka-Munk transformation (Fig. 73) showed that exfoliation and reassembly are accompanied by a slight decrease in the optical bandgap energy $E_g$, allowing the nanosheet-based photocatalysts to use a wider range of radiation to carry out target reactions (Table 18). For instance, upon the exfoliation of the titanates HNT and $HNT_3$, the $E_g$ value decreases from 3.47–3.48 to 3.22 eV, due to which their nanosheets are formally capable of using light with wavelengths up to 385 nm in photocatalysis, while the long-wavelength edge of the intrinsic absorption of the initial protonated forms is only 356 –357 nm. The observed expansion of the light absorption range is apparently caused by a slight shift of the valence band top $E_V$ during the transformation of the interlayer space into the external surface, while the conduction band bottom $E_C$ retains its negative value (Table 18).

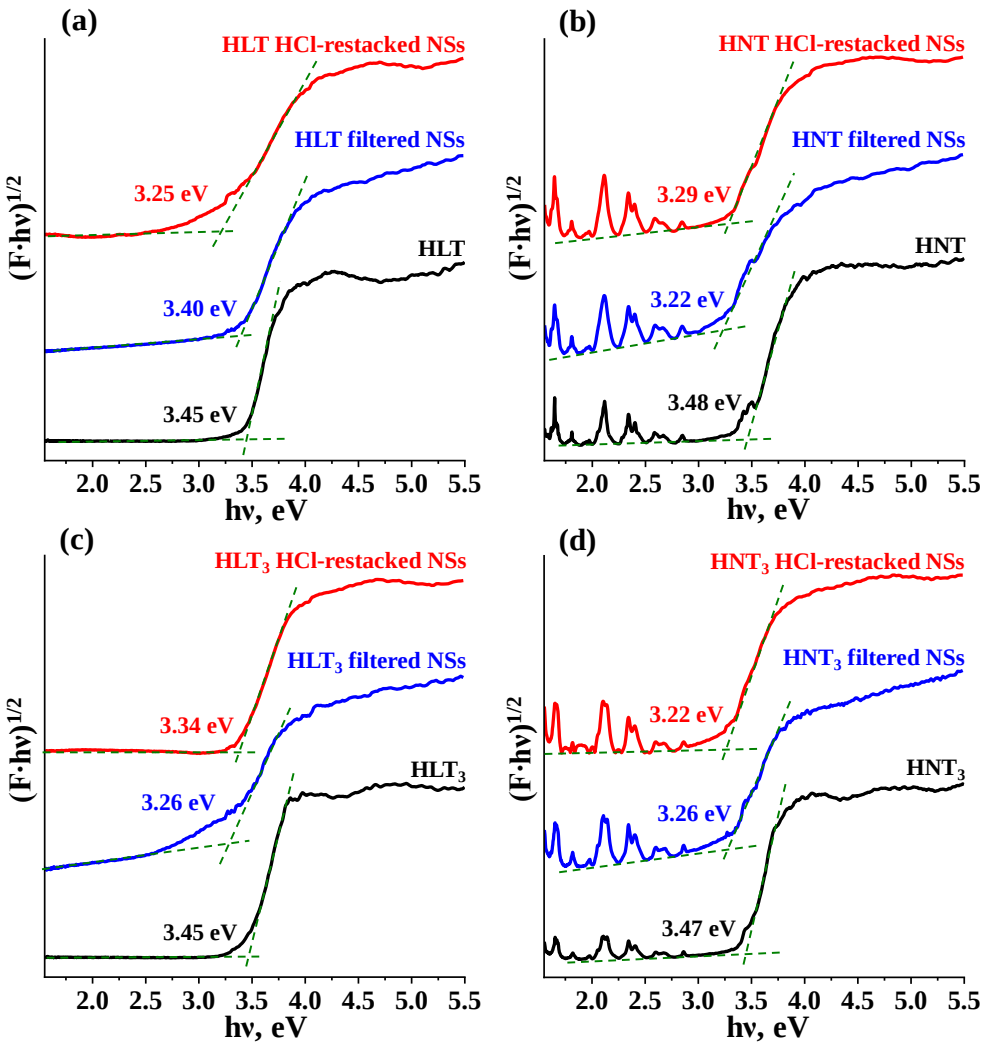


Fig. 73. Kubelka-Munk plots for the protonated titanates and their reassembled nanosheets

Table 18. Characterization of the protonated titanates and their reassembled nanosheets: intrinsic light absorption range (optical bandgap energy $E_g$, long-wavelength absorption edge $\lambda_{max}$), approximate potentials of energy band edges (valence band top $E_V$ and conduction band bottom $E_C$) relative to SHE, maxima $\lambda_{lum}$ and average lifetimes $\tau$ of luminescence upon excitation at a wavelength of 265 nm

| Sample | Light absorption | | Band edges (≈) | | Luminescence | |
|---|---|---|---|---|---|---|
| | $E_g$, eV | $\lambda_{max}$, nm | $E_V$, V | $E_C$, V | $\lambda_{lum}$, nm | $\tau$, μs |
| HLT | 3.45 | 359 | 3.0 | − 0.5 | 360 | 4.70 |
| HLT filtered NSs | 3.40 | 365 | 2.9 | −0.5 | 420 | 0.0071 |
| HLT HCl-restacked NSs | 3.25 | 382 | – | – | – | – |
| HNT | 3.48 | 356 | 2.9 | −0.6 | 360 | 4.77 |
| HNT filtered NSs | 3.22 | 385 | 2.6 | −0.6 | 420 | 0.0042 |
| HNT HCl-restacked NSs | 3.29 | 377 | – | – | – | – |
| $HLT_3$ | 3.45 | 359 | 3.0 | −0.5 | 370 | 4.73 |
| $HLT_3$ filtered NSs | 3.26 | 380 | 2.8 | −0.5 | 430 | 0.0081 |
| $HLT_3$ HCl-restacked NSs | 3.34 | 371 | – | – | 430 | 0.0063 |
| $HNT_3$ | 3.47 | 357 | 2.9 | − 0.6 | 370 | 5.42 |
| $HNT_3$ filtered NSs | 3.26 | 380 | 2.7 | − 0.6 | 430 | 0.0075 |
| $HNT_3$ HCl-restacked NSs | 3.22 | 385 | – | – | 430 | 0.0058 |

3.4.3.4. Average luminescence lifetimes

In order to compare the intensity of radiative recombination of photogenerated charge carriers, reassembled nanosheets of the titanates were examined using time-resolved luminescence spectroscopy (Table 18, Fig. 74). It was shown that exfoliation and reassembly lead to an even more pronounced long-wavelength shift of the luminescence maxima excited at a wavelength of 265 nm than the interlayer modification with the long-chain aliphatic components. Thus, in the case of single-layer titanates, the maxima shift from 360 to 420 nm, and in the case of three-layer titanates, from 370 to 430 nm. The average luminescence lifetime $\tau$ in the case of the reassembled samples turns out to be quite short (0.0042–0.0081 μs), one of the reasons for which may be the relatively disordered nature of the corresponding aggregates, which is favorable for luminescence quenching. That being said, the filtered HLT nanosheets are approximately 1.7 times longer in luminescence lifetime than similar HNT ones, while the corresponding difference between the $HLT_3$ and $HNT_3$ nanosheets does not exceed 1.1 times. It should be especially noted that the luminescence lifetime is also affected by the reassembly method. In particular, filtered $HLT_3$ ($HNT_3$) nanosheets exhibit a 1.3 times higher $\tau$ value than their HCl-restacked counterparts. Taking these data into account, a lower rate of electron-hole recombination (and, other things being equal, higher photocatalytic activity) is expected in the case of the La-containing nanosheets isolated by direct filtration.

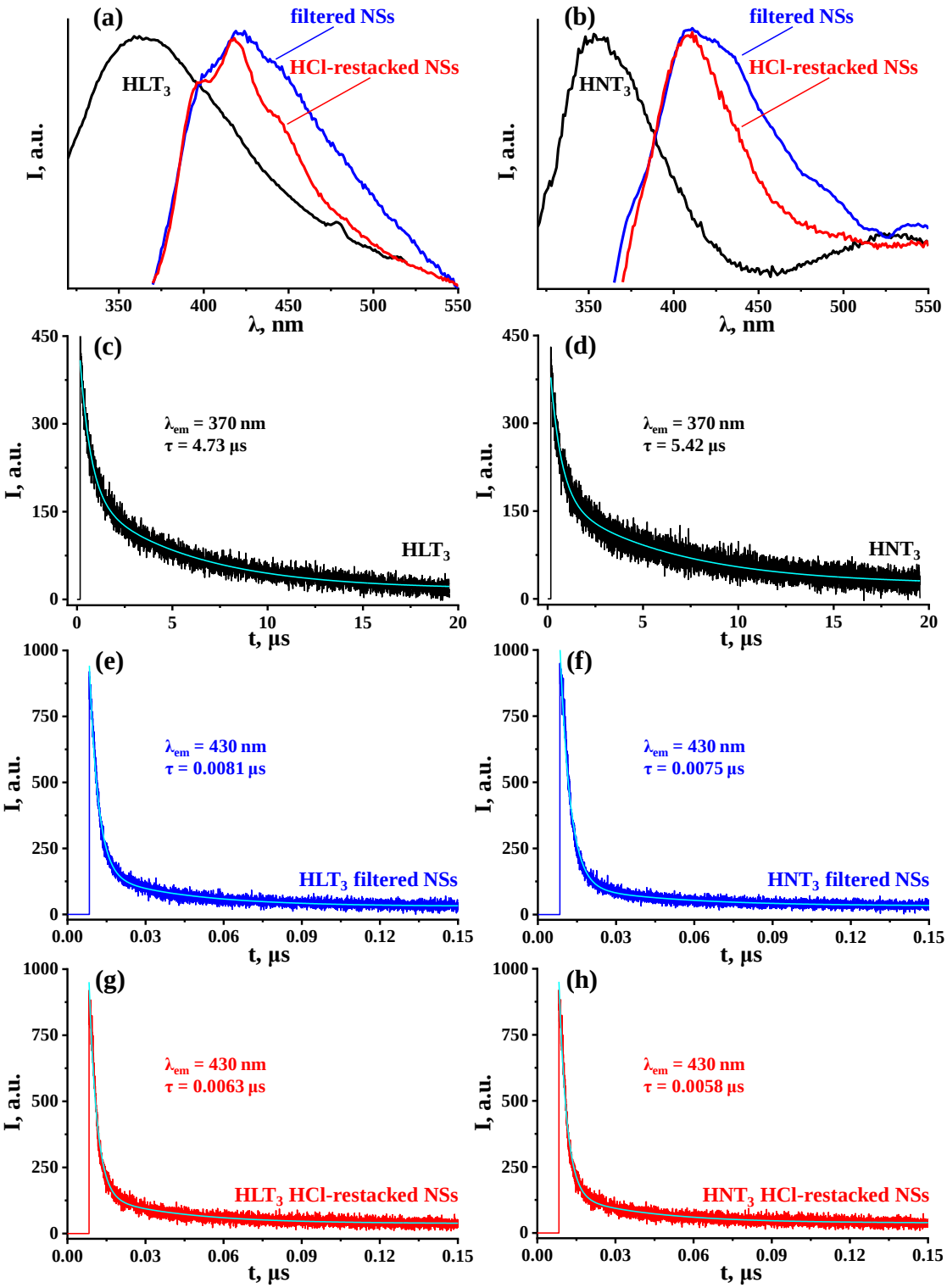


Fig. 74. Luminescence spectra (a, b) and luminescence decay curves (c–h) for the protonated titanates and their reassembled nanosheets upon excitation at a wavelength of 265 nm

3.4.3.5. Morphology, specific surface area and dispersibility

Morphology and specific surface area of the reassembled titanates were studied by SEM and BET methods (Fig. 75, Table 17). As already noted, the powders of the initial protonated compounds consist of lamellar particles with linear dimensions of 0.5–4 μm and a thickness of

200–600 nm. Their reassembled counterparts, in contrast, are formed by curved perovskite nanosheets with irregular edges, assembled into micrometer-sized aggregates. Specific surface area of the reassembled titanates reaches 85 $m^2/g$ and is up to 19 times higher than that found for the protonated forms (3–10 $m^2/g$), which is of great significance for the use of corresponding materials in heterogeneous catalysis and photocatalysis. That being said, the single-layer titanates outperform in the specific surface area the three-layer titanates and the area value is significantly influenced by the reassembly method: in particular, HCl-restacked nanosheets of single-layer and three-layer titanates have a 1.3 and 3 times more developed surface area, respectively, than their filtered analogues (Table 17).

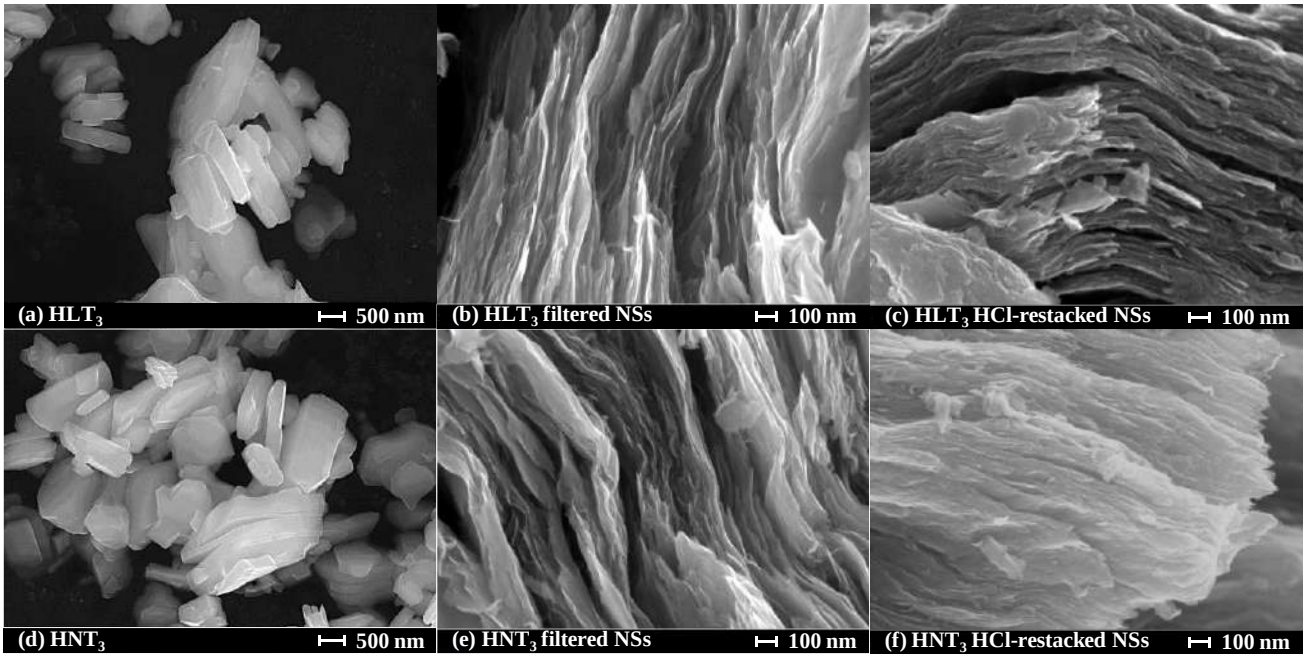


Fig. 75. SEM images of the protonated titanates and their reassembled nanosheets

Particle sizes of the two forms of the reassembled titanates were further compared by laser granulometry after dispersing the samples in water (Fig. 76, a, b). It should be immediately noted that this method allows only a relatively rough comparison of the prevailing particle sizes among themselves, but does not allow one to judge their exact values, since the calculation model used is not adapted for the lamellar morphology of the samples. It was shown that the size distributions for the filtered nanosheets are shifted to the left relative to those for the HCl-restacked analogues. Taking this into account, one would expect a larger specific surface area in the case of the titanates reassembled by direct filtration of the suspensions, which formally does not agree with the results of BET measurements (Table 17). A probable reason for this apparent contradiction is that the specific surface area was

determined for powdered samples, whereas the particle size distributions were obtained after their dispersing in water. Apparently, the filtered nanosheets can be disaggregated much more easily than those precipitated by acid, and, due to this, have on average smaller sizes (larger specific surface area) in suspensions.

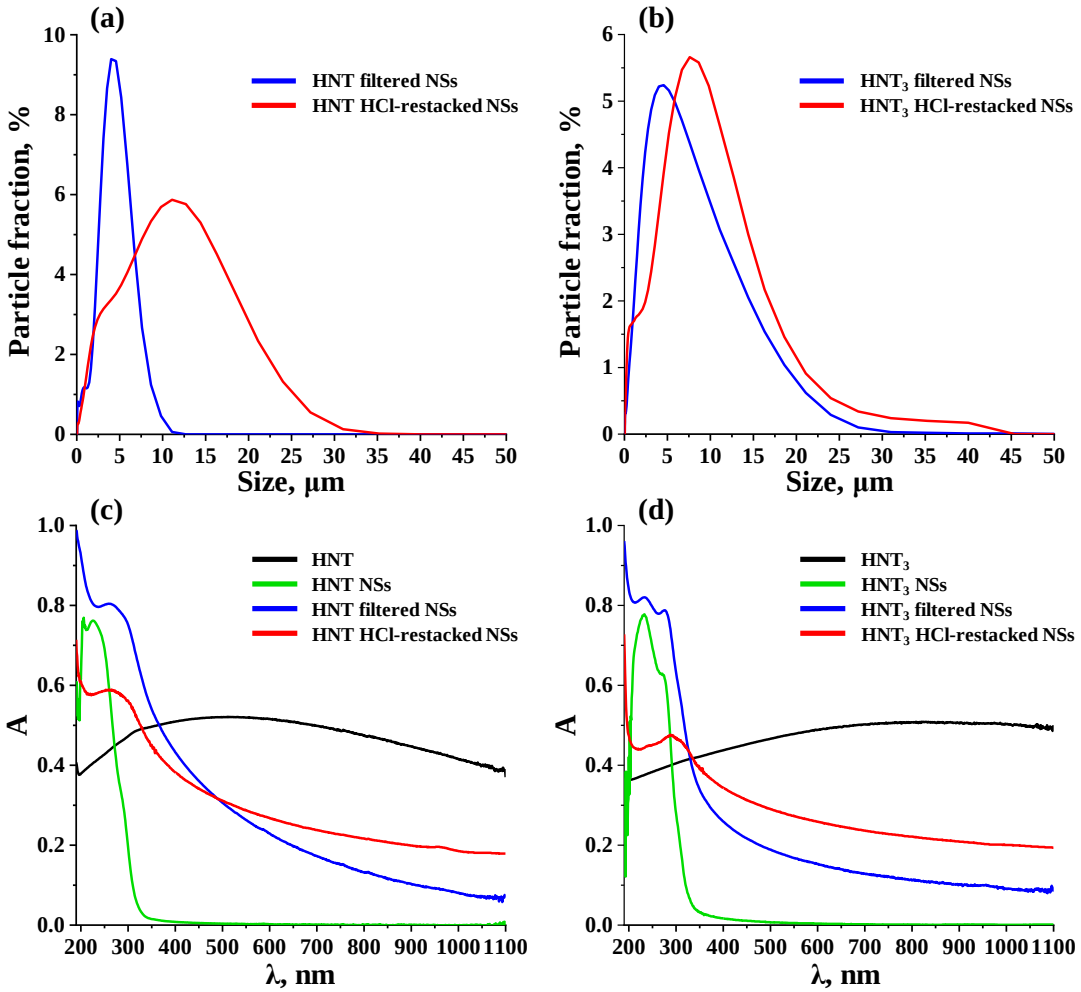


Fig. 76. Size distributions of the reassembled nanosheets measured by laser granulometry (a, b), as well as UV-vis spectra of suspensions of the protonated titanates and three forms of their nanosheets (c, d)

The relationship between the predominant particle sizes of the dispersed protonated titanates, their initial nanosheets and those reassembled in different ways can also be illustrated by the data of spectrophotometric analysis of the corresponding suspensions (Fig. 76, c, d). Thus, in the case of the protonated titanates, a nonzero optical density is observed throughout the entire spectral range, due to intense Mie scattering on their relatively large particles. In the spectra of suspensions of the initial nanosheets taken without reassembly, on the contrary, distinct bands are observed only in the mid-ultraviolet region (200–340 nm), corresponding to the total scattering and absorption by suspended nanoparticles, while in the longer wavelength

range the optical density tends to zero. The spectra of suspensions of both forms of the reassembled and redispersed samples represent a cross between the spectra of the protonated titanates and their initial nanosheets: they show distinct maxima in the ultraviolet region and at the same time maintain non-zero optical density in the rest of the spectrum. This fact indicates that the reassembled titanates occupy an intermediate position in terms of average particle sizes between the protonated forms and the initial nanosheets without reassembly. Moreover, in the case of the filtered nanosheets, the spectral maxima in the ultraviolet range are clearer, and the optical density in the longer wavelength region is lower than in the case of the HCl-restacked analogues, which indicates the smaller particle sizes of the former in a dispersed state and is consistent with the laser granulometry data.

### 3.4.4. Photocatalytic activity of the nanosheets in hydrogen generation reactions

Photocatalytic activity of three forms of the exfoliated titanates (initial, filtered and HCl-restacked NSs) was tested in the reactions of hydrogen evolution from a 1% (mol.) aqueous methanol solution, and in the case of the three-layer compounds – additionally from 1% (mol.) aqueous solutions of glucose, xylose as well as from pure water under ultraviolet radiation. When studying the initial nanosheets without reassembly, pH of their suspensions was adjusted to a value of $\approx 6$, characteristic of those of the protonated titanates.

#### 3.4.4.1. Activity of $HLnTiO_4$ and $H_2Ln_2Ti_3O_{10}$ nanosheets in a 1% (mol.) aqueous methanol solution

Examples of kinetic curves of hydrogen photocatalytic evolution from the aqueous solution of methanol in the presence of exfoliated forms of the titanates are shown in Fig. 77, data on their photocatalytic activity are summarized in Table 19. The kinetic graphs obtained are linear in most cases and indicate that the hydrogen generation rate remains relatively constant throughout the entire measurement time, and when the radiation source is turned off, they reach a plateau.

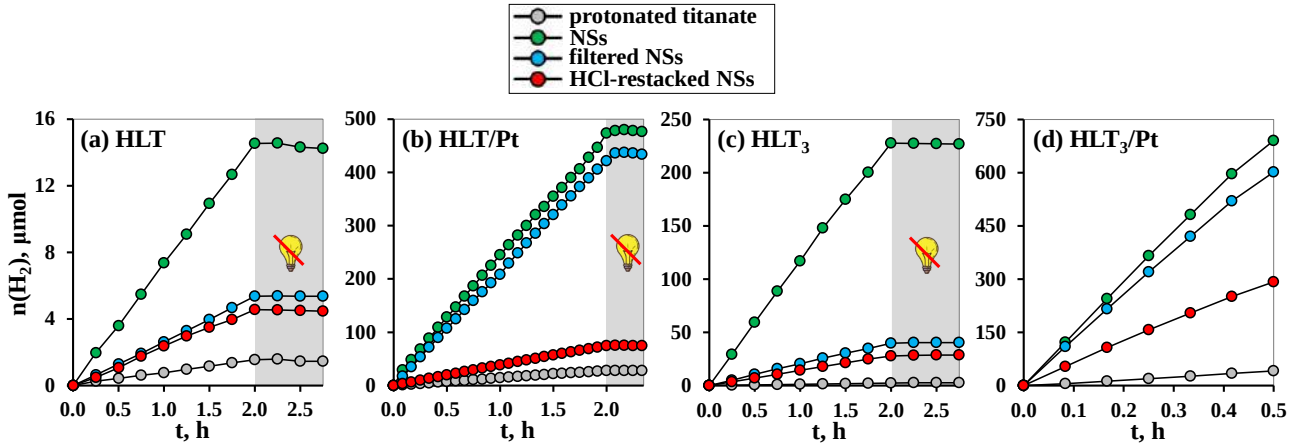


Fig. 77. Kinetic curves of photocatalytic hydrogen evolution from a 1% (mol.) aqueous solution of methanol in the presence of the protonated titanates HLT, $HLT_3$ and photocatalysts based on their nanosheets

As noted earlier, the quantum efficiency φ of hydrogen generation in the presence of unmodified protonated forms of the titanates is relatively low: in the case of both single-layer HLT and HNT samples it is 0.010%, and in the case of three-layer $HLT_3$ and $HNT_3$ ones – 0.017% and 0.027%, respectively. After surface platinization, their activity increases noticeably, reaching φ = 0.19% for HLT/Pt and φ = 1.14% for $HLT_3$/Pt. Exfoliation of the titanates into nanosheets is accompanied by a multiple increase in the hydrogen generation rate from aqueous methanol (Table 19). Particularly, the initial nanosheets without reassembly outperform the protonated compounds in the activity up to 88 times and, after modification with the platinum cocatalyst, provide apparent quantum efficiencies of 3.72% (HLT), 0.12% (HNT), 14.2% ($HLT_3$) and 13.0% ($HNT_3$). That being said, the titanate HLT exfoliated into nanosheets demonstrates the highest activity (18.0 $mmol \cdot h^{-1} \cdot g^{-1}$, 3.72%) among all single-layer Ruddlesden-Popper phases $A'LnTiO_4$ studied to date. Filtered nanosheets of the titanates in question also exhibit a decent level of the photocatalytic activity, being superior to the protonated forms by up to 15 times and providing in a platinized state a quantum efficiency of the target reaction of 3.46% (HLT), 0.10% (HNT), 12.3% ($HLT_3$) and 5.39% ($HNT_3$). At the same time, the nanosheets isolated by the precipitation with acid, which is widespread in the literature, are significantly inferior in the activity to the filtered analogues, although in most cases they turn out to be more efficient than the protonated titanates. After platinization of their surface, the apparent quantum efficiency of hydrogen generation reaches only 0.38% (HLT), 0.082% (HNT), 5.91% ($HLT_3$) and 3.70% ($HNT_3$).

Table 19. Photocatalytic activity of the protonated titanates and their nanosheets in the reaction of hydrogen evolution from a 1% (mol.) aqueous solution of methanol

| Photocatalyst | ω, μmol·h$^{-1}$ | ω′, mmol·h$^{-1}$·g$^{-1}$ | φ, % | $k_{Pt}$ |
|---|---|---|---|---|
| HLT | 0.73 | 0.029 | 0.010 | – |
| HLT/Pt | 14.2 | 0.57 | 0.19 | 19 |
| HLT NSs | 7.21 | 0.58 | 0.12 | – |
| HLT NSs/Pt | 225 | 18.0 | 3.72 | 31 |
| HLT filtered NSs | 2.71 | 0.11 | 0.045 | – |
| HLT filtered NSs/Pt | 209 | 8.36 | 3.46 | 77 |
| HLT HCl-restacked NSs | 2.27 | 0.091 | 0.023 | – |
| HLT HCl-restacked NSs/Pt | 37.2 | 1.49 | 0.38 | 16 |
| HNT | 0.73 | 0.029 | 0.010 | – |
| HNT/Pt | 6.23 | 0.25 | 0.083 | 8.5 |
| HNT NSs | 3.11 | 0.12 | 0.032 | – |
| HNT NSs/Pt | 11.2 | 0.45 | 0.12 | 3.6 |
| HNT filtered NSs | 0.94 | 0.038 | 0.010 | – |
| HNT filtered NSs/Pt | 9.91 | 0.40 | 0.10 | 11 |
| HNT HCl-restacked NSs | 0.51 | 0.020 | 0.005 | – |
| HNT HCl-restacked NSs/Pt | 7.95 | 0.32 | 0.082 | 16 |
| $HLT_3$ | 1.27 | 0.051 | 0.017 | – |
| $HLT_3$/Pt | 85.1 | 3.40 | 1.14 | 67 |
| $HLT_3$ NSs | 112 | 4.48 | 1.16 | – |
| $HLT_3$ NSs/Pt | 1370 | 54.8 | 14.2 | 12 |
| $HLT_3$ filtered NSs | 19.6 | 0.78 | 0.20 | – |
| $HLT_3$ filtered NSs/Pt | 1190 | 47.6 | 12.3 | 61 |
| $HLT_3$ HCl-restacked NSs | 14.1 | 0.56 | 0.14 | – |
| $HLT_3$ HCl-restacked NSs/Pt | 573 | 22.9 | 5.91 | 41 |
| $HNT_3$ | 2.00 | 0.080 | 0.027 | – |
| $HNT_3$/Pt | 69.0 | 2.76 | 0.92 | 35 |
| $HNT_3$ NSs | 21.4 | 0.86 | 0.22 | – |
| $HNT_3$ NSs/Pt | 1260 | 50.4 | 13.0 | 59 |
| $HNT_3$ filtered NSs | 9.73 | 0.39 | 0.10 | – |
| $HNT_3$ filtered NSs/Pt | 523 | 20.9 | 5.39 | 54 |
| $HNT_3$ HCl-restacked NSs | 8.57 | 0.34 | 0.088 | – |
| $HNT_3$ HCl-restacked NSs/Pt | 360 | 14.4 | 3.70 | 42 |

Additional prolonged hydrogen generation experiments were also carried out with the most promising photocatalysts based on the nanosheets of HLT3 and HNT3 using a total duration of 12 h (Fig. 78). It was found that the activity of the samples remains more than 90% of the initial value, provided that the amount of consumed methanol in the reaction solution is replenished.

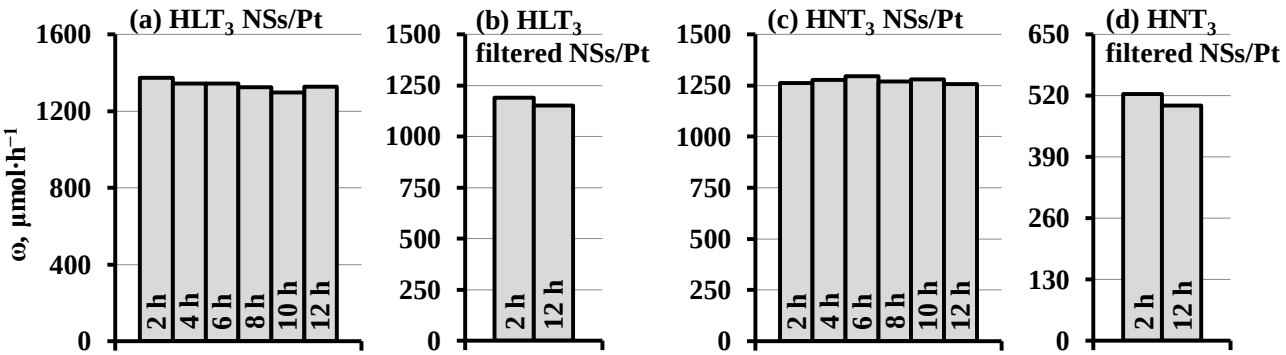


Fig. 78. Activity of the photocatalysts based on $HLT_3$ and $HNT_3$ nanosheets in a 1% (mol.) aqueous solution of methanol under long-term operating conditions

In general, the study of the titanate nanosheets has shown that most La-containing photocatalysts are superior in the activity to Nd-containing analogues, and this difference is most pronounced between platinized materials based on the single-layer compounds HLT and HNT. In particular, both initial and reassembled HLT nanosheets provide tens of times greater hydrogen production efficiency than those of HNT, despite the similarity in chemical composition, bandgap energy, and smaller specific surface area of the HLT nanosheets compared to the HNT ones. A similar difference has already been noted in this work for organic-inorganic derivatives of the corresponding titanates. As shown above, the filtered HLT nanosheets exhibit a longer lifetime of luminescence excited in the intrinsic light absorption range than similar HNT ones, which may indicate a lower rate of the recombination of electron-hole pairs in the former. This fact is consistent with the unequal photocatalytic activity of the HLT and HNT titanates reassembled by filtration, although it does not fully explain the strong difference in the efficiency of their platinization ($k_{Pt}$ in Table 19). Photocatalysts based on the $HLT_3$ nanosheets are also, on average, superior in the activity to materials based on the $HNT_3$ ones, but this difference is much less pronounced. Moreover, as in the case of organic-inorganic derivatives, exfoliated three-layer titanates turn out to be many times more efficient photocatalysts for hydrogen generation than their single-layer analogues. One of the key reasons for this may be the different efficiency of spatial separation of photogenerated charge carriers in the structure of single-layer and three-layer perovskite blocks; however, this assumption does not follow explicitly from the measured luminescence lifetimes and requires special verification.

### 3.4.4.2. Activity of $H_2Ln_2Ti_3O_{10}$ nanosheets in 1% (mol.) aqueous solutions of glucose and xylose

The activity of three forms of nanosheets of the three-layer titanate $HLT_3$ was also tested in the processes of photocatalytic reforming of aqueous solutions of glucose and xylose, which are typical components of plant biomass (Fig. 79, Table 20). It was found that the titanate nanosheets can serve as significantly more efficient photocatalysts for hydrogen production from carbohydrate solutions than the initial protonated form. That being said, the nanosheets reassembled by filtration show the greatest activity, and not the initial ones, which exhibited maximum efficiency in aqueous methanol. Particularly, when moving from the protonated titanate to its filtered nanosheets, the rate of hydrogen generation from glucose and xylose solutions increases by 9.3 and 14 times, and after platinization of the nanosheet surface, an apparent quantum efficiency of 3.6% and 4.4%, respectively, is achieved. Meanwhile, the HCl-restacked nanosheets are in all cases inferior in the activity to the initial and filtered ones.

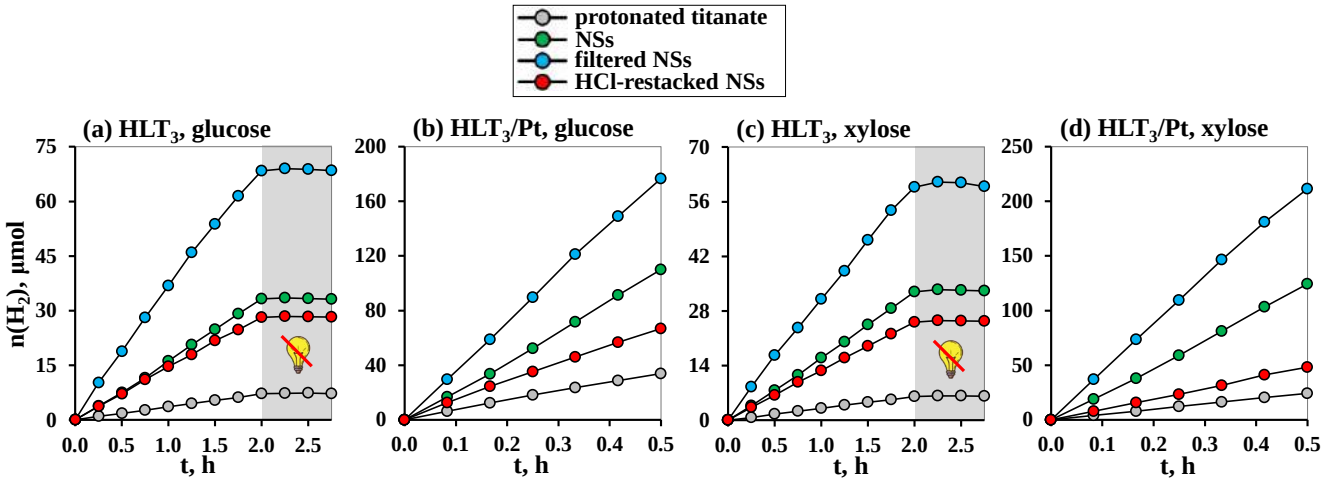


Fig. 79. Kinetic curves of photocatalytic hydrogen evolution from 1% (mol.) aqueous solutions of glucose and xylose in the presence of the protonated titanate $HLT_3$ and photocatalysts based on its nanosheets

Table 20. Photocatalytic activity of the protonated titanate $HLT_3$ and its nanosheets in the reactions of hydrogen evolution from 1% (mol.) aqueous solutions of glucose and xylose

| | Photocatalyst | ω, μmol·h$^{-1}$ | ω′, mmol·h$^{-1}$·g$^{-1}$ | φ, % | $k_{Pt}$ |
|---|---|---|---|---|---|
| glucose | $HLT_3$ | 3.60 | 0.14 | 0.060 | – |
| | $HLT_3$/Pt | 60.5 | 2.42 | 1.01 | 17 |
| | $HLT_3$ NSs | 17.1 | 0.68 | 0.18 | – |
| | $HLT_3$ NSs/Pt | 226 | 9.04 | 2.33 | 13 |
| | $HLT_3$ filtered NSs | 33.5 | 1.34 | 0.34 | – |
| | $HLT_3$ filtered NSs/Pt | 350 | 14.0 | 3.60 | 10 |
| | $HLT_3$ HCl-restacked NSs | 14.0 | 0.56 | 0.14 | – |
| | $HLT_3$ HCl-restacked NSs/Pt | 114 | 4.56 | 1.18 | 8 |

| | Photocatalyst | ω, μmol·h$^{-1}$ | ω′, mmol·h$^{-1}$·g$^{-1}$ | φ, % | $k_{Pt}$ |
|---|---|---|---|---|---|
| xylose | $HLT_3$ | 3.06 | 0.12 | 0.051 | – |
| | $HLT_3$/Pt | 47.7 | 1.91 | 0.79 | 16 |
| | $HLT_3$ NSs | 20.0 | 0.80 | 0.21 | – |
| | $HLT_3$ NSs/Pt | 319 | 12.8 | 3.28 | 16 |
| | $HLT_3$ filtered NSs | 42.7 | 1.71 | 0.44 | – |
| | $HLT_3$ filtered NSs/Pt | 428 | 17.1 | 4.40 | 10 |
| | $HLT_3$ HCl-restacked NSs | 12.5 | 0.50 | 0.13 | – |
| | $HLT_3$ HCl-restacked NSs/Pt | 97.8 | 3.91 | 1.01 | 8 |

### 3.4.4.3. Activity of $H_2Ln_2Ti_3O_{10}$ nanosheets in water

Despite the fact that the energy-efficient production of hydrogen from pure water still remains a serious challenge for most known photocatalysts, exfoliation of the titanates $HLT_3$ and $HNT_3$ into nanosheets made it possible to achieve a decent rate and apparent quantum efficiency of this reaction (Fig. 80, Table 21). In the presence of Pt nanoparticles as a cocatalyst, the greatest activity was demonstrated by the titanates reassembled by direct filtration of the nanosheet suspensions: $HLT_3$ – 12.2 mmol·h$^{-1}$·g$^{-1}$ (φ = 3.15%) and $HNT_3$ – 5.68 mmol·h$^{-1}$·g$^{-1}$ (φ = 1.46%). It was shown that the apparent quantum efficiency of hydrogen generation from pure water in the presence of the filtered $HLT_3$ nanosheets of 2 times higher than that exhibited by similarly platinized $TiO_2$ P25 Degussa, known as one of the most highly active photocatalysts for water splitting under ultraviolet radiation.

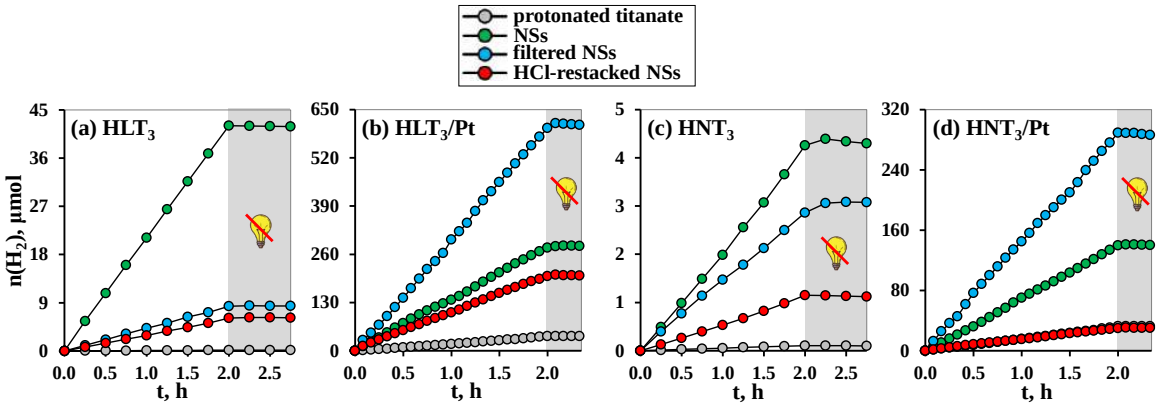


Fig. 80. Kinetic curves of photocatalytic hydrogen evolution from water in the presence of the protonated titanates $HLT_3$, $HNT_3$ and photocatalysts based on their nanosheets

Table 21. Photocatalytic activity of the protonated titanates and their nanosheets in the reaction of hydrogen evolution from water

| Photocatalyst | ω, μmol·h$^{-1}$ | ω′, mmol·h$^{-1}$·g$^{-1}$ | φ, % | $k_{Pt}$ |
|---|---|---|---|---|
| $HLT_3$ | 0.08 | 0.003 | 0.002 | – |
| $HLT_3$/Pt | 19.7 | 0.7 9 | 0.32 | 246 |
| $HLT_3$ NSs | 20.9 | 0.8 4 | 0.21 | – |
| $HLT_3$ NSs/Pt | 139 | 5.56 | 1.42 | 6.7 |
| $HLT_3$ filtered NSs | 4.15 | 0.17 | 0.043 | – |
| $HLT_3$ filtered NSs/Pt | 305 | 12.2 | 3.15 | 73 |
| $HLT_3$ HCl-restacked NSs | 3.01 | 0.12 | 0.031 | – |
| $HLT_3$ HCl-restacked NSs/Pt | 98.6 | 3.94 | 1.02 | 33 |
| $HNT_3$ | 0.05 | 0.002 | 0.001 | – |
| $HNT_3$/Pt | 15.9 | 0.64 | 0.26 | 318 |
| $HNT_3$ NSs | 2.10 | 0.084 | 0.022 | – |
| $HNT_3$ NSs/Pt | 70.6 | 2.82 | 0.73 | 34 |
| $HNT_3$ filtered NSs | 1.39 | 0.056 | 0.014 | – |
| $HNT_3$ filtered NSs/Pt | 142 | 5.68 | 1.46 | 102 |
| $HNT_3$ HCl-restacked NSs | 0.58 | 0.023 | 0.006 | – |
| $HNT_3$ HCl-restacked NSs/Pt | 15.0 | 0.60 | 0.15 | 26 |

### 3.4.5. Influence of reassembly method on photocatalytic activity of the nanosheets

One of the key issues studied in this work was related to the influence of the used form of nanosheets (initial, filtered, HCl-restacked) on the efficiency of photocatalytic hydrogen generation from aqueous-organic solutions and pure water. It was found that the photocatalytic activity of all the studied titanates in aqueous solutions of methanol, as well as that of non-platinized titanates in water, monotonically decreases when going from the initial nanosheets to filtered and then to HCl-restacked ones (Fig. 81, a, c). The highest activity of the initial nanosheets is apparently due to the fact that they have the maximum specific surface area in reaction suspensions, while reassembly is inevitably accompanied by aggregation of nanoparticles and the morphology of the latter cannot be completely restored by redispersing the reassembled sample before photocatalysis. However, when working in aqueous solutions of glucose and xylose, the most efficient photocatalysts are not the initial, but filtered nanosheets (Fig. 81, b). One of possible reasons for this is that the activity of the initial nanosheets is tested in the suspensions containing $TBA^+$ cations along with the target substance being processed. These cations, being electrostatically adsorbed on the surface of the photocatalyst, are capable of sterically limiting the supply of relatively large carbohydrate molecules to the active centers. When operating in aqueous methanol, this effect may not appear due to the significantly smaller size of the alcohol molecules, which apparently

effectively reach the photocatalyst surface despite the presence of $TBA^+$. It should also be noted that among the platinized photocatalysts tested in water, the filtered nanosheets also showed maximum efficiency, although in the absence of the cocatalyst, the initial ones turned out to be the most active. The noted difference could hypothetically be caused by the negative effect of $TBA^+$ cations on the efficiency of reduction of the platinum cocatalyst in the absence of methanol as an additional reducing agent in the reaction solution, but it is not possible to establish the exact cause based on the available data.

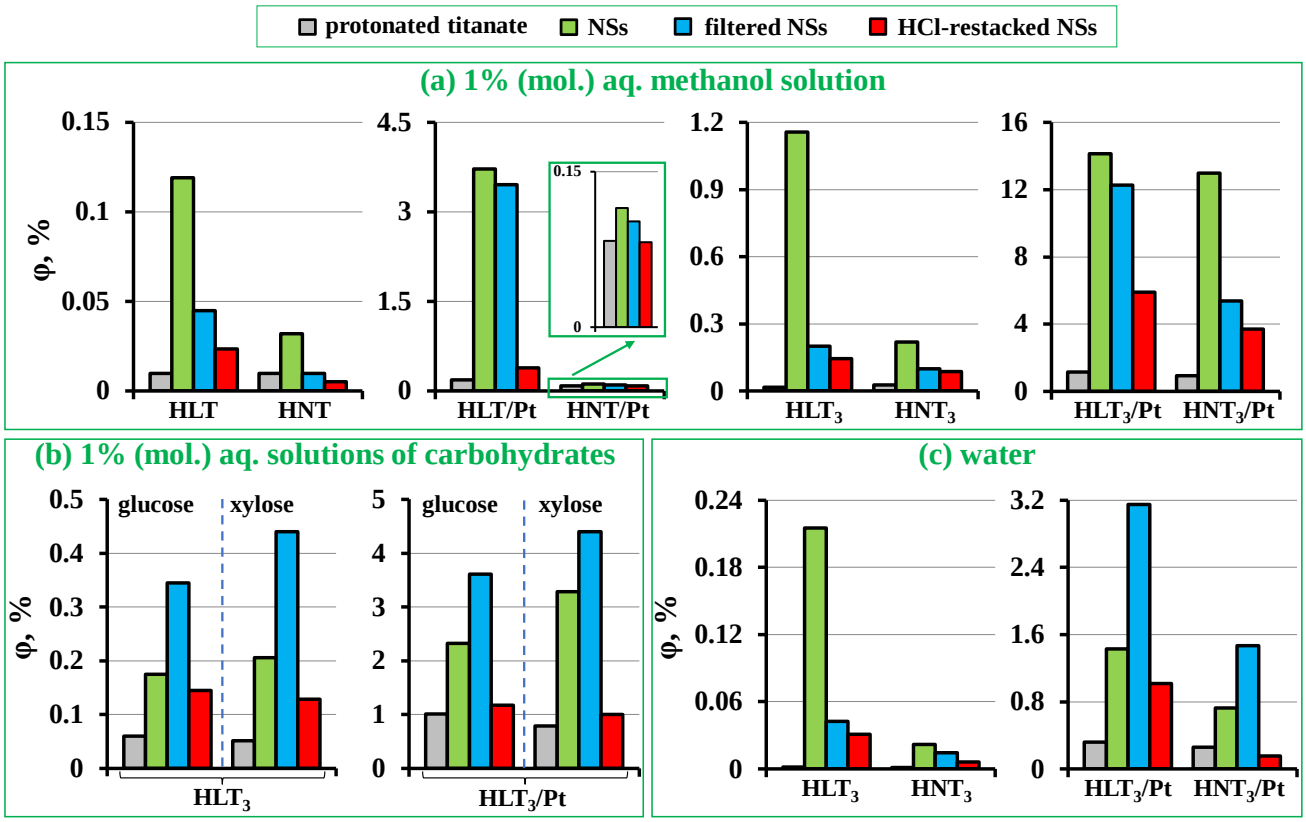


Fig. 81. Influence of used form of the titanate nanosheets on apparent quantum efficiency of photocatalytic hydrogen evolution

Meanwhile, among the reassembled titanates, in all cases, without exception, the filtered nanosheets are superior in the photocatalytic activity to the HCl-restacked ones. This result is somewhat unusual for heterogeneous photocatalysis, since the samples reassembled by filtration have a noticeably lower specific surface area compared to those precipitated with acid, which could cause the increased activity of the latter (Table 17). However, as already noted, the measured specific surface area is a characteristic of powdered samples, and photocatalytic activity is a property of those dispersed in a reaction solution. In accordance with laser granulometry and spectrophotometry data, the filtered nanosheets during ultrasonic treatment before photocatalysis undergo disaggregation much more easily than the HCl-

restacked ones, which causes smaller particle sizes (greater specific surface area) of the former in the final suspensions and, accordingly, their enhanced photocatalytic activity. In addition, the filtered nanosheets are superior to the HCl-restacked analogues in terms of the average lifetime of luminescence excited in the range of their intrinsic light absorption (Table 18), which indirectly indicates a lower intensity of electron-hole recombination in the former. Moreover, the titanates reassembled by filtration, in contrast to those precipitated by acid, are in a sense hybrid organic-inorganic materials with $TBA^+$ cations strongly adsorbed between the perovskite layers. Since during preparation of the reaction suspensions complete disaggregation of the reassembled layers does not occur, under photocatalysis conditions these samples can hypothetically function like the previously considered amine derivatives, having increased accessibility of the interlayer zone for reactant molecules and, accordingly, greater photocatalytic activity, but this issue requires further study.

Thus, the method of isolating perovskite nanosheets by acidifying the initial suspensions, widely used in the literature, turned out to be the least preferable from the point of view of the activity of the final photocatalysts in hydrogen evolution reactions, despite the convenience of practical application.

3.4.6. Stability and composition of reaction suspensions of the nanosheets

Stability of the reaction suspensions of the exfoliated titanates towards precipitation during photocatalytic measurements was controlled by the ratio of the volume concentration of the photocatalyst at the ending and beginning of each experiment ($c_2/c_1$) (Fig. 82). It was found that suspensions of the initial nanosheets after acidification of the medium to $pH \approx 6$, despite the particle coagulation (section 3.4.2), well maintain the volume concentration of the dispersed phase under continuous stirring implemented in the reaction cell. Suspensions of photocatalysts based on the initial and filtered nanosheets are generally superior in the stability to those of the protonated titanates, which may be due to both the smaller particle sizes of the exfoliated samples and the presence of $TBA^+$ cations on their surface sterically complicating coagulation. At the same time, the nanosheets isolated by acidification of the initial suspensions form coarser suspensions upon repeated sonication and undergo greater precipitattion on the walls of the reactor during photocatalysis, despite intensive stirring of the reaction mixture throughout all photocatalytic measurements. However, this does not have a

significant effect on the rate of hydrogen generation, which in most cases is stably maintained during the experiment.

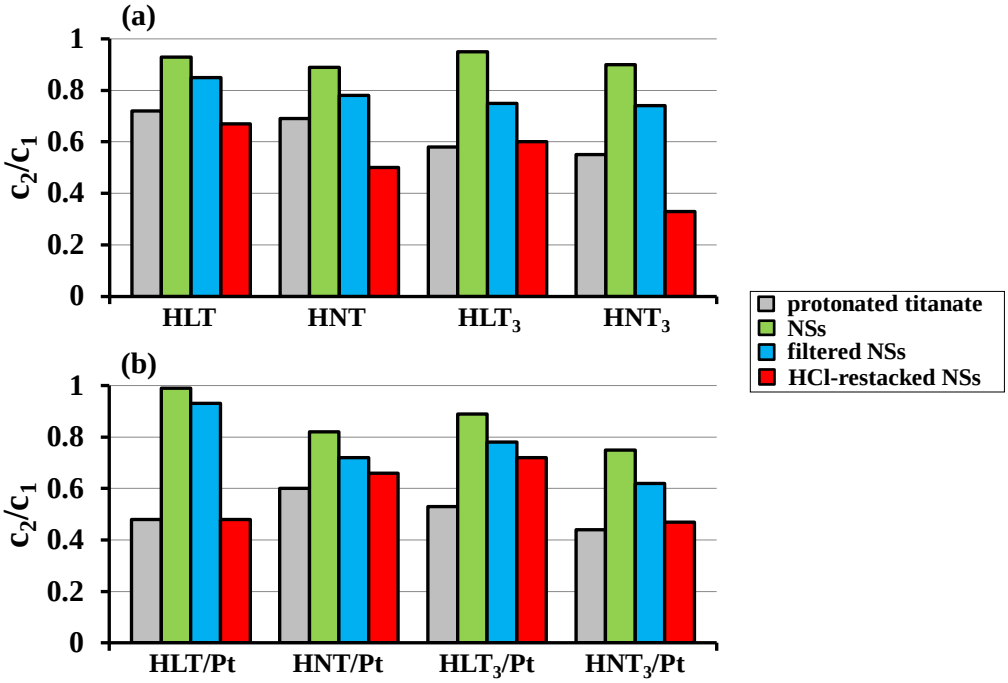


Fig. 82. Ratios of actual volume concentrations of the protonated titanates and photocatalysts based on their nanosheets at the ending and beginning of standard photocatalytic experiments in a 1% (mol.) aqueous solution of methanol

It was also noted that hydrogen generation from aqueous methanol in the presence of the most active photocatalysts based on the nanosheets is accompanied by a decrease in the pH of the reaction solution from 6–7 to 3–4 during the first 2.5 h of irradiation. Analysis of the final solutions by Raman spectroscopy showed that, as in the case of the organic-inorganic derivatives, one of the channels for the target reaction is the oxidation of methanol to formic acid, which, in turn, can react under the conditions of a photocatalytic experiment with an excess of alcohol, giving methyl formate.

3.4.7. Comparison of the titanate nanosheets with those of the niobates $HA_2Nb_3O_{10}$ (A = Ca, Sr)

Along with photocatalysts based on exfoliated Ruddlesden-Popper titanates, considered in this work, the applicant obtained and tested similar materials based on nanosheets of the three-layer Dion-Jacobson niobates $HCa_2Nb_3O_{10}$ ($HCN_3$) and $HSr_2Nb_3O_{10}$ ($HSN_3$) [247]. In this case, their hydrated protonated forms served as precursors for exfoliation, and otherwise the research methodology completely coincided with that used for exfoliating the titanates.

It was found that suspensions of the niobate nanosheets, when the medium is acidified to neutral pH, retain aggregative stability, while those of the titanates undergo particle coagulation. Although under continuous stirring the volume concentration of the latter is well preserved, the above fact may to some extent limit the photocatalytic activity of the initial titanate nanosheets compared to the activity of the niobate ones. At the same time, the physical-chemical features of the reassembled nanosheets (filtered and HCl-restacked) for the titanates and niobates are generally identical. Particularly, when going from the initial oxides to their nanosheets, a moderate narrowing of the bandgap is observed, not exceeding 0.26 eV in absolute value. The filtered nanosheets in both cases represent organic-inorganic materials with strongly bound $TBA^+$ cations. Their aggregates are characterized by a formally larger interlayer distance, increased luminescence lifetimes and better dispersibility in aqueous media, which ensures smaller sizes (more developed surface) of the particles in suspensions, despite the smaller specific surface area in a powdered form. HCl-restacked nanosheets, on the contrary, are practically devoid of residual $TBA^+$ cations, have a smaller interlayer distance and exhibit shorter luminescence lifetimes. Despite the larger specific surface area in a powdered state, the HCl-restacked samples are less susceptible to ultrasonic disaggregation and, therefore, have on average greater particle sizes (less developed surface area) in the reaction suspensions. As a consequence, the photocatalytic activity of the nanosheets precipitated with acid in all cases turns out to be lower than that of the analogues isolated by filtration. At the same time, the ratio of the activity of the initial and filtered nanosheets depends on the reaction solution: in aqueous methanol, the titanate and niobate nanosheets without reassembly are most active while the filtered ones show the best performance in aqueous solutions of carbohydrates.

Data on the rate and apparent quantum efficiency of photocatalytic hydrogen generation in the presence of the platinized protonated oxides, as well as the most highly active forms of the titanate $HLT_3$ and niobate $HCN_3$ nanosheets are presented in the form of bar graphs in Fig. 83. As one can see, the exfoliated titanate noticeably outperforms the niobate in the rate of hydrogen evolution from aqueous methanol (54.8 $mmol \cdot h^{-1} \cdot g^{-1}$ and 37.6 $mmol \cdot h^{-1} \cdot g^{-1}$), but is somewhat inferior to it in the quantum efficiency (14.2% and 20.4%) due to the difference in the bandgap energy. At the same time, the niobate-based materials turn out to be more efficient photocatalysts for reforming carbohydrates. In particular, the activity of the latter in aqueous

solutions of glucose and xylose reaches 23.8 mmol·h$^{-1}$·g$^{-1}$ (9.83%) and 24.2 mmol·h$^{-1}$·g$^{-1}$ (10.0%), respectively, while that of the titanate nanosheets in under the same conditions is 14.0 mmol·h$^{-1}$·g$^{-1}$ (3.60%) and 17.1 mmol·h$^{-1}$·g$^{-1}$ (4.40%). However, in the reaction of hydrogen evolution from pure water, the undisputed leader is the exfoliated reassembled titanate, demonstrating an impressive activity of 12.2 mmol·h$^{-1}$·g$^{-1}$ (3.15%), while the corresponding value for the exfoliated niobate is only 5.74 mmol·h$^{-1}$·g$^{-1}$ (2.4%).

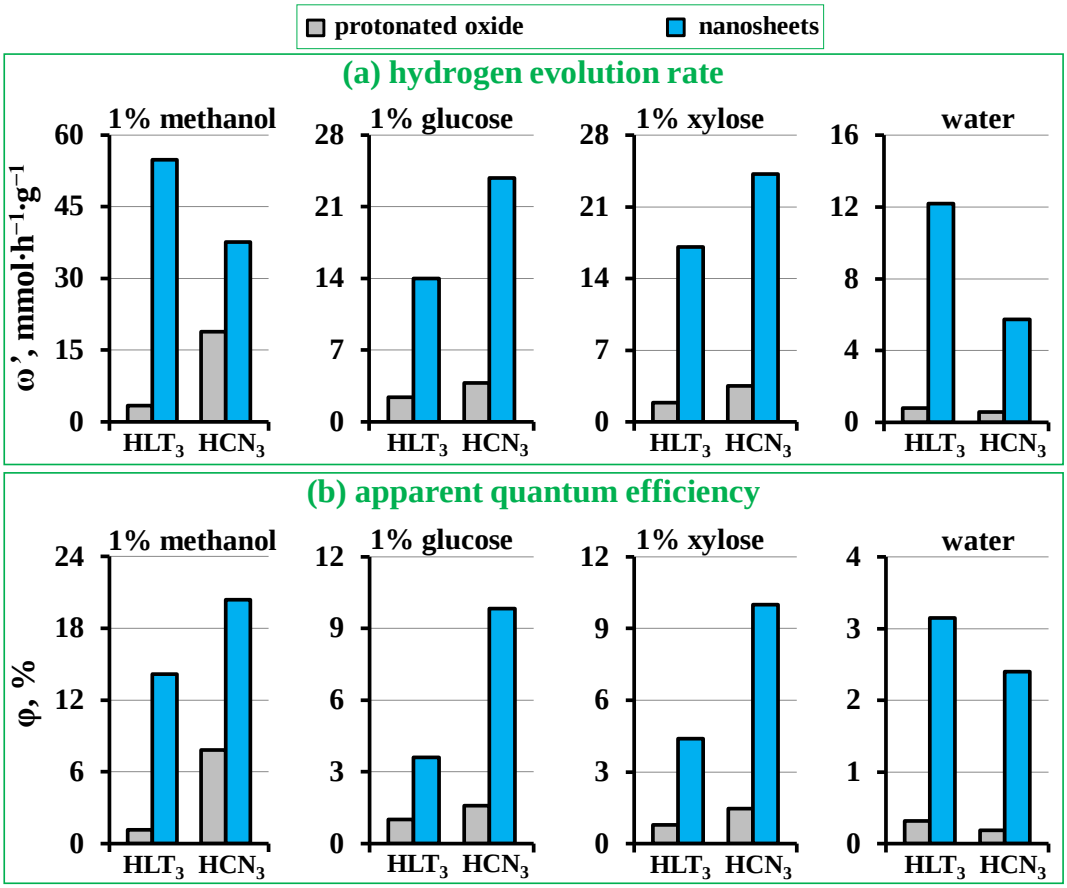


Fig. 83. Comparison of photocatalytic activity of platinized protonated forms and nanosheets of the titanate $HLT_3$ and niobate $HCN_3$ in hydrogen evolution reactions

Thus, the tested photocatalysts based on $HLT_3$ titanate nanosheets are more promising for the processes of producing hydrogen from aqueous methanol solutions and pure water while the materials based on $HCN_3$ niobate nanosheets are more suitable for the photocatalytic reforming of glucose and xylose dissolved in water.

### 3.5. Comparative analysis of photocatalysts based on organic-inorganic derivatives and nanosheets of layered perovskite-like oxides

To summarize this work, it should be emphasized that both interlayer organic modification and exfoliation into nanosheets turned out to be efficient approaches to the

creation of new highly active photocatalysts for hydrogen generation based on ion-exchangeable layered perovskite-like oxides. Fig. 84 in the form of bar graphs presents the maximum values of the rate and apparent quantum efficiency of the corresponding reaction in 1% (mol.) aqueous solutions of methanol, glucose, xylose, as well as in pure water, achieved in the presence of the protonated forms, as well as the most highly active photocatalysts based on organic-inorganic derivatives and nanosheets of the three-layer titanates and niobates.

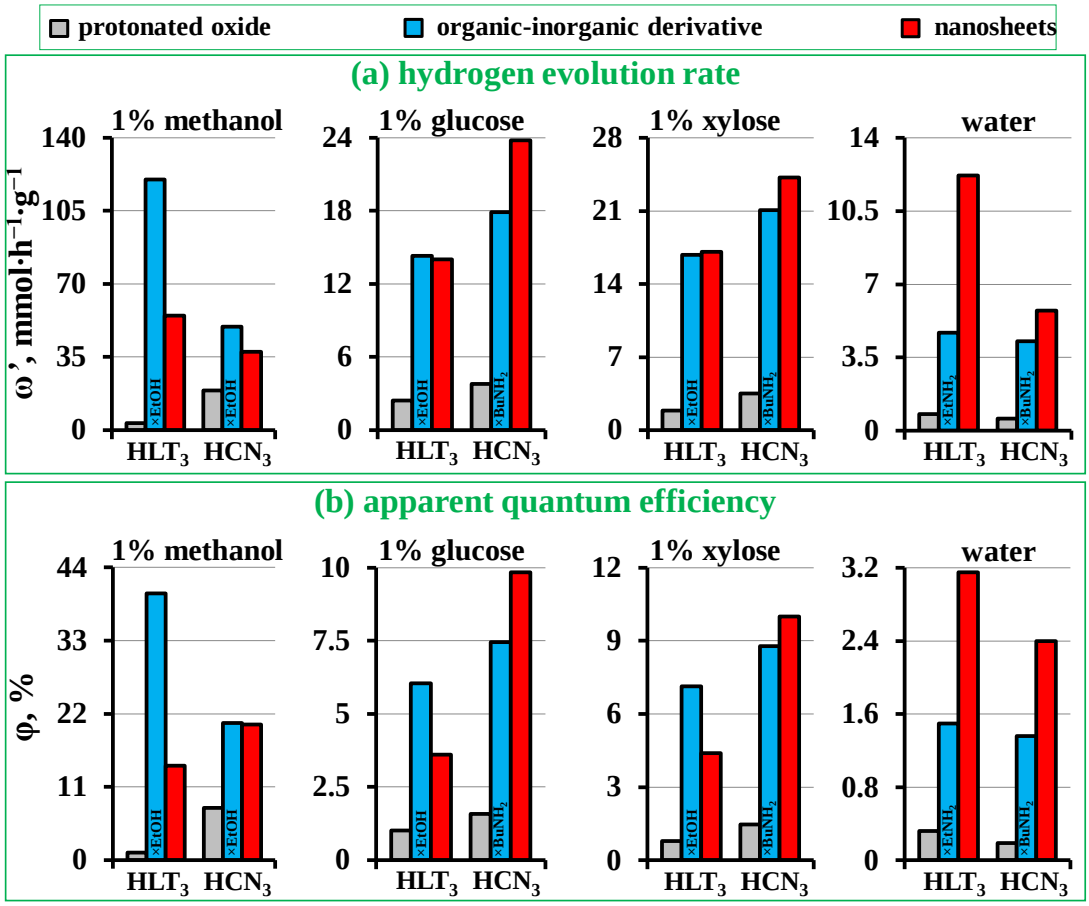


Fig. 84. Comparison of photocatalytic activity of platinized protonated forms, organic-inorganic derivatives and nanosheets of the titanate $HLT_3$ and niobate $HCN_3$ in hydrogen evolution reactions

It was found that among the amine and alcohol derivatives, materials with relatively short-chain interlayer modifiers (ethyl- and *n*-butylamine, ethoxy groups) exhibit the greatest activity after platinization, and among exfoliated forms of the oxides – nanosheets without reassembly (in aqueous methanol) and filtered nanosheets (in carbohydrate solutions and pure water). It is important to note that, despite the effectiveness of both strategies for improving photocatalytic properties, the resulting photocatalysts have different areas of potential application. Thus, when working in aqueous solutions of methanol, the undisputed leaders in the photocatalytic activity are the organic-inorganic derivatives of three-layer titanates

($HLT_3$×$EtNH_2$/Pt among amine derivatives and $HLT_3$×EtOH/Pt among alcohol ones). When moving to solutions of glucose and xylose, the difference in the activity of the organically modified oxides and nanosheets becomes less pronounced, which is probably due to the limited accessibility of the interlayer space of the former for relatively large carbohydrate molecules, which, for steric reasons, have to react predominantly on the external surface of photocatalysts. Finally, the most promising for hydrogen generation from pure water in the absence of any sacrificial agents are photocatalysts based on the nanosheets (primarily, titanate $HLT_3$ reassembled by filtration).

In general, the data obtained indicate that the catalytic properties of the interlayer reaction zone are not equivalent to those of the external surface, which is why the transformation of the first into the second during the exfoliation of layered photocatalysts into nanosheets does not in all cases lead to achieving the level of the photocatalytic activity characteristic of organic-inorganic derivatives possessing the expanded interlayer space.

Moreover, it was shown that the efficiency of hydrogen generation in the presence of the photocatalysts obtained can be additionally increased by further optimizing the reaction conditions (in particular, increasing the concentration of organic substrates and the photocatalyst itself), which allows them to unlock their potential to an even greater extent.

## Resume

In the first half of this work, using the example of titanates $HLnTiO_4$ and $H_2Ln_2Ti_3O_{10}$ (Ln = La, Nd), a new highly effective approach to increasing the photocatalytic activity of layered perovskite-like oxides has been systematically studied – modification of the interlayer space with ionically and covalently bonded organic components. It was shown that in the reactions of hydrogen production from aqueous-organic solutions, amine and alcohol derivatives of the titanates are superior in the activity to the initial protonated compounds and the «gold standard» in photocatalysis $TiO_2$ P25 Degussa up to 117 and 87 times, respectively, and after reduction of Pt nanoparticles as a cocatalyst on the surface and optimization of the reaction conditions, a hydrogen evolution rate of up to 175 $mmol \cdot h^{-1} \cdot g^{-1}$ and an apparent quantum efficiency of up to 58% can be achieved. At the same time, the rate of hydrogen generation in the presence of the most active organic-inorganic derivatives is stably maintained for a long time, despite the fact that intercalated amines and grafted alcohols undergo partial or, in some cases, almost complete degradation already during the first hours of irradiation of the reaction suspensions. In this regard, the photocatalytic properties observed at later stages of the experiment are inherent, strictly speaking, not in the initial organic-inorganic compounds, but in the products of their in situ transformations under photocatalysis conditions. That being said, these products might be stable only in a reaction medium and cannot be isolated in an individual form. At the same time, different amine and alcohol derivatives exhibit unequal photocatalytic activity, which suggests that a specific organic modifier actually plays a significant role in the formation of the final photocatalyst. In general, the organic components significantly expand the interlayer space, considered as an additional reaction zone in photocatalysis, thereby facilitating the supply of reactants to the interlayer reaction centers. Apparently, despite the partial or even almost complete degradation of some organic modifiers, the interlayer space remains expanded at least as long as the photocatalyst is in the reaction medium, which allows the interlayer reaction zone to continue functioning and explains the preservation of high photocatalytic activity. Additionally, the titanate $H_2La_2Ti_3O_{10}$ has been used to yield derivatives with aromatic modifiers, grafting of which in the interlayer space made it possible to achieve a significant reduction in the optical bandgap energy and manifestation of the photocatalytic activity not only under ultraviolet, but also under purely visible radiation. Certain derivatives with aromatic modifiers demonstrated high stability

towards photodegradation of the interlayer organic component and, accordingly, stable preservation of the wide light absorption range during photocatalytic hydrogen production. Thus, interlayer organic modification has proven to be a highly effective approach to improving the photocatalytic properties of ion-exchange layered perovskite-like oxides, which is of interest for further study in both fundamental and applied aspects.

In the second half of this work, a highly efficient method for the liquid-phase exfoliation of the titanates $HLnTiO_4$ and $H_2Ln_2Ti_3O_{10}$ using their amine derivatives as precursors has been developed, which opened the way to the creation of photocatalysts based on their nanosheets that have not previously been described in the literature. It was shown that the exfoliated titanates are up to 88 times superior in the photocatalytic activity to the initial protonated forms and, after platinization, demonstrate a rate and apparent quantum efficiency of hydrogen generation from aqueous organic solutions of up to 54.8 $mmol \cdot h^{-1} \cdot g^{-1}$ and 14.2%, respectively. Despite the decent level of the activity exhibited, the titanate nanosheets are generally inferior to the most active organic-inorganic derivatives of the same compounds, which once again indicates the special role of the interlayer space of the latter in the photocatalytic process and its non-equivalence to the external surface of the photocatalyst. At the same time, photocatalysts based on the titanate nanosheets demonstrate a clear advantage over the organic-inorganic derivatives in the reaction of hydrogen production from pure water in the absence of any sacrificial agents. Moreover, the photocatalytic properties of nanosheets significantly depend on their form used. Particularly, in aqueous methanol solutions, the initial nanosheets without reassembly exhibit the greatest activity, and in carbohydrate solutions, those filtered after liquid-phase exfoliation and redispersed prove to be the most active. At the same time, the nanosheets precipitated with acid are in all cases significantly inferior in the activity to the initial and filtered ones, despite the fact that this approach to isolating perovskite nanosheets is currently the most common in the literature.

A comparative analysis of photocatalytic properties of the above titanates with the those of the niobates $HA_2Nb_3O_{10}$ (A = Ca, Sr), studied by the applicant separately, allowed us to conclude that the noted trends in the increase in photocatalytic activity upon organic modification and the influence of the form of nanosheets used (initial, filtered, precipitated with acid) on the efficiency of hydrogen production in general are common to both objects and with a high degree of probability are universal in nature for a wider range of ion-exchange

layered perovskite-like oxides. The relationships revealed in this case between the structural-chemical characteristics of the compounds and the activity they exhibit are of significant importance for the further research-based creation of new highly efficient and durable photocatalysts.

## Conclusions

1. 60 organic-inorganic derivatives of layered perovskite-like titanates $HLnTiO_4$ and $H_2Ln_2Ti_3O_{10}$ (Ln = La, Nd), representing the products of intercalation of primary amines, grafting of alcohols and aromatic compounds into the interlayer space, have been successfully synthesized and characterized in detail. It has been established that the organic modification leads to a significant expansion of the interlayer space, proportional to the size of the introduced components. In the amine derivatives, ionic bonding occurs between the inorganic matrix and the organic component; in the alcohol derivatives and those with aromatic modifiers, covalent bonding takes place. The resulting derivatives contain on average 0.4 units of organic component per proton of the initial titanate, as well as a certain amount of intercalated water;
2. It has been established that upon the formation of amine and alcohol derivatives, optical bandgap energy of the titanates changes slightly, but the average lifetime of luminescence excited in the region of intrinsic light absorption increases. Grafting of aromatic compounds leads to a pronounced shift of the long-wavelength absorption edge to the visible range;
3. Amine and alcohol derivatives of the titanates have been systematically studied as photocatalysts for hydrogen generation from aqueous-organic mixtures, as well as pure water under ultraviolet radiation. It has been shown that organic modification of the interlayer space is a highly effective approach to enhancing photocatalytic activity, the increase factor of which reaches 117 times. The most active of the obtained samples is the platinum-modified ethanol derivative $H_2La_2Ti_3O_{10}\times EtOH/Pt$, in the presence of which the rate (apparent quantum efficiency) of hydrogen evolution from a 1% (mol.) aqueous solution of methanol reaches 120 $mmol\cdot h^{-1}\cdot g^{-1}$ (40.1%);
4. It has been shown that in many cases the photocatalytic activity of samples in the series of amine and alcohol derivatives changes symbatically with the degree of hydration of their interlayer space;
5. Using the example of selected organic-inorganic derivatives of the titanates, it was shown that the dependences of the photocatalytic activity on the concentration of methanol, concentration of the photocatalyst and the platinum cocatalyst content pass

through a maximum. Moreover, optimization of these parameters makes it possible to achieve the activity of 175 $mmol \cdot h^{-1} \cdot g^{-1}$ (58%);

6. It has been established that the most active derivatives of the titanates can also serve as effective photocatalysts for hydrogen generation from 1% (mol.) aqueous solutions of D-glucose and D-xylose, exhibiting the activity up to 14.3 $mmol \cdot h^{-1} \cdot g^{-1}$ (6.0%) and 16.8 $mmol \cdot h^{-1} \cdot g^{-1}$ (7.0%), respectively. When generating hydrogen from pure water using the same derivatives, the activity up to 3.6 $mmol \cdot h^{-1} \cdot g^{-1}$ (1.5%) is achieved;
7. It has been shown that interlayer organic modifiers of the amine and alcohol derivatives undergo partial degradation during photocatalysis in aqueous-organic media, but it does not affect the activity of the corresponding samples, which is stably maintained for a long time, and hydrogen is actually released from the reaction solution;
8. It has been established that titanate derivatives with aromatic modifiers are capable of functioning as photocatalysts not only under ultraviolet, but also under purely visible radiation. In this case, the most active and stable is the platinized 4-phenylphenol derivative $H_2La_2Ti_3O_{10}$×PhPhOH/Pt, whose activity in the reaction of hydrogen generation from a 1% (mol.) aqueous solution of methanol under purely visible light is 0.82 $mmol \cdot h^{-1} \cdot g^{-1}$ (0.041%);
9. Possible reasons for the high photocatalytic activity of organic-inorganic derivatives were analyzed. The main one is that organic modifiers expand the interlayer reaction zone and thereby significantly increase its accessibility to reactant molecules. Moreover, despite the partial degradation of the organic modifiers, this zone can remain expanded at least as long as the photocatalyst is in the reaction medium, which explains the consistently high activity;
10. A highly efficient method for the liquid-phase exfoliation of the titanates $HLnTiO_4$ and $H_2Ln_2Ti_3O_{10}$ (Ln = La, Nd) into nanosheets in an aqueous solution of tetrabutylammonium hydroxide has been developed and optimized, providing a concentration of the latter in suspensions of up to 2.1 g/L and the yield of up to 95%;
11. Initial nanosheets of the titanates and those reassembled by two different methods (filtration and precipitation with acid) have been used to successfully obtain new photocatalytic materials. It has been established that exfoliation followed by reassembly is accompanied by a decrease in the optical bandgap energy of the titanates;

12. It was found that the reassembly approach significantly affects the physical-chemical properties of the nanosheets. Filtered nanosheets, in contrast to those precipitated with acid, contain tetrabutylammonium cations firmly bound to the surface, exhibit increased luminescence lifetimes and are more easily dispersed in aqueous media, which provides a greater specific surface area in suspensions;
13. Photocatalysts based on the titanate nanosheets have been systematically studied in the reactions of hydrogen generation from aqueous-organic mixtures, as well as pure water under ultraviolet radiation. It has been shown that exfoliation into nanosheets leads to an increase in the activity of the titanates up to 88 times. The most promising of them are platinized photocatalysts based on the nanosheets of $H_2La_2Ti_3O_{10}$, the activity of which in 1% (mol.) aqueous solutions of methanol, D-glucose and D-xylose reaches 54.8 $mmol \cdot h^{-1} \cdot g^{-1}$ (14.2 %), 14.0 $mmol \cdot h^{-1} \cdot g^{-1}$ (3.6%) and 17.1 $mmol \cdot h^{-1} \cdot g^{-1}$ (4.4%), respectively, and in pure water – 12.2 $mmol \cdot h^{-1} \cdot g^{-1}$ (3.2%). That being said, the nanosheets without reassembly demonstrate the greatest activity in an aqueous solution of methanol, and those reassembled by filtration – in aqueous solutions of carbohydrates. The nanosheets precipitated with acid are in all cases inferior in the activity to the filtered ones;
14. It has been established that, other things being equal, the photocatalysts based on three-layer titanates $H_2Ln_2Ti_3O_{10}$ are significantly superior in the activity to the samples based on single-layer compounds $HLnTiO_4$;
15. It has been shown that photocatalysts based on organic-inorganic derivatives of the titanates are the most promising for producing hydrogen from aqueous-organic mixtures, while those based on the nanosheets are preferable for hydrogen generation from pure water.

## Bibliography


1. Gupta A. et al. A review of hydrogen production processes by photocatalytic water splitting – from atomistic catalysis design to optimal reactor engineering // Int. J. Hydrogen Energy. 2022. Vol. 47, № 78. P. 33282–33307.
2. Lin S. et al. Photocatalytic oxygen evolution from water splitting // Adv. Sci. 2021. Vol. 8, № 1. P. 23–25.
3. Lee D. E. et al. State-of-the-art review on photocatalysis for efficient wastewater treatment: attractive approach in photocatalyst design and parameters affecting the photocatalytic degradation // Catal. Commun. 2023. Vol. 183, № 106764.
4. Sharma S. et al. An overview on recent progress in photocatalytic air purification: metal-based and metal-free photocatalysis // Environ. Res. 2022. Vol. 214, № 113995.
5. Zuo C., Su Q., Yu L. Research progress in composite materials for photocatalytic nitrogen fixation // Molecules. 2023. Vol. 28(21), № 7277.
6. Fang S. et al. Photocatalytic $CO_2$ reduction // Nat. Rev. Methods Prim. 2023. Vol. 3, № 62.
7. Gisbertz S., Pieber B. Heterogeneous photocatalysis in organic synthesis // ChemPhotoChem. 2020. Vol. 4, № 7. P. 454.
8. Rodionov I. A. Thermodynamic basis of heterogeneous photocatalysis. St. Petersburg: Lubavitch, 2017. 120 p.
9. Artemyev Y. M., Ryabchuk V. K. Introduction to heterogeneous photocatalysis. St. Petersburg : Publishing House St. Petersburg State University, 1999. 304 p.
10. Parmon V. N. Photocatalysis as a phenomenon: aspects of terminology // Catal. Today. 1997. Vol. 39, № 3. P. 137–144.
11. Matsuoka M. et al. Recent advances in photocatalytic water splitting reactions for hydrogen production // Catal. Today. 2007. Vol. 122, № 1–2. P. 51–61.
12. Rodionov I. A., Zvereva I. A. Photocatalytic activity of layered perovskite-like oxides in practically valuable chemical reactions // Russ. Chem. Rev. 2016. Vol. 85, № 3. P. 248–279.
13. Cieśla P. et al. Homogeneous photocatalysis by transition metal complexes in the environment // J. Mol. Catal. A Chem. 2004. Vol. 224, № 1–2. P. 17–33.
14. Gaya U.I. Heterogeneous photocatalysis using inorganic semiconductor solids.

Dordrecht: Springer, 2014. 213 p.

15. Nadeem M. A. et al. An overview of the photocatalytic water splitting over suspended particles // Catalysts. 2021. Vol. 11(1), № 60.
16. Wood D. et al. An overview of photocatalyst immobilization methods for air pollution remediation // Chem. Eng. J. 2020. Vol. 391, № 123490.
17. Walter M. G. et al. Solar water splitting cells // Chem. Rev. 2010. Vol. 110, № 11. P. 6446–6473.
18. Emeline A. et al. Photo-induced processes in heterogeneous nanosystems. From photoexcitation to interfacial chemical transformations // Int. J. Photoenergy. 2001. Vol. 3, № 1.
19. Maruska H. P., Ghosh A. K. Photocatalytic decomposition of water at semiconductor electrodes // Sol. Energy. 1978. Vol. 20, № 6. P. 443–458.
20. Pervukhin O. K., Panov M. Y., Rakhimov V. I. Fundamentals of chemical kinetics. St. Petersburg: Publishing house of the St. Petersburg State. University, 2012. 172 p.
21. Hoque M. A., Guzman M. I. Photocatalytic activity: experimental features to report in heterogeneous photocatalysis // Materials. 2018. Vol. 11(10), № 1990.
22. Daneshvar N., Salari D., Khataee A. R. Photocatalytic degradation of azo dye acid red 14 in water: investigation of the effect of operational parameters // J. Photochem. Photobiol. A Chem. 2003. Vol. 157, № 1. P. 111–116.
23. Daneshvar N., Salari D., Khataee A. R. Photocatalytic degradation of azo dye acid red 14 in water on ZnO as an alternative catalyst to $TiO_2$ // J. Photochem. Photobiol. A Chem. 2004. Vol. 162, № 2–3. P. 317–322.
24. Daneshvar N. et al. Photocatalytic degradation of the herbicide erioglaucine in the presence of nanosized titanium dioxide: comparison and modeling of reaction kinetics // J. Environ. Sci. Heal. - Part B Pestic. Food Contam. Agric. Wastes. 2006. Vol. 41, № 8. P. 1273–1290.
25. Serpone N. et al. Standardization protocol of process efficiencies and activation parameters in heterogeneous photocatalysis: relative photonic efficiencies $\zeta_r$ // J. Photochem. Photobiol. A Chem. 1996. Vol. 94, № 2–3. P. 191–203.
26. Braslavsky S. E. et al. Glossary of terms used in photocatalysis and radiation catalysis (IUPAC recommendations 2011) // Pure Appl. Chem. 2011. Vol. 83, № 4. P. 931–1014.

27. Lu Q. et al. 2D transition-metal-dichalcogenide-nanosheet-based composites for photocatalytic and electrocatalytic hydrogen evolution reactions // Adv. Mater. 2016. Vol. 28, № 10. P. 1917–1933.
28. Kudo A., Kato H., Nakagawa S. Water splitting into $H_2$ and $O_2$ on new $Sr_2M_2O_7$ (M = Nb and Ta) photocatalysts with layered perovskite structures: factors affecting the photocatalytic activity // J. Phys. Chem. B. 2000. Vol. 104, № 3. P. 571–575.
29. Kato H., Kudo A. Water splitting into $H_2$ and $O_2$ on alkali tantalate photocatalysts $ATaO_3$ (A = Li, Na, and K) // J. Phys. Chem. B. 2001. Vol. 105, № 19. P. 4285–4292.
30. Do T. O., Mohan S. Editorial: Special issue on «Emerging trends in $TiO_2$ photocatalysis and applications» // Catalysts. 2020. Vol. 10(6), № 670.
31. Scaife D. E. Oxide semiconductors in photoelectrochemical conversion of solar energy // Sol. Energy. 1980. Vol. 25, № 1. P. 41–54.
32. Do H. H. et al. Recent progress in $TiO_2$-based photocatalysts for hydrogen evolution reaction: A review // Arab. J. Chem. 2020. Vol. 13, № 2. P. 3653–3671.
33. Zhang H., Chen G., Li X. Synthesis and visible light photocatalysis water splitting property of chromium-doped $Bi_4Ti_3O_{12}$ // Solid State Ionics. 2009. Vol. 180, № 36–39. P. 1599–1603.
34. Piątkowska A. et al. C-, N- and S-doped $TiO_2$ photocatalysts: a review // Catalysts. 2021. Vol. 11(1), № 144.
35. Leung C.-F., Lau T.-C. Organic photosensitizers for catalytic solar fuel generation // Energy and Fuels. 2021. Vol. 35, № 23. P. 18888–18899.
36. Kim D., Dang V. Q., Teets T. S. Improved transition metal photosensitizers to drive advances in photocatalysis // Chem. Sci. 2023. Vol. 15, № 1. P. 77–94.
37. Kochuveedu S. T. Photocatalytic and photoelectrochemical water splitting on $TiO_2$ via photosensitization // J. Nanomater. 2016. № 4073142.
38. Maeda K. et al. Niobium oxide nanoscrolls as building blocks for dye-sensitized hydrogen production from water under visible light irradiation // Chem. Mater. 2008. Vol. 20, № 21, pp. 6770–6778.
39. Pleskov Y. V. Photoelectrochemical conversion of solar energy. Moscow : Chemistry, 1990. 176 p.
40. Kumar A. A review on the factors affecting the photocatalytic degradation of hazardous

materials // Mater. Sci. Eng. Int. J. 2017. Vol. 1, № 3. P. 106–114.

41. Emara M. M. et al. How does photocatalytic activity depend on adsorption, composition, and other key factors in mixed metal oxide nanocomposites? // Colloids Interface Sci. Commun. 2021. Vol. 40, № 100341.
42. Chen F. et al. Atomic-level charge separation strategies in semiconductor-based photocatalysts // Adv. Mater. 2021. Vol. 33, № 2005256.
43. Zhou L., Wang W., Zhang L. Ultrasonic-assisted synthesis of visible-light-induced $Bi_2MO_6$ (M = W, Mo) photocatalysts // J. Mol. Catal. A Chem. 2007. Vol. 268, № 1–2. P. 195–200.
44. Jeong H. et al. Hydrogen production by the photocatalytic overall water splitting on $NiO/Sr_3Ti_2O_7$: effect of preparation method // Int. J. Hydrogen Energy. 2006. Vol. 31, № 9. P. 1142–1146.
45. Huang Y. et al. Hydrothermal synthesis of $K_2La_2Ti_3O_{10}$ and photocatalytic splitting of water // J. Alloys Compd. 2008. Vol. 456, № 1–2. P. 364–367.
46. Amano F. et al. Correlation between surface area and photocatalytic activity for acetaldehyde decomposition over bismuth tungstate particles with a hierarchical structure // Langmuir. 2010. Vol. 26, № 10. P. 7174–7180.
47. Kaplin I. Y. et al. Template synthesis of porous ceria-based catalysts for environmental application // Molecules. 2020. Vol. 25(18), № 4242.
48. Maeda K., Mallouk T. E. Two-dimensional metal oxide nanosheets as building blocks for artificial photosynthetic assemblies // Bull. Chem. Soc. Jpn. 2018. Vol. 92, № 1. P. 38–54.
49. Zhang P. et al. Effective charge carrier utilization in photocatalytic conversions // Acc. Chem. Res. 2016. Vol. 49, № 5. P. 911–921.
50. West A. R. Solid state chemistry and its applications. Wiley, 2014. 556 p.
51. Shimodaira Y. et al. Photophysical properties and photocatalytic activities of bismuth molybdates under visible light irradiation // J. Phys. Chem. B. 2006. Vol. 110, № 36. P. 17790–17797.
52. Bi J. et al. Simple solvothermal routes to synthesize nanocrystalline $Bi_2MoO_6$ photocatalysts with different morphologies // Acta Mater. 2007. Vol. 55, № 14. P. 4699–4705.

53. Bai S. et al. Defect engineering in photocatalytic materials // Nano Energy. 2018. Vol. 53. P. 296–336.
54. Liao C. H., Huang C. W., Wu J. C. S. Hydrogen production from semiconductor-based photocatalysis via water splitting // Catalysts. 2012. Vol. 2(4). P. 490–516.
55. Wang H. et al. Semiconductor heterojunction photocatalysts: design, construction, and photocatalytic performances // Chem. Soc. Rev. 2014. Vol. 43, № 15. P. 5234–5244.
56. Liu B. et al. Thermodynamic and kinetic analysis of heterogeneous photocatalysis for semiconductor systems // Phys. Chem. Chem. Phys. 2014. Vol. 16, № 19. P. 8751–8760.
57. Deletze E. et al. Photocatalytic treatment of colored wastewater from medical laboratories: photodegradation of nuclear fast red // Desalin. Water Treat. 2016. Vol. 57, № 40. P. 18897–18905.
58. Minero C., Vione D. A quantitative evalution of the photocatalytic performance of $TiO_2$ slurries // Appl. Catal. B Environ. 2006. Vol. 67, № 3–4. P. 257–269.
59. Reilly K., Wilkinson D. P., Taghipour F. Photocatalytic water splitting in a fluidized bed system: computational modeling and experimental studies // Appl. Energy. 2018. Vol. 222. P. 423–436.
60. Xu Y., Schoonen M. A. A. The absolute energy positions of conduction and valence bands of selected semiconducting minerals // Am. Mineral. 2000. Vol. 85, № 3–4. P. 543–556.
61. Karimi Estahbanati M. R. et al. Kinetic study of the effects of pH on the photocatalytic hydrogen production from alcohols // Int. J. Hydrogen Energy. 2019. Vol. 44, № 60. P. 32030–32041.
62. Chen Y. W., Hsu Y. H. Effects of reaction temperature on the photocatalytic activity of $TiO_2$ with Pd and Cu cocatalysts // Catalysts. 2021. Vol. 11(8), № 966.
63. Martín-Sómer M. et al. Wavelength dependence of the efficiency of photocatalytic processes for water treatment // Appl. Catal. B Environ, 2018. Vol. 221. P. 258–265.
64. Bahnemann D., Bockelmann D., Goslich R. Mechanistic studies of water detoxification in illuminated $TiO_2$ suspensions // Sol. Energy Mater. 1991. Vol. 24, № 1–4. P. 564–583.
65. Molla M. A. I. et al. Optimization of alachlor photocatalytic degradation with nano-$TiO_2$ in water under solar illumination: reaction pathway and mineralization // Clean Technol.

2019. Vol. 1(1). P. 141–153.

66. Humayun M., Wang C., Luo W. Recent progress in the synthesis and applications of composite photocatalysts: a critical review // Small Methods. 2022. Vol. 6(2), № 2101395.
67. Al-Azri Z. H. N. et al. The roles of metal co-catalysts and reaction media in photocatalytic hydrogen production: performance evaluation of M/$TiO_2$ photocatalysts (M = Pd, Pt, Au) in different alcohol-water mixtures // J. Catal. 2015. Vol. 329. P. 355–367.
68. Lee J., Tan L. L., Chai S. P. Heterojunction photocatalysts for artificial nitrogen fixation: fundamentals, latest advances and future perspectives // Nanoscale. 2021. Vol. 13, № 15. P. 7011–7033.
69. Xia Y., Yin L. Core-shell structured α-$Fe_2O_3$@$TiO_2$ nanocomposites with improved photocatalytic activity in the visible light region // Phys. Chem. Chem. Phys. 2013. Vol. 15, № 42. P. 18627–18634.
70. Jiang X. H. et al. Simultaneous photoreduction of uranium(VI) and photooxidation of arsenic(III) in aqueous solution over g-$C_3N_4$/$TiO_2$ heterostructured catalysts under simulated sunlight irradiation // Appl. Catal. B Environ. 2018. Vol. 228. P. 29–38.
71. Yang H. et al. A facile synthesis of $TiO_2$–CdS heterostructures with enhanced photocatalytic activity // Catal. Letters. 2017. Vol. 147, № 10. P. 2581–2591.
72. Mou H. et al. Fabricating amorphous g-$C_3N_4$/$ZrO_2$ photocatalysts by one-step pyrolysis for solar-driven ambient ammonia synthesis // ACS Appl. Mater. Interfaces. 2019. Vol. 11, № 47. P. 44360–44365.
73. Kalanoor B. S., Seo H., Kalanur S. S. Recent developments in photoelectrochemical water-splitting using $WO_3$/$BiVO_4$ heterojunction photoanode: a review // Mater. Sci. Energy Technol. 2018. Vol. 1, № 1. P. 49–62.
74. Li J. et al. Selectively recombining the photoinduced charges in bandgap-broken $Ag_3PO_4$/$GdCrO_3$ with a plasmonic Ag bridge for efficient photothermocatalytic VOCs degradation and $CO_2$ reduction // Appl. Catal. B Environ. 2021. Vol. 291, № 120053.
75. Li J. et al. Plasmonic metal bridge leading type III heterojunctions to robust type B photothermocatalysts // Ind. Eng. Chem. Res. 2021. Vol. 60, № 23. P. 8420–8429.
76. Zheng D. et al. NiO-$TiO_2$ p-n heterojunction for solar hydrogen generation // Catalysts.

2021. Vol. 11(12), № 1427.

77. Lu X. et al. Fabrication of $Ag_2O/KNbO_3$ heterojunction with high visible-light photocatalytic activity // J. Nanoparticle Res. 2019. Vol. 21, № 251.
78. Guo X. et al. An efficient $ZnIn_2S_4$@$CuInS_2$ core-shell p-n heterojunction to boost visible-light photocatalytic hydrogen evolution // J. Phys. Chem. C. 2020. Vol. 124, № 11. P. 5934–5943.
79. Bard A. J. Photoelectrochemistry and heterogeneous photo-catalysis at semiconductors // J. Photochem. 1979. Vol. 10, № 1. P. 59–75.
80. Abdul Nasir J. et al. Photocatalytic Z-scheme overall water splitting: recent advances in theory and experiments // Adv. Mater. 2021. Vol. 33(52), № 2105195.
81. Tada H. et al. All-solid-state Z-scheme in CdS-Au-$TiO_2$ three-component nanojunction system // Nat. Mater. 2006. Vol. 5, № 10. P. 782–786.
82. Wang X. et al. Enhanced photocatalytic hydrogen evolution by prolonging the lifetime of carriers in ZnO/CdS heterostructures // Chem. Commun. 2009. № 23. P. 3452–3454.
83. Salazar-Marín D. et al. Distinguishing between type II and S-scheme heterojunction materials: a comprehensive review // Appl. Surf. Sci. Adv. 2024. Vol. 19, № 100536.
84. Xu Q. et al. S-scheme heterojunction photocatalyst // Chem. 2020. Vol. 6, № 7. P. 1543–1559.
85. Zhu B. et al. Construction of 2D S-scheme heterojunction photocatalyst // Adv. Mater. 2024. Vol. 36(8), № 2310600.
86. Fujishima A., Honda K. Electrochemical photolysis of water at a semiconductor electrode // Nature. 1972. Vol. 238, № 5358. P. 37–38.
87. Bie C., Wang L., Yu J. Challenges for photocatalytic overall water splitting // Chem. Cell Press, 2022. Vol. 8, № 6. P. 1567–1574.
88. Lin L. et al. Visible-light-driven photocatalytic water splitting: recent progress and challenges // Trends Chem. 2020. Vol. 2, № 9. P. 813–824.
89. Fang S., Hu Y.H. Recent progress in photocatalysts for overall water splitting // Int. J. Energy Res. 2019. Vol. 43, № 3. P. 1082–1098.
90. Wang Z., Li C., Domen K. Recent developments in heterogeneous photocatalysts for solar-driven overall water splitting // Chem. Soc. Rev. 2019. Vol. 48, № 7. P. 2109–2125.

91. Yasuda M., Matsumoto T., Yamashita T. Sacrificial hydrogen production over $TiO_2$-based photocatalysts: polyols, carboxylic acids, and saccharides // Renew. Sustain. Energy Rev. 2018. Vol. 81. P. 1627–1635.
92. Yao Y. et al. Photocatalytic reforming for hydrogen evolution: a review // Catalysts. 2020. Vol. 10(3), № 335.
93. Wei Z., Liu J., Shangguan W. A review on photocatalysis in antibiotic wastewater: pollutant degradation and hydrogen production // Chinese J. Catal. 2020. Vol. 41, № 10. P. 1440–1450.
94. Alsalka Y. et al. Boosting the $H_2$ production efficiency via photocatalytic organic reforming: the role of additional hole scavenging system // Catalysts. 2021. Vol. 11(12), № 1423.
95. Ombaka L. M. et al. Photocatalytic $H_2$ production and degradation of aqueous 2-chlorophenol over B/N-graphene-coated $Cu^0/TiO_2$: a DFT, experimental and mechanistic investigation // J. Environ. Manage. 2022. Vol. 311, № 114822.
96. Fang S., Hu Y. H. Thermo-photo catalysis: a whole greater than the sum of its parts // Chem. Sci. 2022. Vol. 51, № 9. P. 3609–3647.
97. Jing L. et al. Piezo-photocatalysts in the field of energy and environment: designs, applications, and prospects // Nano Energy. 2023. Vol. 112, № 108508.
98. Sang Y., Liu H., Umar A. Photocatalysis from UV/Vis to near-infrared light: towards full solar-light spectrum activity // ChemCatChem. 2015. Vol. 7, № 4. P. 559–573.
99. Rahman M. Z., Kibria M. G., Mullins C. B. Metal-free photocatalysts for hydrogen evolution // Chem. Soc. Rev. 2020. Vol. 49, № 6. P. 1887–1931.
100. Domen K. et al. Photodecomposition of water and hydrogen evolution from aqueous methanol solution over novel niobate photocatalysts // J. Chem. Soc. Chem. Commun. 1986. № 4. P. 356–357.
101. Kudo A. et al. Photocatalytic decomposition of water over $NiO\text{-}K_4Nb_6O_{17}$ catalyst // J. Catal. 1988. Vol. 111, № 1. P. 67–76.
102. Tasleem S., Tahir M. Current trends in strategies to improve photocatalytic performance of perovskites materials for solar to hydrogen production // Renew. Sustain. Energy Rev. 2020. Vol. 132, № 110073.
103. Ma Z. et al. Tackling challenges in perovskite-type metal oxide photocatalysts // Energy

Technol. 2021. Vol. 9(5), № 2001019.

104. Hu Y. et al. Layered perovskite oxides and their derivative nanosheets adopting different modification strategies towards better photocatalytic performance of water splitting // Renew. Sustain. Energy Rev. 2020. Vol. 119, № 109527.
105. Zvereva I. A., Skorobogatov G. A. Synthetic perovskite-like layered oxides: structure, synthesis, properties, applications. St. Petersburg: VVM Publishing House, 2010. 224 p.
106. McCabe E. E. et al. Proper ferroelectricity in the Dion-Jacobson material $CsBi_2Ti_2NbO_{10}$: experiment and theory // Chem. Mater. 2015. Vol. 27, № 24, pp. 8298–8309.
107. Beznosikov B. V., Aleksandrov K. S. Perovskite-like crystals of the Ruddlesden-Popper series // Crystallogr. Reports. 2000. Vol. 45, № 5. P. 792–798.
108. Frit B., Mercurio J. P. The crystal chemistry and dielectric properties of the Aurivillius family of complex bismuth oxides with perovskite-like layered structures // J. Alloys Compd. 1992. Vol. 188. P. 27–35.
109. Kim H. G. et al. A generic method of visible light sensitization for perovskite-related layered oxides: substitution effect of lead // J. Solid State Chem. 2006. Vol. 179, № 4. P. 1214–1218.
110. Ranmohotti K. G. S. et al. Topochemical manipulation of perovskites: low-temperature reaction strategies for directing structure and properties // Adv. Mater. 2011. Vol. 23, № 4. P. 442–460.
111. Gustin L. Synthesis and topochemical manipulation of new layered perovskites. University of New Orleans theses and dissertations, 2016. 112 p.
112. Uppuluri R. et al. Soft chemistry of ion-exchangeable layered metal oxides // Chem. Soc. Rev. 2018. Vol. 47, № 7. P. 2401–2430.
113. Schaak R. E., Mallouk T. E. Perovskites by design: a toolbox of solid-state reactions // Chem. Mater. 2002. Vol. 14, № 4. P. 1455–1471.
114. Suzuki H. et al. Improved visible-light activity of nitrogen-doped layered niobate photocatalysts by $NH_3$-nitridation with KCl flux // Appl. Catal. B Environ. 2018. Vol. 232. P. 49–54.
115. Khan M. S. et al. Nitrogen doped ultrathin calcium/sodium niobate perovskite nanosheets for photocatalytic water oxidation // Sol. Energy Mater. Sol. Cells. 2020.

Vol. 205, № 110283.

116. Suzuki H. et al. Design of nitrogen-doped layered tantalates for non-sacrificial and selective hydrogen evolution from water under visible light // J. Mater. Chem. A. 2016. Vol. 4, № 37. P. 14444–14452.
117. Zong X. et al. Nitrogen doping in ion-exchangeable layered tantalate towards visible-light induced water oxidation // Chem. Commun. 2011. Vol. 47, № 22. P. 6293–6295.
118. Xu X. et al. Layered perovskite compound $NaLaTiO_4$ modified by nitrogen doping as a visible light active photocatalyst for water splitting // ACS Catal. 2020. Vol. 10, № 17. P. 9889–9898.
119. Kawashima K. et al. Understanding the effect of partial $N^{3-}$-to-$O^{2-}$ substitution and $H_+$-to-$K_+$ exchange on photocatalytic water reduction activity of Ruddlesden–Popper layered perovskite $KLaTiO_4$ // Mol. Catal. 2017. Vol. 432. P. 250–258.
120. Huang Y. et al. Photocatalytic property of nitrogen-doped layered perovskite $K_2La_2Ti_3O_{10}$ // Sol. Energy Mater. Sol. Cells. 2010. Vol. 94, № 5. P. 761–766.
121. Wang Y. et al. Tailoring the photocatalytic activity of layered perovskites by opening the interlayer vacancy via ion-exchange reactions // CrystEngComm. 2015. Vol. 17, № 45. P. 8703–8709.
122. Mitsuyama T. et al. Relationship between interlayer hydration and photocatalytic water splitting of $A'_{1-x}Na_xCa_2Ta_3O_{10}\cdot nH_2O$ (A′ = K and Li) // J. Solid State Chem. 2008. Vol. 181, № 6. P. 1419–1424.
123. Hyeon K., Byeon S. Synthesis and structure of new layered oxides $M^{II}La_2Ti_3O_{10}$ (M = Co, Cu, and Zn) // Chem. Mater. 1999. Vol. 11, № 2. P. 352–357.
124. Gopalakrishnan J. et al. Transformations of Ruddlesden−Popper oxides to new layered perovskite oxides by metathesis reactions // Chem. Phys. 2000. Vol. 122, № 26. P. 6237–6241.
125. Zvereva I. A., Silyukov O. I., Chislov M. V. Ion-exchange reactions in the structure of perovskite-like layered oxides: I. Protonation of $NaNdTiO_4$ complex oxide // Russ. J. Gen. Chem. 2011. Vol. 81, № 7. P. 1434–1441.
126. Schaak R. E., Mallouk T. E. $KLnTiO_4$ (Ln = La, Nd, Sm, Eu, Gd, Dy): a new series of Ruddlesden–Popper phases synthesized by ion-exchange of $HLnTiO_4$ // J. Solid State Chem. 2001. Vol. 161, № 2. P. 225–232.

127. Sugimoto W. et al. Conversion of Aurivillius phases $Bi_2ANaNb_3O_{12}$ (A = Sr or Ca) into the protonated forms of layered perovskite via acid treatment // Mater. Res. 2002. Vol. 12, № 6. P. 2946–2952.
128. Yafarova L. V. et al. New data on protonation and hydration of perovskite-type layered oxide $KCa_2Nb_3O_{10}$ // J. Therm. Anal. Calorim. 2021. Vol. 143, № 1. P. 87–93.
129. Rodionov I. A. et al. Effect of protonation on the photocatalytic activity of the $K_2La_2Ti_3O_{10}$ layered oxide in the reaction of hydrogen production // Monatshefte für Chemie – Chem. Mon. 2018. Vol. 149, № 2. P. 475–482.
130. Jacobson A. J., Lewandowski J. T., Johnson J. W. Ion exchange of the layered perovskite $KCa_2Nb_3O_{10}$ by protons // J. Less Common Met. 1986. Vol. 116, № 1. P. 137–146.
131. Domen K. et al. A novel series of photocatalysts with an ion-exchangeable layered structure of niobate // Stud. Surf. Sci. Catal. 1993. Vol. 75. P. 2159–2162.
132. Domen K., Yasuo E., Junko K. Ion exchangeable layered niobates as a noble series of photocatalysts // Res. Chem. Intermed. 1994. Vol. 20, № 9. P. 895–908.
133. Machida M. et al. Photocatalytic property and electronic structure of triple-layered perovskite tantalates, $MCa_2Ta_3O_{10}$ (M = Cs, Na, H, and $C_6H_{13}NH_3$) // J. Phys. Chem. B. 2005. Vol. 109, № 16. P. 7801–7806.
134. Mitsuyama T. et al. Enhanced photocatalytic water splitting of hydrous $LiCa_2Ta_3O_{10}$ prepared by hydrothermal treatment // Bull. Chem. Soc. Jpn. 2008. Vol. 81, № 3. P. 401–406.
135. Takata T. et al. A highly active photocatalyst for overall water splitting with a hydrated layered perovskite structure // J. Photochem. Photobiol. A Chem. 1997. Vol. 106, № 1–3. P. 45–49.
136. Zvereva I. A., Rodionov I. A. Photocatalytic properties of perovskite-type layered oxides // Perovskite: Crystallography, Chemistry and Catalytic Performance. New York: Nova Science Publishers, 2013. P. 181–198.
137. Rodionov I. A. et al. Photocatalytic properties and hydration of perovskite-type layered titanates $A_2Ln_2Ti_3O_{10}$ (A = Li, Na, K; Ln = La, Nd) // Russ. J. Gen. Chem. 2012. Vol. 82, № 7. P. 1191–1196.
138. Takata T. et al. Photocatalytic decomposition of water on spontaneously hydrated

layered perovskites // Chem. Mater. 1997. Vol. 9, № 5. P. 1063–1064.

139. Gomez-Romero P., Sanchez C. Functional hybrid materials. Weinheim: Wiley-VCH, 2004. 434 p.
140. G. Kickelbick. Hybrid materials: synthesis, characterization, and applications. Weinheim: Wiley-VCH, 2007. 516 p.
141. Sugahara Y. Chemical processes employing inorganic layered compounds for inorganic and inorganic-organic hybrid materials // J. Ceram. Soc. Japan. 2014. Vol. 122, № 1427. P. 523–529.
142. Constantino V. R. L. et al. Intercalation compounds involving inorganic layered structures // An. Acad. Bras. Cienc. 2000. Vol. 72, № 1. P. 45–49.
143. Boykin J. R., Smith L. J. Rapid microwave-assisted grafting of layered perovskites with *n*-alcohols // Inorg. Chem. 2015. Vol. 54, № 9. P. 4177–4179.
144. Wang Y. et al. D-glucopyranose-modified compound of Ruddlesden-Popper phases $H_2CaTa_2O_7$: characterization and intercalation with Ag // J. Mater. Chem. A. 2014. Vol. 2, № 37. P. 15590–15597.
145. Takeda Y. et al. Preparation of a novel organic derivative of the layered perovskite bearing $HLaNb_2O_7 \cdot nH_2O$ interlayer surface trifluoroacetate groups // Mater. Res. Bull. 2006. Vol. 41, № 4. P. 834–841.
146. Jacobson A. J., Johnson J. W., Lewandowski J. T. Intercalation of the layered solid acid $HCa_2Nb_3O_{10}$ by organic amines // Mater. Res. Bull. 1987. Vol. 22, № 1. P. 45–51.
147. Suzuki H. et al. Reactions of alkoxyl derivatives of a layered perovskite with alcohols: substitution reactions on the interlayer surface of a layered perovskite // Chem. Mater. 2003. Vol. 15, № 3. P. 636–641.
148. Akbarian-Tefaghi S. et al. Rapid topochemical modification of layered perovskites via microwave reactions // Inorg. Chem. 2016. Vol. 55, № 4. P. 1604–1612.
149. Tahara S. et al. Reactivity of the Ruddlesden−Popper phase $H_2La_2Ti_3O_{10}$ with organic compounds: intercalation and grafting reactions // Chem. Mater. 2007. Vol. 19, № 9. P. 2352–2358.
150. Takahashi S. et al. Formation of methoxy-modified interlayer surface via the reaction between methanol and layered perovskite $HLaNb_2O_7 \cdot xH_2O$ // Inorg. Chem. 1995. Vol. 34, № 20. P. 5065–5069.

151. Tahara S., Sugahara Y. Interlayer surface modification of the protonated triple-layered perovskite $HCa_2Nb_3O_{10}\cdot xH_2O$ with *n*-alcohols // Langmuir. 2003. Vol. 19, № 22. P. 9473–9478.
152. Matsuda T., Udagawa M., Kunou I. Modification of the interlayer in lanthanum-niobium oxide and its catalytic reactions // J. Catal. 1997. Vol. 168, № 1. P. 26–34.
153. Hong Y., Kim S.-J. Intercalation of primary diamines in the layered perovskite oxides, $HSr_2Nb_3O_{10}$ // Bulletin of the Korean Chemical Society. 1996. Vol. 17, № 8. P. 730–735.
154. State S., Unit S. C. Polymerization of aniline in layered perovskites // Mater. Sci. 1995. Vol. 34, № 2–3. P. 175–179.
155. Silyukov O. I., Khramova A. D., Zvereva I. A. Synthesis of organic-inorganic derivatives of perovskite-like layered $HCa_2Nb_3O_{10}$ oxide with monoethanolamine and glycine // Glas. Phys. Chem. 2020. Vol. 46, № 3. P. 256–259.
156. Han Y.-S., Park I., Choy J.-H. Exfoliation of layered perovskite, $KCa_2Nb_3O_{10}$, into colloidal nanosheets by a novel chemical process // J. Mater. Chem. 2001. Vol. 11, № 4. P. 1277–1282.
157. Gopalakrishnan J., Bhat V., Raveau B. $A^ILaNb_2O_7$: a new series of layered perovskites exhibiting ion exchange and intercalation behaviour // Mater. Res. Bull. 1987. Vol. 22, № 3. P. 413–417.
158. Yoshioka S. et al. Hydrosilylation in the 2D interlayer space between inorganic layers: reaction between immobilized C=C groups on the interlayer surface of layered perovskite $HLaNb_2O_7\cdot xH_2O$ and chlorohydrosilanes // J. Organomet. Chem. 2003. Vol. 686, № 1–2. P. 145–150.
159. Wang C. et al. A new carbon intercalated compound of Dion-Jacobson phase $HLaNb_2O_7$ // J. Mater. Chem. 2012. Vol. 22, № 22. P. 11086–11092.
160. Shimada A. et al. Interlayer surface modification of the protonated ion-exchangeable layered perovskite $HLaNb_2O_7\cdot xH_2O$ with organophosphonic acids // Chem. Mater. 2009. Vol. 21, № 18. P. 4155–4162.
161. Takeda Y. et al. Organic derivatives of the layered perovskite $HLaNb_2O_7\cdot xH_2O$ with polyether chains on the interlayer surface: characterization, intercalation of $LiClO_4$, and ionic conductivity // J. Mater. Chem. 2008. Vol. 18, № 30. P. 3581–3587.

162. Schaak R. E., Mallouk T. E. Prying apart Ruddlesden-Popper phases: exfoliation into sheets and nanotubes for assembly of perovskite thin films // Solid State Ionics. 2000. Vol. 12, № 11. P. 3427–3434.

163. Shimizu K. et al. Pillaring of Ruddlesden–Popper perovskite tantalates, $H_2ATa_2O_7$ (A = Sr or $La_{2/3}$), with *n*-alkylamines and oxide nanoparticles // J. Mater. Chem. 2006. Vol. 16, № 8. P. 773.

164. Minich I. A. et al. Synthesis of organic–inorganic hybrids based on perovskite-like bismuth titanate $H_2K_{0.5}Bi_{2.5}Ti_4O_{13}\cdot H_2O$ and *n*-alkylamines // ACS Omega. 2020. Vol. 5, № 14. P. 8158–8168.

165. Minich I. A. et al. Grafting reactions of perovskite-like bismuth titanate $H_2K_{0.5}Bi_{2.5}Ti_4O_{13}\cdot H_2O$ with *n*-alcohols // Ceram. Int. 2020. Vol. 46, № 18. P. 29373–29381.

166. Tong Z. et al. Preparation and characterization of a transparent thin film of the layered perovskite, $K_2La_2Ti_3O_{10}$, intercalated with an ionic porphyrin // Chem. Lett. 2005. Vol. 34, № 5. P. 632–633.

167. Wang Y. et al. Preparation of interlayer surface tailored protonated double-layered perovskite $H_2CaTa_2O_7$ with *n*-alcohols, and their photocatalytic activity // RSC Adv. 2014. Vol. 4, № 8. P. 4047–4054.

168. Gopalakrishnan J., Uma S., Bhat V. Synthesis of layered perovskite oxides, $ACa_{2-x}La_xNb_{3-x}Ti_xO_{10}$ (A = K, Rb, Cs), and characterization of new solid acids, $HCa_{2-x}La_xNb_{3-x}Ti_xO_{10}$ ($0 < x \leq 2$), exhibiting variable bronsted acidity // Chem. Mater. 1993. Vol. 5, № 1. P. 132–136.

169. Uma S., Raju A. R., Gopalakrishnan J. Bridging the Ruddlesden-Popper and the Dion-Jacobson series of layered perovskites: synthesis of layered oxides, $A_{2-x}La_2Ti_{3-x}Nb_xO_{10}$ (A = K, Rb), exhibiting ion exchange // J. Mater. Chem. 1993. Vol. 3, № 7. P. 709–713.

170. Guo T. et al. Synthesis and photocatalytic properties of a polyaniline-intercalated layered protonic titanate nanocomposite with a p−n heterojunction structure // J. Phys. Chem. C. 2010. Vol. 114, № 11. P. 4765–4772.

171. Zhu H., Yao X., Hua S. Nanocomposite of polyaniline and a layered niobate acid host: synthesis, electrochemical studies, and photocatalytic properties // Polym. Compos. 2013. Vol. 34, № 6. P. 834–841.

172. Liu C. et al. The nanocomposite of polyaniline and nitrogen-doped layered $HTiNbO_5$ with excellent visible-light photocatalytic performance // Phys. Chem. Chem. Phys. 2014. Vol. 16, № 26. P. 13409–13417.
173. Zheng B. et al. Facile layer-by-layer self-assembly of 2D perovskite niobate and layered double hydroxide nanosheets for enhanced photocatalytic oxygen generation // Int. J. Hydrogen Energy. 2021. Vol. 46, № 69. P. 34276–34286.
174. Treacy M. M. J. et al. Electron microscopy study of delamination in dispersions of the perovskite-related layered phases $K[Ca_2Na_{n-3}Nb_nO_{3n-1}]$: evidence for single-layer formation // Chem. Mater. 1990. Vol. 2. P. 279–286.
175. Akbarian-Tefaghi S. et al. Rapid exfoliation and surface tailoring of perovskite nanosheets via microwave-assisted reactions // ChemNanoMat. 2017. Vol. 3, № 8. P. 538–550.
176. Payet F. et al. Fast and efficient shear-force assisted production of covalently functionalized oxide nanosheets // J. Colloid Interface Sci. 2022. Vol. 607. P. 621–632.
177. Ebina Y., Sasaki T., Watanabe M. Study on exfoliation of layered perovskite-type niobates // Solid State Ionics. 2002. Vol. 151. P. 177–182.
178. Ebina Y. et al. Restacked perovskite nanosheets and their Pt-loaded materials as photocatalysts // Chem. Mater. 2002. Vol. 1, № 12. P. 4390–4395.
179. Yang Y. et al. Preparation of monolayer $HSr_2Nb_3O_{10}$ nanosheets for photocatalytic hydrogen evolution // Dalt. Trans. 2019. Vol. 48, № 29. P. 11136–11141.
180. Maeda K., Mallouk T. E. Comparison of two- and three-layer restacked Dion–Jacobson phase niobate nanosheets as catalysts for photochemical hydrogen evolution // J. Mater. Chem. 2009. Vol. 19, № 27. P. 4813–4818.
181. Shi J. et al. One-pot fabrication of 2D/2D $HCa_2Nb_3O_{10}$/g-$C_3N_4$ type II heterojunctions towards enhanced photocatalytic $H_2$ evolution under visible-light irradiation // Catal. Sci. Technol. 2020. Vol. 10, № 17. P. 5896–5902.
182. Xiong J. et al. A hybrid of CdS/$HCa_2Nb_3O_{10}$ ultrathin nanosheets for promoting photocatalytic hydrogen evolution // Dalt. Trans. 2017. Vol. 46, № 40. P. 13935–13942.
183. Hu Y. et al. Self-assembled nanohybrid of cadmium sulfide and calcium niobate: photocatalyst with enhanced charge separation for efficient visible light induced hydrogen generation // Catal. Today. 2018. Vol. 315. P. 117–125.

184. Luo D. et al. Visible-light-driven $HSr_2Nb_3O_{10}$/CdS heterojunctions for high hydrogen evolution activity // Int. J. Hydrogen Energy. 2020. Vol. 45, № 4. P. 2896–2908.
185. Xie Z. et al. Noble-metal-free $Co_xP$ nanoparticles: modified perovskite oxide ultrathin nanosheet photocatalysts with significantly enhanced photocatalytic hydrogen evolution activity // Nanotechnology. 2020. Vol. 31, № 32.
186. Li D. et al. Noble-metal-free $Mo_2C$ co-catalsyt modified perovskite oxide nanosheet photocatalysts with enhanced hydrogen evolution performance // Colloids Surfaces A Physicochem. Eng. Asp. 2021. Vol. 615, № 126252.
187. Liu Y. et al. Construction of 2D-composite $HCa_2Nb_3O_{10}$/$CaNb_2O_6$ heterostructured photocatalysts with enhanced hydrogen production performance // New J. Chem. 2018. Vol. 42, № 1. P. 681–687.
188. Li D. et al. Graphene-sensitized perovskite oxide monolayer nanosheets for efficient photocatalytic reaction // Adv. Funct. Mater. 2018. Vol. 28, № 52. P. 1806284.
189. Nishioka S. et al. Excited carrier dynamics in a dye-sensitized niobate nanosheet photocatalyst for visible-light hydrogen evolution // ACS Catal. 2021. Vol. 11, № 2. P. 659–669.
190. Maeda K. et al. Hybrids of a ruthenium(II) polypyridyl complex and a metal oxide nanosheet for dye-sensitized hydrogen evolution with visible light: effects of the energy structure on photocatalytic activity // ACS Catal. 2015. Vol. 5, № 3. P. 1700–1707.
191. Greene W. N., Roy N. Photocatalytic hydrogen evolution from hexaniobate nanoscrolls and calcium niobate nanosheets sensitized by ruthenium(II) bipyridyl complexes // J. Phys. Chem. C. 2009. Vol. 113, № 18. P. 7962–7969.
192. Ida S. et al. Photoluminescence of perovskite nanosheets prepared by exfoliation of layered oxides, $K_2Ln_2Ti_3O_{10}$, $KLnNb_2O_7$, and $RbLnTa_2O_7$ (Ln: lanthanide ion) // J. Am. Chem. Soc. 2008. Vol. 130, № 22. P. 7052–7059.
193. Kawashima K. et al. Protonated oxide, nitrided, and reoxidized $K_2La_2Ti_3O_{10}$ crystals: visible-light-induced photocatalytic water oxidation and fabrication of their nanosheets // ACS Sustain. Chem. Eng. 2017. Vol. 5, № 1. P. 232–240.
194. Sun Y. et al. CdS nanoparticles decorated $K^+Ca_2Nb_3O_{10}^-$ nanosheets with enhanced photocatalytic activity // Mater. Lett. 2018. Vol. 229. P. 236–239.
195. Jiang D. et al. Perovskite oxide ultrathin nanosheets/g-$C_3N_4$ 2D-2D heterojunction

photocatalysts with significantly enhanced photocatalytic activity towards the photodegradation of tetracycline // Appl. Catal. B Environ. 2017. Vol. 201. P. 617–628.

196. Ma X. et al. 2D/2D heterojunctions of $WO_3$ nanosheet/$K^+Ca_2Nb_3O_{10}^-$ ultrathin nanosheet with improved charge separation efficiency for significantly boosting photocatalysis // Catal. Sci. Technol. 2017. Vol. 7, № 16. P. 3481–3491.
197. Ding Y. et al. Microwave-mechanochemistry-assisted synthesis of Z-scheme $HSr_2Nb_3O_{10}/WO_3$ heterojunctions for improved simulated sunlight driven photocatalytic activity // J. Environ. Chem. Eng. 2021. Vol. 9, № 1. P. 104624.
198. Zhou Y. et al. Controllable doping of nitrogen and tetravalent niobium affords yellow and black calcium niobate nanosheets for enhanced photocatalytic hydrogen evolution // RSC Adv. 2016. Vol. 6, № 69. P. 64930–64936.
199. Blasse G. Crystallographic data of sodium lanthanide titanates ($NaLnTiO_4$) // J. Inorg. Nucl. Chem. 1968. Vol. 30. P. 656–658.
200. Byeon S., Kileung P., Park K. Structure and ionic conductivity of $NaLnTiO_4$, comparison with those of $Na_2Ln_2Ti_3O_{10}$ (Ln = La, Nd, Sm, and Gd) // J. Solid State Chem. 1996. Vol. 121, № 121. P. 430–436.
201. Pradhan D. K. et al. Complex impedance studies on a layered perovskite ceramic oxide—$NaNdTiO_4$ // Mater. Sci. Eng. B. 2005. Vol. 116, № 1. P. 7–13.
202. Pradhan D. K. et al. Complex impedance analysis of $NaLaTiO_4$ electroceramics // J. Mater. Sci. Mater. Electron. 2006. Vol. 17, № 3. P. 157–164.
203. Toda K., Kurita S., Sato M. Synthesis and ionic conductivity of novel layered perovskite compounds, $AgLaTiO_4$ and $AgEuTiO_4$ // Solid State Ionics. 1995. Vol. 81, № 3–4. P. 267–271.
204. Sivakumar T., Seshadri R., Gopalakrishnan J. Bridging the Ruddlesden−Popper and the Aurivillius phases: synthesis and structure of a novel series of layered perovskite oxides, $(BiO)LnTiO_4$ (Ln = La, Nd, Sm) // J. Am. Chem. Soc. 2001. Vol. 123, № 46. P. 11496–11497.
205. Kim S. Y. et al. Structure of new layered oxides $M^{II}_{0.5}LaTiO_4$ (M = Co, Cu, and Zn) synthesized by the ion-exchange reaction // Chem. Mater. 2002. Vol. 14, № 4. P. 1643–1648.
206. Neiner D., Golub V., Wiley J. B. Synthesis and characterization of the new layered

perovskite, $Na_{0.10}(VO)_{0.45}LaTiO_4 \cdot nH_2O$ // Mater. Res. Bull. 2004. Vol. 39, № 10. P. 1385–1392.

207. Lavat A. E., Baran E. J. IR-spectroscopic characterization of $NaLn^{III}TiO_4$ and $AgLn^{III}TiO_4$ oxides related to the $K_2NiF_4$ structural type // J. Alloys Compd. 2006. Vol. 419, № 1–2. P. 334–336.
208. Byeon S., Yoon J.-J., Lee S.-O. A new family of protonated oxides $HLnTiO_4$ (Ln = La, Nd, Sm, and Gd) // J. Solid State Chem. 1996. Vol. 127, № 1. P. 119–122.
209. Nishimoto S. et al. Neutron diffraction study on protonated and hydrated layered perovskite // J. Solid State Chem. 2006. Vol. 179, № 11. P. 3308–3313.
210. Nishimoto S., Matsuda M., Miyake M. Novel protonated and hydrated Ruddlesden–Popper phases, $H_xNa_{1-x}LaTiO_4 \cdot yH_2O$, formed by ion-exchange/intercalation reaction // J. Solid State Chem. 2005. Vol. 178, № 3. P. 811–818.
211. Singh S. J., Jayaram R. V. Chemoselective *O*-*tert*-butoxycarbonylation of hydroxy compounds using $NaLaTiO_4$ as a heterogeneous and reusable catalyst // Tetrahedron Lett. 2008. Vol. 49, № 27. P. 4249–4251.
212. Rodionov I. A., Silyukov O. I., Zvereva I. A. Study of photocatalytic activity of layered oxides: $NaNdTiO_4$, $LiNdTiO_4$, and $HNdTiO_4$ titanates // Russ. J. Gen. Chem. 2012. Vol. 82, № 4. P. 635–638.
213. Silyukov O. I. et al. Phase transformations during $HLnTiO_4$ (Ln = La, Nd) thermolysis and photocatalytic activity of obtained compounds // J. Solid State Chem. 2015. Vol. 226. P. 101–106.
214. Reddy V., Hwang D., Lee J. Effect of Zr substitution for Ti in $KLaTiO_4$ for photocatalytic water splitting // Catal. Letters. 2003. Vol. 90, № 3. P. 39–44.
215. Toda K., Watanabe J., Sato M. Crystal structure determination of ion-exchangeable layered perovskite compounds, $K_2La_2Ti_3O_{10}$ and $Li_2La_2Ti_3O_{10}$ // Mater. Res. Bull. 1996. Vol. 31, № 11. P. 1427–1435.
216. Toda K., Watanabeb J., Satob M. Synthesis and ionic conductivity of new layered perovskite compound, $Ag_2La_2Ti_3O_{10}$ // Solid State Ionics. 1996. Vol. 90, № 1–4. P. 15–19.
217. Tan S. et al. Structure and antibacterial activity of new layered perovskite compounds // Trans. Nonferrous Met. Soc. China. 2007. Vol. 17, № 2. P. 257–261.

218. Rodionov I. A. et al. Protonation and photocatalytic activity of the $Rb_2La_2Ti_3O_{10}$ layered oxide in the reaction of hydrogen production // Int. J. Photoenergy. 2017. № 9628146.
219. Rodionov I. A., Fateev S. A., Zvereva I. A. Synthesis of a new layered $Rb_2Nd_2Ti_3O_{10}$ oxide, its hydration and protonation // Glas. Phys. Chem. 2017. Vol. 43, № 6. P. 593–596.
220. Rodionov I. A., Fateev S. A., Zvereva I. A. Effect of protonation on the photocatalytic activity of the layered titanate $Rb_2Nd_2Ti_3O_{10}$ // Russ. J. Gen. Chem. 2017. Vol. 87, № 11. P. 2728–2729.
221. Wu J. et al. Synthesis and photocatalytic properties of layered nanocomposite $H_2La_2Ti_3O_{10}/Fe_2O_3$ // Scr. Mater. 2006. Vol. 54, № 7. P. 1357–1362.
222. Huang Y. et al. Synthesis and photocatalytic properties of $H_2La_2Ti_3O_{10}/TiO_2$ intercalated nanomaterial // J. Porous Mater. 2006. Vol. 13, № 1. P. 55–59.
223. Campbell K. D. Layered and double perovskites as methane coupling catalysts // Catal. Today. 1992. Vol. 13, № 2–3. P. 245–253.
224. Silyukov O. I., Kurnosenko S. A., Zvereva I. A. Intercalation of methylamine into the protonated forms of layered perovskite-like oxides $HLnTiO_4$ (Ln = La and Nd) // Glas. Phys. Chem. 2018. Vol. 44, № 5. P. 428–432.
225. Kurnosenko S. A. et al. Synthesis and thermal stability of new inorganic-organic perovskite-like hybrids based on layered titanates $HLnTiO_4$ (Ln = La, Nd) // Ceram. Int. 2020. Vol. 46, № 4. P. 5058–5068.
226. Kurnosenko S. A. et al. Inorganic-organic derivatives of layered perovskite-like titanates $HLnTiO_4$ (Ln = La, Nd) with *n*-amines and *n*-alcohols: synthesis, thermal, vacuum and hydrolytic stability // Ceram. Int. 2022. Vol. 48, № 5. P. 7240–7252.
227. Kim J. W., Kim A. Absolute work function measurement by using photoelectron spectroscopy // Curr. Appl. Phys. 2021. Vol. 31. P. 52–59.
228. Gopalakrishnan J., Bhat V. $A_2Ln_2Ti_3O_{10}$ (A = potassium or rubidium; Ln = lanthanum or rare earth): a new series of layered perovskites exhibiting ion exchange // Inorg. Chem. 1987. Vol. 26, № 26. P. 4299–4301.
229. Kurnosenko S. A. et al. Photocatalytic activity and stability of organically modified layered perovskite-like titanates $HLnTiO_4$ (Ln = La, Nd) in the reaction of hydrogen evolution from aqueous methanol // Catalysts. 2023. Vol. 13(4), № 749.

230. Kurnosenko S. A. et al. Photocatalytic activity of *n*-alkylamine and *n*-alkoxy derivatives of layered perovskite-like titanates $H_2Ln_2Ti_3O_{10}$ (Ln = La, Nd) in the reaction of hydrogen production from an aqueous solution of methanol // Catalysts. 2021. Vol. 11(11), № 1279.
231. Rodionov I. A. et al. Layered titanate $H_2Nd_2Ti_3O_{10}$ intercalated with *n*-butylamine: a new highly efficient hybrid photocatalyst for hydrogen production from aqueous solutions of alcohols // Front. Chem. 2019. Vol. 7, № 863.
232. Rodionov I. A. et al. Photocatalytic hydrogen generation from aqueous methanol solution over *n*-butylamine-intercalated layered titanate $H_2La_2Ti_3O_{10}$: activity and stability of the hybrid photocatalyst // Catalysts. 2022. Vol. 12(12), № 1556.
233. Kurnosenko S. A. et al. Photocatalytic hydrogen production from aqueous solutions of glucose and xylose over layered perovskite-like oxides $HCa_2Nb_3O_{10}$, $H_2La_2Ti_3O_{10}$ and their inorganic-organic derivatives // Nanomaterials. 2022. Vol. 12(15), № 2717.
234. Moniruddin M. et al. Recent progress on perovskite materials in photovoltaic and water splitting applications // Mater. Today Energy. 2018. Vol. 7. P. 246–259.
235. Li Q., Anpo M., Wang X. Application of photoluminescence spectroscopy to elucidate photocatalytic reactions at the molecular level // Res. Chem. Intermed. 2020. Vol. 46, № 10. P. 4325–4344.
236. Shibata H. et al. Hydroxyl radical generation depending on $O_2$ or $H_2O$ by a photocatalyzed reaction in an aqueous suspension of titanium dioxide // Biosci. Biotechnol. Biochem. 1998. Vol. 62, № 12. P. 2306–2311.
237. Nosaka Y., Nosaka A. Understanding hydroxyl radical (·OH) generation processes in photocatalysis // ACS Energy Lett. 2016. Vol. 1, № 2. P. 356–359.
238. Cui W. et al. Preparation of $Pt/K_2La_2Ti_3O_{10}$ and its photo-catalytic activity for hydrogen evolution from methanol water solution // Sci. China Ser. B. 2006. Vol. 49, № 2. P. 162–168.
239. Rodionov I. A., Mechtaeva E. V., Zvereva I. A. Photocatalytic activity of $TiO_2$-$MO_x$ composites in the reaction of hydrogen generation from aqueous isopropanol solution // Russ. J. Gen. Chem. 2014. Vol. 84, № 4. P. 611–616.
240. Voytovich V. V. et al. Study of *n*-alkylamine intercalated layered perovskite-like niobates $HCa_2Nb_3O_{10}$ as photocatalysts for hydrogen production from an aqueous

solution of methanol // Front. Chem. 2020. Vol. 8, № 300.

241. Voytovich V. V. et al. Synthesis of *n*-alkoxy derivatives of layered perovskite-like niobate $HCa_2Nb_3O_{10}$ and study of their photocatalytic activity for hydrogen production from an aqueous solution of methanol // Catalysts. 2021. Vol. 11(8), № 897.
242. Khramova A. D. et al. Synthesis and characterization of inorganic-organic derivatives of layered perovskite-like niobate $HSr_2Nb_3O_{10}$ with *n*-amines and *n*-alcohols // Molecules. 2023. Vol. 28(12), № 4807.
243. Janković I. A. et al. Surface modification of colloidal $TiO_2$ nanoparticles with bidentate benzene derivatives // J. Phys. Chem. C. 2009. Vol. 113, № 29. P. 12645–12652.
244. Higashimoto S. et al. Photocatalysis of titanium dioxide modified by catechol-type interfacial surface complexes (ISC) with different substituted groups // J. Catal. 2015. Vol. 329. P. 286–290.
245. Kurnosenko S. A. et al. Exfoliation of methylamine and *n*-butylamine derivatives of layered perovskite-like oxides $HLnTiO_4$ and $H_2Ln_2Ti_3O_{10}$ (Ln = La, Nd) into nanolayers // Glas. Phys. Chem. 2021. Vol. 47, № 4. P. 372–381.
246. Kurnosenko S. A. et al. Highly efficient liquid-phase exfoliation of layered perovskite-like titanates $HLnTiO_4$ and $H_2Ln_2Ti_3O_{10}$ (Ln = La, Nd) into nanosheets // Nanomaterials. 2023. Vol. 13(23), № 3052.
247. Kurnosenko S. A. et al. Influence of $HB_2Nb_3O_{10}$-based nanosheet photocatalysts (B = Ca, Sr) preparation method on hydrogen production efficiency // Catalysts. 2023. Vol. 13(3), № 614.
248. Hu Y., Guo L. Rapid preparation of perovskite lead niobate nanosheets by ultrasonic-assisted exfoliation for enhanced visible-light-driven photocatalytic hydrogen production // ChemCatChem. 2015. Vol. 7, № 4. P. 584–587.
249. Zhou H. et al. Assembly of core-shell structures for photocatalytic hydrogen evolution from aqueous methanol // Chem. Mater. 2010. Vol. 22, № 11. P. 3362–3368.
250. Zhang S. et al. Structural evolution of Ni-based co-catalysts on $[Ca_2Nb_3O_{10}]^-$ nanosheets during heating and their photocatalytic properties // Catalysts. 2020. Vol. 10(1), № 13.

## Acknowledgements

The applicant expresses sincere gratitude and deep appreciation to his scientific supervisor Dr. Zvereva I. A., head of the department of chemical thermodynamics and kinetics Dr. Toikka A. M., Ph.D. Silyukov O. I., Ph.D. Rodionov I. A., Ph.D. Minich Y. A., Voytovich V. V., Malygina E. N., Maksimova E. A., Gruzdeva E. O., as well as other employees and students of the scientific group «Thermodynamic and kinetic studies of nanostructured materials» for their interest in work, participation in a number of investigations on its topic and discussion of the results obtained.

The work was carried out with the financial support of the Russian Science Foundation (grants № 19-13-00184, № 20-73-00027 and № 22-73-10110) using the equipment of the resource centers of the Saint Petersburg State University Research park «Center for X-ray diffraction studies», «Center for optical and laser research», «Center for magnetic resonance», «Center for thermogravimetric and calorimetric research», «Center for chemical analysis and materials research», «Interdisciplinary center for nanotechnology», «Center for studies in surface science», «Center for diagnostics of functional materials for medicine, pharmacology and nanoelectronics», «Center for innovative technologies of composite nanomaterials».